TECHNISCHE UNIVERSITÄT MÜNCHEN

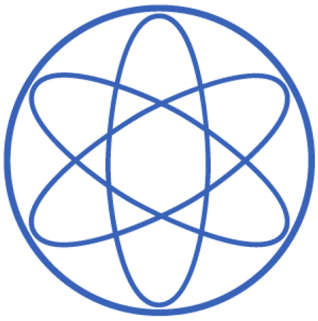

Physik-Department

Forschungs-Neutronenquelle
Heinz Maier-Leibnitz (FRM II)

Qualification of U-Mo Fuel for Research Reactors: Characterisation of the Interfaces Between U-Mo Kernel, Diffusion Barrier and Al Matrix Under Heavy Ion Irradiation

Dissertation

Jingyi Shi

April 2021

Prof. Dr. Winfried Petry
Physik-Department, Lehrstuhl E13

TECHNISCHE UNIVERSITÄT MÜNCHEN

Physik Department

Lehrstuhl für Funktionelle Materialien (E13)

Forschungs-Neutronenquelle Heinz Maier-Leibnitz

Qualification of U-Mo Fuel for Research Reactors: Characterisation of the Interfaces Between U-Mo Kernel, Diffusion Barrier and Al Matrix Under Heavy Ion Irradiation

Jingyi Shi

Vollständiger Abdruck der von der Fakultät für Physik der Technischen Universität München zur Erlangung des akademischen Grades eines

Doktors der Naturwissenschaften (Dr. rer. nat.)

genehmigten Dissertation.

Vorsitzender:		apl. Prof. Dr. Norbert Kaiser
Prüfer der Dissertation:	1.	Prof. Dr. Winfried Petry
	2.	Prof. Dr. Peter Böni

Die Dissertation wurde am 14.04.2021 bei der Technischen Universität München eingereicht und durch die Fakultät für Physik am 29.06.2021 angenommen.

“非淡泊无以明志，非宁静无以致远。”
- 诸葛亮

“A genuine ambition is derived from simplicity of life,
and a grand horizon is conceived in serenity of mind.”
– Zhuge Liang

Abstract

Metallic uranium-molybdenum (U-Mo) alloy fuels are known to suffer from excessive swelling under irradiation due to the build-up of interdiffusion layers (IDLs) with undesirable properties between U-Mo kernels and the surrounding Al matrix. At high burn-ups, additional accelerated swelling due to U-Mo restructuring occurs. Both phenomena can be investigated using swift heavy ion irradiation as a partial replacement of in-pile experiments. The gracefully and independently controllable conditions additionally enable quantitative evaluation of irradiation parameters like dose rate and temperature that are hardly accessible otherwise.

Fuel swelling due to the growth of IDLs was investigated with two main goals:

- To uncover the underlying dynamics, a series of ^{127}I ion irradiations were performed on Al/U-Mo bilayer systems to compare actual and predicted IDL properties. Using an empirical irradiation equivalent model, a fully quantitative comparison between swift heavy ion and in-pile irradiation was first established and successfully verified. Particularly, the growth dynamics as a function of irradiation temperature was determined. An athermal regime and a temperature-dependent regime characterized by a transition temperature were identified. Transmission electron microscopy (TEM) analysis revealed an amorphous-to-crystalline phase transition at the critical temperature, including a change of IDL composition.

- To evaluate solutions for suppressing or delaying the IDL growth, a series of swift heavy ion irradiations on the fuel system Al/X/U-Mo (X = Mo, Zr, W or ZrN) under selected conditions was performed. The irradiation behaviours of the four coating barriers in terms of irradiation dose, temperature, as well as coating thickness and quality were systematically and quantitatively studied. W and ZrN coating barriers show promising results. A comparison with the in-pile results of SELENIUM and SEMPER FIDELIS tests is presented, where a good agreement between ion and in-pile irradiation is seen.

To study the restructuring effect, an uncoated U-Mo foil was irradiated with 80 MeV ^{127}I ions up to an extremely high dose. Electron backscatter diffraction

(EBSD) analysis evidences that polygonization is the underlying mechanism of the observed grain refinement, as the newly formed small grains are separated by mainly low-angle grain boundaries. The obtained threshold dose for the onset of polygonization is found lower than that found in-pile, which is a result of the significantly higher dose rate of ion irradiation and the formation of oxides.

Zusammenfassung

Metallische Kernbrennstoffe aus Uran-Molybdän (U-Mo)-Legierung sind dafür bekannt, dass sie unter Bestrahlung an übermäßiger Schwellung leiden, die auf den Aufbau von Interdiffusionsschichten (IDLs) mit unerwünschten Eigenschaften zwischen U-Mo Partikeln und der umgebenden Al-Matrix zurückzuführen ist. Bei hohen Abbränden kommt es zusätzlich zu einer beschleunigten Schwellung aufgrund von U-Mo Umstrukturierungen. Beide Phänomene können mit schneller Schwerionenbestrahlung als teilweiser Ersatz von in-pile Experimenten untersucht werden. Die schonend und unabhängig steuerbaren Bedingungen ermöglichen zusätzlich eine quantitative Auswertung von Bestrahlungsparametern wie Dosisleistung und Temperatur, die sonst kaum zugänglich sind.

Die Schwellung aufgrund des Wachstums von IDLs wurde mit zwei Hauptzielen untersucht:

- Um die zugrundeliegende Dynamik aufzudecken, wurde eine Serie von ^{127}I Ionenbestrahlungen an Al/U-Mo Doppelschichtsystemen durchgeführt, um die tatsächlichen und vorhergesagten IDL Eigenschaften zu vergleichen. Unter Verwendung eines empirischen in-pile Modells wurde erstmals ein vollständig quantitativer Vergleich zwischen schneller Schwerionen- und in-pile Bestrahlung erstellt und erfolgreich verifiziert. Insbesondere wurde die Wachstumsdynamik als Funktion der Bestrahlungstemperatur ermittelt. Es wurden ein athermisches Regime und ein temperaturabhängiges Regime identifiziert, das durch eine Übergangstemperatur gekennzeichnet ist. Transmissionselektronenmikroskopische (TEM) Analysen zeigten einen amorphen-zu-kristallinen Phasenübergang bei der kritischen Temperatur, einschließlich einer Änderung der IDL Zusammensetzung.

- Um Lösungen zur Unterdrückung oder Verzögerung des IDL Wachstums zu evaluieren, wurde eine Serie von schnellen Schwerionenbestrahlungen auf das Brennstoffsystem Al/X/U-Mo (X = Mo, Zr, W oder ZrN) unter ausgewählten Bedingungen durchgeführt. Frühere Studien haben bereits gezeigt, dass diese Materialien potentielle Kandidaten für eine

Diffusionsbarriere darstellen, jedoch wurden keine quantitativen Analysen unternommen. In dieser Arbeit wurden die Bestrahlungsverhalten der vier Schichtbarrieren in Bezug auf Bestrahlungsdosis, Temperatur, sowie Schichtdicke und Schichtqualität systematisch und quantitativ untersucht. W und ZrN Beschichtungsbarrieren zeigen vielversprechende Ergebnisse. Ein Vergleich mit den in-pile Ergebnissen der SELENIUM und SEMPER FIDELIS Bestrahlungstests wird vorgestellt, wobei eine gute Übereinstimmung zwischen Ionen- und in-pile Bestrahlung zu erkennen ist.

Um den Restrukturierungseffekt zu untersuchen, wurde eine unbeschichtete U-Mo Folie mit 80 MeV ^{127}I Ionen bis zu einer extrem hohen Dosis bestrahlt. Die Analyse mit Elektronenrückstreubeugung (EBSD) belegt, dass die Polygonisierung der zugrundeliegende Mechanismus der beobachteten Kornverfeinerung ist, da die neu gebildeten kleinen Körner hauptsächlich durch Kleinwinkelkorngrenzen getrennt sind. Die hierfür ermittelte Schwellendosis für das Einsetzen der Polygonisierung ist niedriger als die der in-pile Experimente, was auf die deutlich höhere Dosisleistung der Ionenbestrahlung und die Bildung von Oxiden zurückzuführen ist.

Contents

List of Abbreviations

BCC	**B**ody **C**entered **C**ubic
BF	**B**right **F**ield
BOL	**B**eginning **O**f **L**ife
BPM	**B**eam **P**rofile **M**onitor
BSE	**B**ack**S**cattered **E**lectron
DF	**D**ark **F**ield
DC	**D**irect **C**urrent
DPA	**D**isplacements **P**er **A**tom
EBSD	**E**lectron-**B**ack**S**catter-**D**iffraction
EDX	**E**nergy **D**ispersive **X**-Ray spectroscopy
EM	**E**lctron **M**icroprobe
FCC	**F**ace **C**entered **C**ubic
FD	**F**ission **D**ensity
FEM	**F**inite **E**lement **M**ethod
FIB	**F**ocused **I**on **B**eam
FR	**F**ission **R**ate
GB	**G**ain **B**oundary
GIS	**G**as **I**njection **S**ystem
HBS	**H**igh **B**urn-up **S**tructure
HEU	**H**igh-**E**nriched **U**ranium
HRTEM	**H**igh-**R**esolution **T**ransmission **E**lectron **M**icroscopy
IDL	**I**nter**D**iffusion **L**ayer
INFCE	**IN**ternational **F**uel **C**ycle **E**valuation conference
IQ	**I**mage **Q**uality
IPF	**I**nverse **P**ole **F**igure
LEU	**L**ow-**E**nriched **U**ranium
MLL	**M**aier-**L**eibnitz **L**aboratory
PIE	**P**ost-**I**rradiation **E**xamination
PKA	**P**rimary **K**nock-on **A**tom
PVD	**P**hysical **V**apour **D**eposition
RED	**R**adiation-**E**nhanced **D**iffusion
ROI	**R**egion **O**f **I**nterest

RERTR	**R**educed **E**nrichment for **R**esearch and **T**est **R**eactors
RF	**R**adio **F**requency
SADP	**S**elected **A**rea **D**iffraction **P**attern
SE	**S**econdary **E**lectron
SEM	**S**canning **E**lectron **M**icroscopy
SI	**S**econdary **I**on
SiRL	**Si**-**R**ich **L**ayer
SRIM	**S**topping and **R**ange of **I**ons in **M**atter
SZD	**S**tructure **Z**one **D**iagram
TCP	**T**hermal **C**onductive **P**aste
TEM	**T**ransmission **E**lectron **M**icroscopy
TRIM	**TR**ansport of **I**ons in **M**atter
TUM	**T**echnische **U**niversität **M**ünchen
U-Mo	**U**ranium–**Mo**lybdenum
U-10Mo	**U**ranium - **10** wt.%**Mo**lybdenum
U-7Mo	**U**ranium - **7** wt.%**Mo**lybdenum
XRD	**X**-**R**ay **D**iffraction

Chapter 1

Motivation

1.1 The FRM II

The unique properties of neutrons make them more and more essential. For instance, neutrons are able to show the structure and dynamics of materials preciously, which significantly benefits basic material science and thereby makes them a powerful tool in industrial product development and manufacturing. The importance of neutrons in nuclear physics, materials science, and condensed matter is already well known. Beyond that, neutrons are necessary for material irradiation testing and the production of radioisotopes for both industry and medicine [1]. Usually, free neutrons are obtained by fission and spallation, taking place in fission reactors and spallation sources, respectively. Nuclear reactors are often associated with power generation. It is the case for nuclear power plants, which exist predominately for producing electricity. Research reactors, however, serve primarily as neutron sources, while the minor amount of heat is a by-product. During operation, neutron beams are emitted and used for neutron scattering, irradiation testing of materials, production of radioisotopes for nuclear medicine, etc., addressing the needs of a diverse community.

The neutron source Forschungs-Neutronenquelle Heinz Maier-Leibnitz, or FRM II for short, is capable of producing the highest thermal neutron flux of $\sim 8 \cdot 10^{14}\,\mathrm{n}/\left(\mathrm{cm}^2 \cdot \mathrm{s}\right)$ [2] with 20 megawatts of thermal power, making it the most powerful neutron source in Germany, and the one exhibiting the highest flux-to-power ratio among the existing 222 (database [3] at the time of writing) operational research reactors worldwide. The flux-to-power ratio characterises the efficiency of a modern research reactor. The FRM II is a heavy water moderated, light water cooled pool reactor being in user operation since 2005 (Figure 1.1). Its high performance is attributed to the concept of a compact core reactor. The compact core consists of only one single fuel element with a cylindrical geometry, which consists of as many as 113 involute shaped fuel plates separated by cooling channels, as illustrated in Figure 1.2. The plates themselves

have a thickness of 1.36 mm, while the width of the cooling channels is constantly 2.2 mm thanks to the involute-shape. The hafnium control rod moves inside the central hole. With this design and a loading of the core with 8.1 kg high-enriched uranium, one fuel element is sufficient for 60 days of continuous reactor operation at full power i.e. 20 MW.

FIGURE 1.1: Left: overview of FRM II. Right: section of the reactor pool. The fuel element in the central channel is indicated by the red arrow. [4]

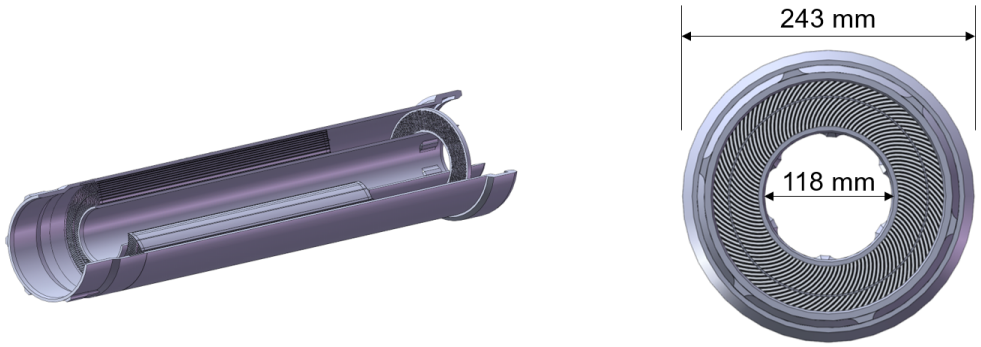

FIGURE 1.2: CAD model of the fuel element of FRM II in the sectional view (left) and seen from below (right). [5]

Currently, FRM II uses high-enriched (93 wt% ^{235}U) uranium in the form of U_3Si_2 powder dispersed in an aluminium matrix as the fuel meat. The fuel plate is completed by cladding the fuel meat with an AlFeNi frame. To avoid the huge peak in the distribution of power density at the outer edge of the core, each plate is graded into two zones with different densities of uranium, i.e. 3.0 gU/cm^3 in the inner zone near the centre of the fuel element and 1.5 gU/cm^3 in the zone near the outer edge. In addition, a boron ring is placed near the bottom of the core to achieve further power flattening. In total, the whole core contains approximately 8.1 kg of uranium.

1.2 From high-enriched to low-enriched uranium fuel

By countering the risk of proliferation, it was first recommended in the late 1970s at the International Fuel Cycle Evaluation (INFCE) conference, that the high-enriched uranium (93 wt% ^{235}U, denoted as HEU) in research reactor fuels should be converted to low-enriched uranium ($<$ 20 wt% ^{235}U, denoted as LEU), which is far below the requirements for manufacturing nuclear weapons. In 1978, the Reduced Enrichment Research and Test Reactor program (RERTR) [6] was launched by the U.S. Department of Energy (DOE). The mission of this program is to minimize the use of weapons-grade uranium worldwide and thus to reduce the risk of proliferation. In practice, the RERTR program is to facilitate the conversion of research and test reactor fuels from HEU to LEU. To achieve a successful conversion, the following aspects should be taken into account: Since only the fuel element will be replaced, the new fuel element should be compatible with the current core installation, which means its size and geometry should not be significantly altered. On the other hand, the thermal power of FRM II remains unchanged, while the high thermal neutron flux is expected to be preserved to fulfill the scientific requirements. To this end, the reduced enrichment needs to be compensated by higher uranium density in the fuel element. Up to now, more than 70 research reactors have been converted [7]. To contribute to these international efforts, FRM II established the research group "High-Density Fuel Development" in 2003, aiming at developing new nuclear fuels with higher uranium densities to reduce the enrichment in fuel elements of research reactors, such as the FRM II.

The most straightforward way to reach a high uranium density is to use pure uranium as fuel meat. However, due to its orthorhombic α-phase, pure uranium can be strongly deformed with increasing temperature, leading to poor irradiation performance. It turned out that with small alloying additions, the uranium can be kept in the metastable γ-phase at room temperature [8]. Investigations of alloying partners revealed that an alloy of uranium and molybdenum (U-Mo) is one of the most prospective candidates for a new high-density LEU fuel [9]. Thanks to its isotropic nature, which is attributed to the bcc crystal structure [10], i.e. the lattice parameter is the same for all dimensions, the U-Mo alloy exhibits an isotropic thermal expansion behaviour, making the fuel expansion due to heat changes or radiation damage well predictable.

U-Mo fuels can be produced in dispersion or monolithic form, depending on

the reactor type. This alloy allows high uranium densities of 8.5 gU/cm^3 [11] and 15.5 gU/cm^3 [11] for dispersion and monolithic fuels, respectively. The common Mo contents in U-Mo monolithic fuel and dispersion fuel are 10 wt% [12] and 7 wt% [13][14], respectively. The two configurations of U-Mo fuel are illustrated in Figure 1.3, where the potential coating barriers are also indicated in red.

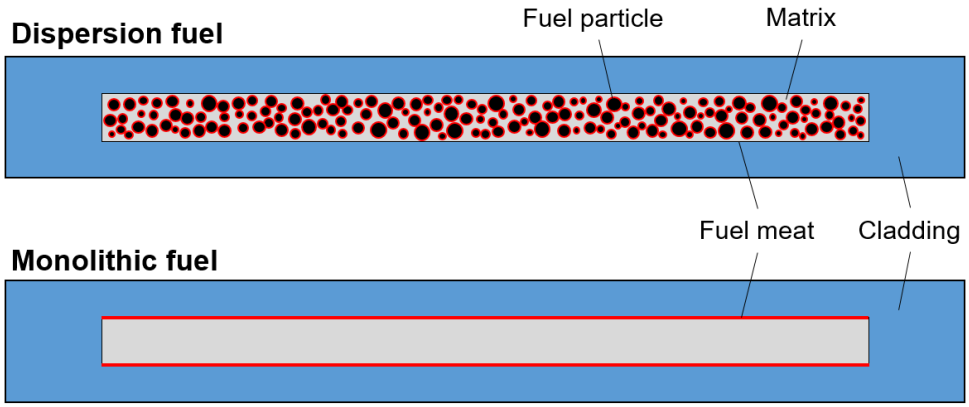

FIGURE 1.3: Schematic illustration of dispersion and monolithic fuel configurations. Potential coating barriers are indicated in red.

The in-pile irradiation performance of U-Mo/Al dispersion fuel was unveiled by IRIS 1 [15], IRIS 2 [16], IRIS-TUM [17] and FUTURE [18][19] in-pile test. As evidenced by the post-irradiation examination (PIE) results of IRIS 2 test (Figure 1.4), interdiffusion layers (IDLs) formed between the U-Mo kernels and Al matrix. The IDLs usually have an amorphous nature. As a result, the generated fission gases cannot be accommodated inside the IDLs and gather in macroscopic bubbles. Further, inferior irradiation properties of the IDLs including low thermal conductivity contribute to the mechanical destabilization of the fuel system. Eventually, with increasing burn-up, the fuel plate suffers from abnormal swelling and pillowing. Therefore, the formation of fission-enhanced IDLs is considered as the main obstacle for the qualification of U-Mo fuels.

Different remedies were adopted to mitigate or even prevent the IDL formation. Starting from the fuel matrix, it was proposed to add Si to the Al matrix to address this problem. The dedicated in-pile irradiation tests, i.e. IRIS-3 [18], IRIS-TUM [20][17] and E-FUTURE [21] [22] tests have shown positive results at the locations where the silicon and the U-Mo have close contact at the beginning of the irradiation. Rapid swelling and pillowing were identified above certain fission densities. It was further found that the addition of Si in the Al matrix can result in the formation of Si-rich layers (SiRLs), which limit the interaction between U-Mo and Al[23]. This finding has led to the suggestion that

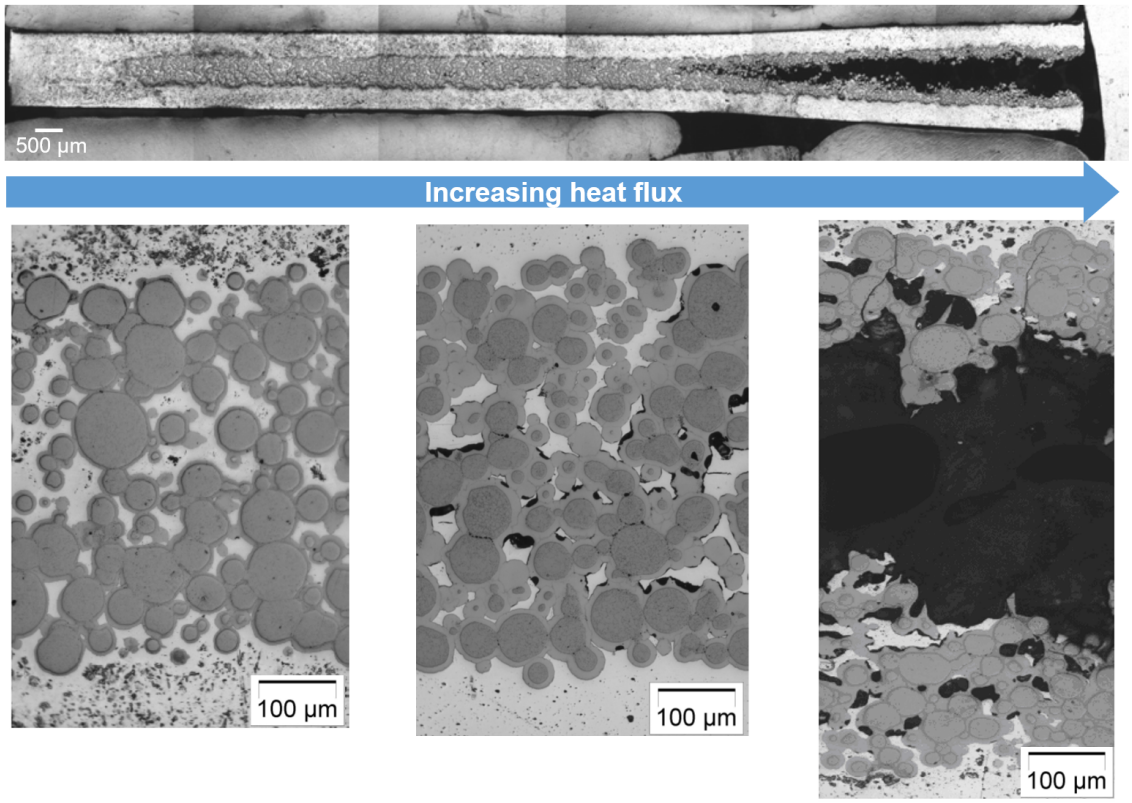

FIGURE 1.4: Cross-sections of U-Mo/Al dispersion fuel plate of IRIS 2 test. [16]

the Si should be applied at the position where it is actually needed, namely the interface between U-Mo and Al.

Hence, the SELENIUM project was launched in 2010, in which a fuel plate loaded with Si coated U-Mo particles was irradiated. The Si coatings physically separated the U-Mo kernels and the Al matrix. The PIE result reveals an improved irradiation behaviour, reflecting in less IDL growth and the absence of pillowing. However, at high fission densities (FDs), the IDL growth resembles that in the fuel plates without any coating layer applied [24]. A more promising protective potential was shown in other plates of the SELENIUM project, in which ZrN coatings were applied on the U-Mo particles. It was found that at low burn-up up to $\sim 3.5 \cdot 10^{21}$ f/cm^3, no IDL between the U-Mo fuel and the Al matrix formed as long as the ZrN coatings are intact [24]. Yet, cracks often occurred in the ZrN coatings, which has been identified as a result of the mechanical treatments applied on the brittle ZrN coatings during the plate fabrication, such as hot rolling. Those cracks provided entrance ports for the diffusion of Al into the U-Mo kernel and vice versa [24]. It was furthermore concluded that accelerated swelling behaviour at high burn-ups should be linked to the recrystallization phenomenon of the U-Mo grains and the evolution of the fission gas bubbles [25].

Meanwhile, researchers have been working on finding out alternative coating barriers. The ongoing SEMPER FIDELIS project newly adopted Mo coatings as diffusion barriers between U-Mo and Al in one of the studied plates, while the other fuel plates further focus on ZrN or Si coatings. The PIE results will be published in the near future.

1.3 Objectives of this thesis

The influence of IDL growth on fuel performance has been demonstrated beforehand. In spite of the mitigation measures, it is still critical to understand the IDL growth behaviour in order to be able to predict it. An empirical IDL growth model has been developed based on in-pile or out-of-pile data. Previous studies have shown that heavy ion irradiation, i.e. irradiation with 80 MeV ^{127}I ions, can create similar irradiation effects to the one caused by solid fission products in U-Mo fuels during in-pile irradiation [26][27][28]. Furthermore, this technique enables the quantitative study of the effects of specific irradiation parameters as most of them are independently controllable. For instance, the measurement of fuel temperature is extremely difficult to undertaken during in-pile irradiation but it is pretty simple during ion irradiation. An the other hand, a recent study successfully established a connection between in-pile and ion irradiation effects [29]. At this moment, it is advantageous to verify the empirical IDL growth model by ion irradiation data. In this thesis, the ion irradiation setup was improved by adding new components and upgrading existing ones. Taking advantage of this, the IDL growth dynamics was systematically and quantitatively investigated and the empirical model was successfully verified.

The microstructure of IDL also plays a role in fuel irradiation behaviour. In-pile irradiated plate-type U-Mo/Al fuels usually reveal an amorphous structure of IDL, while pin-type fuels normally show a crystalline structure of IDL since they are generally operated at higher temperatures due to their geometry [30]. Previous studies showed that the IDL reproduced by heavy ion irradiation is either crystalline [31][32] or amorphous [33]. This thesis first addressed the microstructural change of IDL as a function of irradiation temperature, aiming to understand the amorphous-to-crystalline transition behaviour. The threshold conditions were determined to achieve thorough comprehension.

Material down-selection for metallic diffusion barriers in U-Mo/Al fuel was addressed in a previous study [28]. Yet, no quantitative interpretation about coating effectiveness had been made. Thus, another objective of this thesis was to evaluate three selected transition metals as coating barriers, i.e. Mo, Zr, and W, in

a quantitative manner. The effects of coating thickness and irradiation conditions including irradiation temperature and irradiation dose were investigated.

On the other hand, the promising ceramic coating barrier - ZrN - was further investigated in this thesis, where a systematic and quantitative evaluation in aspects of coating thickness and coating conditions was performed. Since the cracks in the brittle ZrN coatings cannot be avoided as long as the fuel plate has to be subjected to the harsh mechanical process imposed during manufacturing, it is necessary to study their influence and foresee the irradiation behaviour of this kind of fuel. Using the ion irradiation technique, this issue was properly addressed in this thesis.

As pointed out in [25], at high burn-ups, the fuel swelling behaviour is related to the U-Mo swelling, rather than the growth of IDL. The formation of a high burn-up structure (HBS) followed by the U-Mo swelling is strongly influenced by the recrystallization effect associated with fuel restructuring i.e. grain subdivision or refinement. This phenomenon was expected to be further investigated. To reproduce the fuel restructuring, an extremely high irradiation dose should be reached within a reasonable time. Thus, in this thesis, heavy ion irradiation was employed to reproduce the U-Mo restructuring, and the required irradiation dose was achieved within a few days, thanks to the high irradiation dose rate. The underlying mechanism of this phenomenon was investigated and the onset of restructuring was estimated.

Chapter 2

Scientific Background

2.1 Uranium fission and the fission products

It has been over 80 years since nuclear fission was "unexpectedly" discovered by Hahn and Straßmann [34]. The theory behind this phenomenon is already well known and has been comprehensively explained in works of literature such as [35] and [36]. In this section, the principle of specifically uranium fission is briefly given, which is of importance for designing the ion irradiation experiments.

Of all the naturally occurring fissile isotopes, ^{235}U is the only one that exists in nature[1], albeit with a very low abundance ($\sim$ 0.7% [37]). The most naturally abundant isotope of uranium is ^{238}U ($\sim$ 99.28% [37]), which is, however, not fissionable by thermal neutrons[2] as the binding energy resulting from the absorption of a thermal neutron is less than the critical energy required for fission. Yet, ^{238}U is fissionable by fast neutrons.

Even though fission can occur spontaneously, in most cases, the ^{235}U fission is stimulated by capturing a thermal neutron[3]. In general, when ^{235}U undergoes fission, it first turns into $^{236}_{92}$U (initial fission product) after absorbing the neutron. It decays almost instantly into two lighter nuclei called fission products. During this process, other particles such as neutrons (number: 2 or 3) and electromagnetic radiation are released as well. A ^{235}U can fission in many ways resulting in different fission products, for instance:

$$^{235}_{92}\mathrm{U} + ^{1}_{0}\mathrm{n} \rightarrow ^{236}_{92}\mathrm{U} \rightarrow + ^{141}_{56}\mathrm{Ba} + ^{92}_{36}\mathrm{Kr} + 3\,^{1}_{0}\mathrm{n} \tag{2.1}$$

This is only one of the various possibilities. The average fission product mass is around 117 [39]. Yet, only a few fission products near the average are found. It is more common that the ^{235}U nucleus splits asymmetrically, i.e. into one fission product with a higher mass number (85 - 105, mostly 95), and the other one

[1] Other fissile nuclei have been produced artificially.
[2] ^{238}U can undergo fission from fast or high energy neutrons.
[3] The average thermal energy is 0.025 eV[38]

with a lower mass number (130 - 150, mostly 140), as shown in the example of Equation 2.1. In fact, the fission product yield is ruled by statistical probability, i.e., the thermal neutron fission yield of ^{235}U is a function of product nuclide mass number, as illustrated in Figure 2.1, where the yield of ^{239}Pu is shown as well.

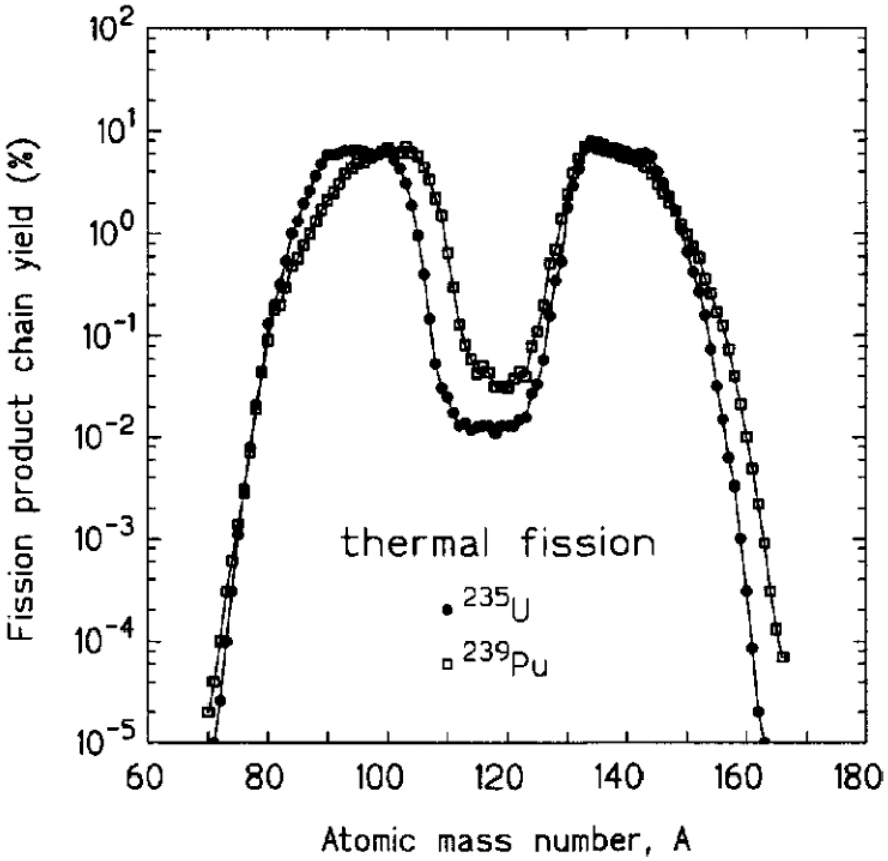

FIGURE 2.1: Fission product yields for the thermal fission of ^{235}U and ^{239}Pu. [40]

During a fission process, most of the energy is released as kinetic energy of the produced fission products resulting from the Coulomb repulsion. Taking the fission of ^{235}U as an example, one fission event releases in average $\sim$200 MeV (corresponds to $3.2 \cdot 10^{-11}$ Joules) energy. Approximately 84% of this energy is in the form of kinetic energy of the fission products, i.e. $\sim$168 MeV. The remaining energy is distributed among the produced neutrons, neutrinos, and gamma- and beta radiation [41]. As explained, fission usually results in two fission product nuclei of uneven mass. According to the law of conservation of momentum, the lighter fission product nucleus initially carries a larger part of the kinetic energy than the heavier one. Hence, the most likely fission products, namely one lighter nucleus with a mass number of 95 and one heavier nucleus with a mass number of 140, carry kinetic energies of 100 MeV and 68 MeV, respectively.

2.2 Radiation damage

Over decades, radiation damage has been extensively studied. For instance, Birnkman [42] focused on the radiation damage in metals; Kelly [43] and Sickafus et al. [44] reviewed the radiation effects in solids. Nuclear materials experience radiation in the form of neutrons, electrons, charged ions, and electromagnetic radiation during fission, which causes damage when the energy is transferred from an incident projectile (a neutron, a high-energy photon or an energetic ion) to the materials. Hence, the study of radiation damage has been largely motivated by the significance of controlling the degradation of nuclear reactor materials caused by irradiation. Matzke [45] studied the radiation damage in nuclear materials. Considering the range of the generated radiations, the fission products are usually confined to the fuel element itself, while the reactor construction materials are mostly subjected to neutron radiation [46]. As this thesis aims to facilitate the development of research reactor fuels, the radiation damage in fuels caused by fission products is addressed, which also greatly outweighs the damage there caused by the other forms of radiation.

A radiation damage event consists of a series of processes, including:

- The incident ion interacts with a lattice atom of the target material;
- The kinetic energy of the incident ion is transferred to the lattice atom resulting in the primary knock-on atom (PKA), occurring typically within $< 10^{-15}$ s [47];
- The lattice atom is displaced from its lattice site if the energy it received exceeds the threshold energy (displacement energy E_d)[4];
- Additional knock-on atoms are created in the region around the ion track, leading to displacements of other atoms (displacement cascade);
- For each displacement, a vacant site or a vacancy is left behind and the displaced atom eventually dissipates its kinetic energy and comes to rest within the crystal lattice as an interstitial. Apparently, the number of interstitials equals the number of vacancies produced[5], forming vacancy-interstitial pairs which are known as Frenkel pairs [49].
- The PKA itself dissipates its kinetic energy and comes to rest, becoming an interstitial.

[4] If the transferred energy does not exceed the displacement energy of the lattice atom, the atom undergoes amplitude vibrations at the original lattice site [48].

[5] It is assumed that no point defects are lost to a surface or a defect sink.

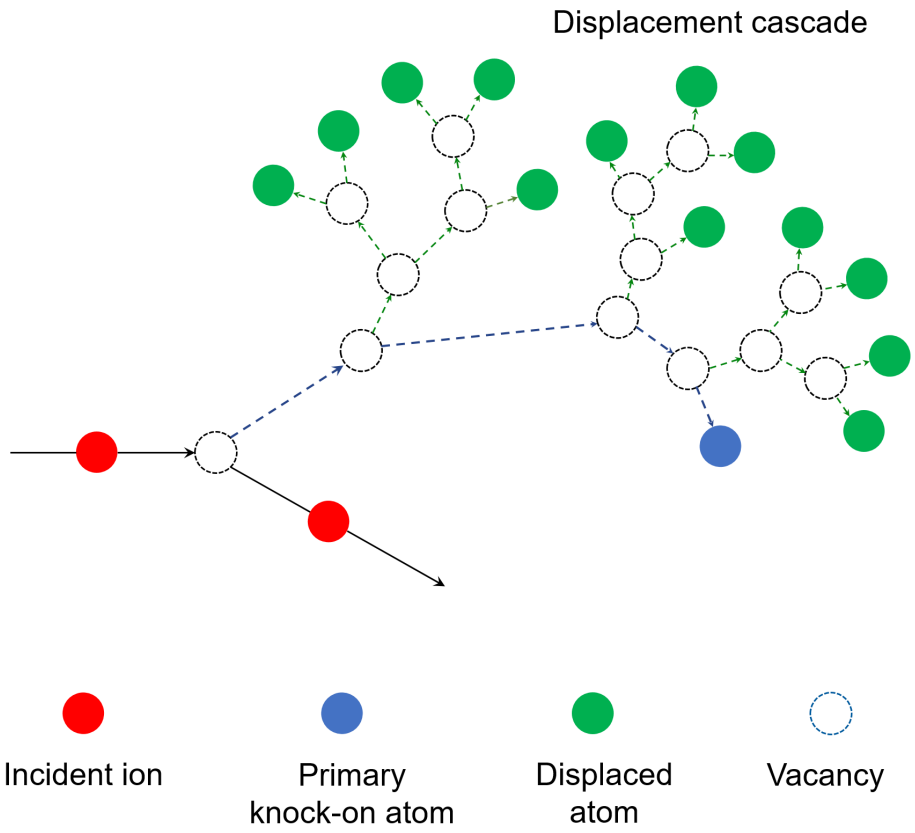

FIGURE 2.2: Formation of a displacement cascade. A tree-like structure of successive collisions is produced, resulting in point defects.

Such a radiation damage event is basically the creation of point defects in cascades, which is schematically shown in Figure 2.2. Besides, atoms close to the sample surface may be sputtered [50]. In fact, the sample preparation in this thesis, which is described in Section 2.5, takes advantage of this effect.

Norgett, Robinson, and Torrens [51] proposed to quantitatively estimate the radiation damage by using the number of Frenkel pairs created by given energy transferred to the PKA, namely the number of displacements per atom (dpa). If this number equals one, it means that each atom has been displaced once on average. Note that the point defects lost to a surface or a sink are not considered, as the numbers of vacancies, interstitials, and Frenkel pairs in the target should be equal. With such a measure, the comparison between different reactor environments and ion irradiations is enabled. Therefore, in this thesis, the radiation damage caused in the designed ion irradiation experiments is calculated in dpa, if a comparison to in-pile irradiation was needed. The approach of calculation is discussed in more detail in Section 2.4.3 of this chapter.

Returning to the fission products of ^{235}U, as they travel in target, such as the fuel element, they lose their kinetic energy by different mechanisms. During

the above-mentioned collision events, the total kinetic energy of the particles involved in a collision is almost conserved [47]. The incident ion loses its energy mostly along the path/track by e.g. ionisation[6]. An energy loss of a charged particle is usually expressed as an average energy loss per unit length. In general, the total energy loss is composed of three contributions [52]:

$$(-\frac{\mathrm{d}E}{\mathrm{d}x})_{\text{total}} = (-\frac{\mathrm{d}E}{\mathrm{d}x})_{\text{e}} + (-\frac{\mathrm{d}E}{\mathrm{d}x})_{\text{n}} + (-\frac{\mathrm{d}E}{\mathrm{d}x})_{\text{r}} \tag{2.2}$$

where:

$$(-\frac{\mathrm{d}E}{\mathrm{d}x})_{\text{e}} = \text{energy lost to target electrons (electronic energy loss)}$$
$$(-\frac{\mathrm{d}E}{\mathrm{d}x})_{\text{n}} = \text{energy lost to target nuclei (nuclear energy loss)}$$
$$(-\frac{\mathrm{d}E}{\mathrm{d}x})_{\text{r}} = \text{energy lost to radiation (radiative energy loss)}$$

The collisions occurring during electronic stopping are often called "inelastic collisions", as they are normally accompanied by electronic excitation or ionization events leading to non-elastic interactions. Likewise, the collisions occurring during nuclear stopping are usually referred to as "elastic collisions" as they can be theoretically treated as elastic two-body problems. The radiative energy loss is only significant for electrons and positrons. For high-energy ions especially swift heavy ions ($E > 50\,\text{MeV}$), such as the fission products of ^{235}U, the radiative energy loss is quite small and can thus be neglected in most cases [53]. Thus, only electronic and nuclear energy loss are considered in the following.

The electronic energy loss depends on the energy of the particle. In this thesis, heavy charged particles are focused, for which the electronic energy loss is defined by Tsoulfanidis [54]:

$$\frac{dE}{dx} = 4\pi r_0^2 q^2 \frac{mc^2}{\beta^2} NZ \left[\ln\left(\frac{2mc^2}{I}\beta^2\gamma^2\right) - \beta^2\right] \tag{2.3}$$

where:

$$\gamma = \frac{T + Mc^2}{Mc^2}$$

In this correlation, r_0 is the classical electron radius which equals $2.818 \cdot 10^{-15}\,\text{m}$; q is the charge of the particle; β is the relative phase velocity of the particle defined as v/c; mc^2 is the rest energy of the electron; N and Z are respectively the atom concentration (number of atoms per m^3) and the density

[6] The electrons are removed from the atom.

of the target material; T stands for the kinetic energy of the particle; and I is the mean excitation potential of the target given by:

$$I = \left(9.76 + 58.8Z^{-1.19}\right) Z \tag{2.4}$$

Note that here $Z > 12$.

The reduced nuclear energy can be expressed by the following correlation proposed by Averback [55]:

$$\frac{d\varepsilon}{dx} = \frac{1}{\varepsilon} \int_0^{\varepsilon} f\left(t^{1/2}\right) dt^{1/2} \tag{2.5}$$

Here ε is the reduced nuclear energy. The scattering function $f\left(t^{1/2}\right)$ is a scaling function, where t is a measure of the penetration depth into an atom during a collision [55].

As mentioned before, the fission products of ^{235}U are highly charged particles with an average initial kinetic energy of 80 MeV. For those high-energy ions, the energy loss due to electronic stopping is dominant [56][57], i.e., the electronic energy loss mainly contributes to the slowing down of the ions. Note that local heating can be generated in this process [57]. When the ions are sufficiently slowed down, the nuclear stopping mechanism becomes increasingly pronounced, which eventually overweights the electronic stopping mechanism. Despite the fact that nuclear energy loss makes up only a small fraction of the overall energy loss, it is the major source of lattice damage [58]. During this process, involved target atoms are displaced permanently from their initial lattice sites. If this event occurs at the interface of two materials, mixing of the atoms from the two materials, namely interdiffusion, can be triggered.

In practice, the nuclear and electronic energy loss can be calculated using the Monte Carlo approach, based on a binary collision approximation. Details are given in Section 2.4.2.

2.3 Ion beam mixing

As explained in Section 2.2, the displacement events resulting from ion-solid interactions can lead to a local rearrangement of atoms, i.e. atomic intermixing, at an interface of two materials. This effect is often referred to as ion-beam mixing and has been adopted in various scientific and industrial applications, such as adhering two layers, broadening the interface of a bilayer system, producing new metallic alloys of controlled composition or even controlled microstructure. The technique ion beam irradiation (usually shorted to ion irradiation) takes

advantage of this effect, providing a unique opportunity to study the damage formation mechanisms and the ion-induced phase formation not only on an atomic level but also in a quantitative manner.

Based on the observation of temperature dependence in several ion beam mixing experiments, two regimes characterised by a critical temperature are suggested to explain the ion beam mixing phenomenon [59][60]:

- **Athermal regime**, in which the mixing event depends solely on the atomic collisions induced by the ion beam. The temperature plays a minor role.
- **Thermal regime**, which occurs above a critical temperature and strongly relies on the temperature.

When a target is subjected to ion irradiation, modifications can be achieved by various mechanisms [61], including ballistic effect, thermal spike, and radiation enhanced diffusion, which are respectively presented in the following sections.

2.3.1 Ballistic effect

Speaking of atomic collisions during ion beam mixing, it is straightforward to consider the ballistic processes. Indeed, in a traditional way, ion beam mixing is merely described by ballistic models. Ballistic mixing occurs in the athermal regime and is composed of two sub-processes, i.e. primary recoil mixing and cascade mixing [58]. The former refers to the primary recoil mixing contribution resulting in displacements in the forward direction of the primary collision, while the latter describes the mixing related to the secondary, tertiary, or even further displacements forming the collision cascade (or displacement cascade). More explanations can be found in [62]. Theoretical models based on a binary collision approximation have been established to analyse the mixing rates [63][64][65]. Yet, those models only verified light elements. For other elements especially heavy elements, significant discrepancies between the prediction and the measurement were found, i.e., the prediction is less by one order of magnitude than that of the measurement.

2.3.2 Thermal spike

On this point, it can be concluded that at least for targets of heavy element such as U, the ballistic models based on binary collision cascade mechanism are not sufficient to explain the ion beam mixing, there should be another mechanism (or mechanisms) contributing to the mixing in the system. Later

on, Peak and Averback [66][67] pointed out that in the early phase, only the ballistic mechanism is operating, resulting in atom displacements through binary collisions creating damage in the form of Frenkel pairs. In a later phase, the residual energy is distributed among the atoms in the cascade volume via many-body collisions, leading to a significant temperature rise of the local lattice. The local temperature can be above the melting point of the target material [68]. As a consequence, the atomic motion resembles that in a liquid. This way, a so-called "spike" of heat is produced, which can largely increase the diffusivity of the atoms and therefore greatly enhance the mixing rate. The latter phase is called "thermal spike mixing". A spike can be described as a compact volume in which all the atoms are in motion, while a thermal spike is specifically a spike in which the energy distribution of moving particles can be described by the Maxwell-Boltzmann statistics [69][70]. A systematic study of low-temperature ion beam mixing in metals by Kim et al. [71] also indicated that the thermal spike mixing has to be incorporated in developing the mixing model, as the predictions made based on the new model agreed well with the measurement.

2.3.3 Radiation-enhanced diffusion

At higher temperatures, accelerated mixing is often observed at the interface in a bilayer system. This is due to the migration of the point defects produced in the previous stage i.e. collision cascade during irradiation, which enhances the mass transport throughout the material. This process is the radiation-enhanced diffusion (RED) which occurs at a later stage when the system starts to cool down.

The theory of RED has been reviewed by Dienes and Damask [72]. Later on, a systematic study focusing on the dependence on temperature, ion dose and ion dose rate has been performed by Sizmann [73]. RED is triggered by a critical temperature called transition temperature, and it only takes place in the thermal regime. For instance, the study of Kim et al. [71] mentioned beforehand does not involve this effect since it focuses on the low-temperature ion beam mixing. The transition temperature and the onset of RED in ion mixing have been explored by Cheng et al. in [59], where a correlation between the cohesive energy[7] of elemental solids and the characteristic temperature was derived.

Rossi et al. [75] investigated the intermixing behaviour of bilayer samples of U/Al, U/Ti, U/Si using ion (Ar or Xe) beam mixing and concluded that below the transition temperature the mixing mechanism is athermal, whereas the mixing is significantly accelerated by radiation if the temperature is above the transition

[7] The binding energy of atoms to form the solid [74]

temperature. The finding further verified the above theory of ion beam mixing. The obtained mixing rate curves all exhibit "Q curve" behaviour, where "Q" stands for "quantity". Q curve commonly refers to the temperature dependence of ion mixing rate [76]. The mixing mechanisms for light and heavy ions under low and high temperatures are illustrated in Figure 2.3.

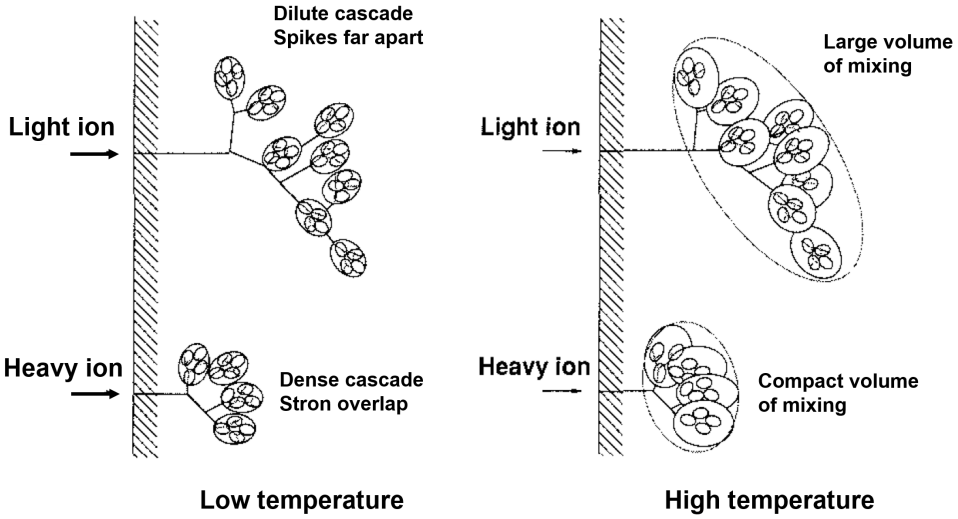

FIGURE 2.3: Different mixing mechanism caused by ion mass and temperature. After [75]

Now considering the U-Mo/Al system of the reactor fuel element, Leenaers [77] and Ye [78] proposed that the U(Mo)-Al intermixing kinetic should also be manipulated by temperature in a way that is similar to the results of Rossi et al. [75], i.e. the mixing quantity should be characterised by a transition temperature, below which the intermixing of U-Mo and Al is athermal, above which the intermixing is largely enhanced by temperature. This will be investigated in Chapter 3.

2.3.4 Mixing enthalpy and Miedema's model

As a result of intermixing between two metals, intermetallic compounds can form [75]. From the point of view of statistical thermodynamics, the change of enthalpy during this process can be assessed by the semi-empirical Miedema's model [79]:

$$\Delta H^f = f(c)[-P(\Delta\phi)^2 + Q\left(\Delta n_{\mathrm{WS}}^{1/3}\right)^2]. \tag{2.6}$$

Here $\Delta\phi$ denotes the electronegativity difference between the two elements, which is defined as $\phi_A - \phi_B$. n_{WS} is the electron density at the boundary of the Wigner–Seitz cell and Δn_{WS} is the created discontinuity in electron density

when solving an A atom in a B host [80]. P, Q are empirical constants with values depending on the material. The term $f(c)$ is a symmetrical function of the concentration of one of the metals, e,.g. metal A:

$$f(c) = \frac{V_A^{2/3}}{(n_{\mathrm{WS}}^{-1/3})_{\mathrm{average}}}, \tag{2.7}$$

here V_{A} is the molar volume of element A, $(n_{\mathrm{WS}}^{-1/3})_{\mathrm{average}}$ is the average electron density at the boundary of A and B, which is defined by:

$$(n_{\mathrm{WS}}^{-1/3})_{\mathrm{average}} = \frac{1}{2}[\frac{1}{(n_{\mathrm{WS}}^{A})^{-1/3} + (n_{\mathrm{WS}}^{B})^{-1/3}}], \tag{2.8}$$

In the case of alloys of a transition metal and a non-transition one, an additional term R arises due to filling of the Brillouin zones of a particular crystal structure, leading to a modification of Equation 2.6:

$$\Delta H^f = f(c)[-P(\Delta\phi)^2 + Q\left(\Delta n_{\mathrm{WS}}^{1/3}\right)^2 - R]. \tag{2.9}$$

Based on this model, a Miedema-calculator was developed by Zhang et al. [81][82], which will be applied in Chapter 5 to calculate the formation enthalpies of the selected Al–X and U-X alloys.

2.4 Simulation of radiation damage

2.4.1 Heavy ion irradiation

As presented above, the radiation damage in U-Mo/Al fuels is mostly caused by fission products. Simulation of this kind of damage can be achieved by irradiating fuel samples with ions that can represent the fission products namely charged energetic particles with an average kinetic energy of 80 MeV. Since typical displacement energies only exceed several tens of eV [83], irradiating using ions with a kinetic energy of 80 MeV can produce considerable damage in a short time.

The ion irradiation experiments of this thesis were performed at the Maier-Leibnitz Laboratory (MLL) accelerator located on the research campus in Garching, Germany. The MLL tandem Van-de-Graaff accelerator is a double stage DC machine. It can be operated at a voltage up to 15 MV with a constant or pulsed beam. As shown in Figure 2.4, various ions can be generated at the ion source. The generated ions are then accelerated twice in the tandem. This is achieved by the stripping system (a thin foil or a small amount of gas) located in

the middle of the tandem system, which removes some electrons of the incoming ions, turning the charge of the ions from negative to positive. The analysing magnet serves as a mass analyser to select ions with a certain charge state, allowing them to pass through and reach the distributor. The distributor is also a magnet that can guide the ion beam to the final destination - the irradiation station of this thesis.

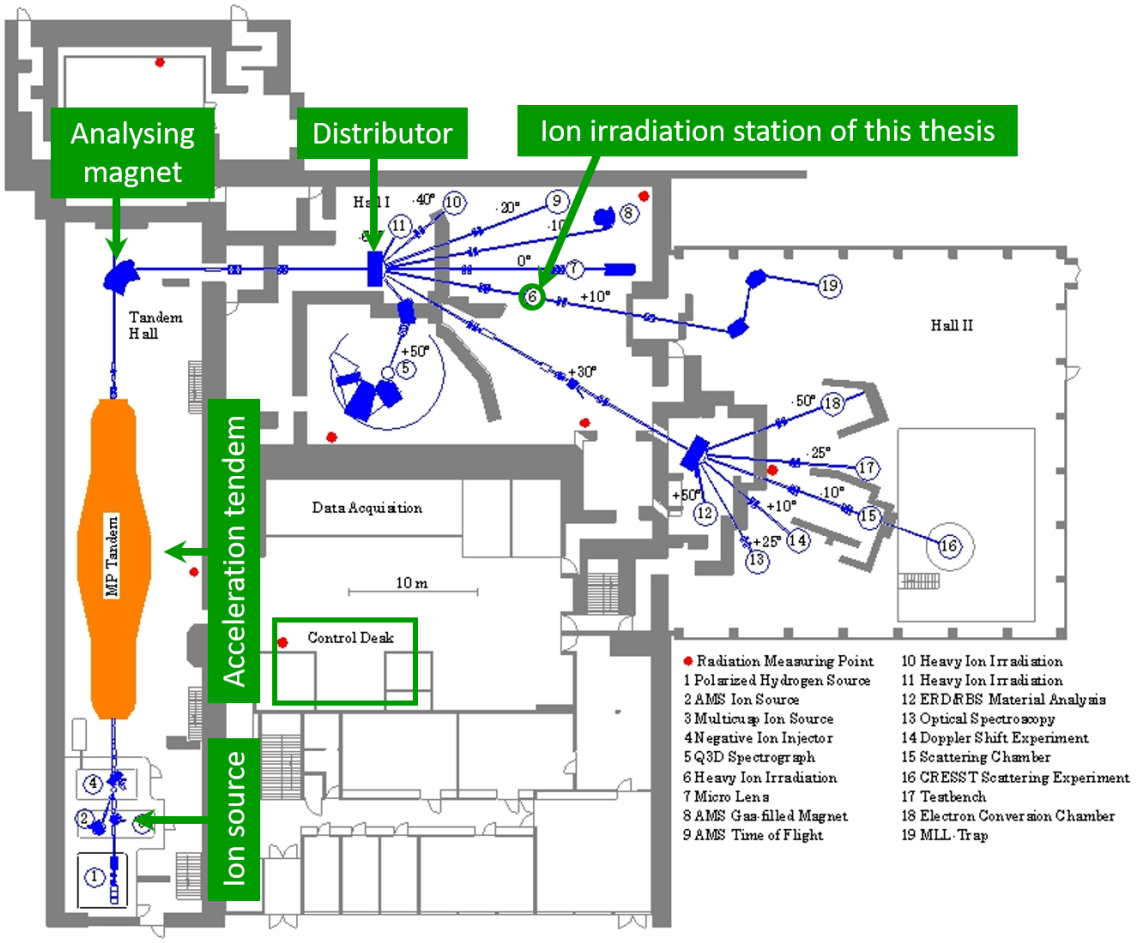

FIGURE 2.4: Layout of MLL tandem accelerator. The ion source, acceleration tandem, analysing magnet, distributer and the irradiation station of this thesis are indicated. After [84]

It has been proven that 80 MeV ^{127}I ions can create similar damage to the one caused by solid fission products in U-Mo fuels during in-pile irradiation [85][26][27][28]. More importantly, this technique allows us to save years of time and an enormous amount of money. More advantages of heavy ion irradiation can be found in [26][27][28].

^{127}I ions at 80 MeV can well represent the fission fragments, because (i) this isotope itself is a common fission product of ^{235}U; (ii) 80 MeV is approximately the average kinetic energy of the fission fragments of ^{235}U, as previously discussed

in Section 2.1. Thus, irradiation with such ions can simulate to a large extent the radiation-enhanced processes e.g. diffusion between different materials. This technique enables quantitative analysis of the effect of specific irradiation parameters as most of them are independently controllable, like temperature and irradiation dose. Beyond that, ion irradiation is able to provide an extraordinarily high ion flux that is equivalent to 20 - 50 times of the peak fission rate of typical in-pile irradiations e.g. E-FUTURE [86] and SELENIUM [25] test, making the high-fission-rate effects under exaggerated conditions distinctly accessible.

To study the interdiffusion behaviour in U-Mo/Al fuels, the interface of U-Mo and Al should be targeted when performing heavy ion irradiation. As shown in Section 2.3 and especially in Figure 2.3, the damage caused by the heavy monochromatic ions is very localized. Thus, the penetration depth of the ions and their energy loss profiles have to be determined in advance. Further, accurate calculation of stopping powers are required to reliably determine energy deposition and radiation damage. As mentioned in Section 2.3, those types of information can be obtained by using the Monte Carlo approach, i.e. the SRIM/TRIM code in particular. Details are presented in the following section.

2.4.2 SRIM/TRIM calculations

SRIM stands for "Stopping and Range of Ions in Matter" [87][88], which is a software package often used in the ion irradiation community. It is capable of simulating ion-solid interactions during ion irradiation and calculating the related quantities such as range, energy deposition and radiation damage. The core of SRIM is the well-known Monte Carlo simulation code "Transport of ions in matter (TRIM)" based on binary collision approximation.

The basic logic of TRIM is described as follows: mono-energetic ions are generated in a single point source, hitting the target at its surface with an incident angle of 0°. After entering the target, a series of independent binary collisions take place. During this process, the ion loses its energy via the interactions with electrons (inelastic) and nuclei (elastic) of the target by two mechanisms i.e. electronic energy loss and nuclear energy loss, respectively. The theory has been explained in Section 2.2. After each collision, the ion changes its direction of flight and keeps moving in a straight-free-flight path until the next collision event. The ion comes to rest when its kinetic energy falls below the stopping threshold[8].

TRIM provides two routes to determine the ion-induced damage profiles:

[8]The ion can also leave the target if it is close enough to the surface after some collisions.

- **Ion distribution and quick calculation of damage (QC)**, in which only the trajectory of the incoming ion is followed. The number of the created defects (Frenkel pairs) is obtained based on the Kinchin-Pease model [89].
- **Detailed calculation with full damage cascades (FC)**, in which all the knock-on atoms produced by the incident ions are followed. In this case, the number of defects is obtained collision-by-collision based on the pre-defined conditions such as the lattice binding energy.

The major difference between the two options is the way of calculating the electronic energy loss, leading to a notable difference in the calculated radiation damage. A comparison between these two approaches has been already discussed by Stoller et al. [90], where the authors suggested to use the QC approach. Recently, Weber and Zhang [91] thoroughly reviewed the difference between the two approaches based on literature-review and experimental investigations, and came to the conclusion that the FC approach provides better accuracy in calculating damage energy, number of displacements and damage depth profiles compared to the QC approach, especially for multi-elemental targets (the irradiation targets involved in this thesis are all multi-elemental). The computing time was considered as a drawback of the FC approach [26], which, however, is no longer a problem nowadays.

Furthermore, it is noticed that at a certain penetration depth, the nuclear energy loss experiences a maximum energy deposition, resulting in a damage peak which is called Bragg peak, at which the highest defect density is expected. To study irradiation caused diffusion behaviour more efficiently, the top coating layer is so adjusted that the Bragg peak appears close to the interface of interest. Another advantage of placing the Bragg peak near the interface is that the effect caused by the predominant irradiation direction at the interface can be neglected, as pointed out by Breitkreutz et al. [29], by placing the Bragg peak near the interface should eliminate the influence of irradiation direction.

Based on the above considerations, in this thesis, the FC approach is adopted for the TRIM calculation, and the Bragg peak is placed near the interface of interest. Figure 2.5 shows the TRIM calculation results of 80 MeV ^{127}I impinging on an Al/U-Mo bilayer system, including the ion range and the energy loss profiles in the target.

2.4.3 Calculation of dpa

A standard for estimating the radiation damage is needed in order to compare the results obtained from different experiments, particularly the results of in-pile

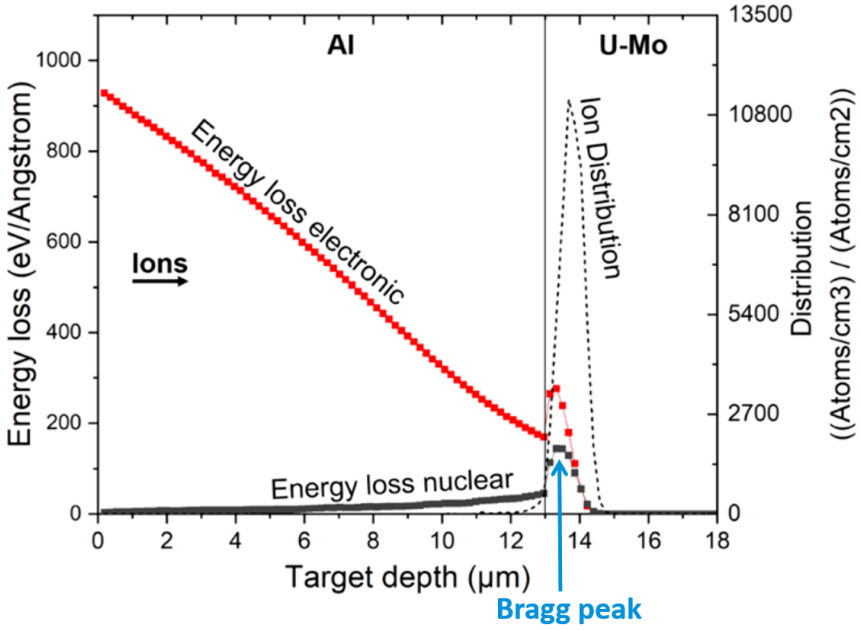

FIGURE 2.5: SRIM/TRIM calculated ion distribution and energy deposition of 80 MeV ^{127}I in an Al/U-Mo bilayer system. The Bragg peak is indicated.

neutron irradiation and ion irradiation. In 1975, Norgett, Torrens and Robinson [51] proposed to evaluate the radiation damage by the number of formed Frenkel pairs, namely the number of displacements per atom (dpa). Up to now, dpa is commonly accepted and widely used in both reactor irradiation and ion irradiation communities when referring to radiation damage.

The principle of simulating neutron radiation damage by ion irradiation has been well explained in [92]. Stoller et al. [90] reported the method of using SRIM/TRIM code to compute dpa from ion irradiation experiments. Weber and Zhang [91] suggested some modifications based on recent studies. Based on these, the author of this thesis decided to use the approach presented in the following to calculate dpa:

- define all the global parameters, e.g. the ion specie and energy, target composition;
- set the displacement threshold energy for Al, gamma-U and Mo to 25 eV [92], 35.6 eV [83] and 60 eV [92], respectively;
- set the lattice binding energy to zero [90];
- run SRIM/TRIM in the FC mode;
- obtain the number of displacements from the generated "VACANCY" file;

- obtain the number of replacement collisions from the generated "NOVAC" file;
- calculate the sum of displacements and replacement collisions as the average number of displaced atoms produced totally [91];
- multiply the value by the given ion fluence [ions/cm^2].
- divide the value by the atomic density of the target material (normalization).
- calculate the average value from both sides if it is a case of an interface.

2.5 PVD - Sputtering

PVD refers to physical vapour deposition, which is a method for producing thin films by vaporizing the target material and depositing it on a substrate. It is called "physical" because there are no chemical reactions involved. As a common PVD technique, sputtering is often used to produce coatings of metals with well-controlled thickness. In fact, the sputtering effect is one of the radiation damage types caused by ions, as briefly mentioned in Section 2.2. Depending on the type of power supply, sputtering can be further divided into DC (direct current), RF (radio-frequency), pulsed sputtering [93]. The DC sputtering is the most straightforward way to deposit conductive materials not only effectively but also economically. Most modern sputtering systems utilize magnetrons to enhance the ionisation of the plasma near the target. Thus, the bombardment of ions is intensified and a higher sputtering rate is achieved. DC magnetron sputtering was used to prepare samples in this thesis which require specific coating thicknesses that match the SRIM/TRIM calculation. For preparing ZrN coatings, pulsed mode was applied to eliminate random arcing phenomena caused due to its lower electrical conductivity and enable stable deposition processes. Further, despite that the samples used in this thesis have a layered structure, they can also represent the dispersion fuel geometry used in in-pile irradiation e.g. SELENIUM [94] and SEMPER FIDELIS [95], because the diameter of the U-Mo particles in dispersion fuels is generally large compared to the range of fission products.

The deposition of a coating layer by sputtering is a result of ion bombardment of the target. As visualized in Figure 2.6, at a suitable gas pressure, the inert gas such as Ar is ionized by the high voltage, burning a Ar plasma filled with Ar ions and electrons between the target and the substrate. The Ar ions are

accelerated towards the target due to the electric field, impinging on the target surface which leads to the emission of target atoms and secondary electrons. The latter is responsible for sustaining the gas discharge running [96]. Figure 2.7 shows pictures of a Ar plasma taken during a Zr sputtering process. Details about this technique are comprehensively summarized in [97] and [98].

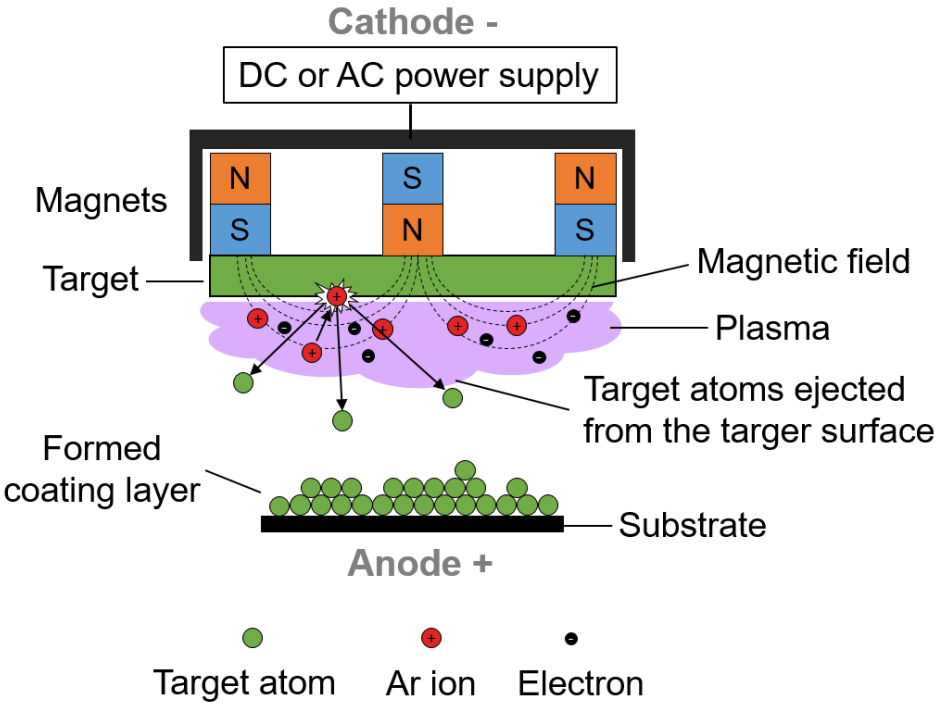

FIGURE 2.6: Schematic illustration of DC magnetron sputtering deposition process.

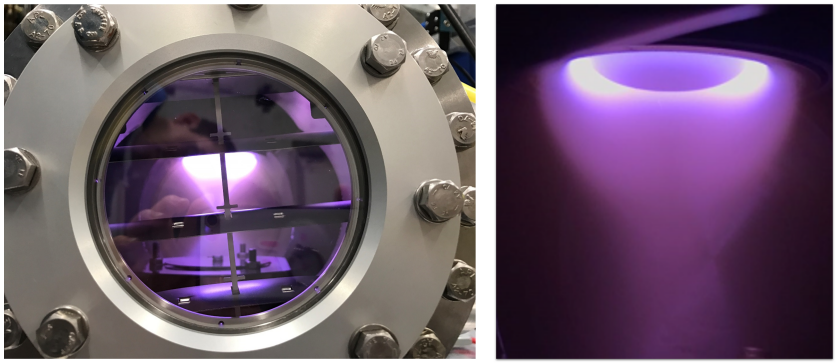

FIGURE 2.7: Burning of argon plasma during a Zr sputtering process.

It is clear that the many sputtering parameters such as voltage, pressure, substrate-target distance, pulse length (if pulsed) have impacts on the thin film growth process. To predict the grown film structure, Anders [99] suggested an extended structure zone diagram (SZD) that explicitly includes plasma and ion effects on film growth, based on the work of Movchan and Demchishin [100]

and [101]. As shown in Figure 2.8, the microstructure of the grown thin film is described as a function of the generalized temperature, the normalized energy and the film thickness. In this SZD, four zones are recognized:

- **Zone 1**: film growth at low temperature and low energy. The growth of porous structure is favoured;
- **Zone T**: a transition zone from tensile to compressive stress, where the diffusivity of target atoms on the substrate surface is enhanced compared to that of zone 1 but still limited by grain boundaries. The growth of densely packed fibrous grains is favoured;
- **Zone 2**: the further enhanced atom diffusivity is no longer limited by grain boundaries. The growth of uniform columnar grain is favoured;
- **Zone 3**: at high temperature and energy, bulk diffusion is allowed which induces a recrystallized grain structure.

In this thesis, Al, Zr, Mo, W, and ZrN coatings were prepared either as top layers (X/U-Mo) or diffusion barrier coatings (Al/X/U-Mo) on the U-Mo substrates by PVD magnetron sputtering. The sputtering parameters were carefully selected by taking into account the SZD.

2.6 Characterisation techniques

Various characterisation techniques were utilized for sample analysis before and after irradiation. The important ones are presented in this section. Analysing a specimen by mean of electrons is attributed to the various interactions between the incident electrons and the specimen. When a focused electron beam impinges on the surface of a specimen, the electrons lose energy by scattering in both elastic and inelastic ways. Thus, a variety of signals are generated from a teardrop-shaped volume (excitation volume) extending up to a few microns into the specimen and emitted as a result of electron-matter interactions [102]. As demonstrated in Figure 2.9, the signals include secondary electrons (SE), backscattered electrons (BSE), X-rays and transmitted electrons. Each signal carries useful information about the specimen. As a matter of fact, the resolution for a certain signal in an electron microscope (EM) depends not only on the probe size, but also strongly on its excitation volume shown in Figure 2.9. The signals of interest can be collected and further analysed with corresponding techniques such as scanning electron microscopy (SEM), energy-dispersive

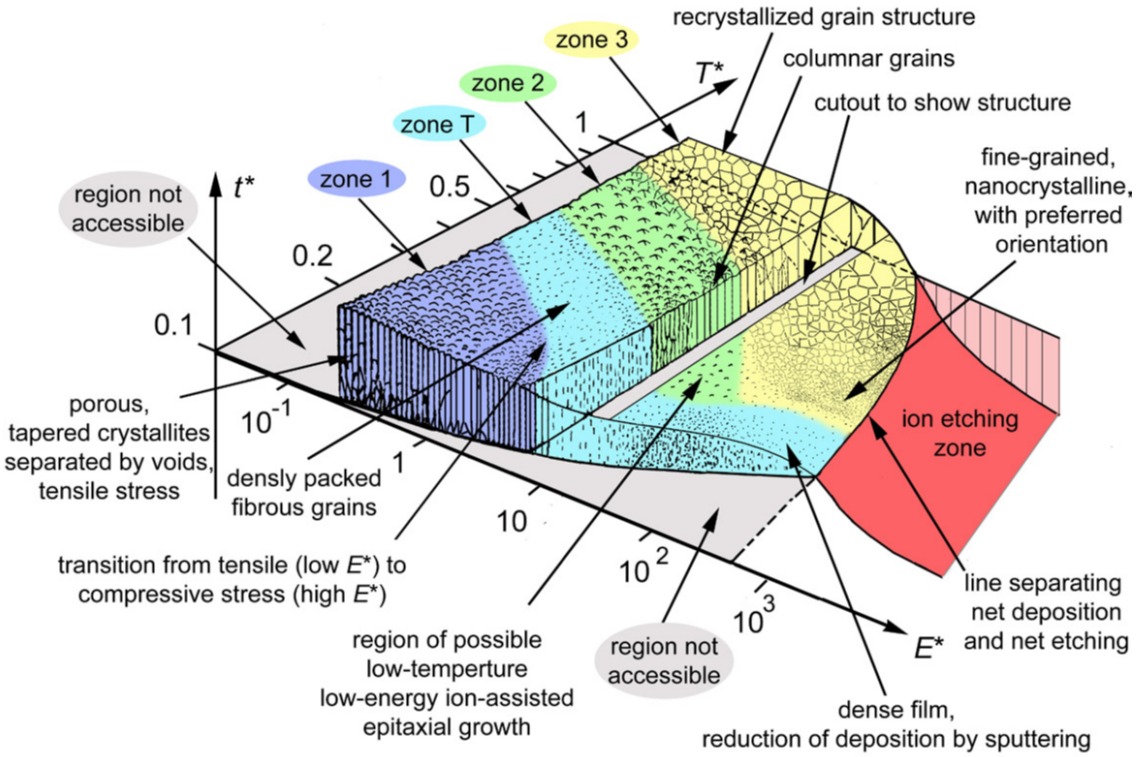

FIGURE 2.8: SZD of thin films deposited by sputtering as a function of generalized temperature, energy flux and sputtering time denoting the film thickness. From [99].

X-ray spectroscopy (EDX), transmission electron microscopy (TEM), scanning transmission electron microscopy (STEM) and electron backscatter diffraction (EBSD), depending on the user's needs. Yet, it is noticed that the transmitted electrons are not able to be obtained from a bulk material as the electrons with regular operating voltage cannot go through bulk specimens. Thus, the technique focused ion beam (FIB) was also utilized in this thesis for preparing thin lamellae typically with a thickness of around 100 nm or less from a bulk specimen.

2.6.1 SEM, TEM and STEM

Microscopes are instruments allowing small features or objects to be seen by utilizing different kinds of radiation for imaging. The most common and traditional ones are optical microscopes (OMs), which are generally easy to access and use. However, conventional optical microscopes have a spatial resolution limited by the nature of visible light, which has a wavelength roughly ranging from 400 to 700 nm. The observation of sub-wavelength structures with OM is difficult due to the diffraction limit [103]. For the main peak of a white-light source with a wavelength of 600 nm, the limit is $\sim$ 333 nm in air [104]. In this thesis, thin layers and microstructures down to several tens of nanometers are

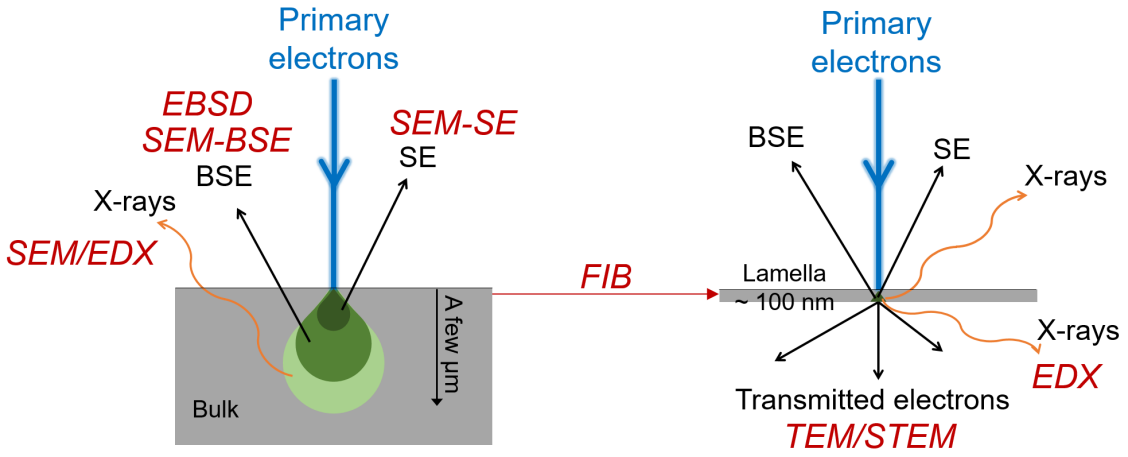

FIGURE 2.9: Signals obtained from (A) a bulk specimen, (B) a lamella specimen by different electron-matter interactions. The excitation volumes (in green) are different for the generated signals. Lamella specimens can be produced from a bulk specimen by FIB.

mainly focused, which cannot be resolved by conventional OMs. Hence, various EM techniques were utilized in this thesis, including SEM, TEM and STEM.

In fact, an EM works very much like an optical microscope, however, it uses a focused beam of electrons instead of light to examine samples, which results in a much higher resolution due to the significantly shorter wavelength of electrons. In an EM system, electromagnetic lenses are used for focusing. SEM, TEM and STEM all use electrons to acquire images of samples. Their typical configurations are schematically illustrated in Figure 2.10. The detailed working principles of these techniques can be found in [105], [106], [107] and [108].

- **SEM** is usually used for examining bulk samples. The imaging is possible with both SE and BSE types of electrons. SEs are resulted from inelastic interactions of the incident electrons with the atoms of the sample. Since they come from the surface or the near-surface regions of the sample, the obtained images provide more detailed surface information. BSEs, on the other hand, arise from elastic collisions of the incident electrons with the atomic nuclei (wide-angle Rutherford scattering), and thus show high sensitivity to the differences in atomic number. The obtained images provide Z-contrast information. In either case, SEM is mostly employed to observe the surface phenomena of materials. Moreover, the X-rays emitted from the sample can be used for compositional analysis if SEM is joined with an EDX detector. The acceleration voltage of SEM during operation is usually up to 30 kV.

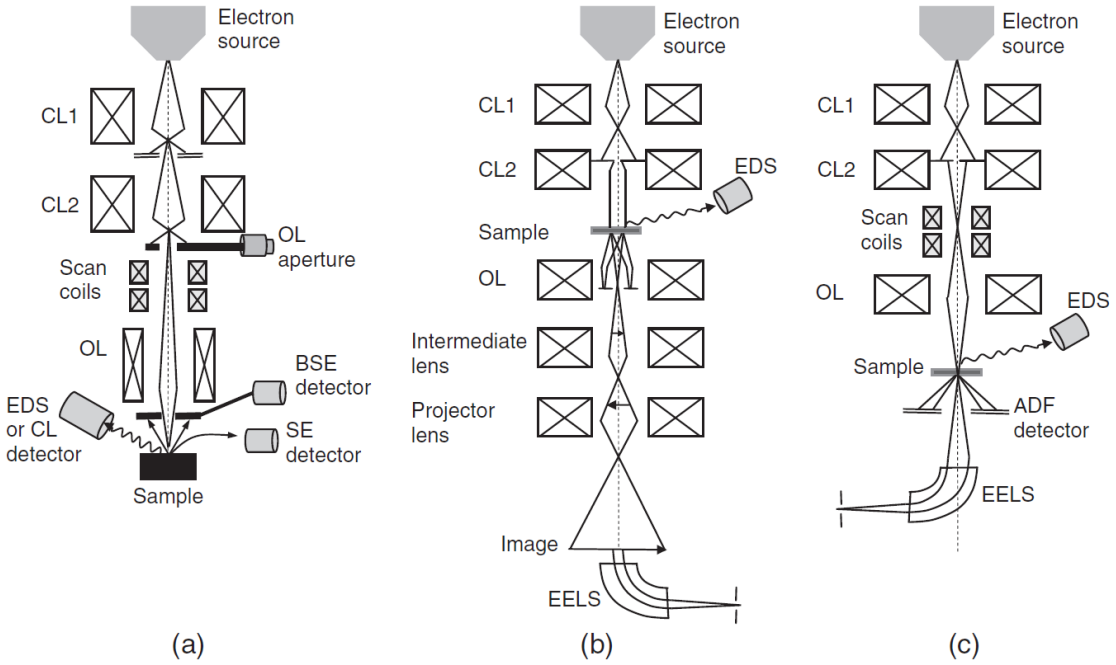

FIGURE 2.10: Schematic drawing of (A) SEM, (B) TEM and (C) STEM. [109]

- **TEM** uses a parallel electron beam perpendicular to the sample plane and processes the transmitted electrons as its name suggests. In this case, images are directed projected onto a screen or a camera. The transmitted electrons carry details about the interior of samples, such as crystallographic information. Due to a much higher resolution (50 pm has been reported in [110]), TEM is able to detect tiny precipitates and dislocations. This advantage is attributed to the much higher acceleration voltages (usually between 60 - 300 kV) they can be operated at, which results in a shorter wavelength (2 pm for 300 kV vs. 7 pm for 30 kV) and thus achieves a higher resolution. However, only thin specimens (lamellae) can be analysed as they allow electrons to pass through them. In the imaging mode, depending on which beam is used, bright field (BF), dark field (DF), high-resolution TEM (HRTEM) images can be obtained. By changing the strength of the intermediate lens, the mode can be switched from imaging to diffraction. In this mode, selected area diffraction patterns (SADP) can be obtained as a projection of the reciprocal lattice, which is often used for determining the crystal structure of materials.

- **STEM** is similar to TEM. It requires thin specimens as well. However, as STEM uses a focused electron beam, images are obtained not by projecting, but by point-by-point scanning which resembles SEM. Compared to TEM,

more types of signals such as characteristic X-rays can be used in STEM (STEM/EDX). Furthermore, the distinguished annular dark-field imaging (HAADF-STEM) benefits many investigations, such as the identification of heavy nanoscale materials at extremely low bulk concentrations [111].

2.6.2 FIB

FIB works in a similar fashion as SEM, with the exception that a finely focused beam of ions (typically Ga ions) instead of the electron beam is used to scan the sample. The interaction with the sample also yields SEs which are often used for imaging. Besides, secondary ions (SI) can also be collected for e.g. chemical analysis. If the kinetic energy transferred from an incident ion is sufficient to overcome the binding energy of the target atoms, sputtering occurs which is used in milling processes. By using a gas injection system (GIS), localized deposition of materials can also be achieved in a FIB. As the size and current of the ion beam for FIB milling/deposition can be precisely controlled, defined structures can be fabricated from the sample. During this process, the ion beam works like a nano scalpel, allowing us to reveal the internal structure of samples and manipulate them at the nanoscale.

In this thesis, the preparation of TEM lamellae is inspired by the in-situ lift-out technique based on [112][113]. Figure 2.11 presented the cycle of preparation of a TEM lamella from an ion-irradiated Al/U-Mo fuel sample:

- A protective layer (usually Pt) is deposited onto the specimen surface in the selected region.
- Two chunks are removed from the pre-defined regions by ion milling, exposing the early form of the lamella.
- The lamella is separated from the bulk material by ion milling (free cutting), and then transferred to a TEM lift-out grid by a manipulator. The lamella was fixed on the grid by deposition.
- Thinning and polishing are performed on the lamella to achieve the electron transparency that is necessary for TEM investigations. The final thickness is usually around or below 100 nm.

Indeed, the preparation of a TEM lamella out of this Al/IDL/U-Mo structure is tricky due to the multiphase material with different hardnesses. The ion beam current as well as the other parameters should be properly adjusted according to the material.

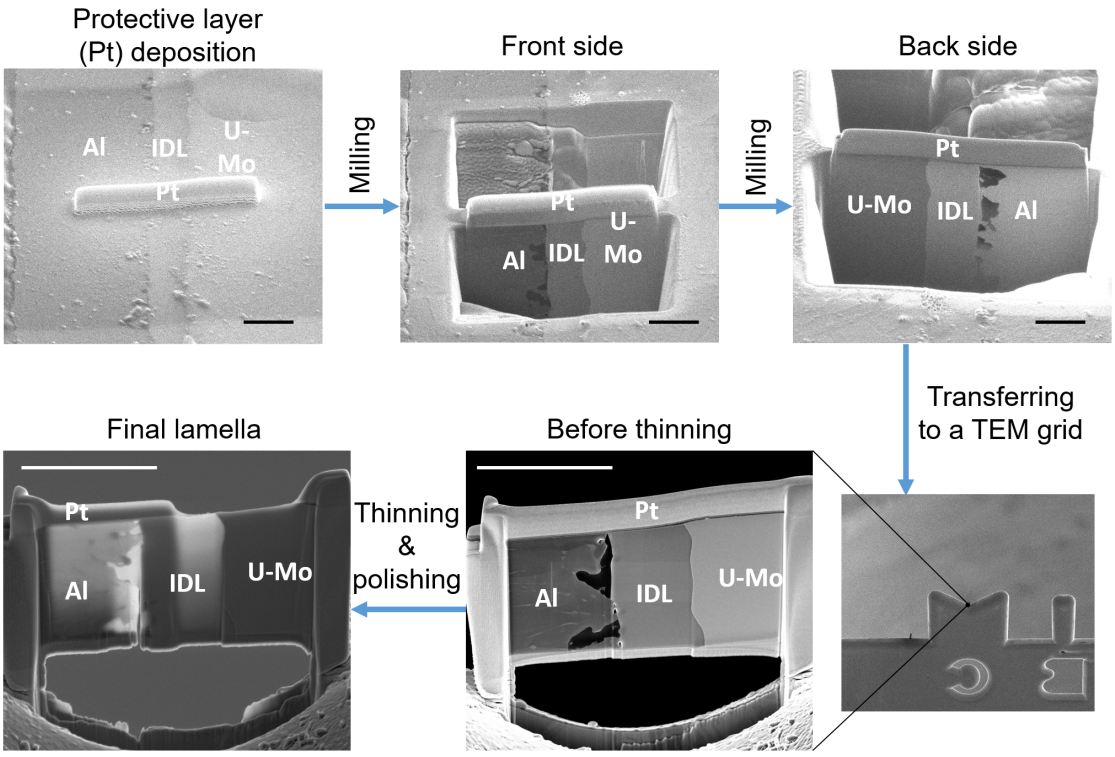

FIGURE 2.11: Cycle of preparation of a TEM lamella from an irradiated Al/U-Mo fuel sample based on the in-situ lift-out FIB technique. Scale bar: 5 µm.

Another important application of FIB is the sample preparation for EBSD. As the EBSD diffraction signal is adopted from the uppermost layer (a few nanometers) of the sample, the surface of the sample should be carefully prepared before performing EBSD, including removing the defects and impurities introduced during the mechanical polishing. In the case of U-Mo samples used in this thesis, the surface preparation is even more demanding. As U-Mo is known to be extremely prone to oxidation, and such oxidation can lead to indexing problems in EBSD, the surface preparation is recommended to be performed in situ, i.e. in the same instrument of EBSD, to avoid contact with air during sample transfer. Hence, in this thesis, the EBSD investigation was performed in a FIB-SEM instrument equipped with an EBSD detector. Figure 2.12 shows a common configuration of a FIB/SEM setup, in which the sample surface was first subjected to an ion polishing process (Figure 2.12A) prior to EBSD (Figure 2.12B).

2.6.3 EBSD

EBSD is already a well-established method and allows determining larger area grain characteristics, including crystallographic orientations, misorientations, phases and grain structures [114]. As shown in Figure 2.9, EBSD also takes

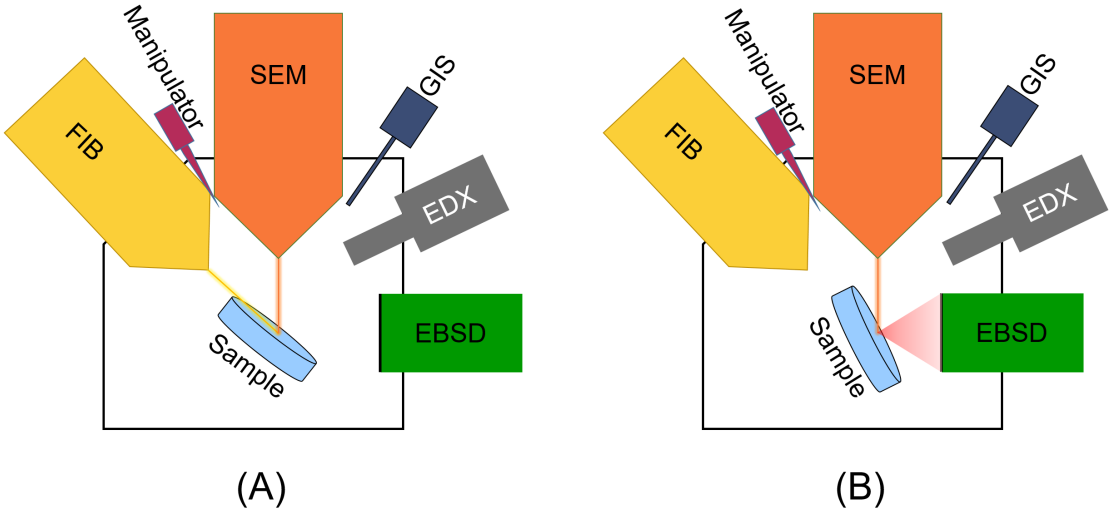

FIGURE 2.12: Schematic drawing of a commonly used configuration of SEM/FIB/EDX/EBSD setup, where (A) FIB polishing is in operation; (B) EBSD is in operation. A manipulator, a GIS system and an EDX detector are also indicated in the instrument.

advantage of BSEs, but it uses the diffraction of them from the crystallographic planes of the investigated sample [115]. When electrons impinge the surface of a sample, diffraction along the crystallographic planes occurs when Bragg's law is satisfied. The diffracted electrons interfere constructively, forming a pattern of intersecting bands on the screen of the EBSD detector. These bands represent their reflecting planes in the sample and are known as Kikuchi lines. The width and the intensity of Kikuchi lines are directly related to the spacing of the atoms in the crystallographic plane, while the angles of the bands are directly related to the angles between the crystallographic planes. The resulting patterns are known as Kikuchi patterns. The formation of Kikuchi pattern is schematically explained in Figure 2.13, where a typical Kikuchi pattern is shown as well. Note that not all lattice planes can be observed due to the existence of destructive interference.

The Kikuchi pattern can be transformed to an EBSD orientation map (or inverse pole figure map) via transformation, which includes determining the width between each pair of lines and the angles between each set of planes then comparing to the database. Nowadays, the indexing can be performed fully automatically in the software based on Hough transform. An EBSD grain map shows the grains with colours representing their orientations, based on which the mechanical properties of the materials can be extrapolated. In the fuel development community, EBSD is often used to characterise grain size and orientation, thereby interpreting the observed irradiation behaviour.

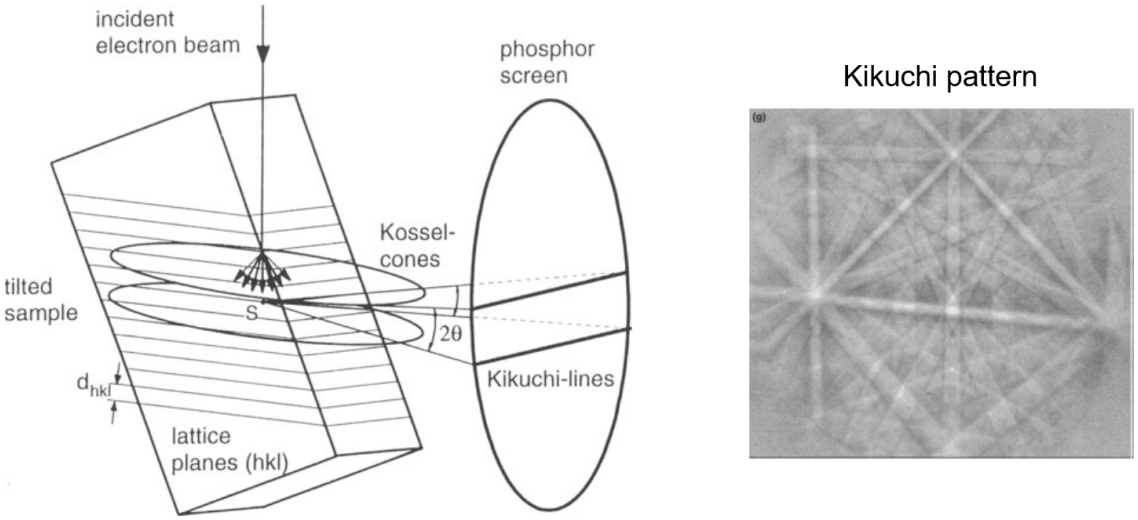

FIGURE 2.13: Left: principle of formation of Kikuchi-lines. Right: a typical Kikuchi pattern. [114]

Chapter 3

Heavy ion and in-pile irradiations: quantitative comparisons

3.1 Introduction

As mentioned in Chapter 1, due to its inferior irradiation properties, the excessive growth of IDL in U-Mo/Al fuels can lead to pillowing and breakaway swelling. A comprehensive understanding of this phenomenon is imperative to predict the IDL behaviour in order to find proper solutions. Based on the data of several in-pile irradiation tests, an empirical model has been developed by Kim and Hofman [13], which predicts the thickness of the generated IDL between U-Mo und Al in the U-Mo/Al fuel system without protective measures:

$$Y_{\mathrm{IDL}}^2 = A \cdot \dot{f}^p \cdot \exp\left(-\frac{q}{T}\right) \cdot t \cdot f_{\mathrm{Mo}} \tag{3.1}$$

In this equation, Y_{IDL} is the IDL thickness in µm. The Arrhenius equation including temperature T and irradiation time t is taken from the out-of-pile IDL growth correlation, which describes the interdiffusion due to thermal activation. The term including fission rate $\dot{f}$ is applied to take the fission-enhanced-diffusion into account. Besides, $A = 2.6 \cdot 10^{-8} \mu m^2 cm^{3p} s^{p-1}$ is the proportionality factor; p is the exponent of the fission rate $\dot{f}$ that has been averaged over the irradiation time t (in seconds); $q = 3850K$ is the fit parameter to normalize the average irradiation temperature T (in Kelvin); the last term f_{Mo} is the correction factor for the molybdenum content of the fuel, e.g. 0.85 for U-10wt.%Mo [13]. No uncertainties were reported for these fit constants, an average deviation of 15% between measured IDL thickness and using this equation predicted IDL thickness was estimated by Breitkreutz [29] based on the data provided by Kim [13].

Due to the highly intercorrelated radiation parameters in a reactor such as fission rate, burn-up, and temperature, the proposed dependences cannot be properly verified in-pile. Considering its gracefully and independently

controllable parameters, heavy ion irradiation was proposed to verify this in-pile IDL growth model, i.e. the correlation 3.1. In order to have comparable irradiation effects, Breitkreutz [29] derived two correlations to convert ion flux $\dot{\Phi}$ and ion fluency Φ to equivalent fission rate $\dot{f}$ and equivalent fission density n, respectively:

$$\dot{f} = \dot{\Phi}\xi/2 \tag{3.2}$$

$$n = \Phi\xi/2 \tag{3.3}$$

Here, ξ is the relative total energy deposition calculated by using SRIM code. Its physical meaning is the number of fission fragments that yield the same effect as one ion. As ion flux describes the number of ions per cm^2 and second, while fission density refers to the number of fission fragments per cm^3 and second, the factor ξ naturally has a unit of $1/\mu m$ to account for the simulated volume. The value of ξ depends on ion species and the energy deposition while penetrating the irradiated material(s). In a bilayer system, the energy deposition at the interface is directly linked to the thickness of the top layer. In this study, the samples are composed of a U-Mo substrate and an Al top layer. As a result, during the ion irradiation experiments, the samples experienced a reversed irradiation direction (ions travel from Al to U-Mo) as the one actually found in-pile (fission fragments originate from U-Mo). Three Al layer thicknesses were investigated, i.e. 13 µm, 9 µm and 6 µm. Table 3.1 lists the ξ value at the interface for the three structures.

TABLE 3.1: Value of ξ for different Al thicknesses

Al thickness [µm]	13	9	6
ξ [1/µm]	0.21	0.3	0.41

Thus, a correlation of the IDL thickness to the ion flux is established:

$$Y_{IDL}^2 = A \cdot (\dot{\Phi}\xi/2)^p \cdot \exp\left(-\frac{q}{T}\right) \cdot t \cdot f_{Mo} \tag{3.4}$$

The verification of this IDL growth correlation has been preliminarily conducted in [29] using the ion irradiation data from [116], where a good agreement was shown by comparing the calculated IDL thickness to the during PIE measured values. In that study, the local ion flux was not accessible as the ion flux profile could not be determined during irradiation. Under such

circumstances, an empirical value for the exponent of fission rate i.e. $p = 0.5$ ([117][118]) was employed in Equation 3.4. In this way, a proportionality between the IDL thickness and the ion flux was established, and thereby the ion flux profile can be reconstructed based on the measured IDL thickness profile.

As a part of this thesis, a beam profile monitor (BPM) was constructed and utilized to determine the ion flux profile. Ion irradiations were performed before and after the application of the BPM. Thus, the verification of the IDL growth model was undertaken using two approaches:

- Before the commissioning of the BPM, the ion flux profile could not be directly measured during the beamtime campaigns. The ion flux profiles were reconstructed by applying a proportionality between the IDL thickness and the ion flux derived based on the assumption $p = 0.5$ in Equation 3.4, which is the same idea applied in [29]. This approach is presented in Section 3.5.

- After the commissioning of the BPM, the ion flux profiles could be obtained from the BPM measurements. Local ion fluxes could be extracted from the profile and used for calculating the predicted IDL thicknesses without making any assumptions. This approach is summarized in Section 3.6.

In what follows, the sample preparation, the technical preparation work and the determination of ion flux and fluence profile are presented. The results obtained from the two approaches are summarized. At the end of this chapter, a comparison between in-pile and ion irradiation is given, and the temperature effect on IDL growth dynamics is discussed, aiming to strengthen the understanding of the influences of irradiation conditions.

3.2 Sample preparation

An Al layer was PVD-sputtered on a U-Mo substrate, making up a bilayer structure. The principle of PVD sputtering has been described in Chapter 2, Section 2.5. The density of the Al layer was determined as $\rho = 2.3\,\mathrm{g/cm^3}$ by measuring the total weight of deposited Al and dividing it with the volume of the layer. This value is slightly lower than that of the bulk material ($2.7\,\mathrm{g/cm^3}$). During the ion irradiation experiment, the ions impinge perpendicularly on the Al surface (incident angle $\alpha = 0°$). This geometry facilitates a direct interpretation and benefits the quantitative analysis.

Using this sample geometry, the ions during irradiation travel from Al to U-Mo, which is opposite to the movement direction of the in-pile fission products,

i.e. from U-Mo (origin) to the Al matrix. As argued in Chapter 2, Section 2.4.2, this opposite ion direction should have a minimum effect on the IDL growth, if the Al thickness is so adjusted that the Bragg peak of the nuclear loss of the incoming ions lands at the Al/U-Mo interface. On the other hand, placing the Bragg peak near the interface of interest also benefits the irradiation experiment as the irradiation time is can be minimized due to the high damage rate. In order to deposit the Bragg peak at the Al/U-Mo interface, SRIM/TRIM calculations were performed to calculate the top layer thickness, namely the Al thickness. As shown in Figure 3.1(A), with a 13 µm Al layer on the top, the Bragg peak of nuclear energy loss curve lands at the Al/U-Mo interface, where the electronic energy loss curve and the ion distribution profile are also presented. When IDL grows at the interface, the curves are slightly shifted as shown in Figure 3.1(B).

3.3 Design and construction of a stage system for high-temperature ion irradiation

One of the research objectives of this thesis is to investigate the temperature effect. Yet, with the available sample stage (referred to as "old stage"), the ion irradiation can only be operated at low temperatures i.e. under 200 °C, owing to the geometry of the stage and the limited heating power of the attached heating wire. Besides, the measured temperature on the old stage showed a significant fluctuation, especially at temperatures above 140 °C. This is due to the logic of temperature control, which was done by a simple on/off control of the air cooling. A new sample with precise control of temperature and being able to be operated at high temperatures above 200 °C was therefore urgently needed.

Hence, in the scope of this thesis, a new irradiation stage system was planned, constructed and applied in the thereafter performed irradiation experiments. A CAD model and a picture of it are shown in Figure 3.2. Following improvements were made to allow the ion irradiation experiments to be performed in a much more precise manner:

- The heating source is a ceramic plate-like heating element with a width (15 mm) slightly larger than that of the samples (10 mm). It is located centred behind the samples, ensuring a symmetrical and possibly homogenous heating for the samples. As a comparison, the old stage was heated by a thin heating wire attached to the side of the stage.
- Samples are securely fixed to the stage by a stainless steel mask. Three slits were cut on the mask for placing Pt 100 sensors for temperature

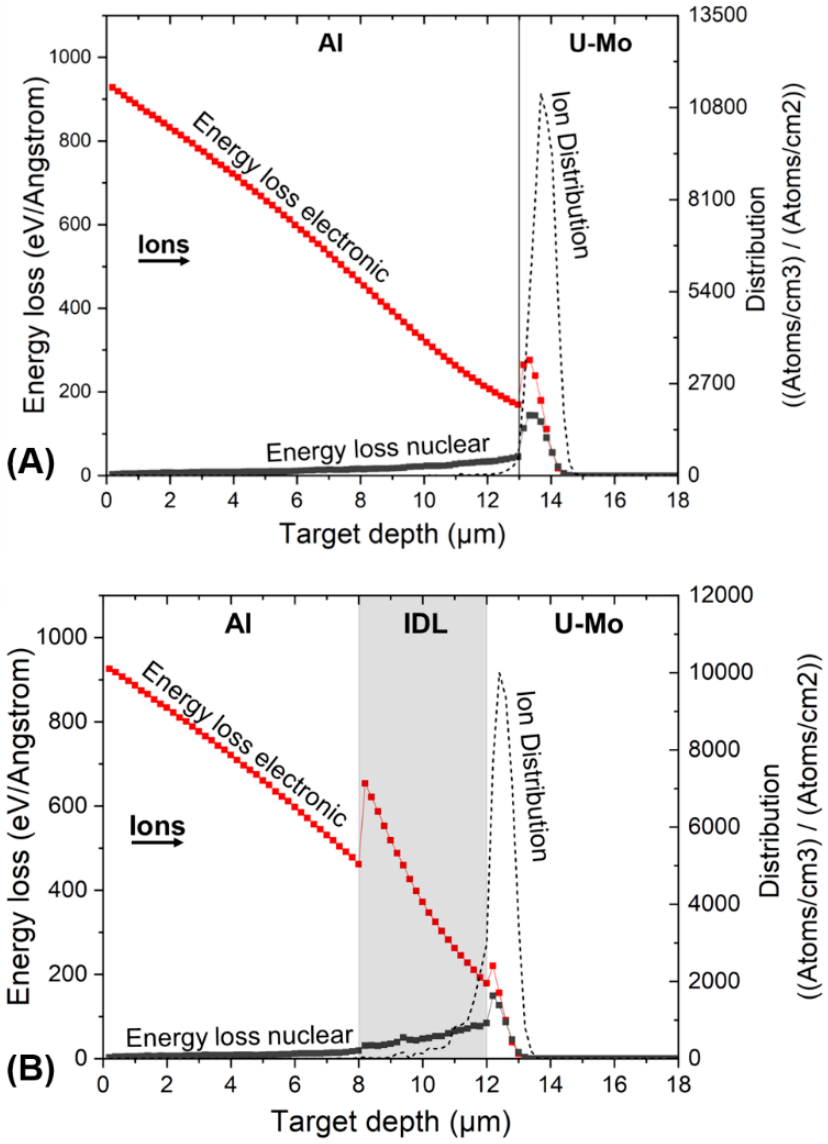

FIGURE 3.1: SRIM/TRIM calculated ion distribution and energy deposition of 80 MeV ^{127}I in (A) Al/U-Mo system and in (B) Al/IDL(4 μm)/U-Mo system.

measurement of the samples. These sensors are fixed by additional screws. In this way, the position of the sensor can be easily and independently adjusted. For instance, the sample should be fixedly attached to the stage to ensure a good heat transfer, whereas the Pt 100 sensor, whose body is mainly ceramic, should be fixed with a much smaller force to avoid breaking. On the old stage, the Pt 100 sensor was clamped between the mask and the sample, in which way the sensor went broken easily if the sample is fixedly screwed to the stage.

- The temperature is controlled by a PID controller, which monitors the actual temperature and accordingly adjusts the heating power in real-time during

irradiation. As a result, the temperature stayed fairly stable during each irradiation. This control mechanism also allows the sample to stay at the set temperature despite occasional fluctuations of ion beam.

- A plate-like transmission detector made by tantalum (the same material as the Faraday cup) with a central hole was designed. During the beam adjustment, the magnetic lenses of the beamline are adjusted so that the ion beam passes through the central hole of the transmission detector. In the ideal case, no signal is detected on the tantalum plate. As the diameter of the central hole equals the diameter of the three holes on the stainless steel mask for fixing the samples, and the position of the central hole is aligned vertically with the three holes, the ion beam spot can land in the defined area of the sample by moving the stage to the sample position with the linear feedthrough.

- Due to the geometry of the irradiation chamber, a longer stage for loading more samples is unfortunately not possible. Thus, the new stage system aimed at reducing the time and effort required for sample exchange. For this purpose, a removable holder (indicated in Figure 3.2) was designed to hold samples. During sample exchange, one only needs to remove this small holder instead of dismounting the whole stage system which is the case for the old stage. Furthermore, an additional removable holders was in use, with which the samples for the new cycle can be prepared in advance.

- A quick access door was utilized, which largely simplified the sample exchange procedure and thereby saved a lot of time. In total, the sample exchange can be completed within a few minutes. As a comparison, the sample exchange without these improvements took around 40 min and much more effort, as during which the whole stage as well as the heating element had to be removed and the front flange of the irradiation chamber had to be dismounted.

3.4 Ion flux and fluence profile

During irradiation, the mono-energetic ion beam was transmitted straight to the sample surface, the ions impinged the sample on the Al layer perpendicularly. No beam wobbling[1] was used. The irradiation profile, i.e. the beam distribution

[1] Wobbling: The focused ion beam is moved rapidly in both x and y directions by electric fields, aiming to increase the homogeneity of the ion flux. In this case, the exact local ion flux is difficult to access. Therefore, beam wobbling was not used in this thesis.

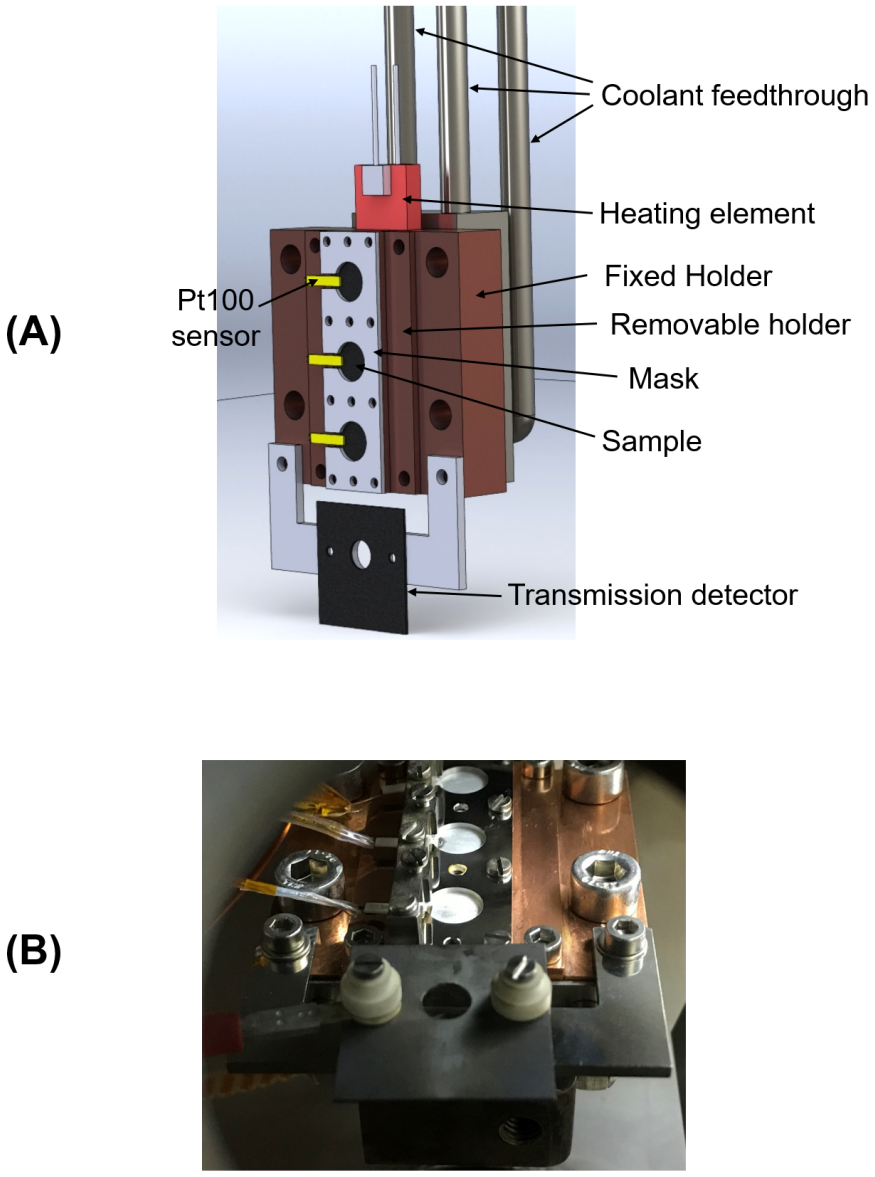

FIGURE 3.2: New high-temperature stage constructed in this thesis. (A) CAD model; (B) Picture taken from the irradiation chamber.

covering the pre-defined area of the sample has a bivariate Gaussian distribution, which results from the focusing system and was later proven by the BPM. As a consequence, the averaged ion flux $\dot{\Phi}$ and the integral of it over irradiation duration t, i.e. the ion fluence Φ, follow a bivariate Gaussian distribution, too. These parameters are related by:

$$\Phi = \int \dot{\Phi} \mathrm{d}\tau = \dot{\Phi} \cdot t \tag{3.5}$$

$$\int \int \Phi \mathrm{d}x \mathrm{d}y = N \tag{3.6}$$

The ion fluence profile can be expressed as:

$$\Phi = \Phi_{max} \cdot f_G(x, y) \tag{3.7}$$

Here $f_G(x, y)$ is the probability density function for a bivariate Gaussian, while Φ_{max} is the maximum fluence occurring at the centre of the elliptical beam spot:

$$\Phi_{max} = \frac{N}{2 \cdot \pi \cdot (w_a \cdot w_b)} \tag{3.8}$$

w_a, w_b and w are the Gaussian widths (standard deviations) in the semi-major axis a, the semi-minor axis b and the polishing axis l of the elliptical beam footprint, respectively. The axes are shown in Figure 3.3 and can be measured with OM. The measurement of IDL thickness profile was taken on the polished cross-section. The following equation holds:

$$\frac{w_a}{a} = \frac{w_b}{b} = \frac{w}{l} \tag{3.9}$$

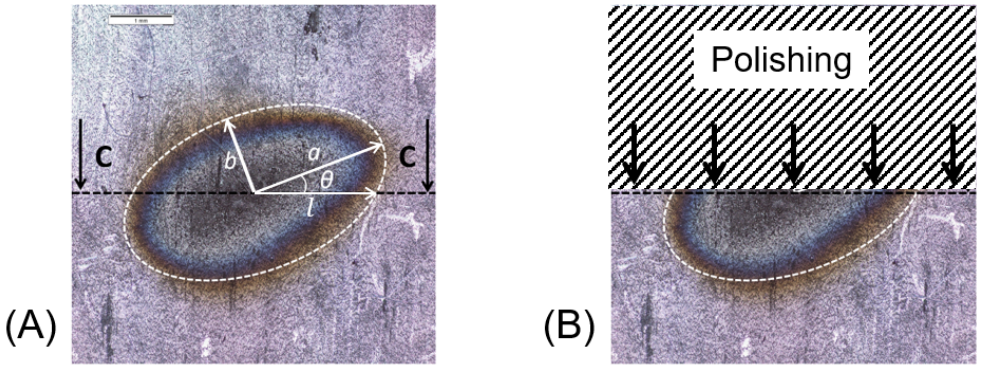

FIGURE 3.3: (A) Characteristic elliptical footprint left by the ion beam after irradiation. Sample: S4-7. (B) The sample was vertically polished until reaching the beam spot centre during PIE.

Thus, the maximum fluence is given by:

$$\Phi_{max} = \frac{N}{2 \cdot \pi \cdot (a \cdot \frac{w}{l} \cdot b \cdot \frac{w}{l})} = \frac{N}{2 \cdot \pi \cdot a \cdot b \cdot (w/l)^2} \tag{3.10}$$

On the other hand, the probability density function $f_G(x, y)$ can be expressed as:

$$\begin{aligned} f_{\mathrm{G}}(x,y) &= \exp[-(\frac{(x-x_0)^2}{2\cdot w_{\mathrm{a}}^2}+\frac{(y-y_0)^2}{2\cdot w_{\mathrm{b}}^2})] \\ &= \exp[-l^2\cdot(\frac{(x-x_0)^2}{2\cdot a^2\cdot w^2}+\frac{(y-y_0)^2}{2\cdot b^2\cdot w^2})] \end{aligned} \tag{3.11}$$

Here $(x_0,\ y_0)$ is the coordinate of beam centre. Hence, the ion fluence distribution and the corresponding ion flux distribution can be respectively expressed as:

$$\Phi(x,y) = \frac{N}{2\cdot\pi\cdot a\cdot b\cdot(w/l)^2}\cdot\exp[-l^2\cdot(\frac{(x-x_0)^2}{2\cdot a^2\cdot w^2}+\frac{(y-y_0)^2}{2\cdot b^2\cdot w^2})] \tag{3.12}$$

$$\dot{\Phi}(x,y) = \frac{N}{2\cdot\pi\cdot a\cdot b\cdot(w/l)^2\cdot t}\cdot\exp[-l^2\cdot(\frac{(x-x_0)^2}{2\cdot a^2\cdot w^2}+\frac{(y-y_0)^2}{2\cdot b^2\cdot w^2})] \tag{3.13}$$

To obtain the number of ions N from the beam current, the charge state must be taken into account. Ions are usually multiply charged, which means each ion carries a charge greater than a single electronic charge, which arises two definitions of for beam current, i.e. electrical current I_{elec} (unit: eμA) and particle current I_{part} (unit: pμA). They are related by:

$$I_{\mathrm{part}} = I_{\mathrm{elec}}/Q \tag{3.14}$$

Q is the charge state of the ions. During irradiation, the electrical I_{elec} can be determined using a Faraday cup. Thus, the total number of ions N can be obtained by:

$$N = \int I_{\mathrm{part}}\mathrm{d}\tau = \int I_{\mathrm{elec}}\cdot Q\mathrm{d}\tau \tag{3.15}$$

Since only the IDL thickness profile on the polished cross-section i.e. along the polishing axis is measured during PIE, the determination of ion flux and ion fluence profile is only needed at the plane of the cross-section. Thus, the two-dimensional analysis can be reduced to one dimension. As shown in Figure 3.4, any straight cut through the centre of a bivariate Gaussian brings up a univariate Gaussian. The ion flux at the C-C section was a univariate Gaussian:

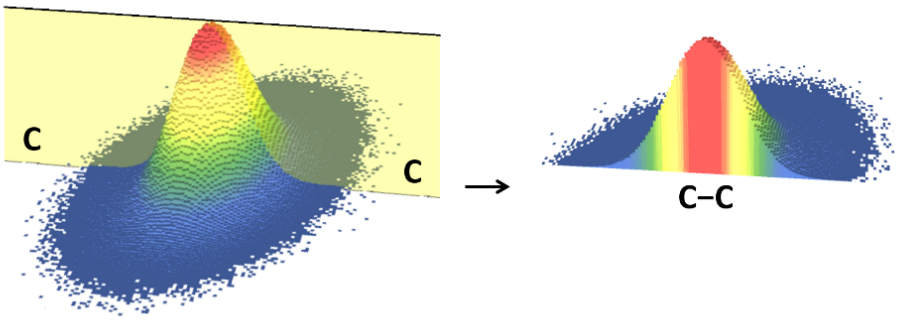

FIGURE 3.4: Visualization of a bivariate Gaussian distribution. The simulation was performed in Mathematica[119]. A random cut C-C through the centre leads to a univariate Gaussian distribution on the obtained cross-section.

In this case, the transverse profile of the ion fluence $\Phi(x)$ and the ion flux $\dot{\Phi}(x)$ at the plane of the polishing axis can be described with a univariate Gaussian function $f_G(x)$:

$$\begin{aligned}\Phi(x) &= \Phi_{max} \cdot f_G(x) \\ &= \frac{N}{2 \cdot \pi \cdot a \cdot b \cdot (w/l)^2} \cdot \exp[-\frac{1}{2}(\frac{(x-x_0)^2}{w^2})]\end{aligned} \tag{3.16}$$

$$\begin{aligned}\dot{\Phi}(x) &= \dot{\Phi}_{max} \cdot f_G(x) \\ &= \frac{N}{2 \cdot \pi \cdot a \cdot b \cdot (w/l)^2 \cdot t} \cdot \exp[-\frac{1}{2}(\frac{(x-x_0)^2}{w^2})]\end{aligned} \tag{3.17}$$

At this point, it is clear that once the total number of ions N, the Gaussian width w of the ion beam profile, the distance l between the centre and the border of the footprint along the polishing line and the centre coordinate x_0 are known, the profile of ion fluence and ion flux can be reconstructed by using Equation 3.16 and Equation 3.17, respectively. The determination of the Gaussian width w and the centre coordinate x_0 of the ion beam profile is performed the following ways:

- For the irradiation experiments performed at an earlier time, i.e. before the installation of the BPM, the ion flux profile could not be measured. As mentioned at the beginning of this chapter, a proportionality between the Y_{IDL} and $\dot{\Phi}$ was obtained by defining $p = 0.5$ in Equation 3.4:

$$Y_{IDL} \propto \dot{\Phi}^{\frac{1}{4}} \tag{3.18}$$

By employing this proportionality correlation, the Gaussian width w and the centre coordinate x_0 can be adopted from the IDL thickness profile. Thus, the ion flux profile can be reconstructed. This approach is therefore considered semi-quantitative as it is based on assumption and the value of p cannot be justified as it would lead to circular reasoning. The experiment results are summarized in Section 3.5.

- For the irradiation experiments carried out after utilizing the BPM, the space-resolved beam intensity can be directly determined. The resulted centre coordinate x_0 and Gaussian width w of the intensity profile can be directly applied for the ion flux profile due to the linearity of the light output of the chromox screen of the BPM. This linearity property has been confirmed in [120]. The ion flux profile can thus be reconstructed. This approach is fully quantitative as it is purely based on measurement. The experiment results are presented in Section 3.6.

3.5 Profile reconstruction - approach 1

Five samples were irradiated before the use of BPM. The irradiation parameters are summarized in Table 3.2.

TABLE 3.2: Irradiation parameters

Sample ID	S3-2	S3-4	S4-1	S4-5	S4-7
Al Thickness [µA]	13	13	13	13	13
Total ions [ions]	$9.5 \cdot 10^{15}$	$3.55 \cdot 10^{15}$	$5.13 \cdot 10^{15}$	$3.37 \cdot 10^{15}$	$4.29 \cdot 10^{15}$
Irradiation time [h]	12.5	3.5	6.7	9.3	11
Temperature [°C]	140	180	200	275	220

After irradiation, the samples were embedded in transparent resin and then polished to expose the cross-section along the polishing axis, on which the distribution of IDL thickness is determined. Based on the distribution function 3.17 and the correlation between the IDL thickness and the ion flux, i.e. Equation 3.18 , the distribution of IDL thickness at the cross-section of polishing follows:

$$Y(x) = Y_{\max} \cdot \exp^{\frac{1}{4}}[-\frac{1}{2}(\frac{(x-x_0)^2}{w^2})] \tag{3.19}$$

Here Y_{max} stands for the maximum IDL thickness. Thus, once the IDL thicknesses along the polishing axis l is determined with SEM, the Gaussian width w and the coordinate x_0 of beam centre can be obtained by fitting the measured data with Equation 3.19, with which the profile of ion flux and ion fluence can be reconstructed by using Equation 3.16 and Equation 3.17, respectively. This approach is designated as **approach 1**.

For the five irradiated samples, the measurement and the fit result are shown in Figure 3.5 and Table 3.3. The reconstructed ion flux and ion fluence profiles are summarized in Figure 3.6. Eventually, the predicted IDL thickness using the empirical IDL growth model can be calculated with Equation 3.4 and compared with the measurement. The fit constants of Equation 3.4 can be verified with the data obtained from ion irradiation as well. The comparison and verification are summarized in Section 3.7.

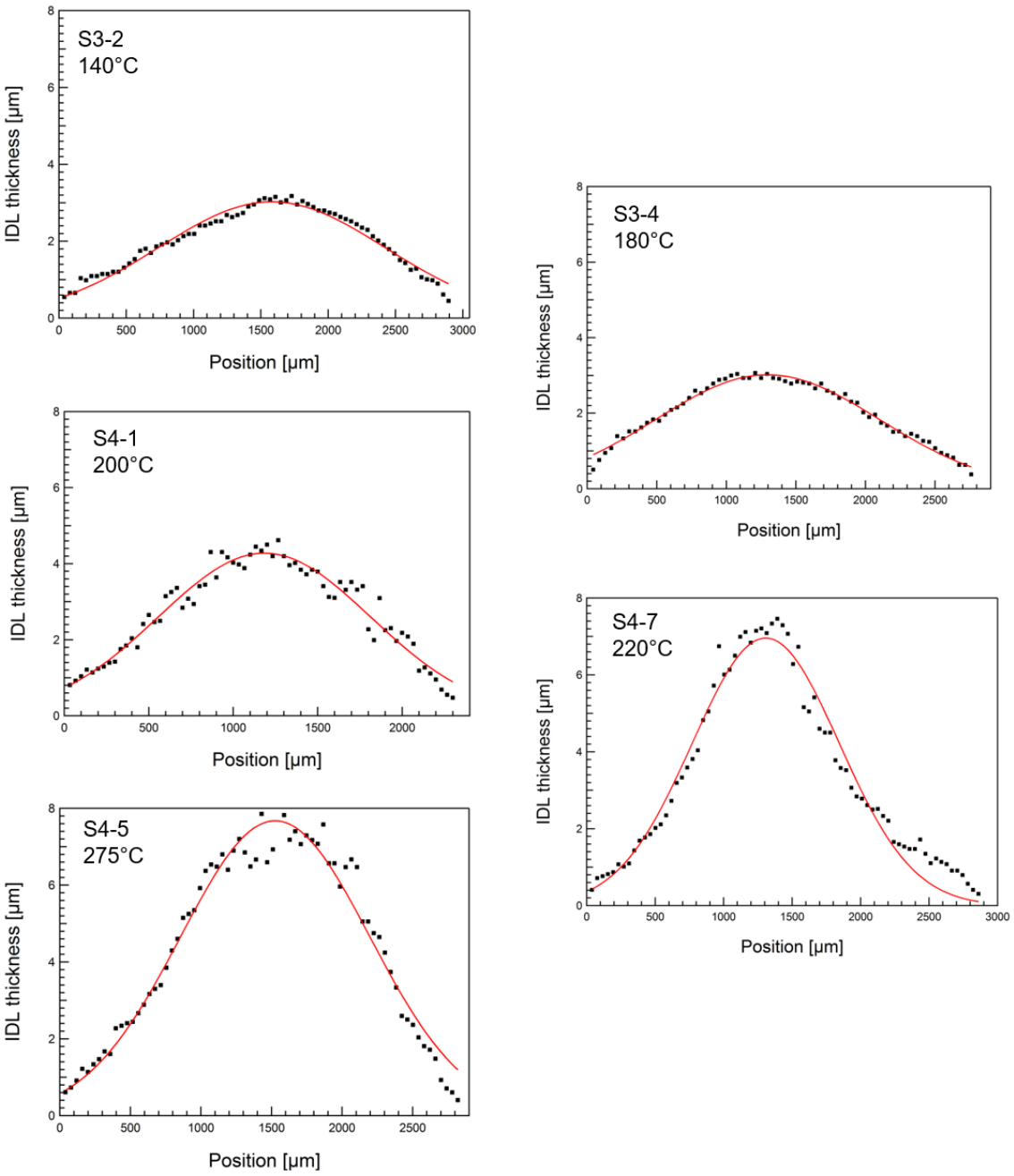

FIGURE 3.5: Measured IDL thickness distribution on the prepared cross-sections and the fit plots.

TABLE 3.3: Fit results

Fit parameter	S3-2	S3-4	S4-1	S4-5	S4-7
Y_{max} [µm]	3.02	3.02	4.28	7.68	6.96
Gaussian width w [µm]	420.98	402.12	314.79	335.49	268.49
Centre coordinate x_0 [µm]	1580.7	1296.3	1184.5	1525.7	1306.9

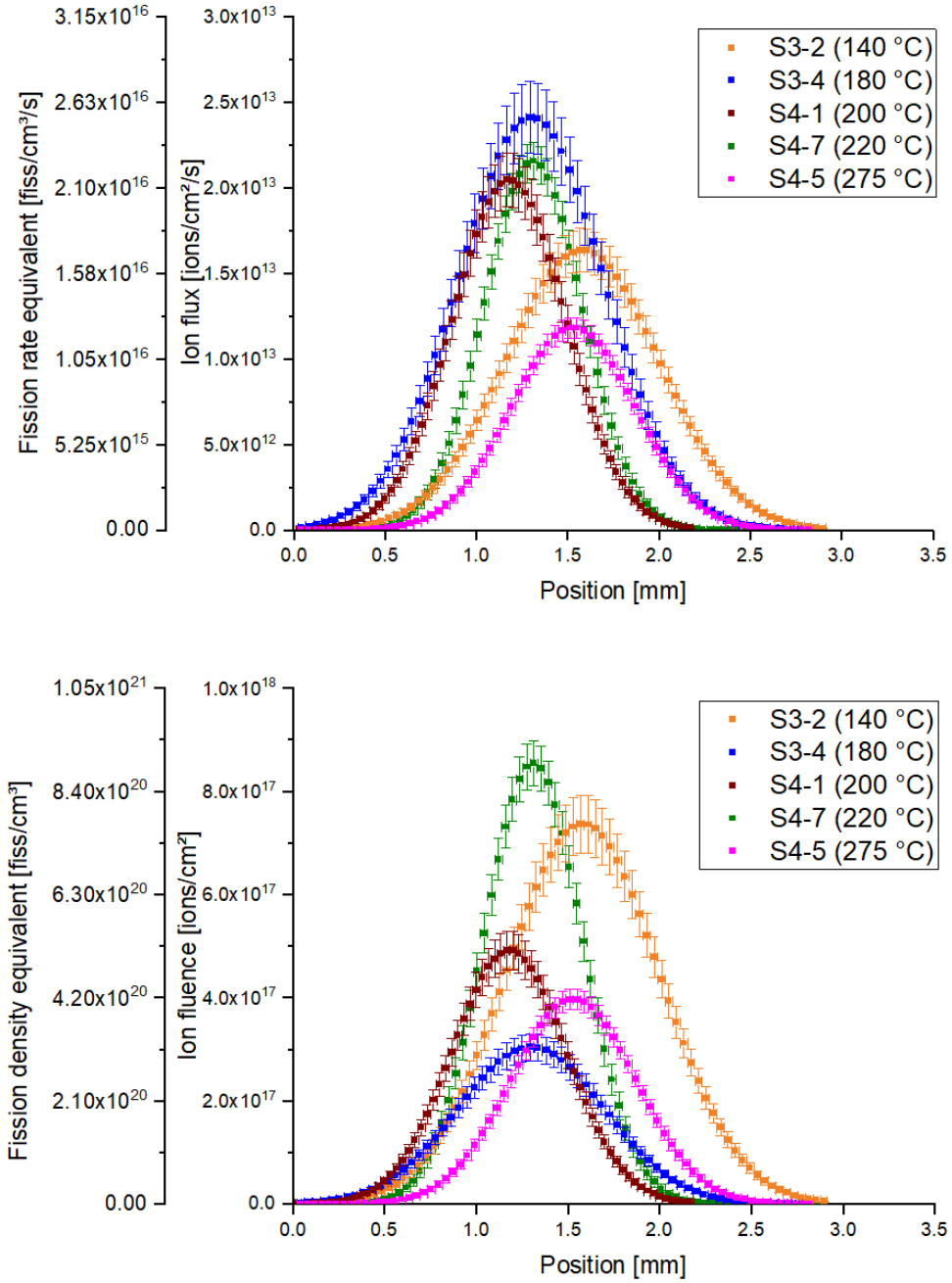

FIGURE 3.6: Reconstruction of flux and fluence profiles using approach 1.

3.6 Profile reconstruction - approach 2 (fully quantitative)

3.6.1 Beam profiling and monitoring

A quantitative analysis relies on accurate measurements of ion dose and profiles. To this end, the beamline was reconstructed to include the BPM and have a better

arrangement of the components. The important components and their positions in the beamline are shown in Figure 3.7. During the beamtime, the beam spot was carefully adjusted and monitored in several ways with different components, including:

- A control slit is situated in the front part of the beamline. This component consists of four successively placed tantalum plates that can be moved in X+, X-, Y+, Y- directions on the plane perpendicular to the ion beam. The four plates are electrically insulated from each other, and each of them is connected to an ammeter to detect ion signals. The four plates are slightly shifted from each other, forming a slit in the centre. The ion beam must travel through this slit before it reaches the irradiation chamber. By adjusting the positions of the four tantalum plates, the slit, and thereby the position of the ion beam, can be manipulated. This is usually carried out in the beam tuning phase.

- The beam transmission was determined by the transmission detector for more accurate measurement of ion dose. It is usually carried out in the beam tuning phase.

- The beam current was measured by the Faraday cup for the calculation of ion dose. The measurement interrupts the irradiation.

- The beam intensity profile was acquired by the chromox screen of the BPM and was later used for the reconstruction of ion flux profile. The measurement interrupts the irradiation.

- The beam spot profile was continually monitored by a CCD camera viewing the sample under irradiation. Due to the real-time monitoring, it can immediately noticed if the beam is abnormal. This monitoring does not interrupt the irradiation.

- The beam spot profile can be additionally visualized by a turnable quartz glass, during which the beam power needs to be weakened by a "sieve" to protect the quartz glass from the powerful ion beam. It was usually performed in the beam tuning phase to examine the beam transmission.

The beam spot visualized by different profiling and monitoring mechanisms is shown in Figure 3.8. In this fashion, the ion dose and profiles were obtained with high confidence [121], which laid the foundation for the mission of this study - fully quantitative analysis of IDL growth dynamics.

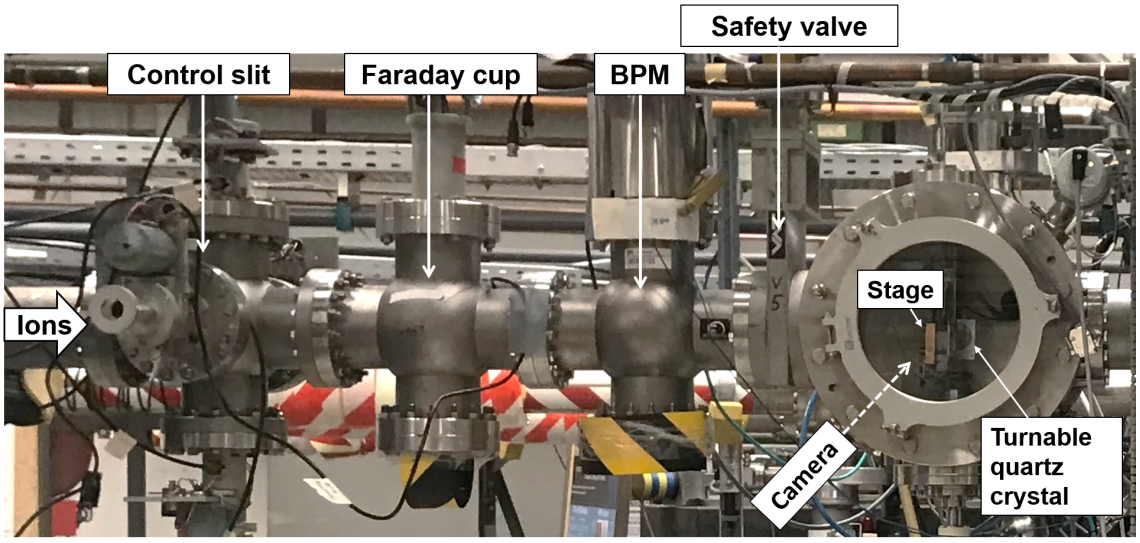

FIGURE 3.7: Components for beam positioning, profiling and monitoring in the beamline.

3.6.2 Analysis

A fully quantitative comparison between heavy-ion and in-pile irradiation can be drawn by directly measuring the space-resolved beam intensity during irradiation. The obtained information such as the centre coordinate and the Gaussian width can be used to determine the ion flux profile. This approach is referred to as **approach 2**.

In total five samples were irradiated. The irradiation parameters are summarized in Table 3.4. It is worth noting that different Al thicknesses are applied here in order to explore its effect on the IDL growth dynamics.

TABLE 3.4: Irradiation parameters

Sample ID	S8-10	S8-11	S10-5	S10-6	S8-12
Al Thickness [µA]	13	13	9	9	6
Total number of ions	$2 \cdot 10^{16}$	$2 \cdot 10^{16}$	$8.1 \cdot 10^{15}$	$1 \cdot 10^{16}$	$1.5 \cdot 10^{16}$
Irradiation time [h]	23	19	20	18.2	28.5
Temperature [°C]	70	140	110	140	140

Figure 3.9 shows the beam intensity profiles obtained by the BPM during irradiation. The profiles were fitted with the Gaussian function in order to determine the Gaussian width and the centre coordinate, with which the ion flux and fluence profiles can be obtained with Equation 3.16 and Equation 3.17, respectively. The fit curves are shown in the same figure. Some data points of

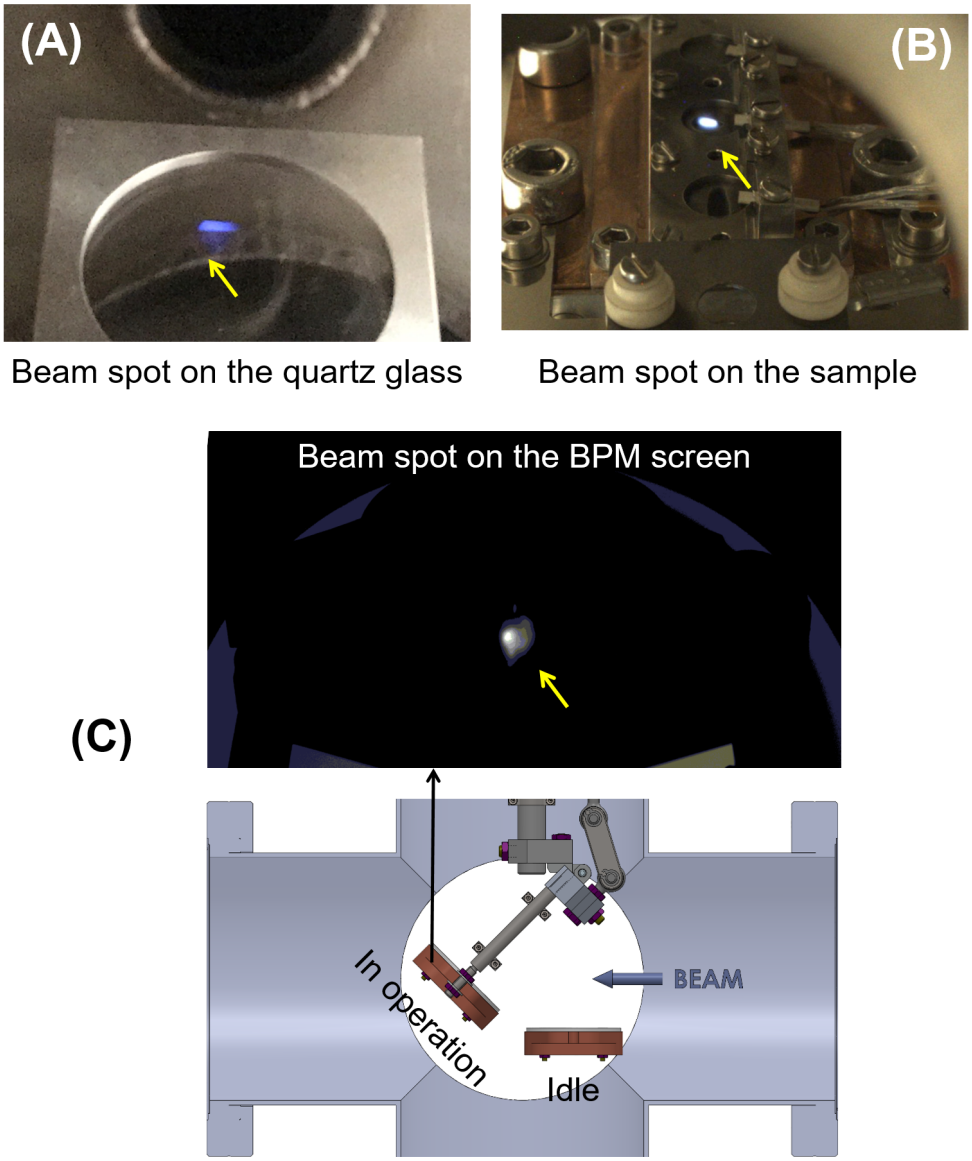

FIGURE 3.8: Beam spot visualized by different mechanisms. (A) Image of a beam spot (weakened) shown on the quartz glass. (B) Image of a beam spot shown on the sample captured by the CCD camera. (C) Illustration of the operating principle of the BPM with an acquired image of beam intensity profile.

sample S8-10 and S8-11 deviate notably from the expected Gaussian distribution, which is caused by the fluctuations of the ion beam during irradiation. At the beam centres of sample S10-6 and S8-12, the maximum BPM intensity (saturation) was reached, where a "plateau" with a constant value is shown in the intensity profile (marked in blue). Those data points were removed in the Gaussian fit to obtain realistic results. Furthermore, the fission rate and density profiles are obtained by using Equation 3.2 and Equation 3.3, respectively. Eventually, the reconstructed ion flux and ion fluence profiles with their equivalent fission effects

are summarized in Figure 3.10, where multiple y-axes are used to distinguish the different Al thicknesses.

In order to compare these two approaches, approach 1 was additionally performed on S8-11 of this irradiation campaign. By fitting the IDL thickness profile with Equation 3.19, the Gaussian width and the centre coordinate were obtained. Transferring them to the ion flux profile, the local ion fluxes can be determined and the predicted IDL thicknesses can be calculated with Equation 3.4. The measurement, the predicted IDL thickness profile obtained by using the fully quantitative approach (approach 2), and the predicted IDL thickness profile obtained by using approach 1 are compared in Figure 3.11, where a good agreement is seen considering the uncertainties. This verification confirmed that using the proportionality $Y_{\mathrm{IDL}} \propto \dot{\Phi}^{\frac{1}{4}}$, i.e. the assumption $p = 0.5$ for the reconstruction of ion flux profile is reasonable.

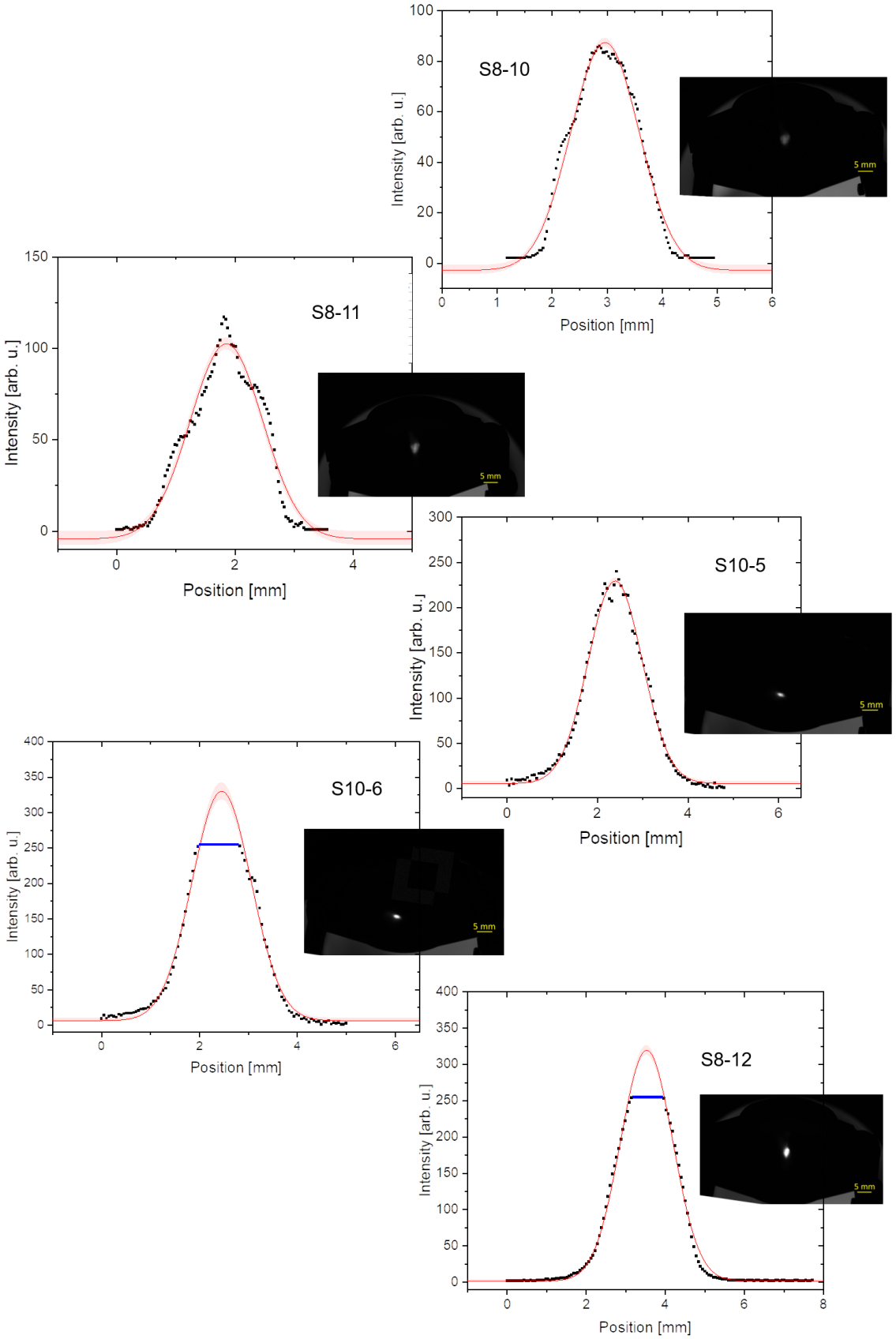

FIGURE 3.9: Beam intensity profiles along the polishing axis obtained by BPM. The red curves are Gaussian fits with a 95% confidence interval to the profiles. At the beam centres of sample S10-6 and S8-12, the saturation of BPM intensity was reached. The resulting "plateau" with a constant value (marked in blue) in both cases were removed in the Gaussian fit.

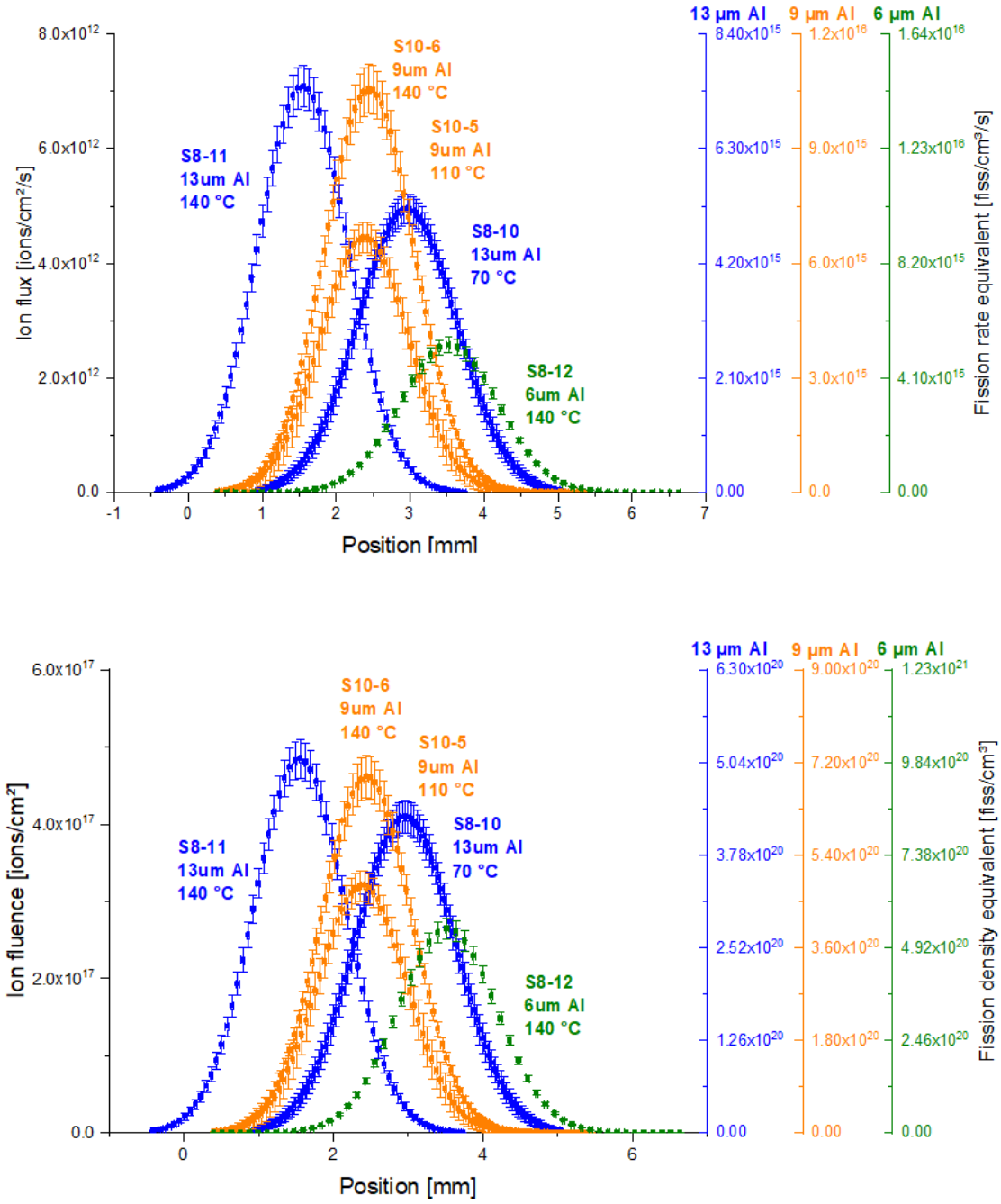

FIGURE 3.10: Ion flux and fluence profiles obtained using approach 2.

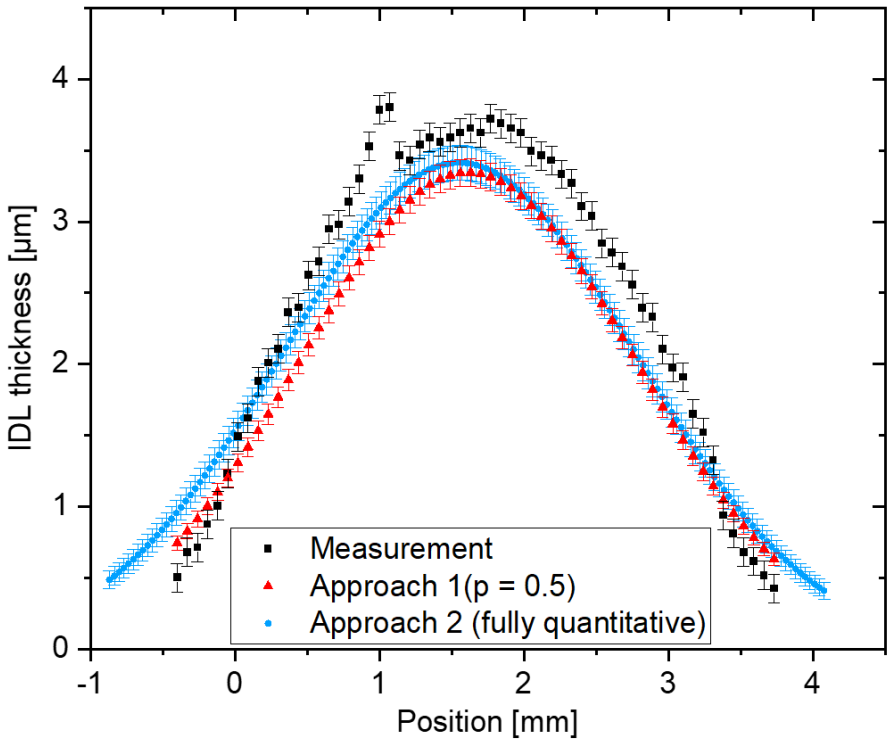

FIGURE 3.11: Comparison of IDL thickness profiles obtained by measurement, approach 1 and approach 2 for sample S8-11. The deviated data points of the measurement are caused by beam fluctuations.

3.7 Discussion

3.7.1 Comparison between in-pile and ion irradiation

With the obtained ion flux profiles, the IDL thicknesses can be calculated with approach 1 ($p = 0.5$) or approach 2 (fully quantitative), based on the in-pile IDL growth model. The attained values should be compared with the measurement for verification. The deviation between the calculation and the measurement is defined as:

$$\text{Deviation} = \frac{\text{calculation} - \text{measurement}}{\text{measurement}} \times 100\% \tag{3.20}$$

The deviation between the measured IDL thickness and the calculation based on approach 1 is shown in Figure 3.12. The deviations are generally small, indicating that the two datasets match well within the experimental accuracy. Note that the in-pile IDL growth correlation i.e. Equation 3.1 itself comes with an uncertainty of $\sim 15\%$ as mentioned in Section 3.1.

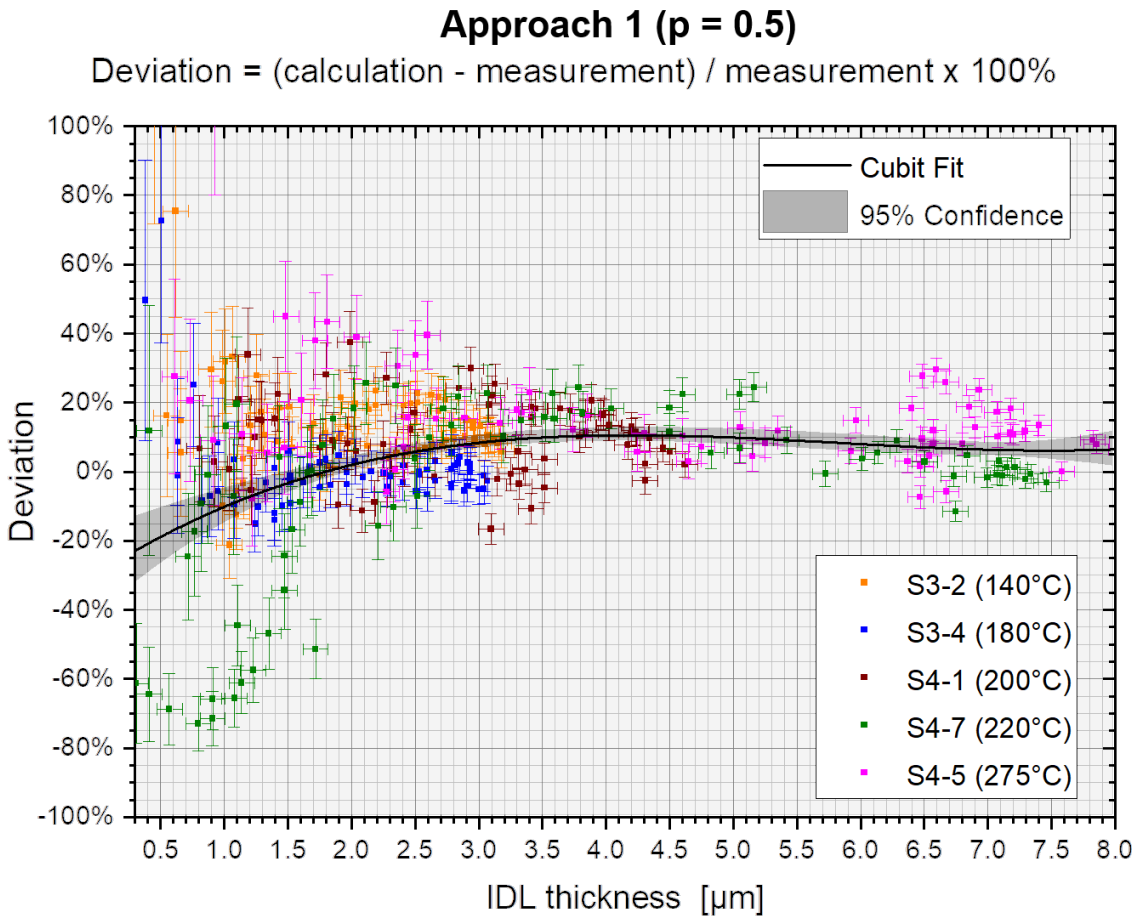

FIGURE 3.12: Deviation between the IDL thickness calculated with ion irradiation data using approach 1 and the directly measured IDL thickness. The cubic fit visualizes a trend.

Based on approach 2, Figure 3.13, Figure 3.14 and Figure 3.15 present the deviations between the measurement and the calculation of IDL thickness for samples with a 13 µm, 9 µm and 6 µm Al top layer, respectively. Despite the notable scattering for thin IDLs below 1 µm, which is caused by the fluctuation of measured IDL thickness, a good agreement between the calculation and the measurement is obtained.

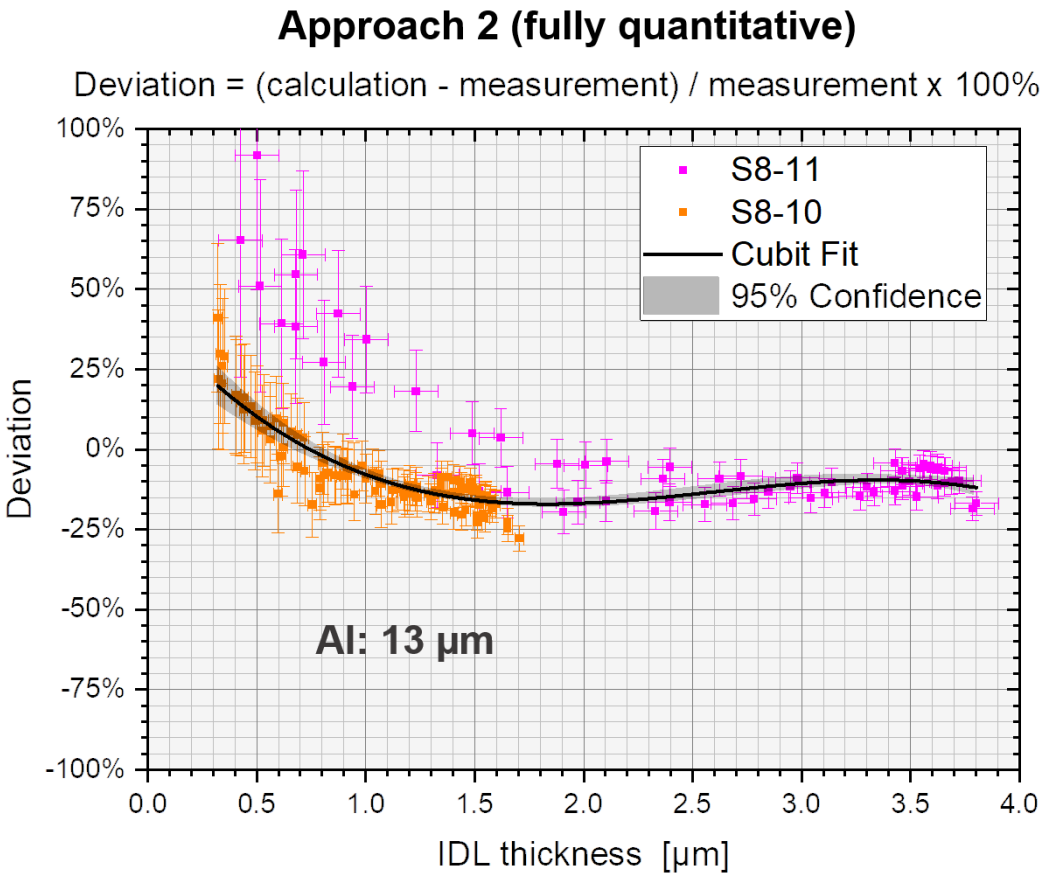

FIGURE 3.13: Deviation between the IDL thickness calculated using approach 2 and the directly measured IDL thickness for samples with a 13 µm Al layer. The cubic fit visualizes a trend.

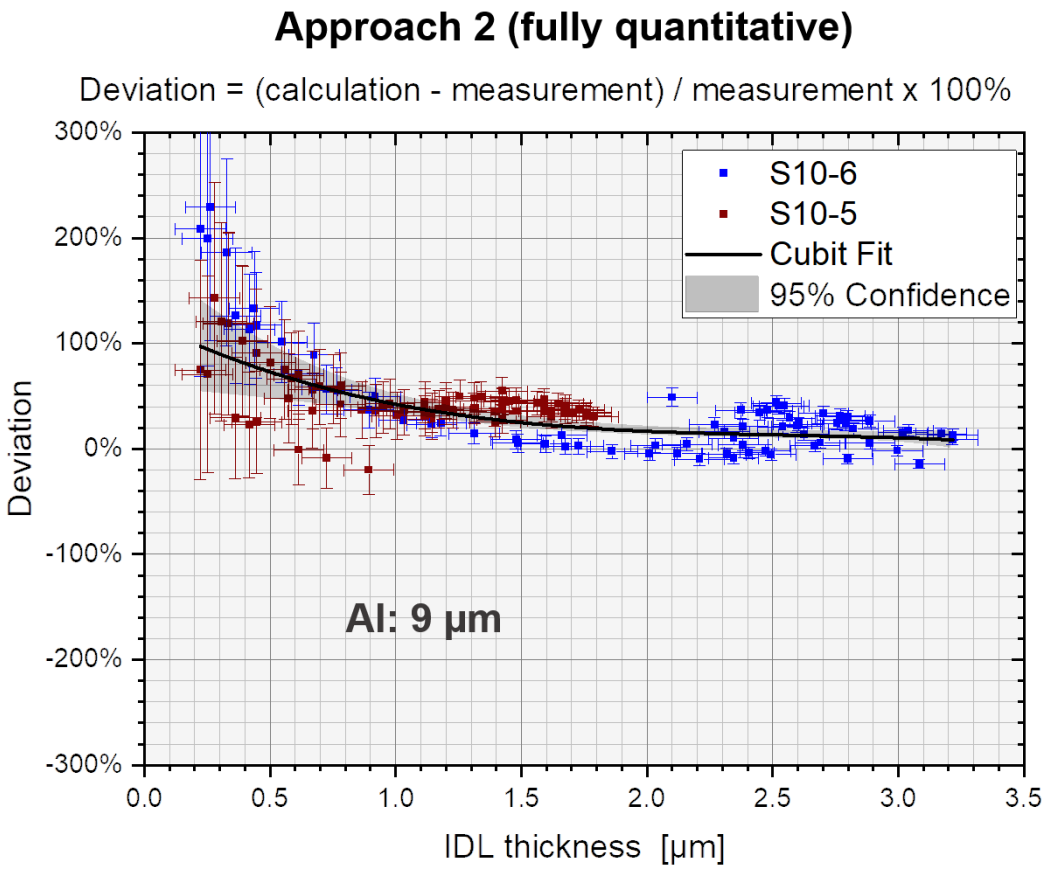

FIGURE 3.14: Deviation between the IDL thickness calculated using approach 2 and the directly measured IDL thickness for samples with a 9 µm Al layer. The cubic fit visualizes a trend.

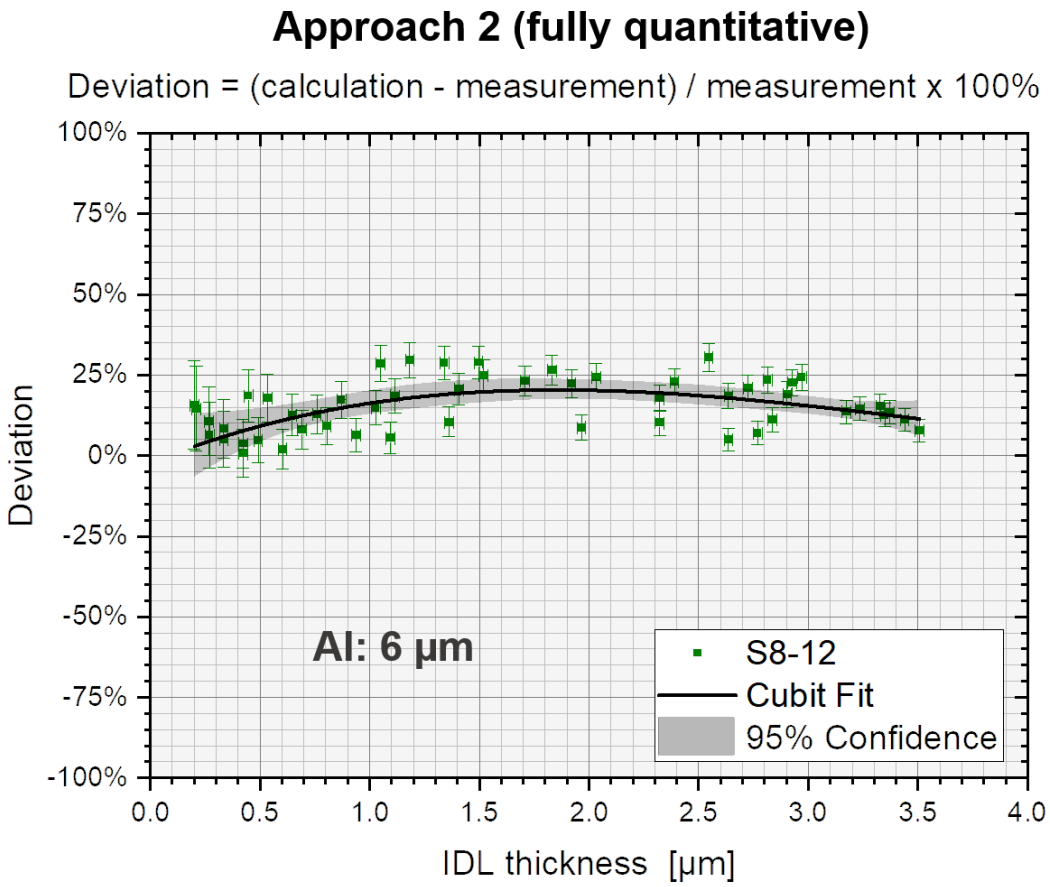

FIGURE 3.15: Deviation between the IDL thickness calculated using approach 2 and the directly measured IDL thickness for the sample with a 6 µm Al layer. The cubic fit visualizes a trend.

The fitting constants presented in the in-pile growth model can be verified by solving Equation 3.4 for each parameter, with the values taken from measurements and the ion flux values obtained by using approach 1 or approach 2. The results are plotted against IDL thickness.

The plots of A over the equivalent fission density obtained from approach 1 and approach 2 are shown in Figure 3.16 and Figure 3.17, respectively. In the former case, a value of $A = 2.06 \cdot 10^{-8} \mu m^2 cm^{3p} s^{p-1}$ is given by constant fitting, whereas in the latter case, a value of $A = 1.97 \cdot 10^{-8} \mu m^2 cm^{3p} s^{p-1}$ is obtained. The in-pile value $A = 2.6 \cdot 10^{-8} \mu m^2 cm^{3p} s^{p-1}$ is also indicated in both graphs as a comparison. The deviation between the ion irradiation result and in-pile value is around 20% in both cases.

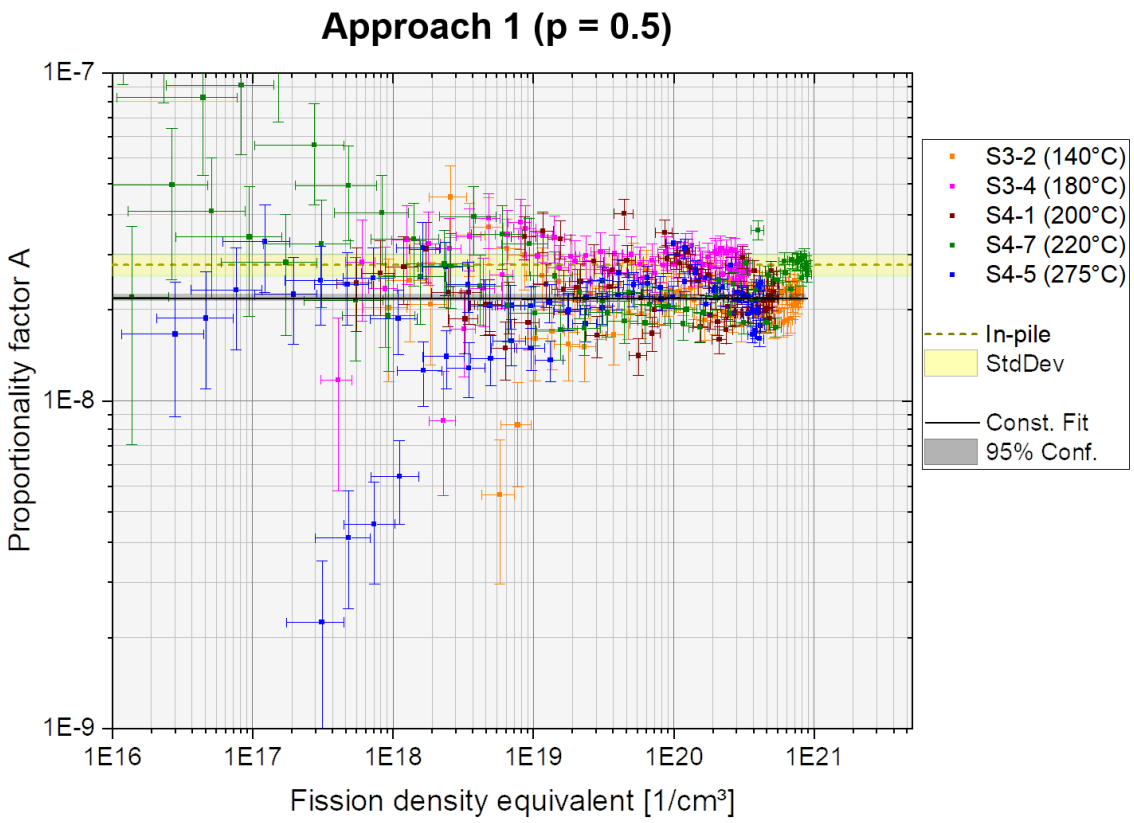

FIGURE 3.16: Calculated proportionality factor A with the obtained ion irradiation data using approach 1. The constant fit gives a value of $A = 2.06 \cdot 10^{-8} \mu m^2 cm^{3p} s^{p-1}$, which is close to the in-pile constant $A = 2.6 \cdot 10^{-8} \mu m^2 cm^{3p} s^{p-1}$.

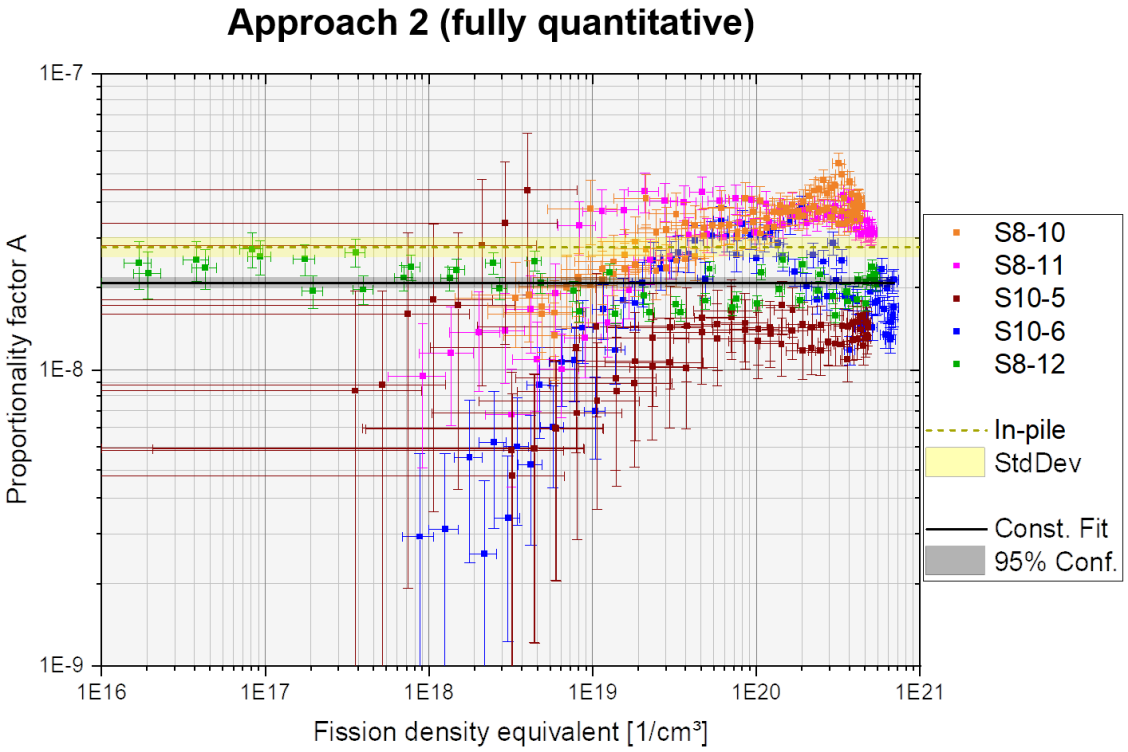

FIGURE 3.17: Calculated proportionality factor A with the obtained ion irradiation data using approach 2. The constant fit gives a value of $A = 1.97 \cdot 10^{-8} \mu m^2 cm^{3p} s^{p-1}$. The in-pile constant $A = 2.6 \cdot 10^{-8} \mu m^2 cm^{3p} s^{p-1}$ is also indicated.

In the case of approach 1, the in-pile value $p = 0.5$ has been used in the reconstruction of ion flux profile, Thus, the absolute value of the exponent can no longer be verified with the obtained ion irradiation data, as it would result in a circular statement. In the case of approach 2, the determination of ion flux profile was purely based on the measurement. Therefore, with the obtained ion irradiation data, this in-pile constant $p = 0.5$ can be verified. The obtained results are shown in Figure 3.18. The constant fit gives a value of $p = 0.502$, which is very close to the in-pile constant $p = 0.5$.

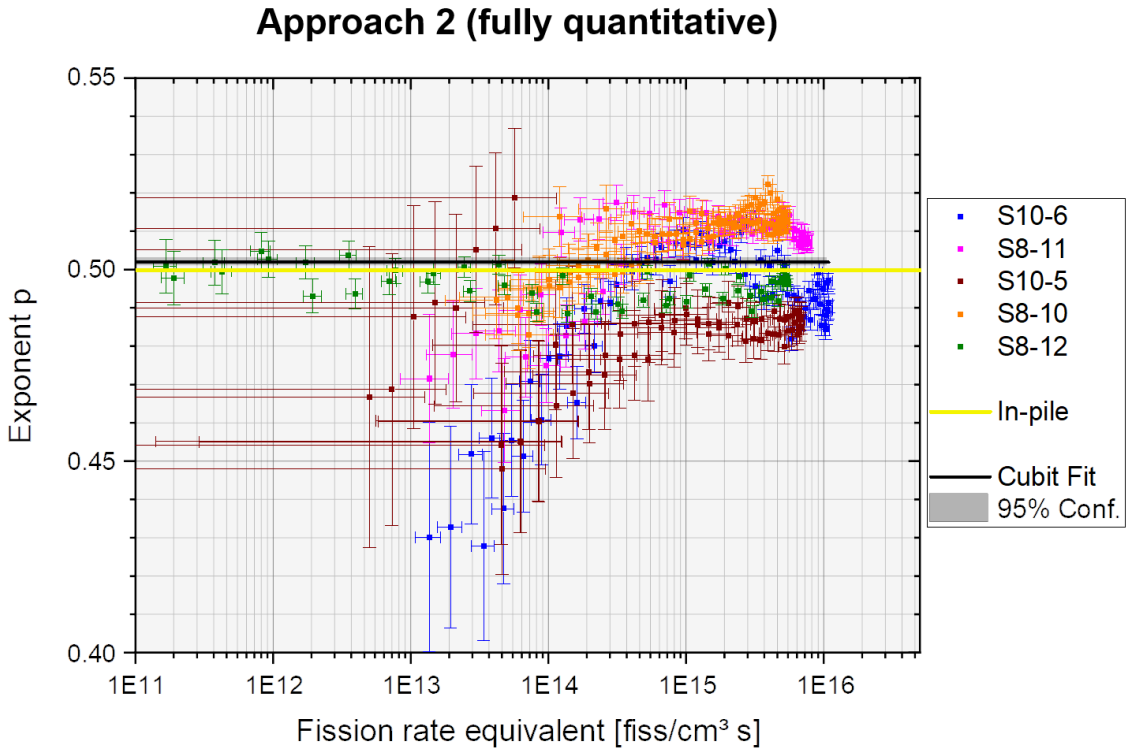

FIGURE 3.18: Exponent p of fission rate is plotted as a function of fission rate equivalent, whereby the fission rate equivalent is obtained using approach 2. Here $A = 1.97 \cdot 10^{-8}\mu m^2 cm^{3p} s^{p-1}$ is taken from the analysis above. The constant fit gives a value of $p = 0.502$, which is very close to the in-pile constant $p = 0.5$.

The ion irradiations in this work were performed at different temperatures ranging from 70 °C to 275 °C. Thus, the temperature dependence of IDL growth can be well addressed. For instance, the normalization parameter q in the in-pile model Equation 3.1 can be verified by fitting the ion irradiation data. Note that the temperature measurement was taken from close to the beam spot edge, and the temperature of which is $5-10$ °C lower than that of the beam centre according to the simulation[2]. This temperature difference is considered small compared to the temperature values and was therefore not taken into account in this analysis.

Considering Equation 3.1, by dividing the IDL thickness by the term of fission rate and time, a normalized IDL thickness Y^* is defined as a function of irradiation temperature, i.e.

$$Y^{*2} = \frac{Y_{\mathrm{IDL}}^2}{A \cdot \dot{f}^p \cdot t \cdot f_{\mathrm{Mo}}} = \exp\left(-\frac{q}{T}\right). \tag{3.21}$$

This way, the effect of ion flux (fission rate equivalent) and irradiation time are eliminated by normalization, the irradiation temperature is the only variable

[2] A example of simulation is presented in Chapter 6, Section 6.2. In that case the temperature difference was determined around 20 °C due to a higher beam power.

in the function. Thus, the normalized peak IDL thicknesses Y^* obtained from the samples that irradiated at different conditions can be compared. In Figure 3.19, the normalized IDL thicknesses Y^* to the second power are plotted as a function of temperature, and the data points are fitted with function $\exp(-q/T)$, leading to a fit constant of $q = (3860 \pm 43)$ K, which is very close to the in-pile value $q = 3850$ K also shown in Figure 3.19. The good agreement confirms the reliability of using ion irradiation data in evaluating the temperature effect on the IDL growth dynamics. This finding also answered the open question proposed in [29], in which additional experiments at different temperatures were required to access the verification of the normalization parameter q.

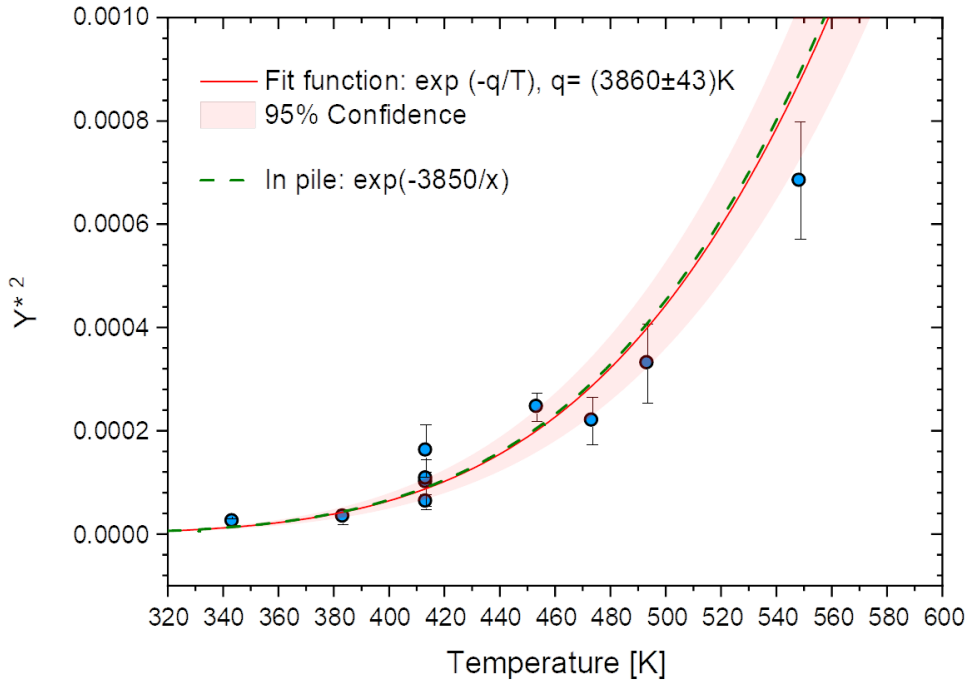

FIGURE 3.19: Normalized IDL thickness to the second power is plotted as a function of irradiation temperature. The data were fitted with function $\exp(-q/T)$, giving a fit constant of $q = (3860 \pm 43)$ K, which matches very well with the in-pile empirical value, namely $q = 3850$ K.

3.7.2 Transition temperature and Q curve

As argued in Section 2.2, two characteristic regimes of ion mixing divided by a transition temperature $T_{\text{transition}}$ are identified in the ion beam mixing process, below $T_{\text{transition}}$ the mixing is basically independent of temperature as the driving force is ballistic effect; above $T_{\text{transition}}$ the mixing is dominated by radiation-enhanced diffusion (RED) exhibiting Arrhenius behaviour. In order to quantitatively evaluate the temperature effect on the IDL growth, the

normalized peak IDL thickness Y^* to the fourth power was plotted against $1000/T$, visualising a Q-curve behaviour as shown in Figure 3.20. Here Q stands for "quantity" as explained in Section 2.3.3. The values of other parameters are taken from the above calculations performed with approach 2. The onset of radiation-enhanced diffusion in ion mixing occurs as observed between $180 - 200\,°C$. Ye et al. [122] conducted similar ion irradiations of Al/U-Mo bilayers with Xe and reported a transition temperature of $\sim 170\,°C$, which is slightly below the one obtained here. The difference is perhaps caused by the difference in ion species and in thickness of the top layer: 80 MeV I for ions and 13 µm Al top layer were applied in this study, whereas 60 MeV Xe for ions and 10 µm for Al top-layer were used in [122]. Moreover, the uncertainty and deviation caused in temperature measurement could also lead to the result.

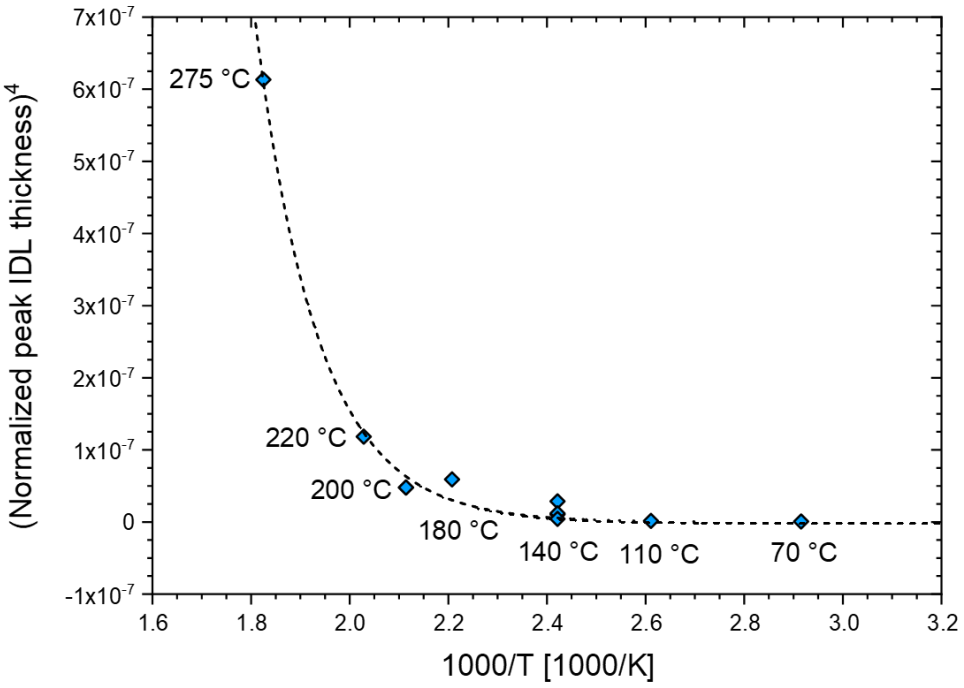

FIGURE 3.20: The fourth power of normalized peak IDL thickness Y^* is plotted as a function of inverse temperature, resulting in a Q-curve behaviour. A transition is seen around $180 - 200\,°C$.

Chapter 4

Temperature effect on IDL microstructure

4.1 Introduction

In Chapter 3, the growth dynamics of IDL was intensively studied. Yet, the microstructural evolution of IDL during irradiation is still one of the primary research interests. It has been proven that the IDL induced by heavy ion irradiation can be crystalline [31][32] or amorphous [33], depending on irradiation conditions. This chapter aims at the characterisation of microstructural changes of ion-irradiated U–Mo/Al fuel samples with increasing temperature, in order to understand the phase evolution in the IDL of U–Mo/Al fuel.

In this chapter, the five samples studied in Chapter 3 Section 3.5 for IDL growth dynamics, which were respectively irradiated at 140 °C, 180 °C, 200 °C, 220 °C and 275 °C, are further investigated for exploring the temperature effect on the microstructure of IDL. The irradiation parameters were already summarized in Table 3.2. As a reference temperature, 140 °C was selected based on the estimated fuel peak temperature when the FRM II is operated with U-Mo fuels, i.e. $120 - 130$ °C [123], and a consideration of a safety margin of 10 °C. 220 °C is the general maximum fuel temperature observed in plate-type fuel tests [18][124]. 180 °C is an intermediate value. Further, the critical temperature for the amorphization of an interaction product in a U–Mo/Al dispersion fuel was estimated lower than 250 °C [125], and the highest temperature 275 °C selected here aims to cover this range.

After irradiation, the five samples were first analysed by SEM/EDX. Figure 4.1 shows the SEM images taken from the beam centre area of each sample. It can be clearly seen that the temperature has a significant impact on the IDL growth: Its thickness increases notably with rising temperature and reaches $\sim$7 µm in the sample irradiated at 275 °C. It should be mentioned that according

to the IDL growth model presented in Chapter 3, the increased volume of IDL is not solely attributed to the thermally activated diffusion, but also by the received local irradiation dose which corresponds to a burn-up equivalent. Four TEM lamellae were prepared by FIB from sample S3-2 (140 °C), S4-1 (200 °C), S4-7 (220 °C) and S4-5 (275 °C), respectively, for the study of the microstructure using TEM. The TEM lamella from sample S4-7 was finalized ∼0.8 mm away from the beam centre. The lamellae of the other three samples were lifted out from the beam centre area. As an example, the FIB preparation process of sample S4-7 is shown in Figure 4.1.

The local equivalent radiation effects, i.e. the ion fluence and the fission density equivalent of the locations where the TEM lamellae were lifted out, were calculated with the method presented in Section 3.5. The results are summarized in Table 4.1. Even though the calculated burn-up equivalents for the selected locations are not exactly the same, e.g. the burn-up equivalent of the selected location of sample S4-7 (220 °C) differs by one order of magnitude, the differences between those burn-up equivalents are considered small when comparing to that of in-pile irradiation. Further, the increase of IDL due to higher temperature is more pronounced than that due to higher fission density considering the Arrhenius relationship of the IDL growth model explained in Chapter 3. At these selected locations, a maximum equivalent fission density of $\sim 7 \cdot 10^{20}\,\mathrm{f/cm^3}$ was achieved, whereas the fission density of in-pile irradiations could reach a maximum of $\sim 5 \cdot 10^{21}\,\mathrm{f/cm^3}$. For instance, during the SELENIUM test, fission rates up to $8.9 \cdot 10^{14}\,\mathrm{f/\left(cm^3 \cdot s\right)}$ during the first days of irradiation were seen. A maximum in-pile target burn-up of $5.3 \cdot 10^{21}\,\mathrm{f/cm^3}$ [86] was reached. The IDLs obtained from these ion irradiations thus simulate the IDLs generated in the early stage of in-pile irradiations, however, with significantly higher damage rates corresponding to a fission rate up to $2.5 \cdot 10^{16}\,\mathrm{f/\left(cm^3 \cdot s\right)}$.

After irradiation, the PIE was first performed on the prepared cross-section samples at TUM with a Zeiss EVO MA 25 equipped with a Thermo Fischer ultra-dry EDX detector, to give an overview of the cross-sections and to identify appropriate areas for further TEM investigations. The preparation of TEM lamellas was performed with a FEI Helios 600 NanoLab dual beam FIB at Centre Pluridisciplinaire de Microscopie Electronique et de Microanalyse (CP2M) in France. TEM and STEM/EDX analyses were carried out at CEA Cadarache with a Thermo Scientific™ Talos F200S S/TEM instrument operated at 200 kV.

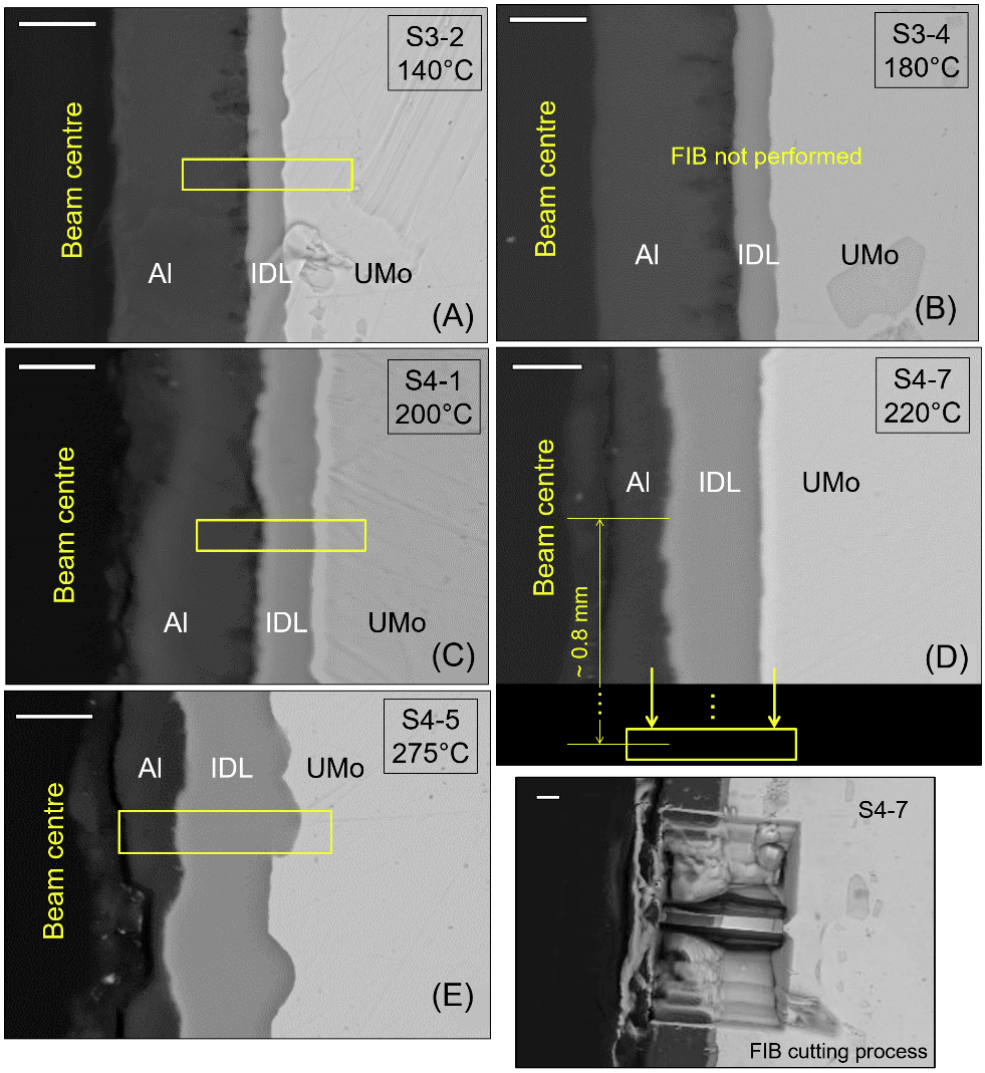

FIGURE 4.1: SEM cross sectional overview of the samples irradiated at 140 °C, 180 °C, 200 °C, 220 °C and 275 °C, respectively. The marked areas indicate the regions in which the lamella preparation and the TEM characterisation took place. Scale bar: 5 µm.

TABLE 4.1: Calculated radiation effects at FIB positions

Sample	T [°C]	Ion fluence [ions / cm^2]	FD equivalent [f / cm^3]
S3-2	140	$(7.4 \pm 0.4) \cdot 10^{17}$	$(7.7 \pm 0.5) \cdot 10^{20}$
S4-1	200	$(4.9 \pm 0.3) \cdot 10^{17}$	$(5.2 \pm 0.4) \cdot 10^{20}$
S4-7	220	$(1.0 \pm 0.9) \cdot 10^{17}$	$(1.1 \pm 0.6) \cdot 10^{19}$
S4-5	275	$(2.6 \pm 0.1) \cdot 10^{17}$	$(2.7 \pm 0.2) \cdot 10^{20}$

4.2 Compositional analysis

The composition of the induced IDL in U-Mo/Al samples, e.g. the Al/(U + Mo) ratio, is a key parameter to understand the IDL growth mechanism. EDX

measurements were first conducted with SEM/EDX on the cross-section samples at TUM, and later repeated on the TEM lamellas with STEM/EDX at CEA Cadarache. The spatial resolution of a TEM is better than that of an SEM. One should also keep in mind that cross-section samples, i.e. bulk specimens, were used for the SEM/EDX measurements, whereas thin lamellas were used for the STEM/EDX measurements. The excitation volumes for X-rays are significantly different, i.e. spheres with a diameter of the order of 1 µm in SEM and disks (a bit more than the electron beam diameter times the lamella thickness) in TEM. More explanation about these techniques can be found in Section 2.6.

Table 4.2 and Table 4.3 list the IDL composition of the studied five samples measured with SEM/EDX at TUM and with STEM/EDX at CEA, respectively. In both tables, the atomic ratios of $\mathrm{Al}/(\mathrm{U}+\mathrm{Mo})$ are given as well to compare IDL composition. The EDX analysis reveals oxidation and carbon contamination. The oxidation probably came from the sample preparation and/or the storage, while the carbon contamination might originate from the SEM chamber, e.g. the residual carbon tape and the hydrocarbon contamination. In the SEM/EDX result (Table 4.2), oxygen and carbon also participated in the EDX quantifications, making the sum of the atom percent of Al, U and Mo less than 100%, while during the STEM/EDX measurements (Table 3) only U, Mo and Al were taken into account in the quantifications. Nevertheless, the results in both cases are normalized, the calculated $\mathrm{Al}/(\mathrm{U}+\mathrm{Mo})$ ratios are therefore not affected whether the quantification included oxygen and carbon or not. Thus, the results obtained by the two techniques can be directly compared. The STEM/EDX measurement was not performed on sample S3-4 since no lamella was prepared out of it. All the measurements were performed at the beam centre area except for sample S4-7 (220 °C), of which the CEA measurement was taken from the prepared TEM lamella which is ∼0.8 mm away from the beam centre, whereas the TUM measurement was performed on the bulk material in the beam centre region. The IDL compositions will be further discussed together with the microstructural evolution in Section 4.4.

4.3 Microstructural evolution of IDL

The microstructural evolution was studied in detail through a series of bright field images (BF) and selected area diffraction (SAD) measurements. Besides these conventional TEM imaging techniques, STEM high-angle annular dark field (HAADF) imaging was applied as well. This technique is more suitable to identify the mixing phases as it can well distinguish between uranium (Z=92),

TABLE 4.2: IDL composition measured by SEM/EDX at TUM. The measurements also took oxygen and carbon into account, making the sum of the atom percent of Al, U and Mo less than 100%.

Sample	T [°C]	Al atom-%	U atom-%	Mo atom-%	Al/(U + Mo)
S3-2	140	79.4 ± 1.1	13.2 ± 0.6	3 ± 0.3	4.9 ± 0.8
S3-4	180	84.6 ± 1.2	11.9 ± 0.5	3.5 ± 0.3	5.5 ± 0.8
S4-1	200	56 ± 1.5	8 ± 0.6	1.9 ± 0.4	5.7 ± 0.8
S4-7	220	69.4 ± 1.7	8.8 ± 0.7	2.4 ± 0.4	6.2 ± 0.8
S4-5	275	85.6 ± 2.1	9.8 ± 0.8	2.6 ± 0.5	7.9 ± 0.8

TABLE 4.3: IDL composition measured by STEM/EDX at CEA Cadarache.

Sample	T [°C]	Al atom-%	U atom-%	Mo atom-%	Al/(U + Mo)
S3-2	140	84.4 ± 7.7	11.6 ± 1.8	4.0 ± 0.6	5.3 ± 0.8
S3-4	180	Not measured			
S4-1	200	85.1 ± 7.5	11.1 ± 1.7	3.9 ± 0.6	5.7 ± 0.8
S4-7	220	87.7 ± 6.7	8.6 ± 1.2	3.7 ± 0.5	6.8 ± 0.8
S4-5	275	87.9 ± 6.9	9.9 ± 1.4	2.2 ± 0.4	7.3 ± 0.9

aluminium (Z=13) and the IDL (Z between 13 and 92). This is due to the fact that the contrast of HAADF images is proportional to the product of density, thickness and the 3/2 power of the mean atomic number (Z) of the area observed.

4.3.1 Irradiation temperature 140 °C

As shown in Figure 4.2, three zones along the ion penetration direction can be recognized in the TEM BF image: Aluminium, IDL and U-Mo. The difference in IDL thickness ("thicker" and "thinner") is due to a two-step thinning across the lamella, as the three phases, namely Al, IDL and U-Mo, have significantly different hardnesses to FIB. The SADPs taken from the IDL show a complete amorphization, as only diffuse rings were observed. As a characteristic of amorphous structure, the nearest neighbour distance is determined as 2.4 ± 0.1 Å all over the IDL, which is in good agreement with the value reported by Chiang et al. [33]. Al and U-Mo remain crystalline. The bright points shown in the SADP in the U-Mo region correspond to (211) and (110) of γ-U-Mo. The presented diffraction rings indicate nano-polycrystalline UO_2 structure originating from the oxidation. The corresponding interatomic spacing d in Å has been deduced from the position of the rings in reciprocal space.

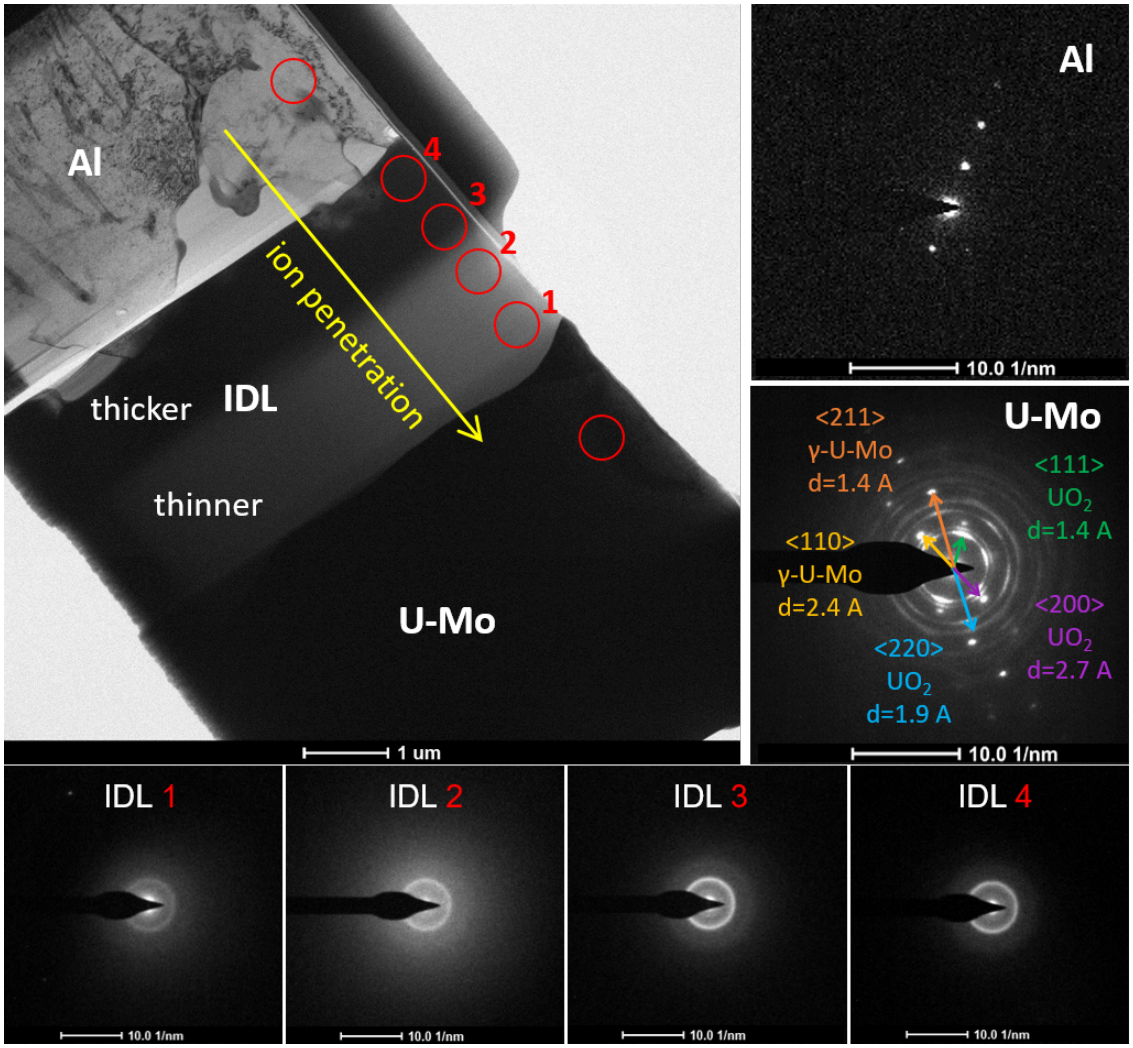

FIGURE 4.2: A TEM BF image of the TEM lamella from sample S3-2 (140 °C). Surrounding are the associated SADPs taken form the selected four zones in the IDL.

4.3.2 Irradiation temperature 200 °C

Figure 4.3 shows the TEM image of S4-1 (200 °C). The corresponding SADP reveals that the IDL still stays amorphous with the nearest neighbour distance of 2.4 ± 0.1 Å, while the Al and the U-Mo regions remain crystalline. The second diffuse ring corresponding to around 4.8 Å, i.e. twice the distance of 2.4 Å measured in the IDL of sample S3-2 (140 °C). This might be interpreted as an indication of the onset of ordering in the IDL. This interpretation is consistent with both the measurements performed in sample S4-7 (220 °C) and sample S4-5 (275 °C). However, trivial explanations like that this second ring corresponds to a larger structure coming from contaminations cannot be excluded on the basis of the present data. UO_2 nanograins are still observed on the U-Mo part due to surface oxidation.

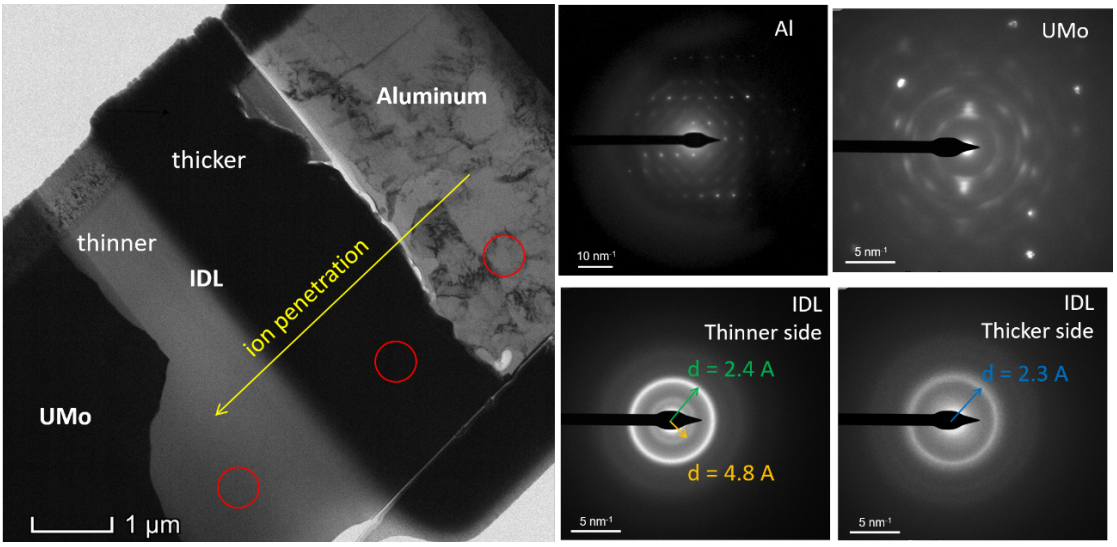

FIGURE 4.3: Left: TEM BF image of S4-1 (200 °C). Right: SADPs with the measurement of interatomic spacing value.

4.3.3 Irradiation temperature 220 °C

Modifications of the microstructure at the Al/IDL interface were observed in the TEM BF image (A, B) and in the STEM HAADF image (C) in Figure 4.4. In order to examine the microstructure, electron diffraction patterns were taken across the region of interest, as indicated by the red arrow. Some particles/grains (white contrast in Figure 4.4(C)) with a feature size of $\sim$ 10 nm appeared close to the Al part, propagating over 250 nm into IDL. These particles have been identified as nanograins by the SADPs as shown in Figure 4.4 and Figure 4.5. Indeed, small bright spots making up rings were observed. Each bright spot resulted from Bragg reflection from individual crystallites. The ratios of the measured d_{hkl} correspond to those obtained from a primitive cubic system, from which the lattice parameter could be estimated close to 4.4 Å. EDX measurements (Figure 4.6) indicate that these nanograins consist of U, Mo and Al. The Al/(U + Mo) ratio variation measured from the U-Mo to the Al layer is shown in Table 4.4.

TABLE 4.4: Compositional analysis of the different regions in IDL shown in Figure 4.6.

Region	Al atom-%	U atom-%	Mo atom-%	Al/(U + Mo)
IDL (amorphous)	88 ± 7	9 ± 1	4 ± 1	6.8 ± 0.8
Nanograins in A	87 ± 7	10 ± 2	3 ± 1	6.7 ± 0.8
Nanograins in B	92 ± 4	3 ± 0	5 ± 1	11.5 ± 0.7
Large particle	95 ± 5	4 ± 1	/	23.8 ± 1.0

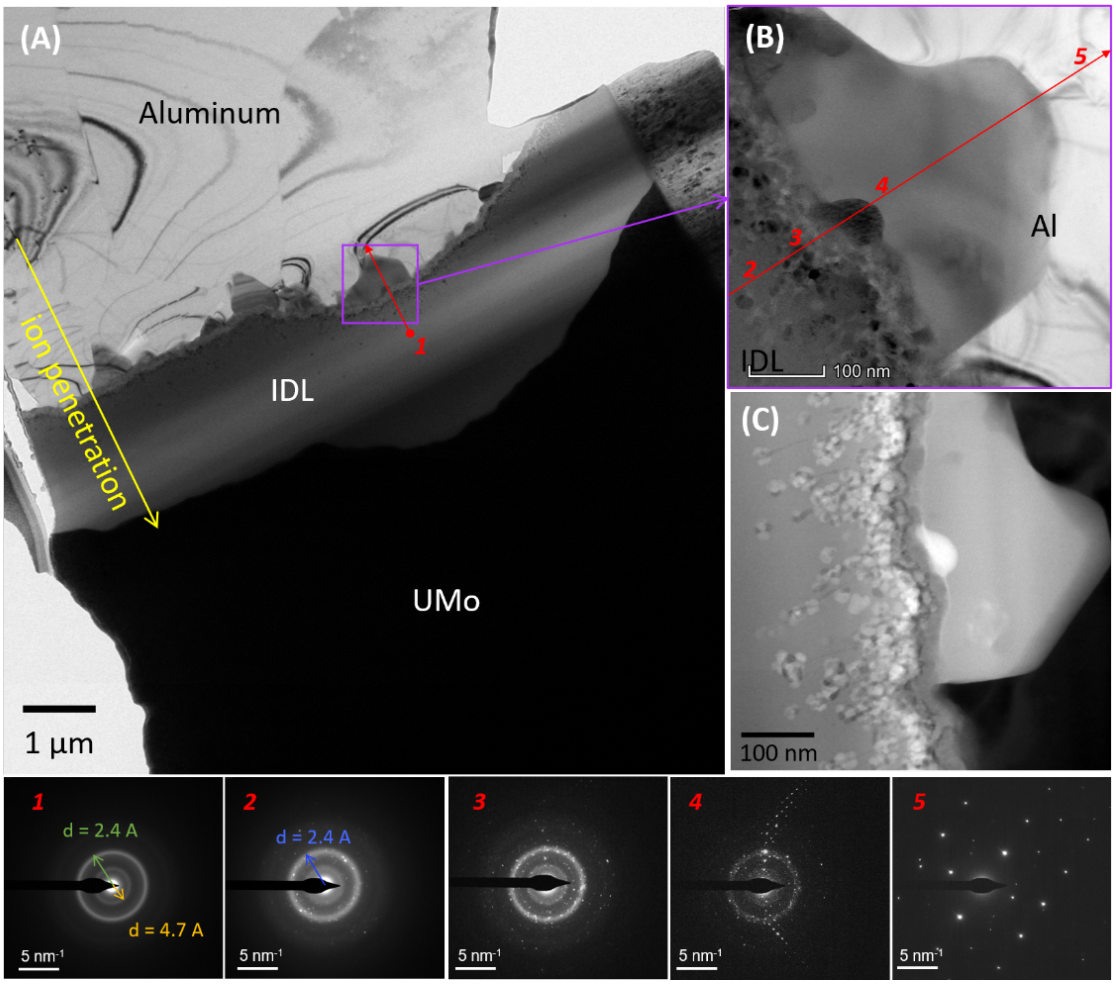

FIGURE 4.4: (A) TEM BF image of the lamella taken from sample S4-7 (220 °C). (B) Details of the Al/IDL interface, where the locations for SADPs are marked with numbers. (C) The HAADF image of (B) in STEM mode. The corresponding SADPs are shown below: 1) the middle of IDL, 2) IDL close to Al, 3) IDL closer to Al, 4) a large grain between Al and IDL, 5) Al.

As shown in Figure 4.4, towards the U-Mo part, region 2 reveals a mixture of an amorphous structure and a few nanograins (diffuse ring and some bright spots). Region 1 is still fully amorphous. The measured nearest neighbour distance equals to 2.4 Å. Moving to region 4, the structure of which corresponds to some grains of a few hundred nanometres revealing a crystalline structure with very high interatomic distances of 8 Å. These grains could be an intermetallic compound with 95 at%Al and 5 at%U. There is no mention in the literature of an Al-U intermetallic with such a composition, perhaps because it corresponds to an out-of-equilibrium phase. Region 5 is located inside Al and reveals a crystalline structure as expected. It is concluded that the crystallization was initiated at the Al/IDL interface, propagating towards the U-Mo.

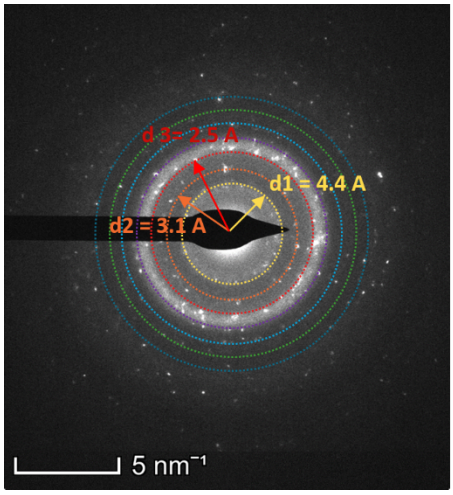

n	Plane	Measured d_{hkl}	*d1/dn*
1	100	4.4	1
2	110	3.1	1.4
3	111	2.5	1.8
4	200	2.2	2
5	210	2	2.2
6	211	1.8	2.4
7	220	1.6	2.8

FIGURE 4.5: Analysis of the SADP of the nanograins observed in Figure 4.4, at SADP No. 3. The crystal structure is primitive cubic with a lattice parameter close to 4.4 Å.

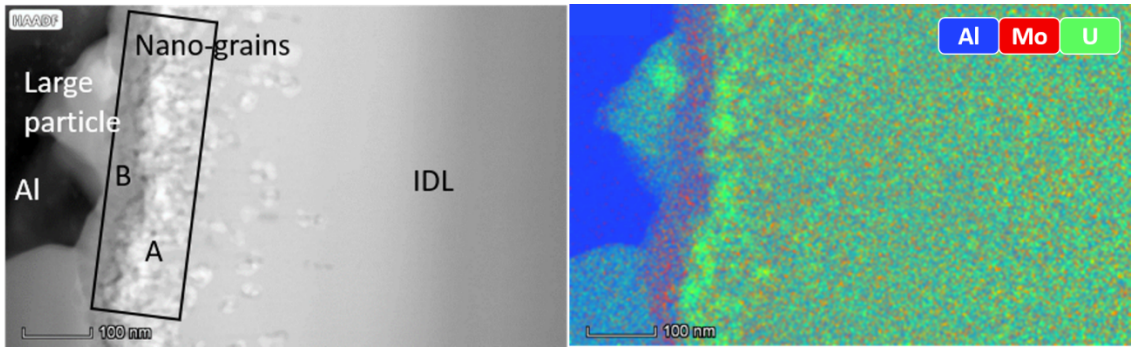

FIGURE 4.6: SEM image and combined EDX map (Al=blue, Mo=red, U=green) of an area covering the Al, the nanograins at the Al/IDL interface and the amorphous part of the IDL of S4-7 (220 °C).

4.3.4 Irradiation temperature 275 °C

The microstructure of sample S4-5 (275 °C) is presented in Figure 4.7. The BF image and the STEM HAADF image both show that nanograins are present almost everywhere in the IDL. Furthermore, when compared to the nanograins in Figure 4.4, the nanograins in Figure 4.7 seem to spread along the ion trajectories, forming string-like structures. It is worthwhile to mention that large grains between Al and IDL are still observed. The electron diffraction patterns of three selected areas in the IDL are also shown in Figure 4.7. The SADPs of region 2 and region 3 confirm that the nanograins are primitive cubic with a lattice parameter close to 4.4 Å, which is in good agreement with that of S4-7 (220 °C) (Figure 4.4). The population of nanograins decreases along the ion penetration direction: Region 3 and region 2 consist mainly of nanograins, while region 1 is dominated by amorphous structure. Figure 4.8 shows an HRTEM image revealing the atomic structure of the nanograins.

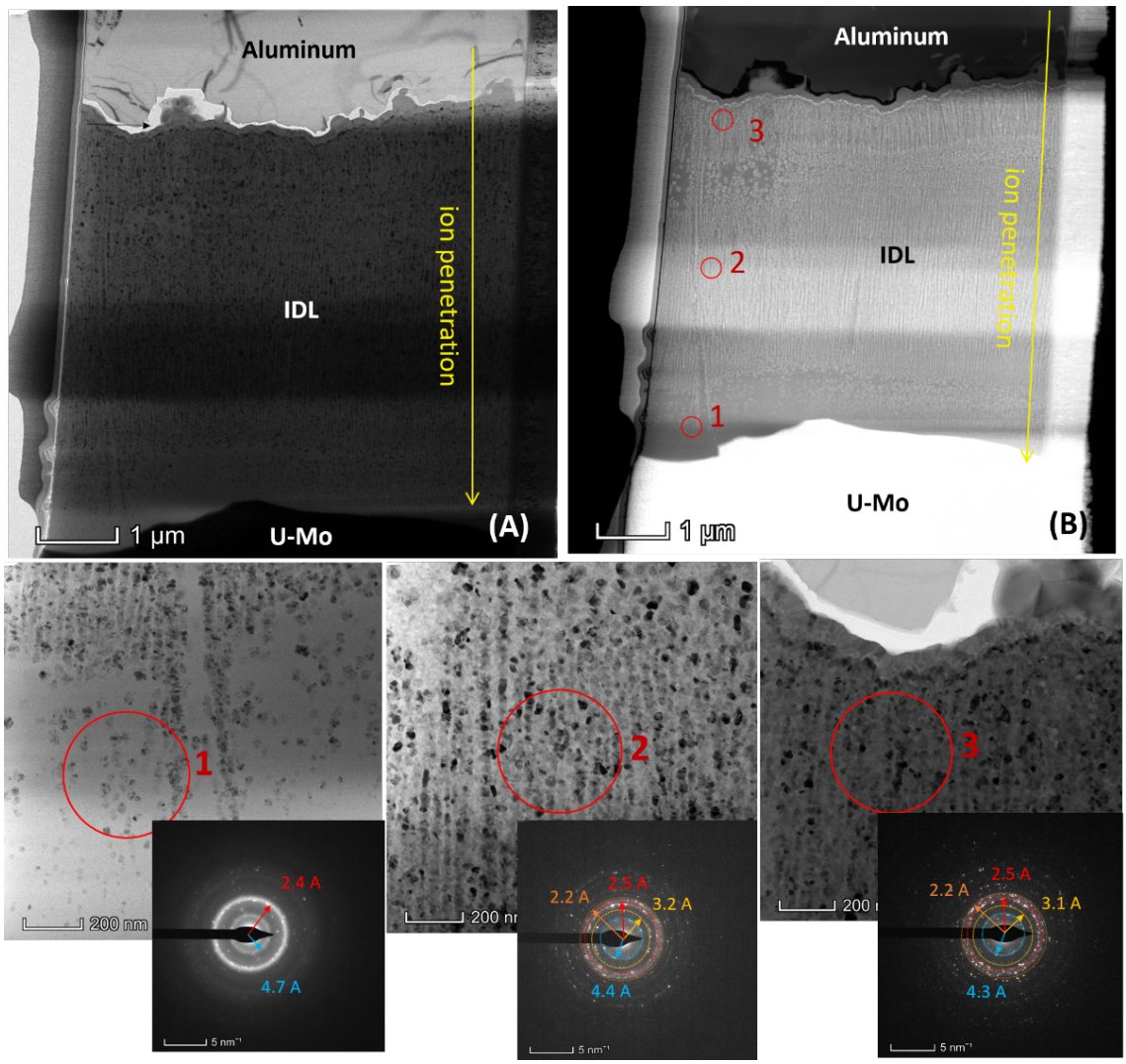

FIGURE 4.7: (A) TEM BF image and (B)STEM HAADF image of the lamella taken from sample S4-5 (275 °C). SADPs of the marked regions were shown as well.

4.4 Discussion

As summarized in Figure 4.9 and Table 4.5, the IDL microstructural characteristics change with increasing irradiation temperature: At low temperature, i.e. 140 °C and 200 °C, the whole IDL stays amorphous; when the irradiation temperature reaches 220 °C, nanograins start to form from the Al layer. At the irradiation temperature of 275 °C, nanograins propagate towards the U-Mo and cover the most of the IDL region.

According to Ryu [125], there are two contributions to the microstructure of IDL, i.e. thermal annealing rate and the irradiation damage rate. At high temperatures, thermal annealing promotes the recovery of the damage caused by irradiation, while a high fission rate produces more defects and disorder. The competition between the thermal annealing rate and the damage rate

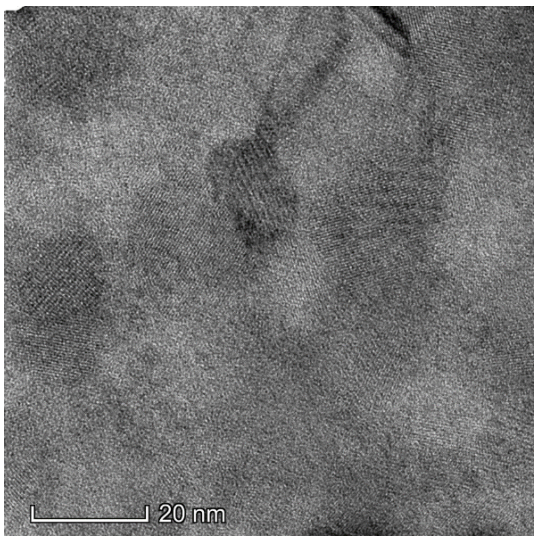

FIGURE 4.8: HRTEM image of the nanograins of $\sim$ 10 nm in the IDL of the sample irradiated at 275 °C.

TABLE 4.5: Characteristics of IDLs as shown in Figure 4.9

Sample	T [°C]	IDL structure	Nearest neighbour distance [Å]
S3-2	140	Amorphous	2.4
S4-1	200	Amorphous	2.4
S4-7	220	Amorphous + a few nanograins $\sim$ 10 nm	Amorphous region: $2.4 - 2.5$
S4-5	275	Amorphous + a few nanograins $\sim$ 10 nm	Amorphous region: 2.4

regulates the crystallinity of the IDL during irradiation. With the presented high flux ion irradiation conditions, the maximum equivalent fission rate, i.e. $2.5 \cdot 10^{16}\,\mathrm{f}/\left(\mathrm{cm}^3 \cdot \mathrm{s}\right)$, is more than 10 times higher than the peak fission rate of SELENIUM test which is $\sim 8.9 \cdot 10^{14}\,\mathrm{f}/\left(\mathrm{cm}^3 \cdot \mathrm{s}\right)$.

Thus, the findings can be well explained as follows: In the samples ion-irradiated at temperatures below 200 °C, the irradiation damage rate predominates. As a result, the IDLs in those two samples stay fully amorphous. In the U-Mo/Al sample irradiated at 220 °C, thermal annealing rate started to outweigh the damage rate. Consequently, nanograins began to form. When the irradiation temperature reaches 275 °C, thermal annealing rate predominates and the generated IDL contains therefore a lot of nanograins. These nanograins were identified as having a cubic Pm-3m structure like UAl_3, which is also the major interaction phase obtained from the U-Mo/Al diffusion couple test [126]. The crystallization onset temperature of an amorphous IDL is therefore determined between 200 °C and 220 °C at the given conditions.

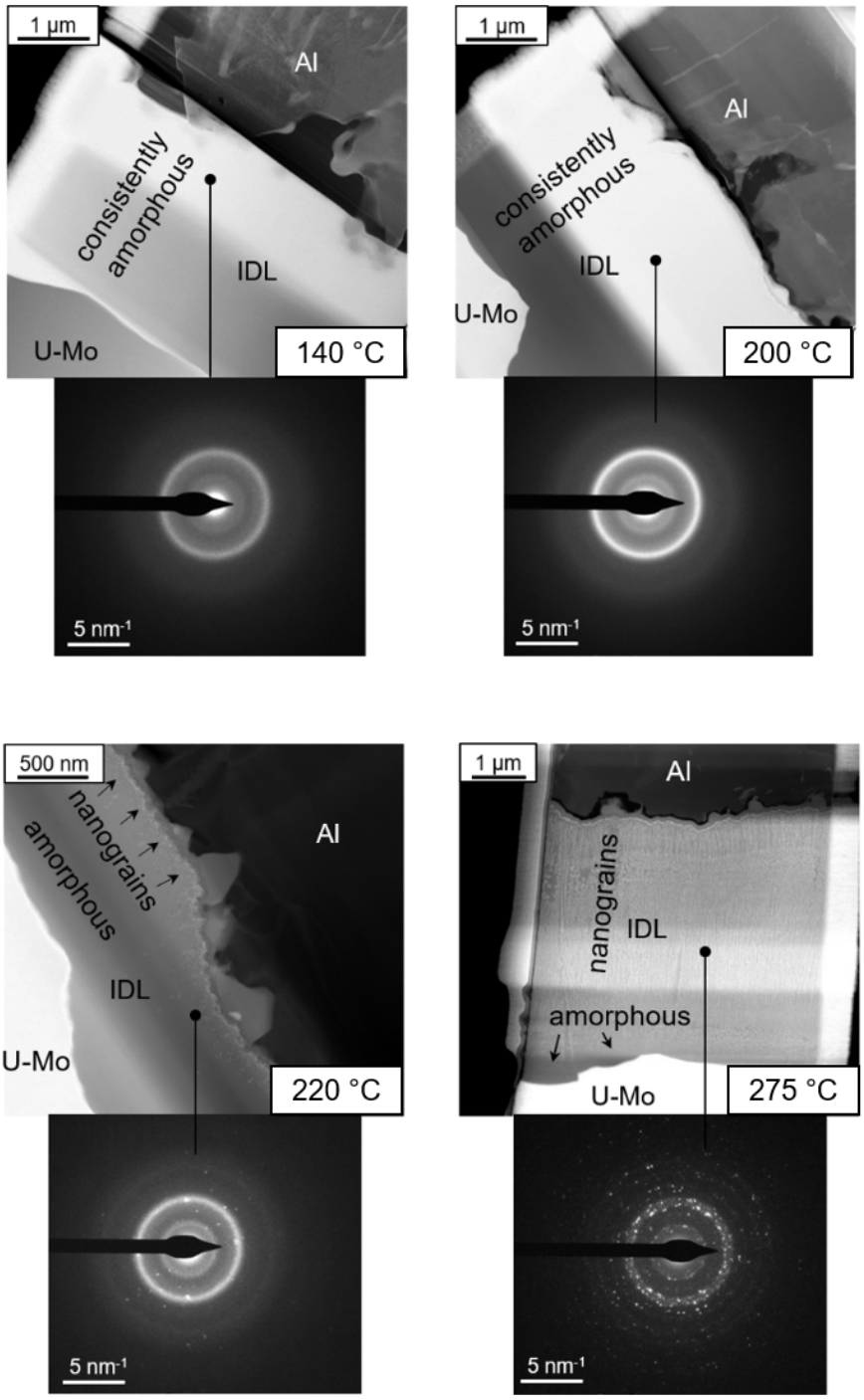

FIGURE 4.9: Microstructural evolution in IDL induced in U-Mo/Al systems by ion irradiation from 140 °C to 275 °C.

In-situ annealing studies on in-pile irradiated U–9wt.%Mo dispersion fuel with neutron diffraction analysis were conducted by Golosov et al. [127]. The results showed that recrystallization to UAl_3 occurred in the amorphous $(U,Mo)Al_x$ phase at annealing temperatures above $300-350\,°C$. The phase

transition temperature[1] is in relatively good agreement with the result obtained here considering the different spatial resolution and the sensitivity of both analytical techniques. Recrystallization of the interaction product in Al/U-Mo based fuels often takes place in irradiated pin-type fuels, given that this kind of fuel is generally operated at higher temperatures because of its geometry [30]. A recent ion irradiation study of Miao et al. [128] utilized 60 MeV Xe ions to induce Al-U-Mo interaction at various temperatures, where the formation of nanocrystalline precipitates in the amorphous IDL occurred at 215 °C, which is highly consistent with the result of this thesis.

For the amorphous IDLs obtained in this study, the values of nearest neighbour distance i.e. $2.4 - 2.5$ Å, are given in Table 4.5, which coincide well with the result 2.39 ± 0.04 Å from in-pile tests determined by Van den Berghe [19], as pointed out in [31]. The observed nanograins were identified as having a lattice parameter around 4.4 Å and $4.3 - 4.4$ Å in sample S4-7 (220 °C) and S4-5 (275 °C), respectively. Identical values given the smearing of the diffraction rings. As mentioned beforehand, the IDL recrystallization was observed in annealing experiments performed on in-pile irradiated U-Mo/Al fuel samples, where UAl_3 is identified as the recrystallization product, which crystallizes in the cubic Pm-3m space group and presents a lattice parameter of 4.266 Å [129]. Thus, it is likely that the nanograins observed here have the same space group (Pm-3m) but a slightly different lattice parameter. Besides, the indexing of SADPs is less accurate and has some limitations compared to XRD analysis, which provides more reliable data for inter-reticular distances and lattice parameter.

As explained in Chapter 2, thermal annealing leads to thermodynamic equilibrium, whereas the ion and in-pile irradiated samples are in a non-equilibrium state due to irradiation damage at relatively low temperatures. As a result, the IDLs obtained here present non-equilibrium Al-U-Mo mixtures. From a compositional point of view, in sample S4-7 (220 °C), the nanograins close to the amorphous IDL (Figure 4.6, region A) and the nanograins close to the Al layer (Figure 4.6, region B) reveal an $Al/(U + Mo)$ ratio of ~ 6.7 and ~ 11.5, respectively, as shown in Table 4.4. This suggests that those nanograins are highly non-stoichiometric and can accommodate large amounts of Al under irradiation, which might be responsible for the difference in the lattice parameters.

The directional crystallization, i.e. crystallization of IDL starting from the IDL/Al interface and propagating towards the U-Mo, is very likely an effect of ions. The SRIM/TRIM simulation in Figure 3.1 of Chapter 3 shows that as the

[1] The phase transition temperature should not be confused with the transition temperature of IDL growth dynamics investigated in Chapter 3.

IDL develops, the curve of electrical energy loss of the incoming ions is shifted notably, resulting in a much higher energy deposition at the Al/IDL interface than at the IDL/U-Mo interface. As explained in Chapter 2, local heating can be generated by electronic energy loss. The release of a large amount of energy by the electronic energy loss mechanism at the Al/IDL interface could have led to the crystallization starting from there. The relatively low intrinsic thermal conductivity of the IDL, which has been measured to $3-4\,\mathrm{W/(mK)}$ in [130], makes this mechanism possible. Another evidence is the way the nanograins are arranged in the IDL of sample S4-5 (275 °C), namely string-like and parallel to the ion trajectories, as shown in Figure 4.7. Similar effects such as ion tracks around the ion path are often observed in insulating materials, see for example [131] and [132]. Furthermore, the higher Al concentration of IDL near the Al/IDL interface may also have facilitated the onset of crystallization, as the stable phases of uranium aluminium are all Al-rich (UAl_2, UAl_3, and UAl_4). Further irradiations in the reverse irradiation direction are needed to provide a global understanding of the directional effect of IDL crystallization.

The $\mathrm{Al/(U+Mo)}$ ratio of IDL obtained from Table 4.2 and Table 4.3 are illustrated in Figure 4.10. Both measurements agree well within error margins. In both measurements, the Al proportion in IDL rises with increasing irradiation temperature, which indicates an enhanced Al atomic flow from the Al into IDL during irradiation. It is worthwhile to mention that in in-pile irradiation experiments, such as IRIS1 [133], IRIS2 [133] and FUTURE [18], the $\mathrm{Al/(U+Mo)}$ ratio decreases with increasing irradiation temperature, as pointed out by Ryu [125]. This inconsistency is due to the different microstructure of the generated IDL. On the one hand, in in-pile irradiation experiments, IDLs are always interspersed with fission products, meanwhile, the local uranium is being consumed by fission. These complex mechanisms are not present in ion irradiation experiments. On the other hand, the IDLs obtained from the above-mentioned three in-pile tests are completely amorphous. In this work, the IDLs are purely amorphous (140 °C and 200 °C) or a mixture of amorphous phase and nanograins. The completely amorphous IDL obtained from sample S3-2 (140 °C) irradiation has an $\mathrm{Al/(U+Mo)}$ ratio of 5 ± 1, which is in good agreement with the ratios of the amorphous IDLs reported for the three in-pile tests, namely 3.3 to 7. At elevated ion irradiation temperatures, i.e. 220 °C and 275 °C, nanograins are found among the amorphous IDLs. These nanograins are highly non-stoichiometric and can accommodate large amounts of Al under irradiation, resulting in high $\mathrm{Al/(U+Mo)}$ ratios up to 7. Further, by applying certain irradiation conditions, e.g. sufficiently high temperature,

a pure crystallized UAl_x IDL ($x = 2, 3$ or 4) can form, whose $Al/(U+Mo)$ ratio is limited to 4. In brief, the $Al/(U+Mo)$ ratio depends strongly on the microstructure of the IDL, i.e., one should always indicate the corresponding phase when referring to the $Al/(U+Mo)$ ratio.

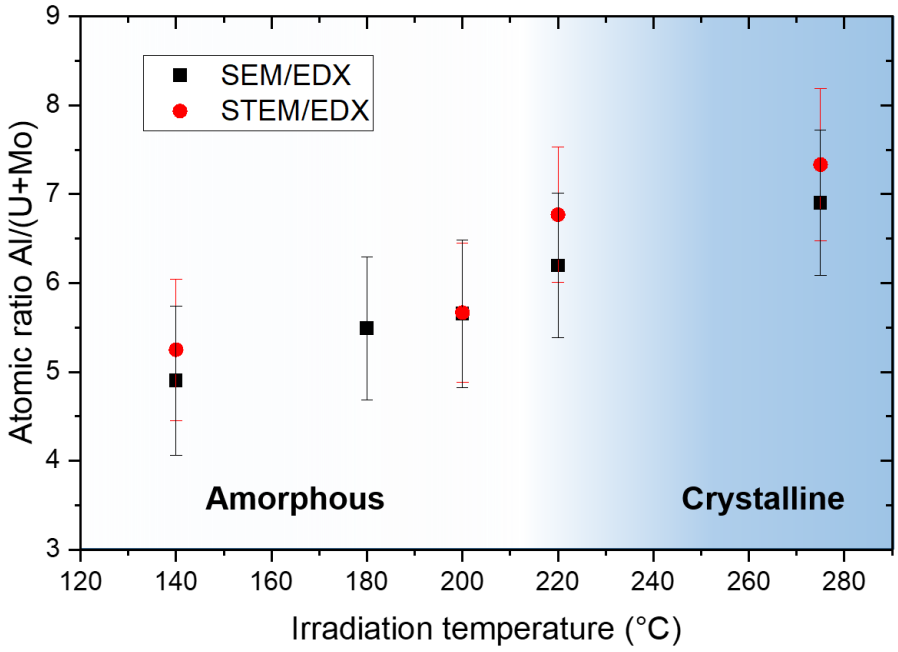

FIGURE 4.10: $Al/(U+Mo)$ ratio of IDL measured by SEM/EDX and STEM/EDX for samples irradiated different irradiation temperatures. The IDL crystallinity is indicated as well.

4.5 Conclusion

Based on the TEM analysis it is clear that the irradiation temperature has a significant impact on the microstructure of the IDL. SADPs show that the IDLs are fully amorphous at irradiation temperatures not higher than 220 °C. Around 220 °C, the IDL undergoes a microstructural modification from amorphous to nanocrystalline starting from the Al/IDL interface, whereby the irradiation effect i.e. the fission rate equivalent and fission density equivalent are $\sim 2.7 \cdot 10^{14}\,\mathrm{f}/\left(\mathrm{cm}^3 \cdot \mathrm{s}\right)$ and $\sim 1.1 \cdot 10^{19}\,\mathrm{f/cm}^3$, respectively. When the irradiation temperature reaches 275 °C, crystalline nanograins propagate into U-Mo and dominate the IDL phase, likely following the ion penetration direction considering the sample geometry. It cannot be excluded that this directional dependence is solely related to the particular irradiation geometry, namely ions impinging on Al and travelling to U-Mo rather than the other way around

which occurs in-pile. The nanograins are identified as having a Pm-3m like UAl_3 structure but with a lattice parameter close to 4.4 Å, which can be a result of a distortion of a non-stoichiometric UAl_3 structure caused by the accommodation of large amounts of Al under irradiation. Furthermore, as the irradiation temperature rises, the $Al/(U + Mo)$ ratio of the IDL increases in the samples irradiated up to a comparable burn-up equivalent. This can be explained by the enhanced Al atomic flow driven by increased temperature.

Chapter 5

Quantitative evaluation of selected diffusion barriers

5.1 Transition metals

The application of a diffusion barrier between U-Mo and Al is an advantageous option to inhibit the undesired interdiffusion between them. Refractory transition metals have been proposed as promising candidates for diffusion barriers based on their mechanical and thermal properties like ductility, high melting point and excellent thermal conductivity [134]. Among the transition metals, Mo, Zr and W are considered as promising barrier materials based on thermodynamic considerations and their low neutron absorption rates. Using 80 MeV ^{127}I ions, Chiang et al. [135] conducted ion irradiations at 200 °C on a 300 nm Mo and a 900 nm Zr coated U-Mo/Al samples, where a constant ion fluence of $\sim 1 \cdot 10^{17}$ ions/cm^2 was estimated. The results show that no Al-U-Mo IDLs formed in both samples, while intermixing phases were observed at the Al/coating and the coating/U-Mo interfaces. To achieve a thorough understanding of the irradiation behaviour of transition metals Mo, Zr and W as diffuion barriers, in this study, a systematic and quantitative evaluation of Mo, Zr and W coated U-Mo/Al fuel samples was undertaken by using heavy ion irradiation. The effects of coating thickness and irradiation dose are especially focused.

5.1.1 Formation enthalpies of Al–X and U-X alloys

The behaviour of a diffusion coating barrier during irradiation can be theoretically predicted by thermodynamic considerations. Nevertheless, the sample under ion irradiation or in-pile irradiation is in a non-equilibrium state, for which the phase diagrams are no more applicable because they only hold in an equilibrium state. Under this circumstance, the formation enthalpy of the

system can be calculated by using the semi-empirical Miedema's model which has been explained in Chapter 2.

Figure 5.1 (A) and (B) shows the calculated formation enthalpies of the coating material against Al and U, respectively, where the enthalpy in each case is plotted against the concentration of the coating material in atomic percent. In addition, the formation enthalpy of U-Al is plotted in black in both graphs, representing the sample without a coating between U-Mo and Al. All parameters and constants used in the model are taken from [136] and [137]. The calculations were performed by using a Miedema-calculator developed by Zhang et al. [81][82]. The obtained results indicate that, at the Al/X interface, the formation enthalpies of all the four binary systems, i.e. Al-W, Al-Mo, Al-Zr and Al-U show exothermic behaviour, which means the two elements in those binary systems tend to interact. The formation of Al-U and Al-Zr compounds are more exothermic than that of Al-W and Al-Mo compounds. Considering the X/U-Mo interface, the formation enthalpy of U-Mo and U-W shows endothermic behaviour, in which case interdiffusion does not tend to occur spontaneously as such reactions require energy. Zr has a slightly negative formation enthalpy against U, while the U-Al reaction shows a significant exothermic behaviour, implying that the chance of U-Al intermixing is high, which agrees with the observation in irradiated U-Mo/Al fuels as presented in Chapter 3. Based on these calculations, during irradiation, interdiffusion is expected to occur at the Al/coating interface in general, especially between Al and Zr. On the other hand, interdiffusion layer is not expected to form at the Mo/U-Mo and W/U-Mo interfaces, whilst slight interaction might take place at the Zr/U-Mo interface.

5.1.2 Experiment

To increase the efficiency of ion irradiation, the maximum nuclear energy loss should be placed at the place of interest in order to maximize the irradiation effect as already explained in Chapter 2. In the case of bilayer systems, the Bragg peak was targeted at the interface of the two layers. In trilayer systems e.g. Al/X/U-Mo, where the ions impinge on the Al surface, the Bragg peak was placed at the X/U-Mo interface. The reason is that the energy loss drops drastically at the interface as demonstrated in Figure 3.1 of Chapter 3. If the Bragg peak is placed at the Al/X interface, the irradiation damage at the X/U-Mo interface might be insufficient to create an observable effect. The following coating thicknesses were studied: 50 nm, 150 nm, 500 nm and 2 µm for the Mo barrier; 200 nm and 5 µm for the Zr barrier; 200 nm, 500 nm, 1 µm and 2 µm for

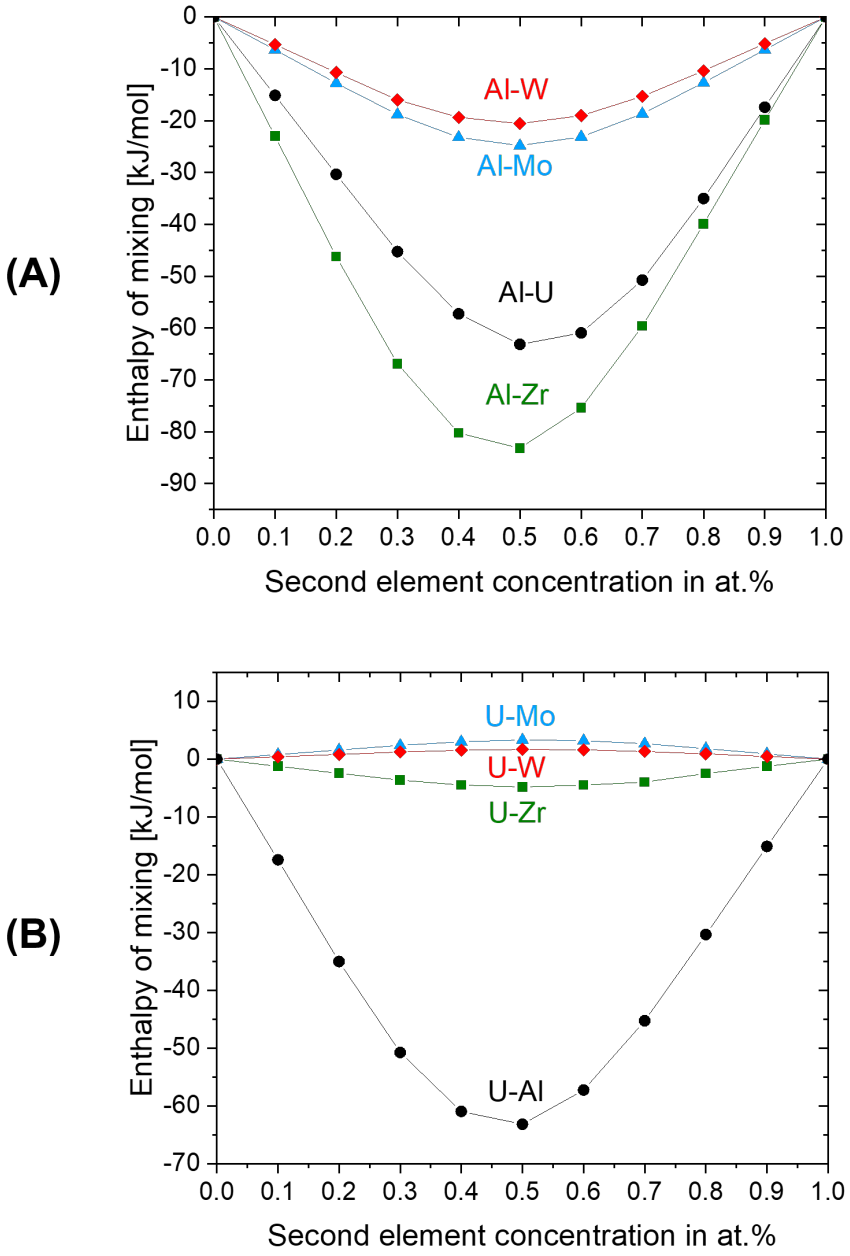

FIGURE 5.1: Calculated formation enthalpies as a function of the second element concentration in (A) Al-X and (B) U-X binary systems based on Miedema's model.

the W barrier. The thickness of the top layer, namely Al, were determined by performing SRIM/TRIM calculations. The results are shown in Figure 5.2 - 5.4.

The ion irradiations were performed with 80 MeV ^{127}I ions at 140 °C to simulate in-pile conditions. The irradiation parameters are summarized in Table 5.1. During PIE, the samples were polished until reaching the beam centre in order to expose the cross-section of the irradiated region.

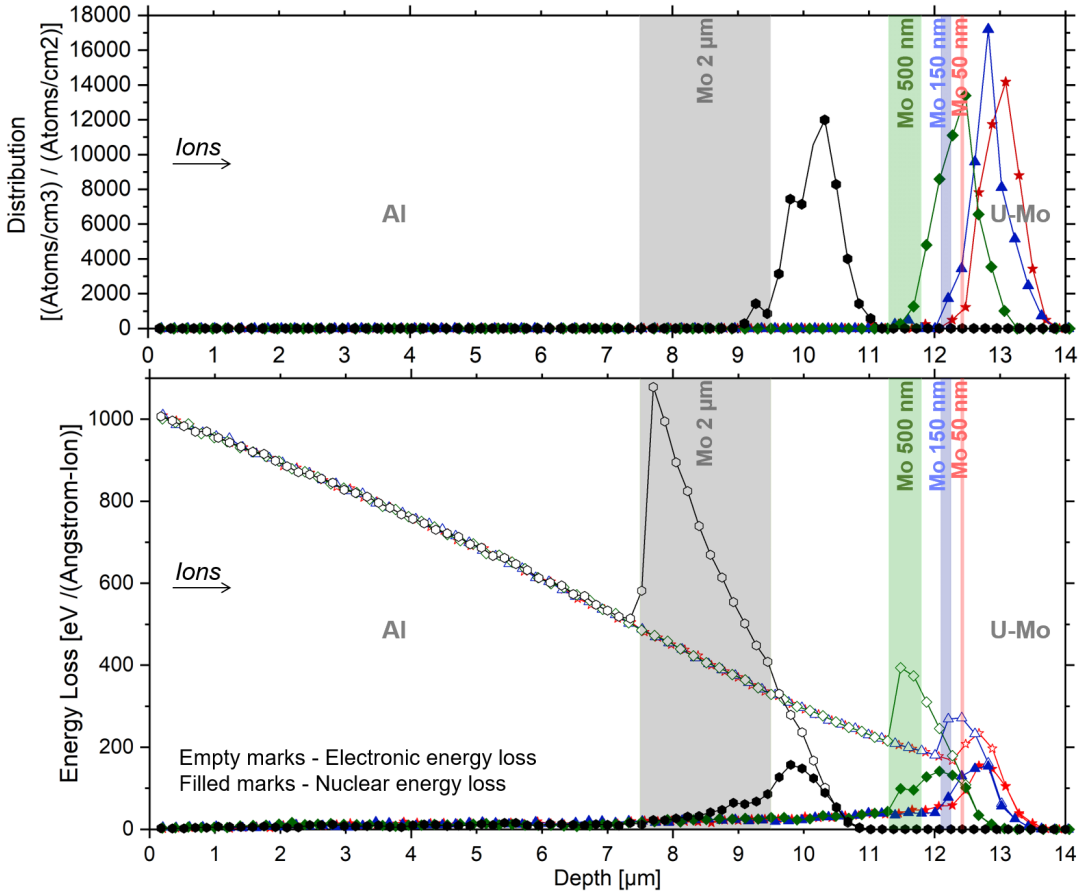

FIGURE 5.2: SRIM/TRIM calculated ion distribution and energy losses profiles in the Al/Mo/U-Mo trilayer samples.

TABLE 5.1: Irradiation parameters

Sample ID	Coating	Total ions [ions]	$\dot{\Phi}_{max}$ [ions/ $(cm^2 \cdot s)$]	Φ_{max} [ions/cm^2]
S8-13	50 nm Mo	$2 \cdot 10^{16}$	$4.3 \cdot 10^{12}$	$4.3 \cdot 10^{17}$
S8-16	150 nm Mo	$2 \cdot 10^{16}$	$1 \cdot 10^{12}$	$4.2 \cdot 10^{17}$
S8-14	500 nm Mo	$2.1 \cdot 10^{16}$	$7.4 \cdot 10^{12}$	$4.3 \cdot 10^{17}$
S9-1	2 µm Mo	$9.7 \cdot 10^{15}$	$6.1 \cdot 10^{12}$	$4.8 \cdot 10^{17}$
S8-15	200 nm Zr	$2 \cdot 10^{16}$	$6.7 \cdot 10^{12}$	$4.2 \cdot 10^{17}$
S8-17	5 µm Zr	$2 \cdot 10^{16}$	$3.9 \cdot 10^{12}$	$3.3 \cdot 10^{17}$
S11-1	200 nm W	$1.6 \cdot 10^{16}$	$7.2 \cdot 10^{12}$	$7 \cdot 10^{17}$
S11-2	500 nm W	$1.5 \cdot 10^{16}$	$6.6 \cdot 10^{12}$	$7.1 \cdot 10^{17}$
S11-3	1 µm W	$1.5 \cdot 10^{16}$	$1.3 \cdot 10^{13}$	$7 \cdot 10^{17}$
S11-4	2 µm W	$1.5 \cdot 10^{16}$	$1.4 \cdot 10^{13}$	$7 \cdot 10^{17}$

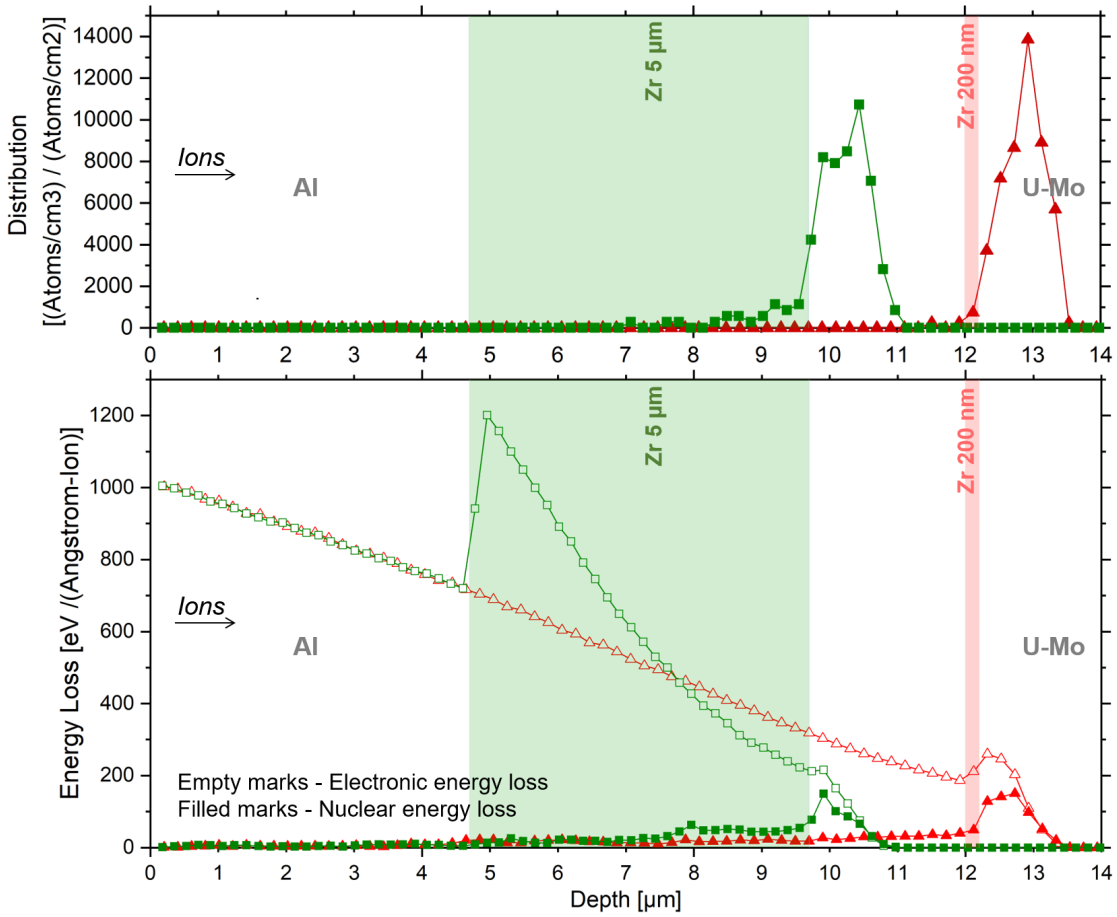

FIGURE 5.3: SRIM/TRIM calculated ion distribution and energy losses profiles in the Al/Zr/U-Mo trilayer samples.

5.1.3 Results

5.1.3.1 Mo coating

After irradiation, the high-energy ion beam left a semi-elliptical footprint on the sample surface (Figure 5.5), which provides information on the geometry of the beam spot. Figure 5.6 summarizes the SEM cross-sectional images obtained in (A) non-irradiated region, (B) low-fluence irradiated region and (C) beam centre, respective. The local ion dose profile was determined based on the approach explained in Section 3.7, while the equivalent fission densities were calculated using correlation 3.3. The obtained values of each region are given above the corresponding image. This way, the irradiation behaviour of these coated samples with increasing irradiation effect is visualized.

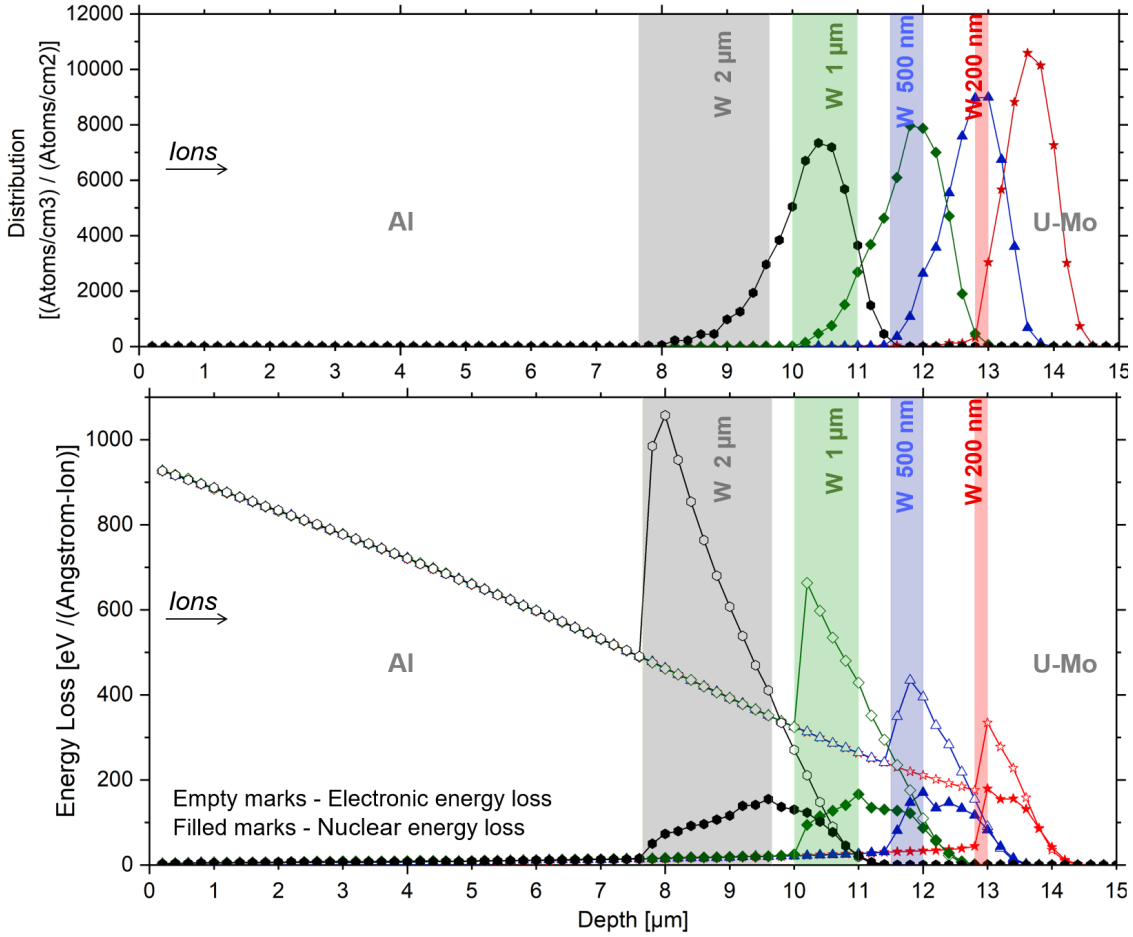

FIGURE 5.4: SRIM/TRIM calculated ion distribution and energy losses profiles in the Al/W/U-Mo trilayer samples.

50 nm and 150 nm

As shown in Figure 5.6, in the 50 nm Mo and 150 nm Mo coated samples, the coating barriers are recognisable in the enlarged SEM images of the non-irradiated region (region A), where the non-irradiated original structure of the sample is shown. At an ion fluence of $1.4 \cdot 10^{17}$ ions/cm^2 (region B), a U-Mo-Al IDL developed, accompanied by the formation of a Mo-rich phase between the U-Mo-Al IDL and the Al layer resulted from the Mo-Al intermixing. No pure Mo left in region B of the two samples. In region C, the ion fluence reached at $4.2 - 4.3 \cdot 10^{17}$ ions/cm^2, where significant U-Mo-Al interactions are observed, by which the Al layer was further consumed. However, the thickness of the Mo-Al intermixing layer remains unchanged. This indicates that the formed Mo-Al intermixing phase did not further react with Al or U-Mo, but was rather "transparent" to the atomic transport between U-Mo and Al, which allows the Al atoms to go through the intermixing layer and eventually meet U-Mo.

One can therefore conclude that neither 50 nm Mo nor 150 nm Mo is capable of suppressing the unwanted U-Mo-Al interdiffusion.

500 nm

In region B of the 500 nm Mo coated sample, an ion fluence of $1.4 \cdot 10^{17}$ ions/cm^2 was received, which induced a significant Mo-Al intermixing phase with likely the complete consumption of the Mo coating layer and a slight consumption of the Al layer. Yet, almost no U-Mo-Al IDL developed at the interface. Moving to region C, the thickness of the Mo-Al intermixing phase was increased to a certain extent. Similar to the 50 nm Mo and 150 nm Mo coated samples, the completely formed Mo-Al intermixing layer shows its transparency to the U-Mo-Al interdiffusion, evidenced by (i) the almost unchanged thickness of the Mo-Al intermixing phase; (ii) the notable consumption of the Al layer compared to region B; and (iii) and the generated U-Mo-Al IDL between the U-Mo and the Mo-Al intermixing.

2 µm

Increasing the coating thickness to 2 µm, a Mo-Al intermixing phase of ~1 µm and the remaining Mo coating of ~1.6 µm were revealed at the interface between Al and U-Mo in region B. Region C was subjected to an ion fluence of $4.8 \cdot 10^{17}$ ions/cm^2, where a strong intermixing occurred between Mo and Al as there was more Mo available for this interaction compared to the 500 nm Mo coated sample. Regardless, the Mo coating was not completely consumed - a Mo coating of roughly 1 µm remained. No U-Mo-Al interdiffusion took place yet as it was likely delayed by the Mo-Al intermixing. Figure 5.7 shows clearly the effect of ion fluence: with the increasing ion fluence, the Al-Mo intermixing layer grows continuously with the observable consumption of Mo and Al. All the phases in those samples were identified by EDX line scans shown in Figure 5.8, which unveils an Al/Mo atomic ratio of around 6 of the formed Mo-Al intermixing layer. The Al/(U+Mo) atomic ratio of the U-Mo-Al IDL lies between 4 and 5, which agrees well with the result of the IDL generated in the uncoated Al/U-Mo sample irradiated at 140 °C (Figure 4.10 of Chapter 4). Further, the deposited I ions are detected in U-Mo close to the IDL/U-Mo or Mo/U-Mo interface, where the high irradiation damage is also seen in form of fine cracks, which shows a good agreement with the SRIM/TRIM calculations.

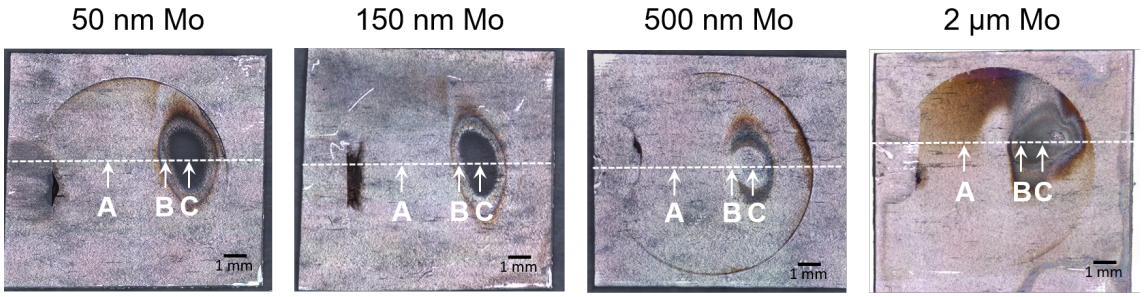

FIGURE 5.5: Footprint on the Mo coated samples after irradiation.

5.1.3.2 Zr coating

Two U-Mo/Zr/Al samples with respectively 200 nm and 5 µm Zr coating were investigated. The images of as-irradiated samples are shown in Figure 5.5. Likewise, region A, B and C for analysis are indicated.

200 nm

As shown in the SEM cross-sectional image of region B of the 200 nm Zr coated sample, the Zr coating was completely consumed by the interaction with Al after being subjected to an ion fluence of $1.4 \cdot 10^{17}$ ions/cm^2. Very similar to the 150 Mo coated sample, the formed intermixing phase, in this case being the Zr-Al intermixing layer, shows transparency to the U-Mo-Al interdiffusion, resulting in the formation of a U-Mo-Al IDL of $\sim$1 µm between the U-Mo and the Zr-Al intermixing layer. Increasing the ion fluence to $4.2 \cdot 10^{17}$ ions/cm^2, the U-Mo-Al IDL reaches $\sim$5 µm, while the Zr-Al intermixing remains almost unchanged. This again proves that once the coating layer is completely consumed by the formation of the Al-coating intermixing phase, the U-Mo-Al interdiffusion becomes unstoppable since the formed Mo-Al or Zr-Al layer shows transparency to the atomic transport between Al and U-Mo.

5 µm

In the non-irradiated area (region A) of the 5 µm Zr coated sample, the original three phases can be clearly identified, namely U-Mo, Zr and Al. Moving to region B, a thin Zr-Al intermixing layer ($<$ 500 nm) formed at the Al/Zr interface after being subjected to an ion fluence of $1.1 \cdot 10^{17}$ ions/cm^2. The thickness of the Zr coating seems to be increased a bit, which should be the effect of the non-homogeneity of the coating thickness. Region C reveals the irradiation behaviour of the sample structure after receiving an ion fluence of

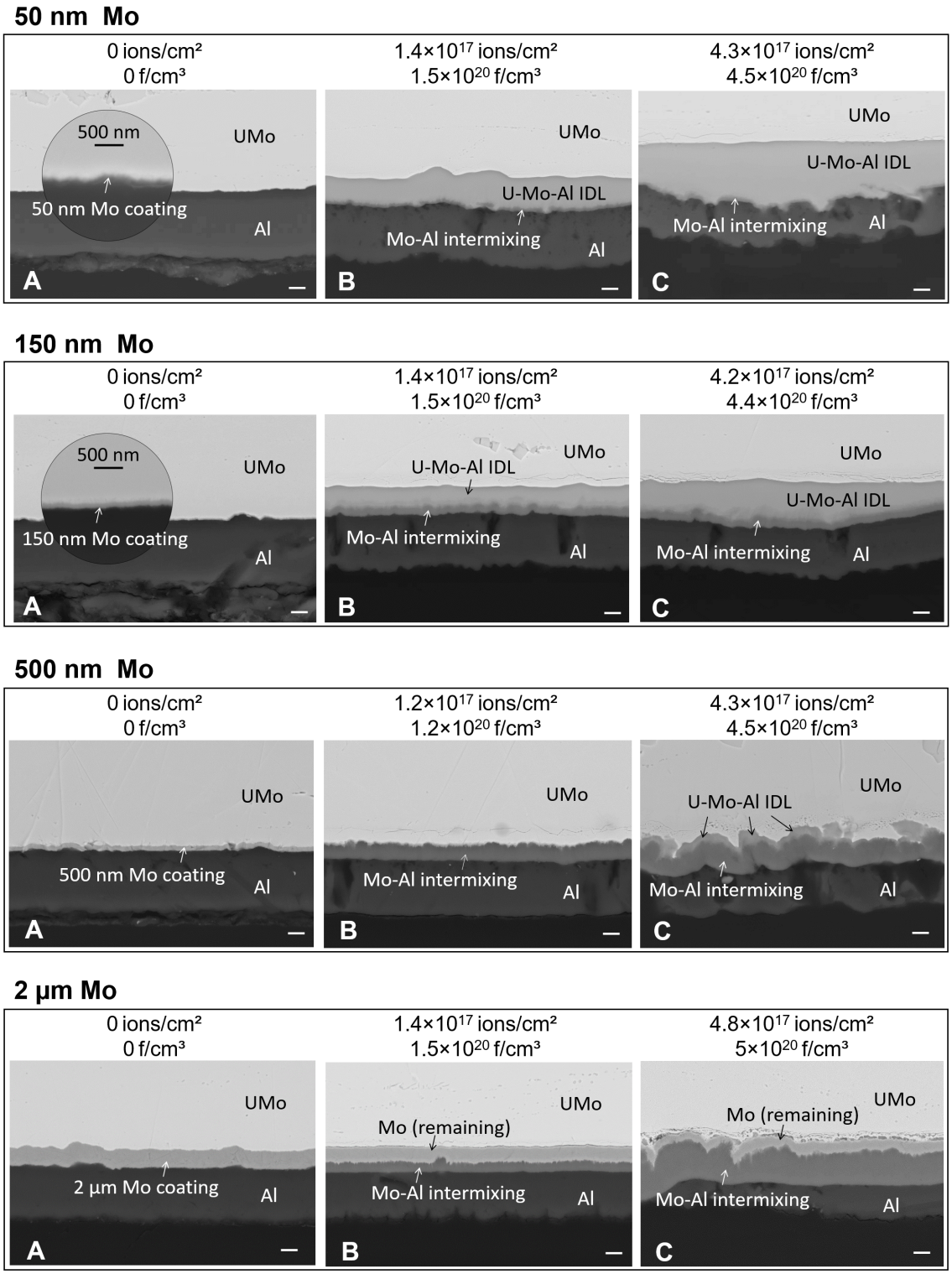

FIGURE 5.6: Cross-sectional SEM images of the Mo coated samples after irradiation, respectively taken from non-irradiated zone (A), low-dose irradiated zone (B) and peak-dose irradiated zone (C). Ions impinged on Al. Scale bar: 2 µm.

$3.3 \cdot 10^{17}$ ions/cm^2, where a Zr-Al intermixing phase grew up to $\sim$1 µm. The thickness of the Zr-Al intermixing layer is still small. This is probably due to

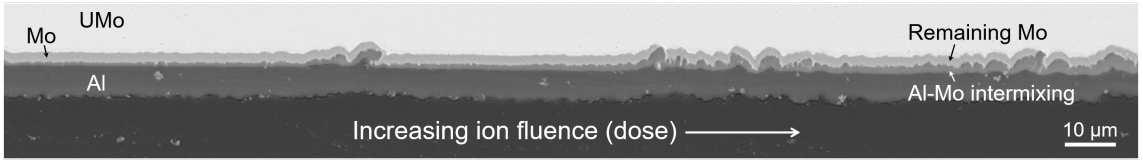

FIGURE 5.7: Structure evolution of the 2 µm Mo coated sample with increasing irradiation dose (ion fluence).

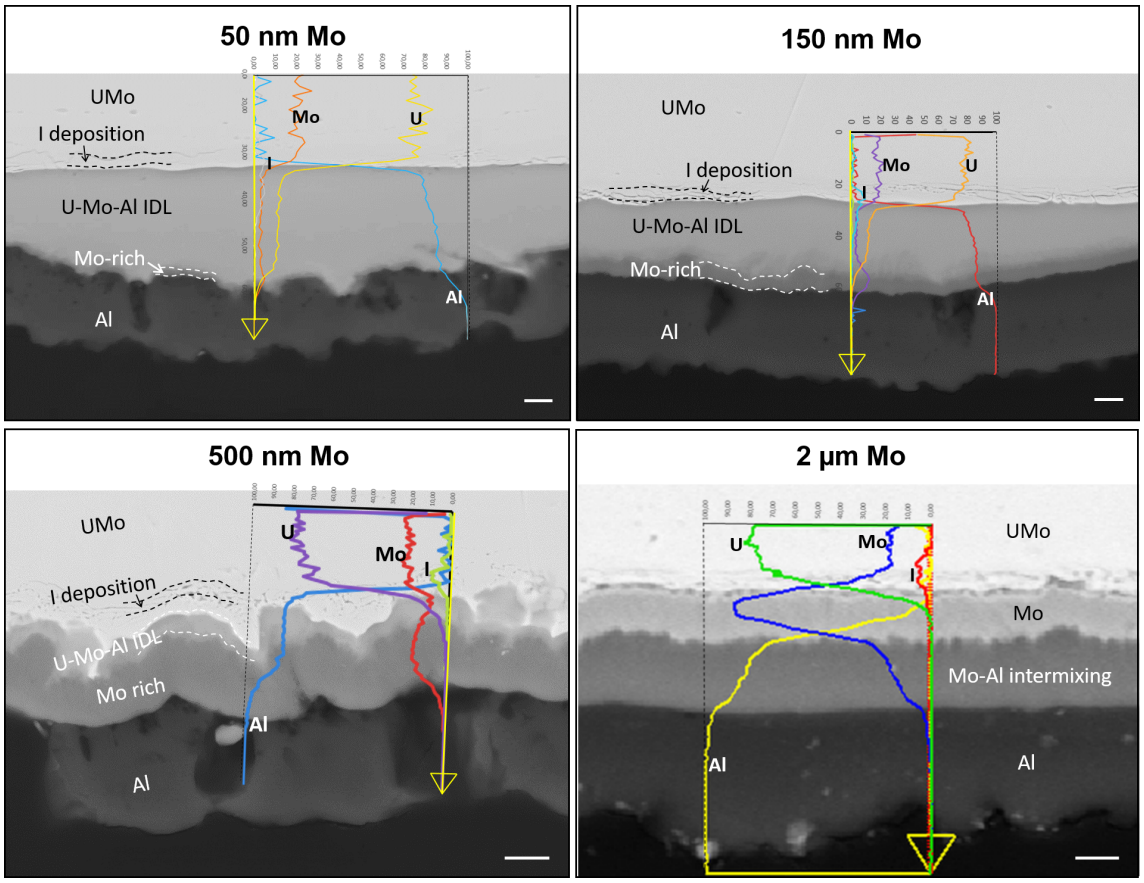

FIGURE 5.8: EDX analysis of the peak-dose irradiated zones (region C) of the Mo coated samples. Scale bar: 2 µm.

the fact that the Al/Zr interface lies rather far away from the Bragg peak and was thus subjected to less irradiation damage. No U-Mo-Al IDL is shown in this sample, i.e. the interactions between U-Mo and Al are entirely absent. The EDX line scan evidences an Al/Zr atomic ratio of around 6 for the Al/Zr intermixing layer, and an Al/(U+Mo) ratio of between 4 - 5 for the U-Mo-Al IDL, which also agrees with the result of the IDL generated in the uncoated Al/U-Mo sample irradiated at 140 °C (Figure 4.10 of Chapter 4).

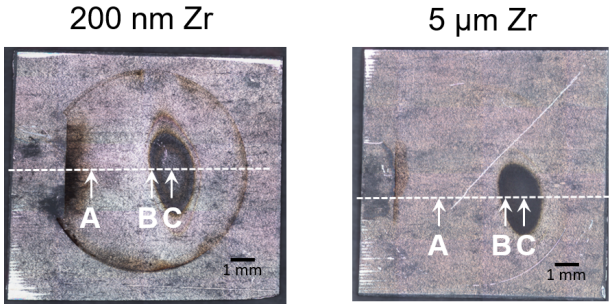

FIGURE 5.9: Footprint on the Zr coated samples after irradiation, scale bar: 2 µm.

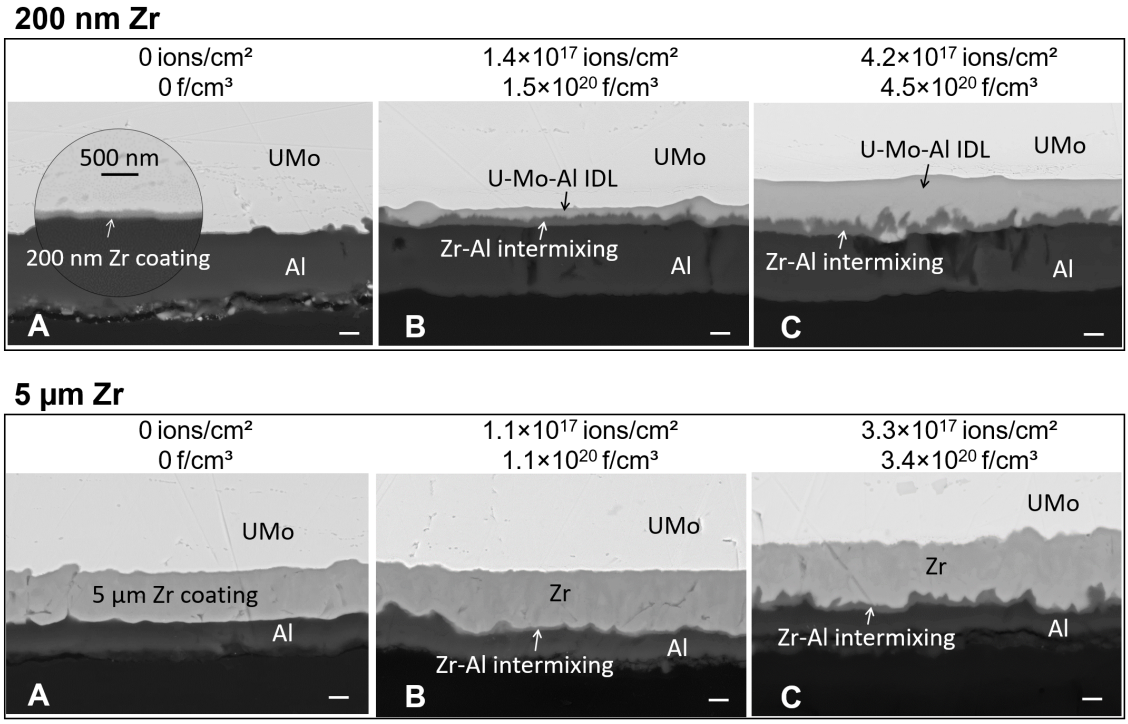

FIGURE 5.10: Cross-sectional SEM images of Zr coated samples after irradiation, respectively taken from non-irradiated zone (A), low-dose irradiated zone (B) and peak-dose irradiated zone (C). Ions impinged on Al. Scale bar: 2 µm.

5.1.3.3 W coating

The W coated samples shows a more optimistic result - at the given magnification, the irradiation effect is only recognised in the regions of beam centre which were subjected to an ion fluence of $7.1 \cdot 10^{17}$ ions/cm^2, or a fission density equivalent of $\sim 7.5 \cdot 10^{20}$ f/cm^3. Hence, only this region and the non-irradiated region of each sample were focused during PIE. The sample production and some details on the irradiation can be found in [138]. The picture of irradiated samples and the corresponding cross-sectional SEM images are shown in Figure 5.12.

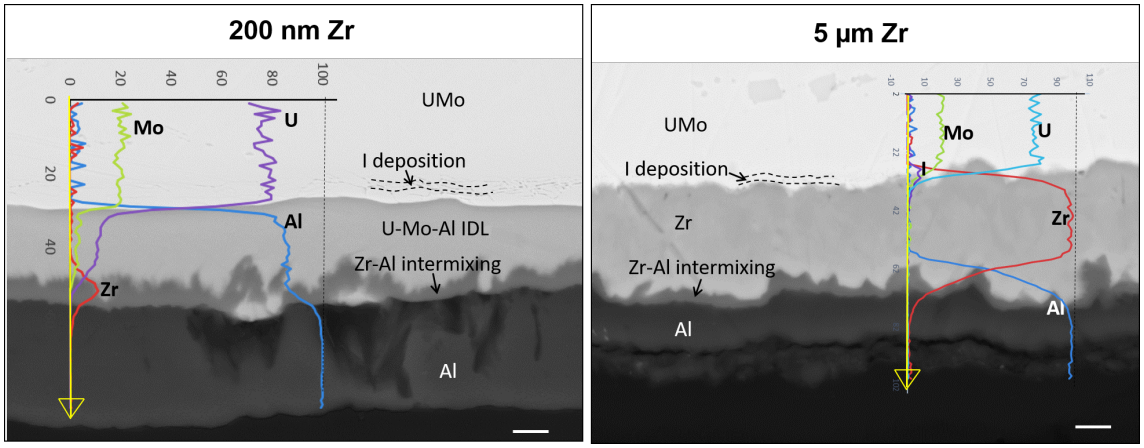

FIGURE 5.11: EDX analysis of the peak-dose irradiated zones (region C) of the Zr coated samples. Scale bar: 2 µm.

200 nm

In the non-irradiated region of the 200 nm W coated sample, apart from the W coating, two additional intermixing layers are observed, i.e. Al-W and W-U-Mo-Al intermixing layers identified by EDX line scan. These intermixing layers are probably originated from the sample production, during which the U-Mo substrate was subjected to heat treatment reaching ~600 °C to ensure good adhesion of the coating. This likely has caused thermal diffusions. Consequently, Al interacted with W and U-Mo, forming a W-U-Mo-Al intermixing layer, leaving behind a W-rich layer instead of the original W coating layer. The thickness of the W-rich layer is around 200 nm. At the beam centre, it was seen that the ion irradiation mainly enhanced the interdiffusion between Al and W, resulting in a final Al-W intermixing layer of ~500 nm. The W-U-Mo-Al layer, however, did not increase in thickness. Furthermore, a longitudinal crack is observed in Al, which could be caused during the mechanical polishing process.

500 nm

The 500 nm W coated sample also shows the presence of Al-W and W-U-Mo-Al intermixing layers in the non-irradiated region as a result of the heat treatment during sample production. The EDX line scan reveals a small peak of Al at the W/U-Mo interface. It is speculated that the W-U-Mo-Al layer performed as a sink for Al atoms. In the beam centre region, the Al-W intermixing phase grew up to ~1 µm, with some consumption of W. Consequently, the thickness of the W (or W-rich, as it contains an amount of Al) layer reduced to ~200 nm. Below the W-rich layer, a thin intermixing layer containing W, U, Mo and Al

can be identified according to the result of the EDX line scan - albeit not clearly recognisable in the SEM image. A crack propagating through the Al layer is shown in this sample as well.

1 µm

In the 1 µm W coated sample, a thin W-U-Mo intermixing layer is still observed in the non-irradiated region. Nevertheless, when it reaches this thickness, the W coating barrier can finally block the way of Al to U-Mo, as no Al-U-Mo intermixing is identified by EDX line scan. The W coating was partially consumed by the development of the Al-W intermixing phase. The thickness of the W-U-Mo intermixing layer remained unchanged in thickness when compared to the non-irradiated region. Similar to the 500 nm W sample and the 1 µm W coated sample, a mechanical crack is observed in Al.

2 µm

The 2 µm W coated sample behaved like the 1 µm W coated sample: a thermally induced W-U-Mo intermixing layer ($<$ 100 nm) formed at the W/U-Mo interface 1 µm W coated, shown in the non-irradiated region; An Al-W intermixing layer of $\sim$200 nm grew at the Al/W interface in the region subjected to the maximum irradiation dose (beam centre), where the W-U-Mo intermixing layer did not further develop. The thickness of the Al-W intermixing layer is smaller than that in the 1 µm W coated sample, which should be attributed to the different energy deposition at the Al/W interface caused by the different distances to the Bragg peak. It is worth noting that no cracks in Al were found in this sample.

5.1.4 Discussion

Mo, Zr and W as diffusion coating barrier in the U-Mo/Al fuel system were examined by heavy ion irradiation. In the Mo coated samples, the Al layer interacted actively with the Mo coating. Once there was no pure Mo left, the atomic transport between Al and U-Mo was triggered, during which the Al atoms passed through the Al-Mo intermixing layer and formed an Al-U-Mo IDL near the U-Mo. During this process, the thickness of the Mo-Al intermixing layer remains almost unchanged. At the given ion fluence, i.e. $4.8 \cdot 10^{17}$ ions/cm^2 (equivalent to a fission density of $\sim$ $5 \cdot 10^{20}$ f/cm^3), no Al-U-Mo IDL was

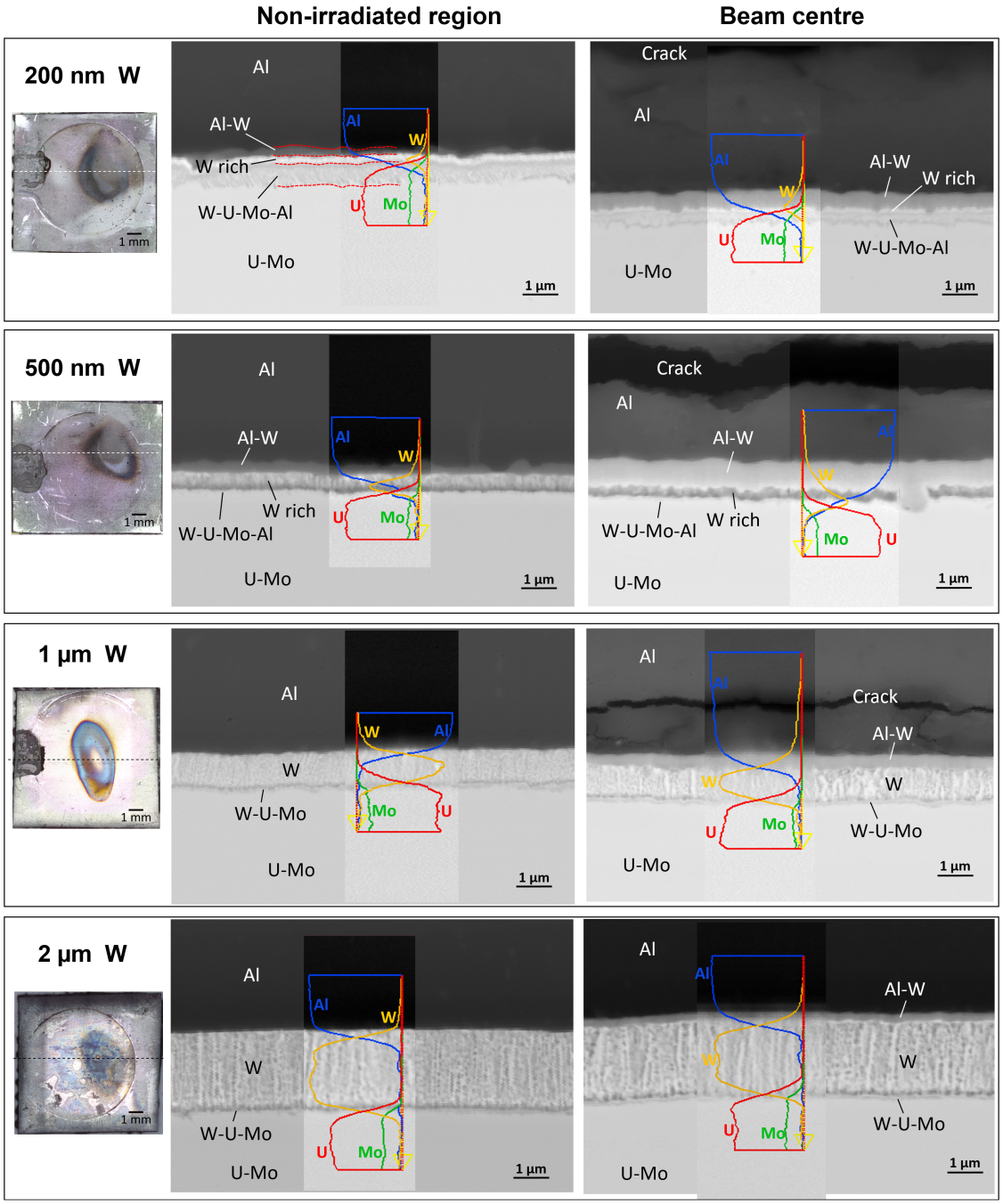

FIGURE 5.12: Images of as-irradiated samples and corresponding cross-sectional SEM images with EDX analysis. Ions impinged on Al.

generated in the 2 µm Mo coated sample. Yet, the drastically growing Mo-Al intermixing layer largely altered the fuel structure. Within the framework of SEMPER FIDELIS project, a U-Mo/Al fuel plate with a certain fraction of 1 µm Mo coated U-Mo particles was in-pile irradiated. Figure 5.13 compares the result of the 150 nm Mo coated sample in this study and the recently published PIE result of SEMPER FIDELIS tests [139][140]. In both case, the fuel structures were

modified significantly with increasing irradiation dose (ion fluence or fission density): the Al interacted strongly with the Mo coating under irradiation, resulting in the formation of an Al-Mo intermixing phase. When the Mo was completely consumed, a Mo rich Mo-Al intermixing layer was built, triggering the formation of a U-Mo-Al IDL as the atomic transport was allowed by the Mo rich layer. This is evidenced by EDX in Figure 5.14. The thicknesses of IDL induced by ion irradiation and by in-pile irradiation at location with the highest dose/fission density reached 5 µm (Figure 5.13(A3)) and 10 µm (Figure 5.13(B4)), respectively. Note that the maximum fission density of the in-pile irradiated location of the SEMPER FIDELIS plate reaches ∼10 times of the irradiation effect of the ion irradiated location, whereas the local fission rate equivalent of the ion irradiation is more than 20 times higher than the local fission rate of the in-pile SEMPER FIDELIS irradiation. The two results agree very well in regard to fuel structure evolutions, despite the reverse irradiation direction. This result again demonstrates that the swift heavy ion irradiation technique is a proper tool for simulations of in-pile irradiation.

In the Zr coated samples, a 200 nm Zr coating had been totally consumed before the ion fluence reached $1.4 \cdot 10^{17}$ ions/cm^2. Similar to the Mo coated samples, the generated Zr-Al intermixing layer shows transparency to Al atoms, prompting the build-up of a U-Mo-Al IDL. A similar transparency behaviour was observed in in-pile irradiated fuels under high fission rate e.g. in the SELENIUM test when the fuel plate was subjected to high fission rates at beginning of life (BOL), as pointed out in [141]. It seems that no excessive intermixing occurred in the 5 µm Zr coated sample, except for the growth of a thin Zr-Al intermixing layer. Further, the Al-U-Mo IDLs formed in Mo and Zr coated samples have a similar Al/(U+Mo) ratio, which agrees with the result obtained from the IDL generated in the uncoated Al/U-Mo sample irradiated at the same temperature i.e. 140 °C.

The W coating barrier shows the most promising behaviour among the three coating materials - no excessive intermixing occurred when the coating thickness is above 1 µm. No significant structural modifications due to irradiation were observed in those samples. The cracks shown in the Al layer of the W coated samples were probably introduced during the mechanical grinding and polishing process of PIE.

At last, it is worth to mention that in all the irradiated samples, no notable intermixing was observed at the coating/U-Mo interface. The observed results agree with the thermodynamic considerations to a great extent (Figure 5.1(B)).

By comparing the obtained SEM cross-sectional micrographs, it is clear that the thickness of the intermixing layers is related to the ion fluence. To

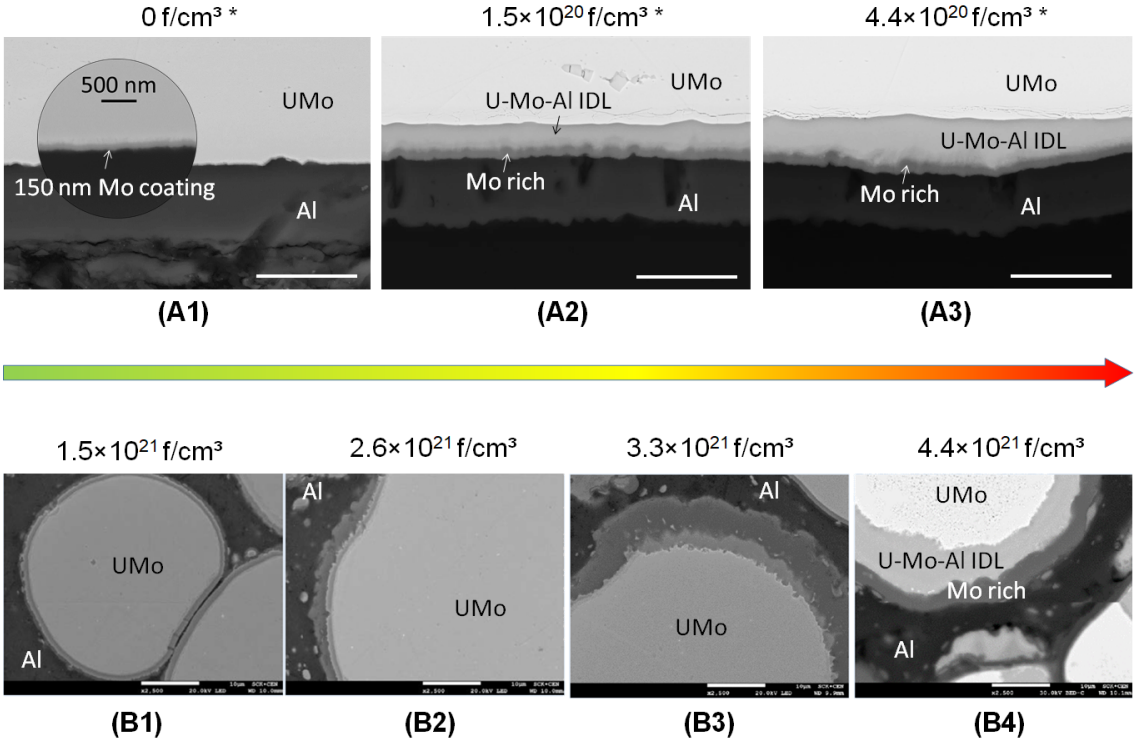

FIGURE 5.13: Comparison of the behaviours of the U-Mo/Al fuel system with a Mo coating barrier under ion irradiation and under in-pile irradiation. (A1) to (A3): The evolution of fuel structure with an increasing ion irradiation dose obtained in this study. The corresponding fission density equivalent (marked with an asterisk) is indicated. (B1) to (B4) are taken from [139] and show the evolution of fuel structure with increasing burn-up in SEMPER FIDELIS in-pile test. In both cases, Al interacted strongly with Mo coating under irradiation, resulting in the formation of an Al-Mo intermixing phase. When the Mo coating was fully used up, a Mo rich Mo-Al intermixing layer formed, allowing the atomic transport between Al and U-Mo which eventually led to the growth of U-Mo-Al IDL. At the highest dose/fission density, a thick U-Mo-Al IDL formed, which largely altered the fuel structure. Besides, HBS is observed in the U-Mo of the SEMPER FIDELIS fuel from a fission density of $\sim 3.3 \cdot 10^{21}$ f/cm^3. Scale bar: 10 µm.

quantitatively evaluate this effect, the thickness of the whole intermixing phase is plotted as a function of ion fluence (Figure 5.15). Considering that the intermixing layers are mostly amorphous, and this nature plays a crucial role in the fuel swelling and destabilization, all the intermixing phases were taken into account in the calculation. The quantity "entire intermixing layer" of y-axis refers to the overall thickness of all the intermixing phases. In general, due to the rapidly growing intermixing phases with ion fluence, Mo coating is not recommended as diffusion barrier material in U-Mo/Al fuels. This conclusion is in contradiction to the conclusion presented in [28], where Mo was suggested as a very promising candidate for diffusion barriers in U-Mo/Al fuels. Yet, in [28], only one Mo coated sample was studied, and it was reported that the formed

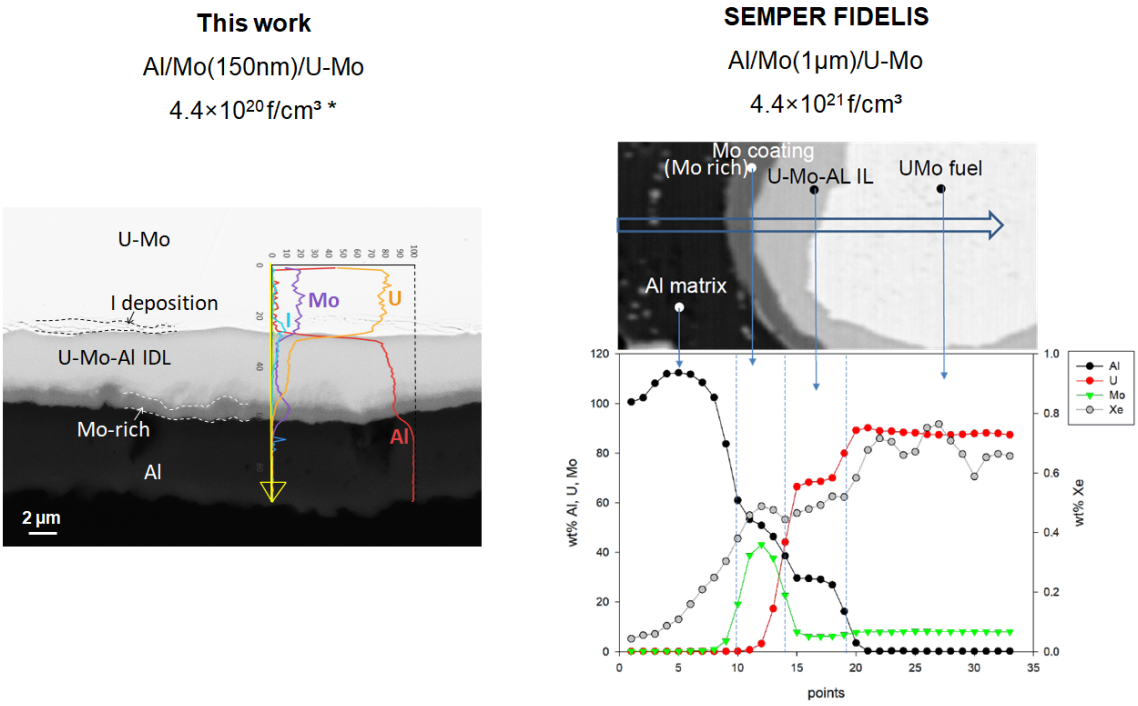

FIGURE 5.14: Left: EDX result of the 150 nm Mo coated sample irradiated at an irradiation dose of $\sim 4.4 \cdot 10^{20}\,\mathrm{f/cm^3}$ in this study. This value is marked with an asterisk as it is an equivalent value which was calculated from the ion fluence. Right ([139]): EDX result of the SEMPER FIDELIS plate with Mo coating irradiated at a fission density of $\sim 4.4 \cdot 10^{21}\,\mathrm{f/cm^3}$. Scale bar: 10 µm.

Mo-Al compound have protected the sample structure from further ion collisions. However, in this study, the results of the four Mo coated samples reveal that the Mo-Al intermixing phase not able to prevent the U-Mo-Al interaction caused by ion irradiation, as this intermixing phase shows transparency to the atomic transport between Al and U-Mo. Given the much slower growing of the intermixing phases, the 5 µm Zr coating and the 2 µm W coating seem more effective in suppressing the fuel swelling. Nevertheless, one should keep in mind that the irradiation dose i.e. the ion fluence reached in this study corresponds to $\sim$ 10% of the fission density usually achieved in-pile, such as in the SELENIUM and SEMPER FIDELIS tests. The consumption rate of the coating as a function of irradiation dose should be further investigated to find out the suitable coating thickness. On the other hand, the effect of irradiation dose rate, namely the ion flux in this study, should not be excluded: The maximum ion flux in this experiment reached $\sim 7 \cdot 10^{15}\,\mathrm{ions}/\left(\mathrm{cm^2 \cdot s}\right)$, which corresponds to a fission rate equivalent of $\sim 7.4 \cdot 10^{15}\,\mathrm{f}/\left(\mathrm{cm^3 \cdot s}\right)$. This value is almost an order of magnitude larger than the peak fission rate achieved in the E-FUTURE [86] and the SELENIUM [25] irradiations. Further, the excessive interaction between

the coating and the Al layer shows that further investigations focusing on the coating/Al interface are still needed.

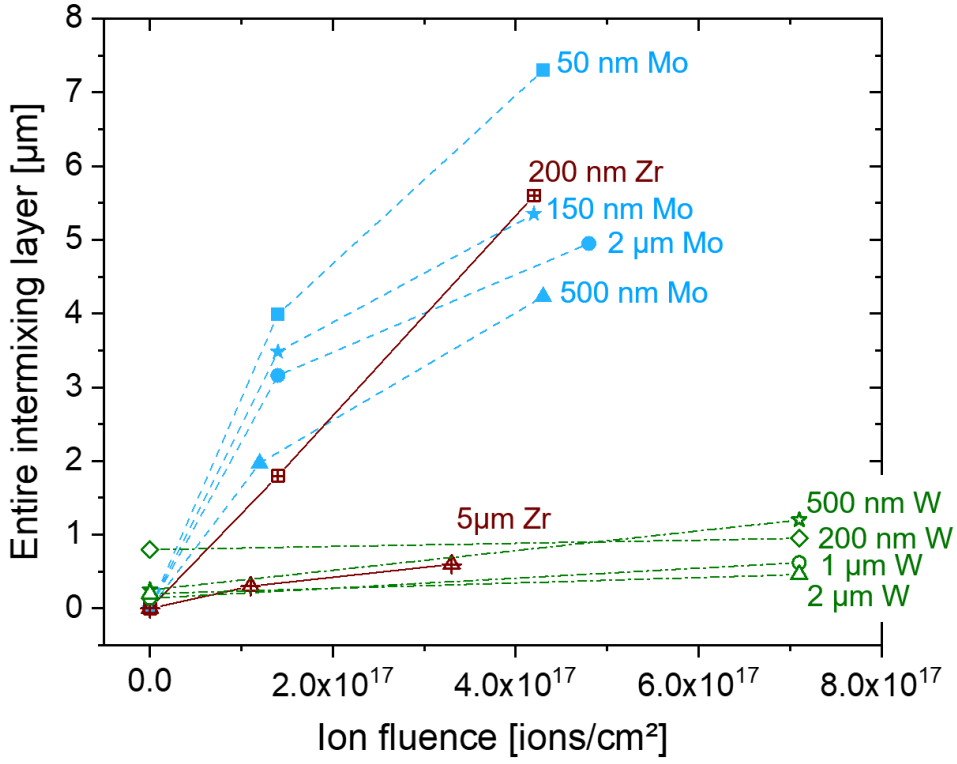

FIGURE 5.15: Thickness of the entire intermixing layer in Mo, Zr and W coated samples as a function of ion fluence.

5.2 Transition metal nitride - ZrN

5.2.1 Background

Transition metal nitride ZrN as a diffusion barrier in U-Mo/Al based fuels was recently set into focus. A ZrN coating is considered a very promising diffusion barrier based on the following properties of this material: high melting point, high hardness, chemical inertness and thermodynamic stability. The results obtained from the in-pile test of mini-rod U-Mo fuels with ZrN coating irradiated in the Russian MIR reactor [142] as well as the out-of-pile annealing tests of ZrN coated U-Mo/Al dispersion fuels [94] have shown a positive effect of ZrN coatings in suppressing U-Mo-Al interaction. Jungwirth et al. [143] have conducted ion irradiation experiments on a ~1000 nm ZrN coated U-Mo dispersion fuel sample at 200 °C. It was found that no IDL formed as long as the ZrN coatings are intact, while notable IDLs developed at the locations where

the ZrN coating shows damages. The SELENIUM project, being the first in-pile irradiation of ZrN coated U-Mo dispersion fuel, was launched in 2010. The PIE results reveal that at low burn-up of $\sim 3.5 \cdot 10^{21}$ f/cm^3, no IDL of the U-Mo fuel with the Al matrix formed as long as the ZrN coatings are intact. In contrast, IDLs with mostly a volcano-like shape form where defects or cracks are displayed. At high fission rate locations, IDLs further formed under seemingly intact coating layers. No pillowing was observed [144]. Yet, it has to be considered that SEM micrographs only show intersecting 2D snapshot planes of more complex 3D geometries, i.e. coating damages may be hidden in another plane leading to the observed phenomenon. This has later been confirmed by Miller et al. [145] by advanced PIE based on 3D reconstruction using FIB-SEM performed. Thus, it can be concluded that the cracks in ZrN coating are responsible for the growth of U-Mo-Al IDL, as they provide entrance ports for the diffusion of Al into the U-Mo kernel and vice versa. Indeed, examinations of fresh EMPIrE and SEMPER FIDELIS fuel plates revealed that the plate rolling can lead to deformation of U-Mo particles, resulting in damages i.e. cracks in the brittle ZrN coatings [95]. Despite of the cracks, the ongoing SEMPER FIDELIS irradiation campaign once again shows the promising protective potential of a ZrN coating against Al-U-Mo intermixing as presented in [139] and [140].

Since cracks are almost unavoidable during fuel manufacturing, it is therefore vital to predict the behaviour of such fuels under different irradiation conditions. In this regard, ion irradiation is an optimal tool, not only because most parameters of ion irradiation are independently controllable, but also this technique is able to provide an extraordinarily high damage rate in a much shorter time, making the high-fission-rate effects under exaggerated conditions distinctly accessible. In the following, a systematic investigation of the ZrN coating barrier in U-Mo/Al fuels is presented.

5.2.2 Experiment

Similar to the transition metal coated samples, a tri-layer structure was used for this study, where a ZrN coating and an Al top layer were subsequently deposited onto a U-Mo substrate by PVD sputtering. The PVD sputtering technique has also been used in the SELENIUM [94], the SEMPER FIDELIS [95] and the EMPIrE [146] projects for preparing ZrN coatings. The traditional magnetron sputtering technique has been introduced in Chapter 2. For the ceramic ZrN coating, reactive pulsed-DC magnetron sputtering is a more common option [147] as it can greatly reduce the arcing event resulted from charge accumulation due to

the lower electrical conductivity of ZrN ($1.98 \cdot 10^6\,\Omega^{-1}\mathrm{m}^{-1}$ at room temperature [148]) compared to common metals such as Al ($3.45 \cdot 10^7\,\Omega^{-1}\mathrm{m}^{-1}$ at room temperature [149]). To this end, a dedicated DC magnetron sputtering device with the option "pulse mode" was constructed and commissioned. A CAD model and a picture of the final device are shown in Figure 5.16. A closer look into the chamber and the composition of the stage system are presented in Figure 5.17. The commissioning is presented in detail in [97], where numerous tests were performed to find out the proper sputtering parameters for stoichiometric ZrN. These parameters were adopted in this study. The sputtering of the Al top layer was carried out in the same device without pulse, since it is not necessary for sputtering of pure metals that have much higher electrical conductivities. Between the two deposition steps, i.e. the deposition of ZrN and the deposition of Al, the samples were stored in a vacuum desiccator to avoid oxidation of the ZrN coatings. Such oxidation has been reported in [150] and can degenerate the performance of this diffusion barrier during irradiation. The densities of sputtered ZrN and Al are determined as $6.5\,\mathrm{g/cm^3}$ and $2.5\,\mathrm{g/cm^3}$, which are slightly lower than the densities of the corresponding bulk materials i.e. $7.09\,\mathrm{g/cm^3}$ and $2.7\,\mathrm{g/cm^3}$, respectively.

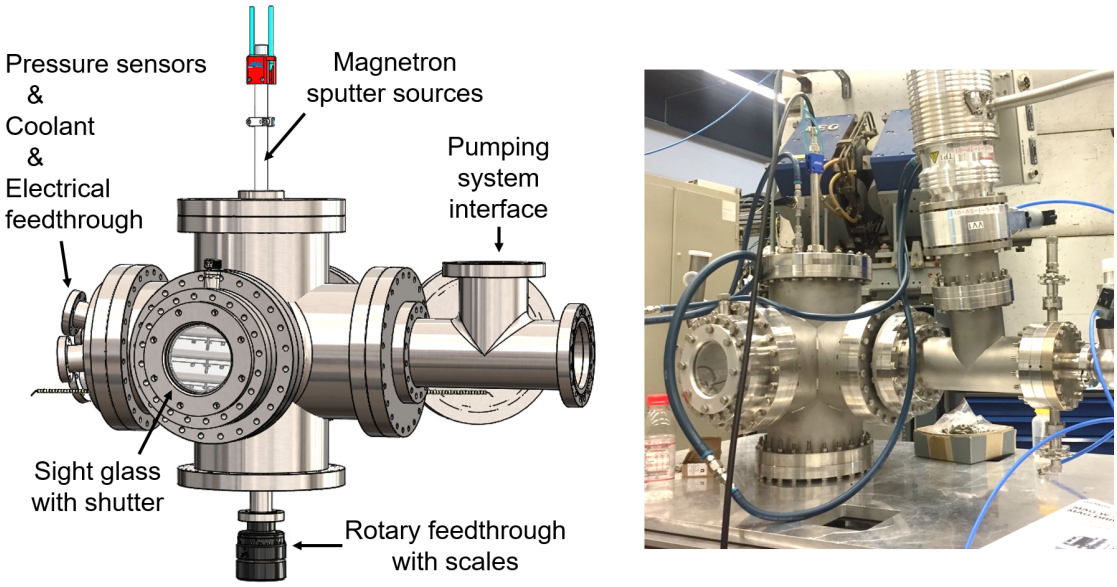

FIGURE 5.16: The dedicated sputtering device for ZrN coating in this study. Left: CAD model; Right: Picture of the device.

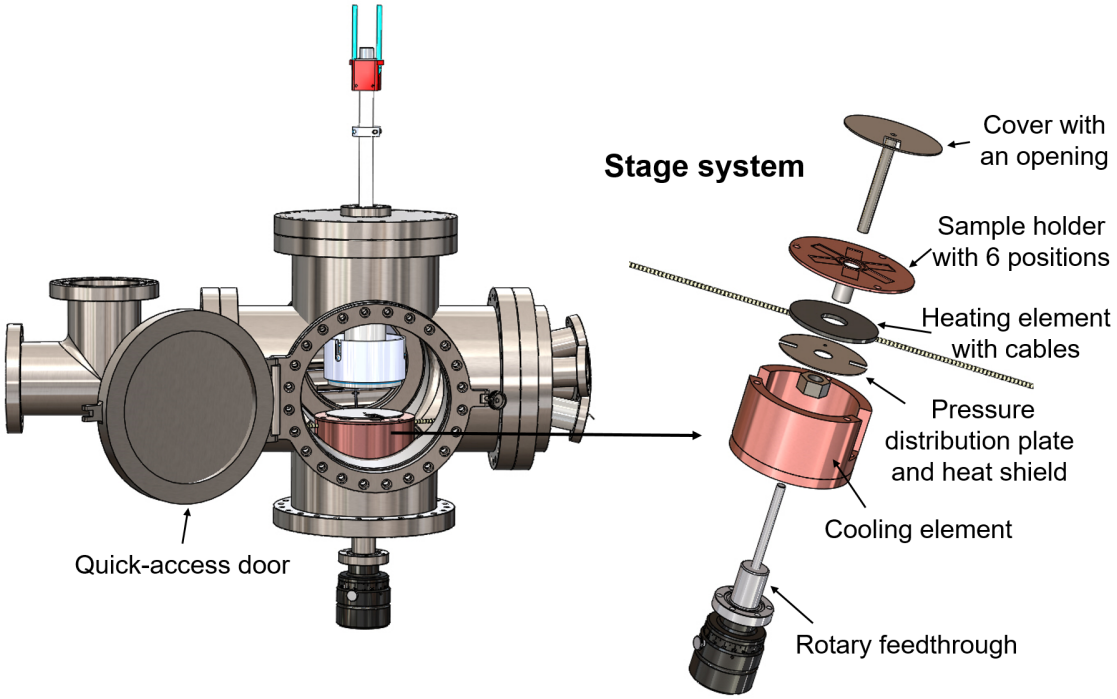

FIGURE 5.17: Sputtering stage system and its location in the sputtering chamber.

5.2.3 Effect of coating thickness

For studying the effect of coating thickness, three tri-layer samples were prepared with a 500 nm, a 200 nm and a 100 nm ZrN coating, respectively. The thickness of the Al layer, i.e. ~11 µm, was estimated by SRIM/TRIM code, assuring that the Bragg peak lands close to the second interface, namely the ZrN/U-Mo interface, as shown in Figure 5.18. The reason for this has been stated in Section 5.1.2. All the irradiations were performed at 140 °C. The other irradiation conditions are summarized in Table 5.2. The irradiation experiment was performed before the utilization of BPM. The reconstruction of ion flux profile by using the IDL thickness profile (approach 1 in Chapter 3) is also not applicable because the IDL growth was suppressed by the ZrN barrier. Thus, the ion flux and the ion fluence at the beam centre were estimated using the BPM profiles taken in the beam time periods after the installation of BPM, where the beam current and the observable diameter of the two beam time periods are similar. During PIE, cross-sections of the three samples were prepared by embedding and polishing. The first analysis was performed at TUM with a Zeiss EVO MA 25 SEM. A comparison between the non-irradiated regions and the irradiated regions is presented in Figure 5.19. No Al-U-Mo IDL is observed at the given resolution. The ZrN coatings stay intact after irradiation.

To have a closer look at the interface, further studies focusing on

TABLE 5.2: Irradiation parameters

Sample ID	Coating	Total ions [ions]	Estimated $\dot{\Phi}_{max}$ [ions/ $(cm^2 \cdot s)$]	Estimated Φ_{max} [ions/cm^2]
S6-1	500 nm ZrN	$1 \cdot 10^{16}$	$1.7 \cdot 10^{13}$	$5 \cdot 10^{17}$
S5-3	200 nm ZrN	$1 \cdot 10^{16}$	$1.1 \cdot 10^{13}$	$5 \cdot 10^{17}$
S6-4	100 nm ZrN	$1 \cdot 10^{16}$	$1.6 \cdot 10^{13}$	$5 \cdot 10^{17}$

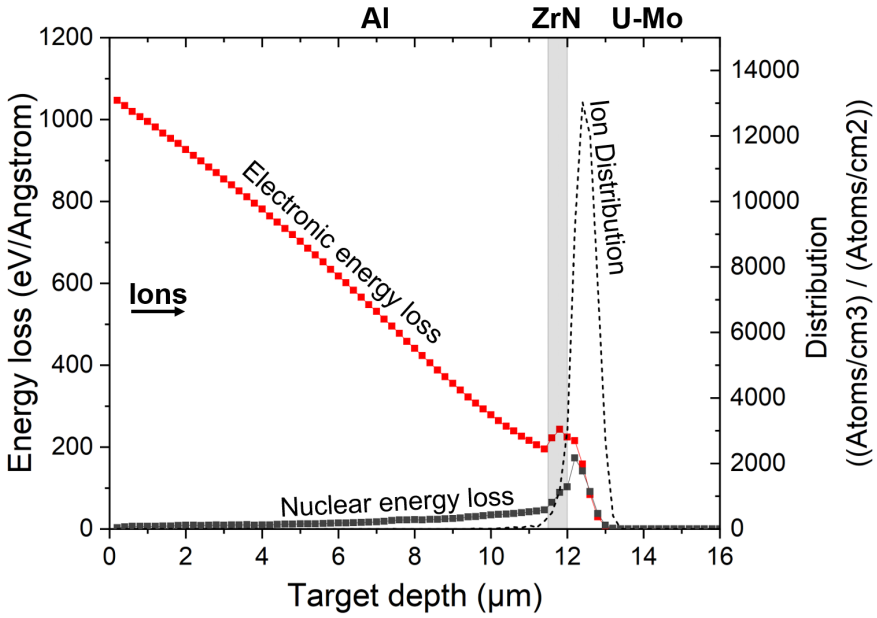

FIGURE 5.18: SRIM/TRIM calculated ion distribution and energy losses profiles in the Al/ZrN/U-Mo tri-layer system.

microstructure and composition were conducted on the 200 nm and 100 nm ZrN coated samples at the Argonne National Laboratory (ANL) with an FEI Strata 400 FIB/SEM dual beam system equipped with Energy Dispersive X-Ray (EDX) detector. As shown in Figure 5.20, after irradiation, the original ZrN coating turned into an intermixing phase consisting of multiple layers, which were identified by EDX (Table 5.3) as ZrN-Al intermixing layer, the ZrN-U-Mo intermixing layer and the remaining ZrN coating, respectively. To rule out the potential artefacts introduced by mechanical polishing during the cross-section specimen preparation, FIB milling was applied to prepare new cross-sections that are perpendicular to the mechanically polished ones. Figure 5.21 shows the SEM images of the trenches milled in the 200 nm ZrN and the 100 nm ZrN coated samples. For each sample, a non-irradiated region and the beam centre region were taken for comparison purposes. In the beam centre regions, multiple layers are clearly identified at the interface, which confirms that the ZrN layer

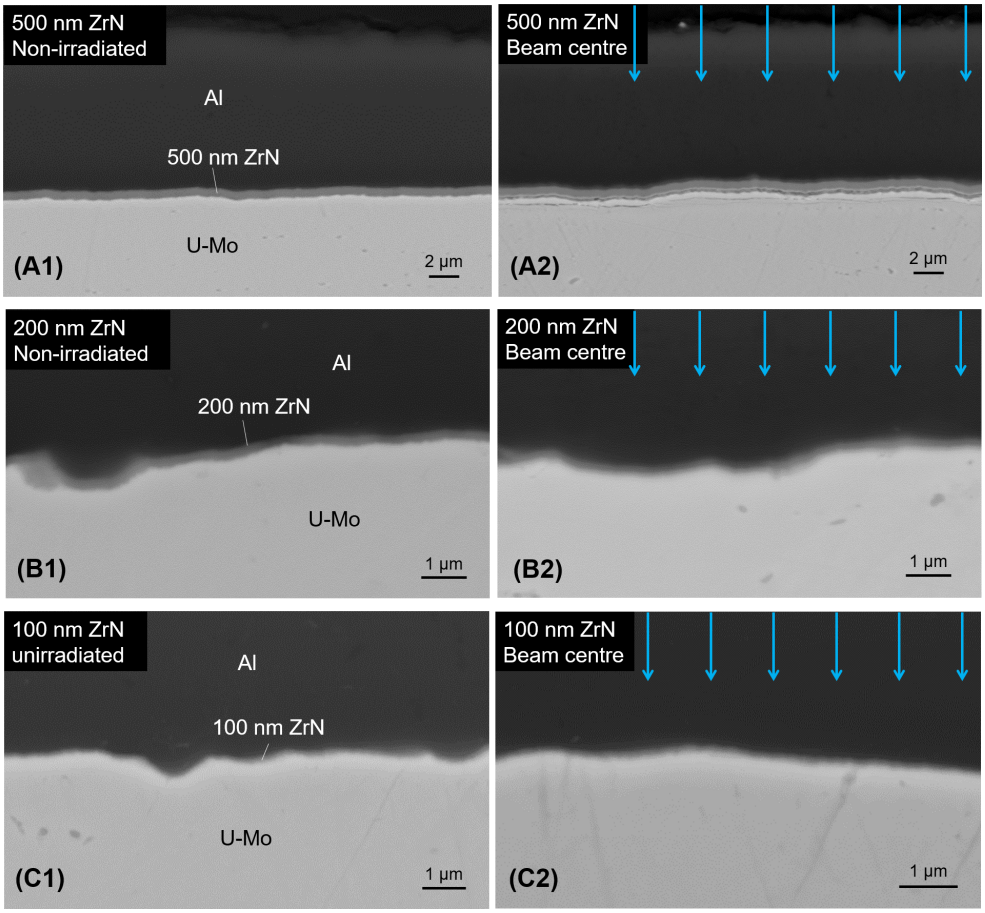

FIGURE 5.19: SEM characterisation of non-irradiated (left) and ion-irradiated regions of the 500, 200 and 100 nm ZrN coated samples. The irradiated regions are taken from the area irradiated by the beam centre.

reacted with Al and U-Mo under irradiation. Further, many voids formed in the Al layer in the beam centre region. Void formation induced by ion irradiation was also observed by Miao et al. [128], where Al/U-Mo bilayer samples were irradiated with high-energy Xe ions in the same irradiation direction as the one presented here, i.e. ions impinge on the Al surface. In Miao's study, the location and arrangement of the voids clearly suggested Kirkendall effect. In this study, nevertheless, one cannot conclude that the voids observed in Al were caused by Kirkendall effect due to their arrangement. Indeed, Kirkendall effect usually leads to a band of voids located close to the interface.

5.2.4 Coating with cracks

5.2.4.1 Characterisation of the ZrN coatings in a fresh SELENIUM fuel plate

As the cracks in the ZrN coatings cannot be avoided in the fuel manufacturing process, as mentioned in Section 5.2.1, it is necessary to systematically evaluate

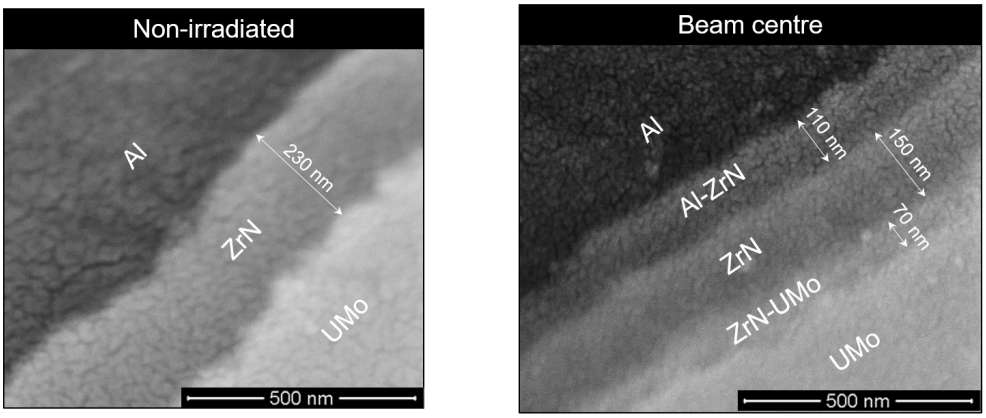

FIGURE 5.20: FE-SEM images of the 200 nm ZrN coated sample non-irradiated region (left) and the beam centre region (right). It shows clearly that after irradiation, two additional layers, i.e. an Al-ZrN intermixing layer and a ZrN-U-Mo intermixing layer formed at the interface around the ZrN coating.

TABLE 5.3: Compositional analysis of the interlayers

Interlayer	Al [at%]	U [at%]	Zr [at%]	N [at%]
Al-ZrN	55.41	-	15.94	28.65
ZrN	0.00	-	45.70	54.30
ZrN-U-Mo	0.00	59.90	40.10	-

the irradiation behaviour of this kind of fuel. With this intention, Al/ZrN/U-Mo tri-layer samples were prepared by PVD, after which artificial cracks were introduced in the ZrN coating. These samples were irradiated with 80 MeV ^{127}I under selected conditions. To properly reproduce the cracks that were found in the dispersion fuels, a cut-out sample of an as-fabricated SELENIUM fuel plate was first characterised. A picture of it is shown in Figure 5.22, where the dark fuel particles are visible in the bright Al matrix at the sample cross-section. This as-fabricated plate is a twin plate of U7MD1231 [144] prepared within the SELENIUM project, in which atomized U-Mo alloy particles are coated with 1 µm ZrN and dispersed in a pure Al matrix. The production of the coated particles for the SELENIUM plate has been reported in [144]. To characterise the ZrN coatings at different locations, the cut-out sample was further divided into four parts by a diamond wire saw, as illustrated in Figure 5.23. Each part was prepared by mechanical grinding and polishing for cross-sectional observations. The first grinding/polishing step aimed to remove the damage caused by sawing (∼1 mm).

The prepared cross-section samples were analysed by SEM. Figure 5.24 shows an overview of the fuel structure, where U-Mo particles with a size of several

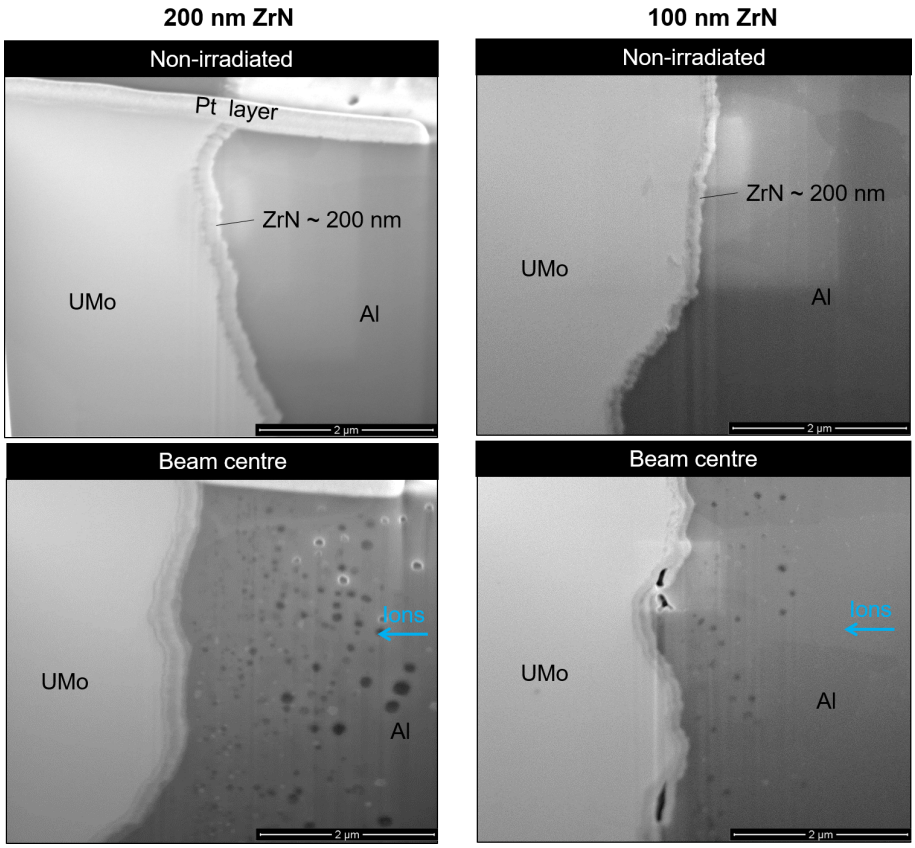

FIGURE 5.21: SEM images of the trenches milled in the 200 nm ZrN coated sample and the 100 nm ZrN coated sample. For each sample, a non-irradiated region and the beam centre region were taken for comparison purposes. Void formation was observed in the beam centre region of both samples.

tens of microns are distributed in the Al matrix. Some particles are round and covered by integral coatings as shown in Figure 5.25. Some particles however reveal deformation and show damage in the ZrN coatings. In general, three types of coating damage can be identified: (i) cracks in the ZrN coating of severely deformed particles (Figure 5.26) caused by high pressure; (ii) cracks in the ZrN coating on undeformed particles (Figure 5.27), probably caused by thermal expansion mismatch between coating and substrate during the fabrication; and (iii) coating delamination (Figure 5.28). The width of crack type (i) ranges from several hundreds of nanometres up to several micrometres, while the cracks of type (ii) are much thinner ($<$ 100 nm) and mostly show in the radial direction, i.e. perpendicular to the fuel kernel. Reproduction of cracks of type (i) and type (ii) are presented in Section 5.2.4.2. Delamination is the result of weak bonding of the ZrN coating to the particle surface. This type of damage was not addressed in this study.

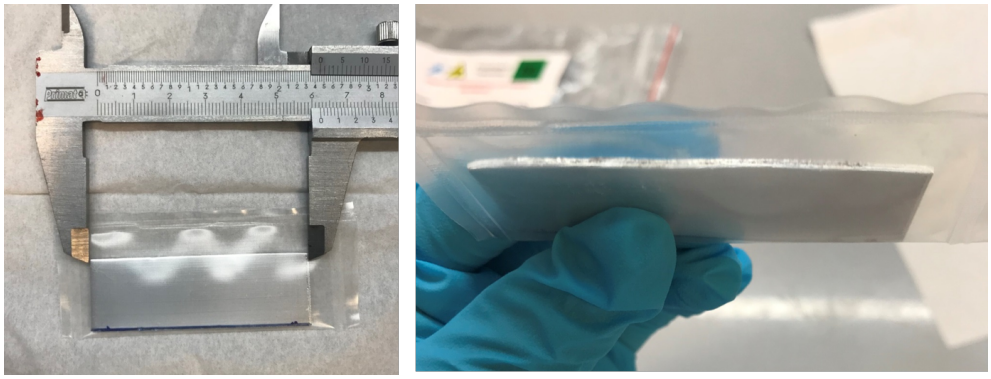

FIGURE 5.22: Photos of the cut-out sample from the as-fabricated fuel plate. The fuel particles (black) are visible at the cross-section.

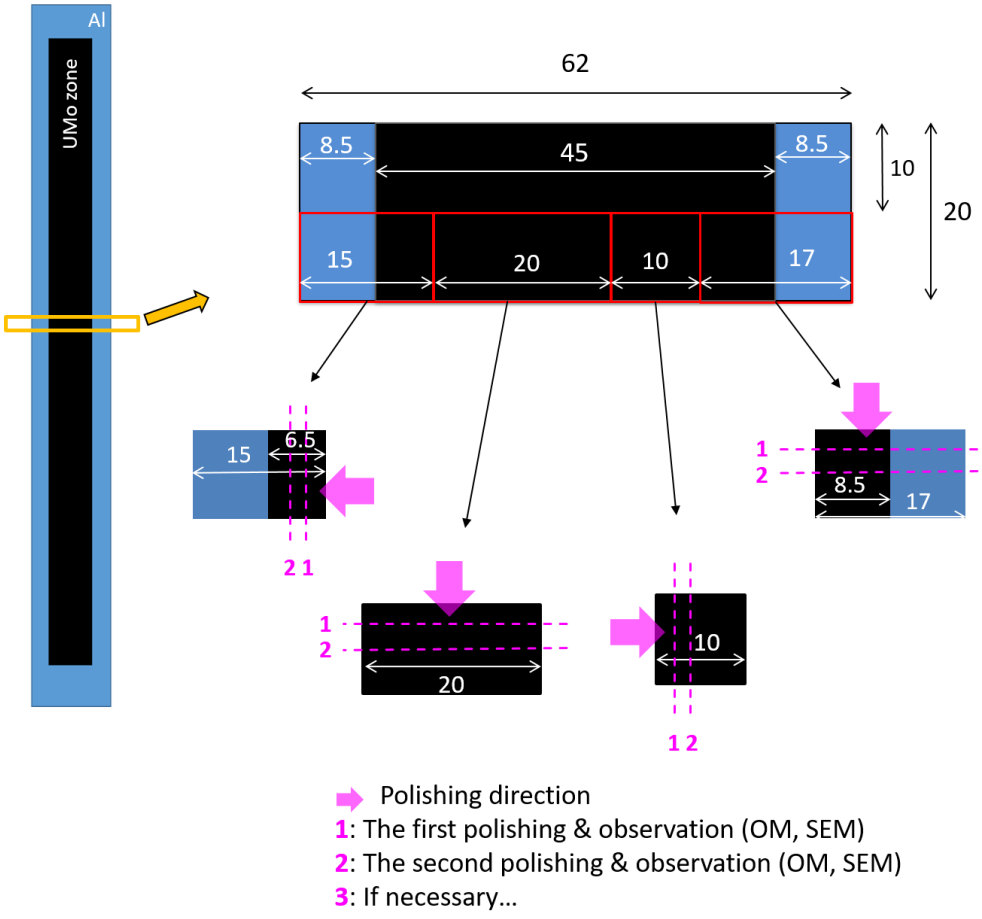

FIGURE 5.23: Schematic overview of the sample preparation for the characterisation of the ZrN coatings in a SELENIUM plate.

5.2.4.2 Crack reproduction and ion irradiation

In order to reproduce the crack of type (i) and (ii), numerous preliminary tests were undertaken (reported in [151]). It turned out that two approaches are suitable: local deformation using a Vickers hardness tester with a pyramidal diamond point and uniform pressing with a hydraulic press. The crack

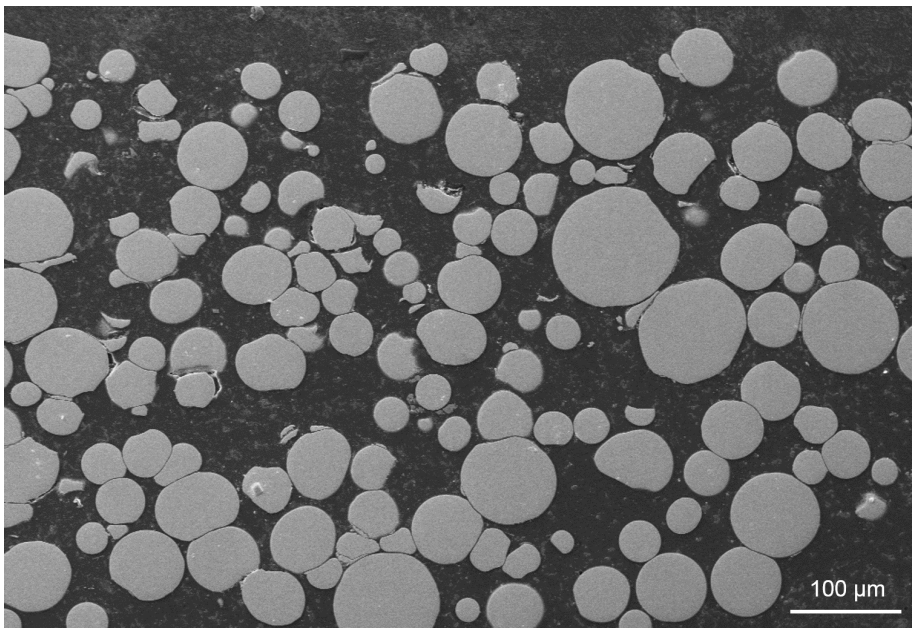

FIGURE 5.24: Overview of a cross-section sample.

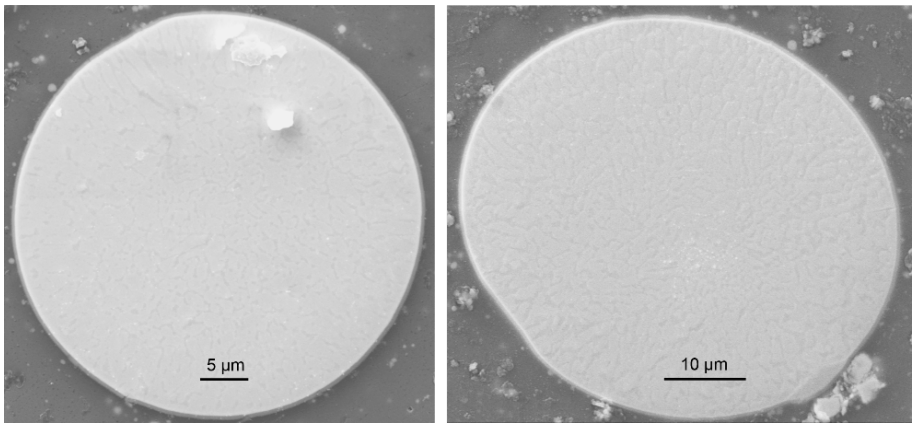

FIGURE 5.25: Undeformed spherical fuel particles surrounded by integral ZrN coatings.

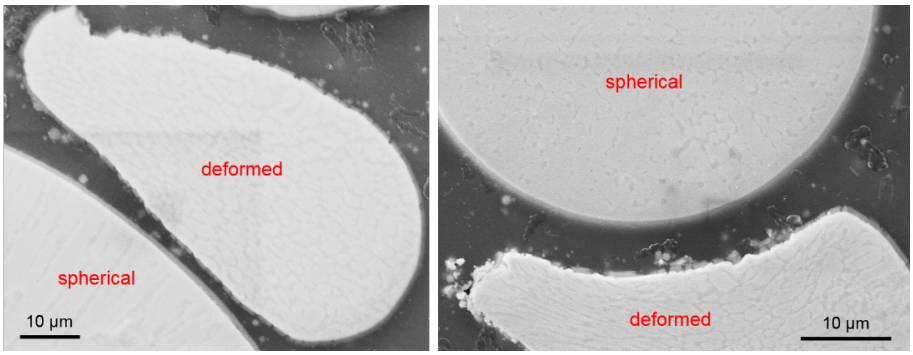

FIGURE 5.26: Crack type (i): cracks in the ZrN coating on severely deformed particles. As a comparison, no crack was observed in the coating of the neighbouring spherical particle.

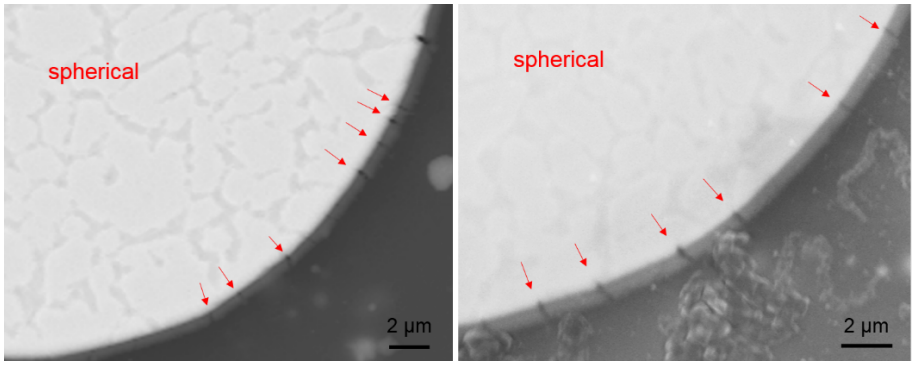

FIGURE 5.27: Crack type (ii): fine cracks in the ZrN coating of undeformed spherical particles.

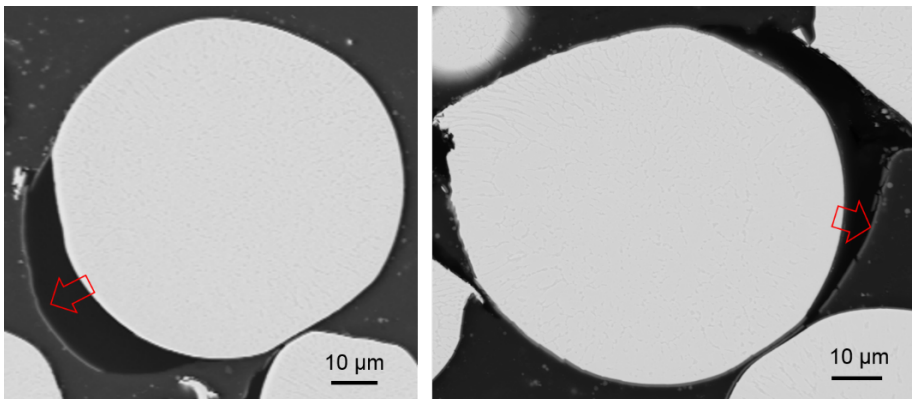

FIGURE 5.28: ZrN Coating delamination.

reproduction was performed on the ZrN coated U-Mo structure, i.e. before the preparation of the top Al layer.

Figure 5.29(A) shows an as-sputtered ZrN/U-Mo bilayer, where the initial ZrN coating is free of cracks. After the indention with the Vickers hardness tester at a hardness scale of HV5 (hardness scale), a wide crack formed in the centre of the indentation. This type of crack is called central crack. They normally have a width of $1-4$ µm and therefore represent crack type (i). Around the centre crack, fine cracks with a width typically $<$ 500 nm (mostly $<$ 100 nm) are generally observed, which presents the cracks of type (ii). Crack reproduction using the hydraulic press was performed at 100 bar, where the pressure was applied over an area of $\varnothing$ 5mm. As a result, the produced cracks are randomly distributed over the pressed area, with a width ranging from a few tens of nanometers to several microns, addressing crack type (i) and type (ii).

Eventually, five ZrN coated U-Mo samples with cracks in the coatings were prepared. Three of them were prepared using the Vickers hardness tester, and two of them were prepared using the hydraulic press. As the last step of

the sample preparation, these samples were coated with an 11 µm Al layer to complete the tri-layer structure.

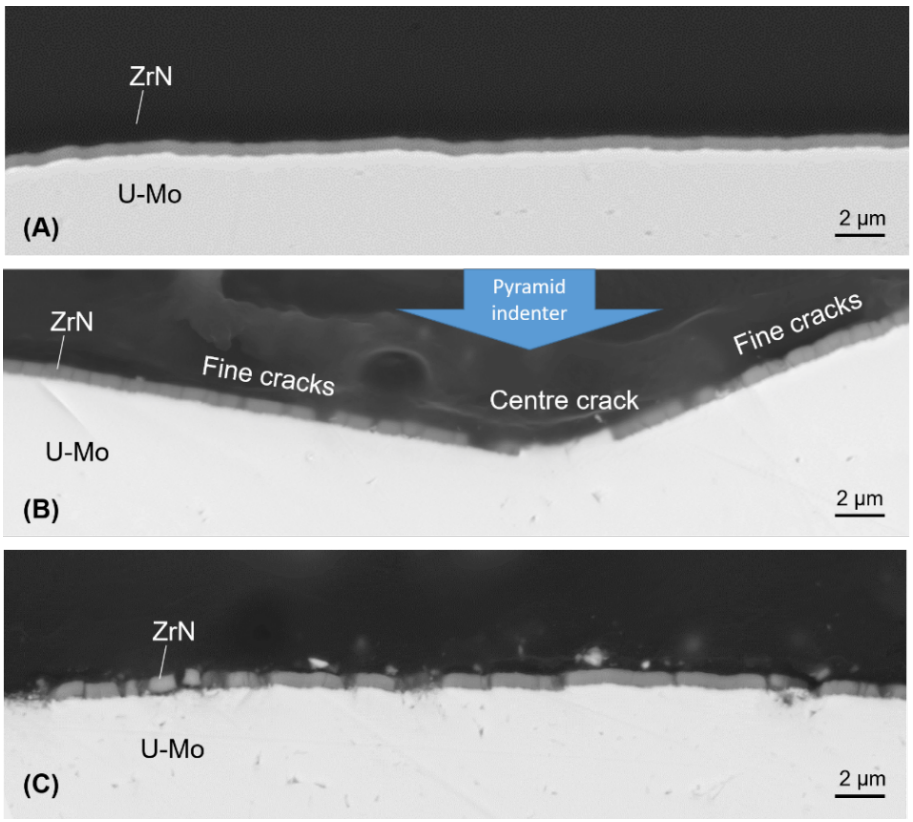

FIGURE 5.29: Cross-sectional SEM micrographs of (A) as-sputtered ZrN/U-Mo sample, (B) ZrN coated U-Mo sample with cracks in coating prepared with the Vickers hardness tester at HV5 (hardness scale) and (C) ZrN coated U-Mo sample with cracks in coating prepared with the hydraulic press at 100 bar applied over an area with a diameter of 5 mm.

During the ion irradiation experiment, these five samples were irradiated with 80 MeV ^{127}I under selected conditions as summarized in Table 5.4. After irradiation, all the samples were embedded into epoxy resin and then polished to reveal the cross-section through the ion beam centre. For instance, two samples prepared by the Vickers hardness tester and by the hydraulic press are shown in Figure 5.30(B) and Figure 5.30(C), representatively. An as-sputtered sample is shown in Figure 5.30(A) as a reference.

5.2.4.3 PIE Results

For each irradiated sample, different regions characterised by irradiation dose (ion fluence) were analysed to investigate the irradiation behaviour. In the samples prepared by the Vickers hardness tester, four Vickers indentations located respectively in the non-irradiated region, the low-fluence irradiated

TABLE 5.4: Irradiation parameters

Sample ID	Name	Thickness of the ZrN coating	Cracks made by	Temperature [°C]	Dose [Total ions]
S8-4	BV1	500 nm	Vickers	140	$1 \cdot 10^{16}$
S8-1	BV2	500 nm	Vickers	140	$2 \cdot 10^{16}$
S8-5	BV3	500 nm	Vickers	200	$1 \cdot 10^{16}$
S8-3	BP1	500 nm	Pressing	140	$1 \cdot 10^{16}$
S8-6	BP2	500 nm	Pressing	200	$1 \cdot 10^{16}$

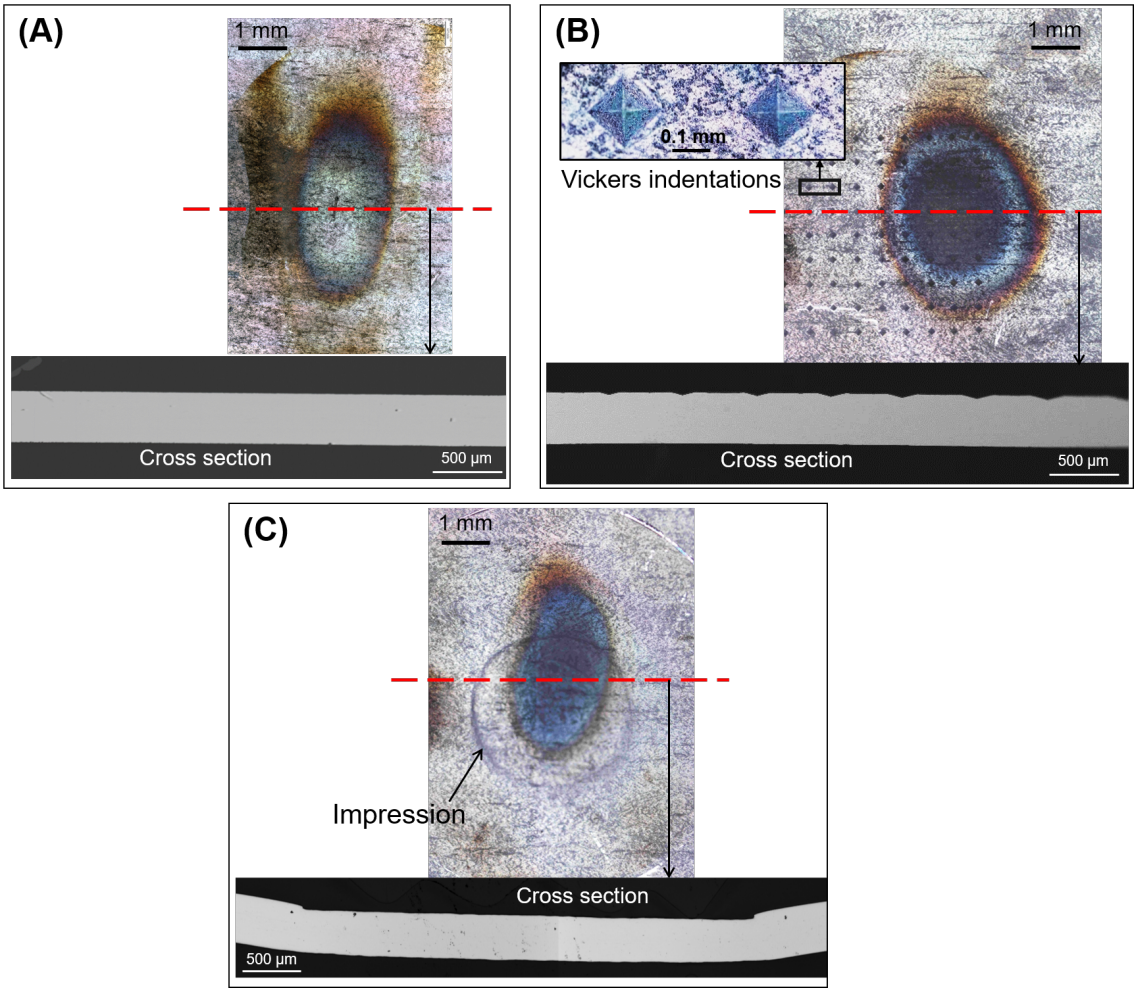

FIGURE 5.30: Cross-section preparation during PIE: (A) Sample without crack reproduction, (B) sample with cracks prepared by using the Vickers hardness tester, (C) sample with cracks prepared by using the hydraulic press. The beam footprints are shown on the sample surface after irradiation. The irradiated samples were embedded into epoxy and then polished until reaching the beam spot centre as indicated by the red dashed lines.

region, the middle-fluence irradiated region and the high-fluence irradiated

region (beam centre region) are selected for analysis. The local ion fluence and the average ion flux were calculated with the method presented in Chapter 3.

Sample BV1 was irradiated at 140 °C. As shown in Figure 5.31, region A (non-irradiated) shows cracks in the ZrN coating. No U-Mo-Al IDLs are found in this region as expected. A thin layer was observed under the ZrN coating, which was probably induced thermally during the PVD process. Still no IDLs are observed in region B (low-fluence irradiated). IDLs started to form from region C at the locations where the ZrN coating is missing. Besides, region C reveals fewer cracks compared to region A, which is probably due to the healing effect caused by irradiation enhanced diffusion bonding in the ZrN coating. In region D (high-fluence-irradiated), an IDL ~1 µm was built up at the location of the centre crack.

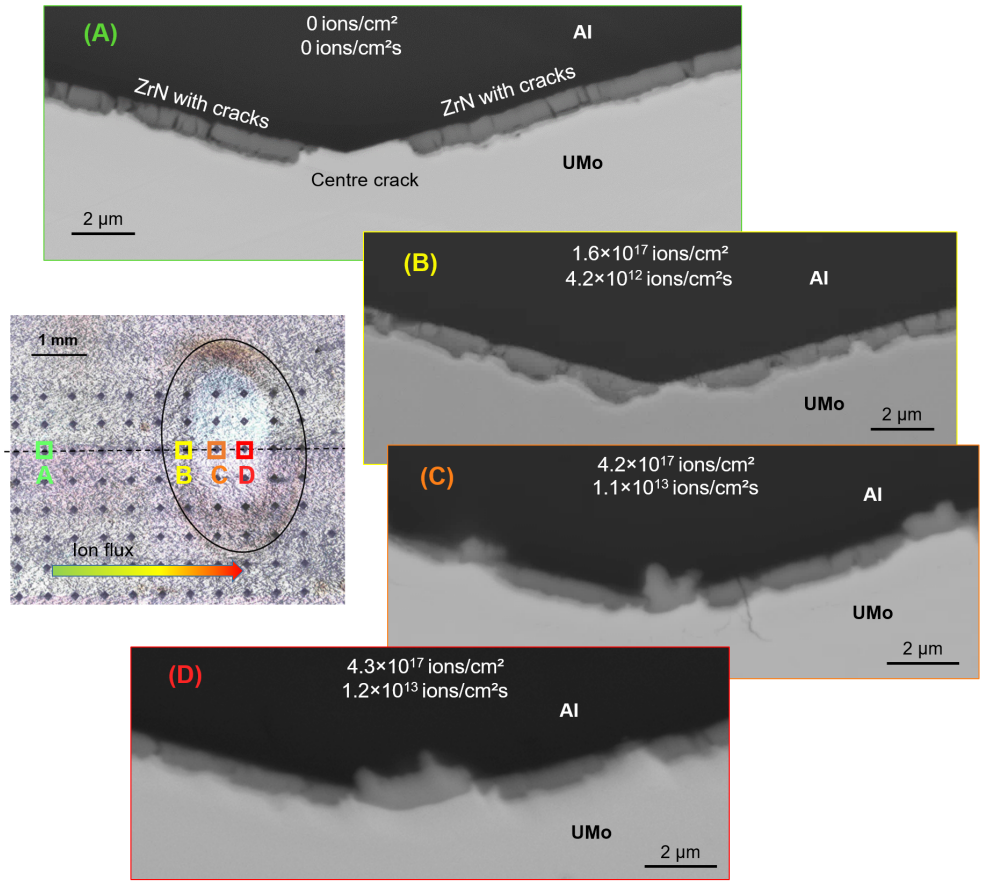

FIGURE 5.31: Sample BV1 after irradiation and the SEM image of (A) non-irradiated region, (B) low-fluence irradiated region, (C) middle-fluence irradiated region and (D) high-fluence irradiated region. The calculated local fluence and flux are indicated.

Sample BV2 was also irradiated at 140 °C but up to twice the total fluence (ions in total) of BV1. As shown in Figure 5.32, no IDLs are observed in region A as it was not exposed to the ion beam. In region B, the coating layer becomes

thinner and irregular, indicating that some interactions might have occurred. In region C, a U-Mo-Al IDL with the shape of a volcano is found at the position of the central crack. Further, two interlayers are recognised by EDX, i.e. the Al-ZrN intermixing layer and the remaining ZrN layer. Moving to region D, a U-Mo-Al IDL of ~4 µm formed at the position of the central crack, evidenced by EDX. An Al-ZrN intermixing phase is identified between the Al and the U-Mo, where no pure ZrN layer remains. Besides, some small peaks are shown next to IDL at the central crack, as indicated by the black arrows. Due to their limited volume, the chemical composition of the peaks cannot be analysed with the given technique. Based on the Z-contrast of the BSE image, these peaks are assumed to be the onset of the interaction between the U-Mo and the Al in the Al-ZrN intermixing phase.

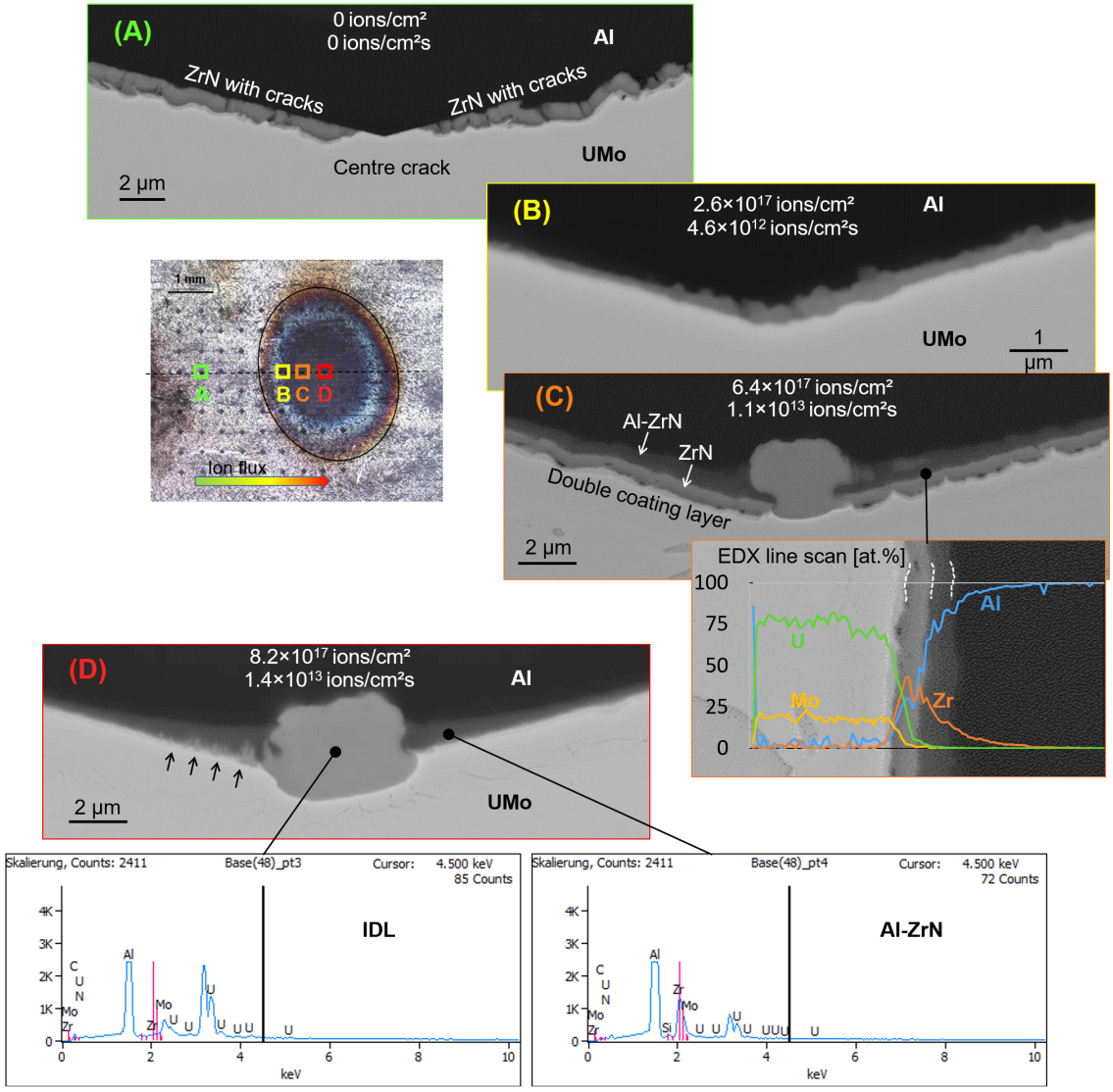

FIGURE 5.32: Sample BV2 after irradiation and the SEM image of (A) non-irradiated region, (B) low-fluence irradiated region, (C) middle-fluence irradiated region and (D) high-fluence irradiated region. The calculated local fluence and flux are indicated.

Sample BV3 was subjected to the same total fluence as sample BV1, but at a higher temperature, namely 200 °C, aiming to study the temperature effect. The PIE results are presented in Figure 5.33. A thin IDL is seen in the non-irradiated region A, which was probably generated during the sample production. In the low-fluence irradiated region B, only a thin IDL of ∼500 nm formed at the position of the central crack. No other IDLs are identified in this region. In region C, more and thicker IDLs developed at the coating cracks. Most of them have a volcano feature, being the result of the IDL grow dynamics: IDLs grew at the cracks and burst through them, resembling the volcanic eruption. The direction of the "eruption" is indicated by the curvature of the coating layer around volcano-like IDLs, which is likely from U-Mo to Al. A double coating layer consisting of an Al-Zr-N layer and the remaining ZrN coating layer is observed in this region as well. Besides, two island-like IDLs (circled in Figure 5.33C) are observed in region C. They are considered to be parts of other IDLs located in other planes deeper or higher than the observation plane. As shown in the high-fluence irradiated region D, the intensively generated IDLs (thickness ∼10 µm) completely breached the coating layer, directly establishing the contact of Al and U-Mo, which in turn accelerated the IDL growth. The growth of IDL consumed a large amount of Al. At some positions, the Al layer was completely used up. Eventually, the IDLs almost filled this deformed area. During this process, the torn ZrN coating in form of fragments was pushed into the formed IDL as shown in Figure 5.33D (circled in white), which again confirms that the Al-U-Mo diffusion was not through the coating layer, but rather through the cracks in it.

The pressed samples, i.e. sample BP2 and BP2, reveal randomly distributed cracks. As shown in Figure 5.34, only a few thin IDLs (circled) are found even in the beam centre region of BP1, which was irradiated at 140 °C. The EDX spectra identified the ZrN coating and the U-Mo-Al IDL by the amount of Zr. The detected Al in the ZrN coating is perhaps due to the interaction between ZrN and Al or the measurement resolution or both. No double coating layer was observed in BP1. Sample BP2 was irradiated at 200 °C, the cross-sectional SEM image reveals many volcano-like IDLs and the double coating layer structure. The curvature of the coating layer at the edges of the volcano-like IDLs and the distribution of the coating fragments agree to observation in BV3 (Figure 5.33D). No Al-U-Mo IDL occurs as long as the ZrN coating layer is still intact. Compared to the non-irradiated sample (Figure 5.29), the irradiated samples reveals much fewer cracks in the ZrN coating, which is perhaps due to the healing of fine cracks during irradiation.

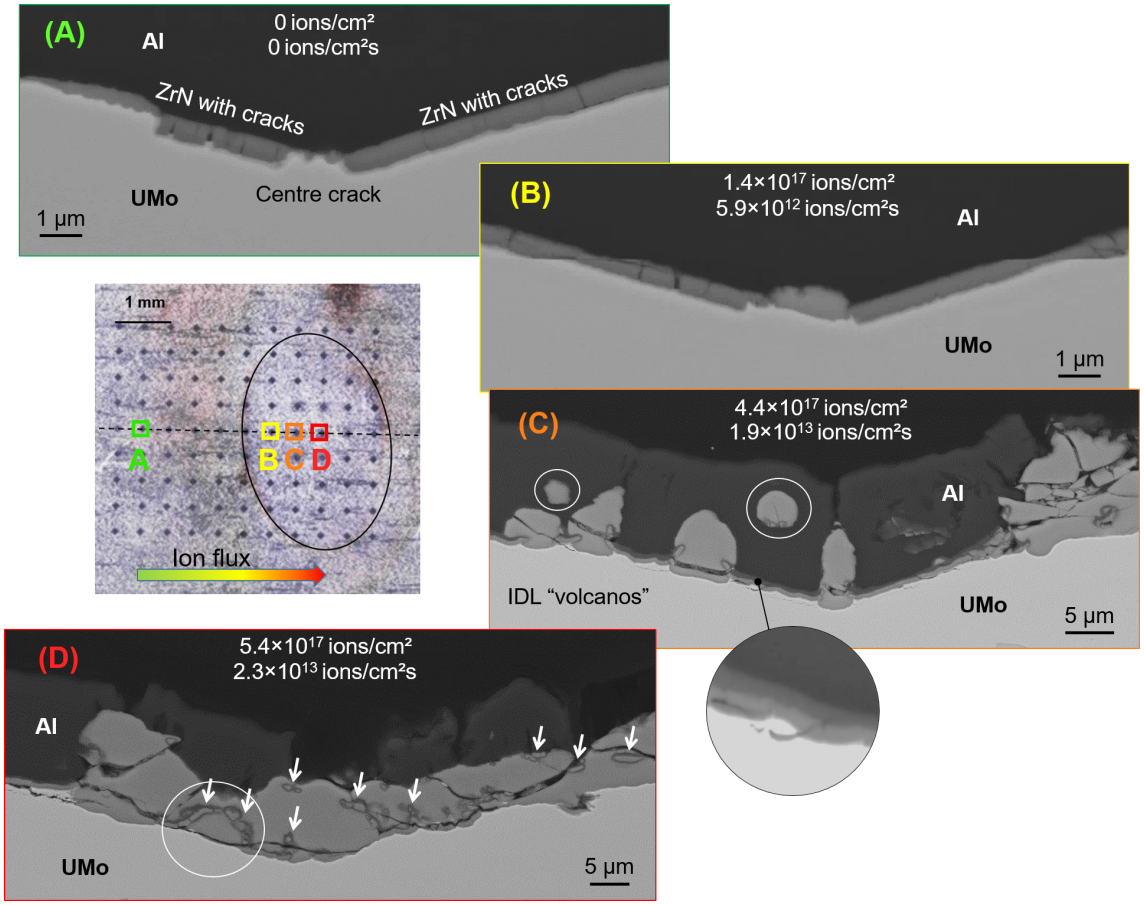

FIGURE 5.33: Sample BV3 after irradiation and the SEM image of (A) non-irradiated region, (B) low-fluence irradiated region, (C) middle-fluence irradiated region and (D) high-fluence irradiated region. The calculated local fluence and flux are indicated. The coating fragments are indicated by the white arrows. The circled coating fragments show the direction of the IDL eruption.

5.2.5 Discussion

The as-sputtered ZrN coatings show an integral structure. Three prepared Al/ZrN/U-Mo tri-layer samples i.e. S6-1, S5-3 and S6-4 with respectively 500 nm, 200 nm and 100 nm ZrN thickness were irradiated with 80 MeV ^{127}I ions to study the influence of coating thickness. During the PIE, it was found that the ZrN coatings in all three samples remain intact, as a result, no U-Mo-Al IDLs formed in these samples. The FIB/SEM analysis reveals that the coating layer reacted tardily[1] with Al and U-Mo under irradiation, resulting in an Al-ZrN layer and a ZrN-U-Mo layer, respectively. Void formation was observed in the Al layer of the beam centre region, which is unlikely caused by Kirkendall effect due to the arrangement of the voids.

The characterisation of an as-fabricated SELENIUM fuel plate shows that

[1]The reaction rate is much lower than the U-Mo-Al interaction.

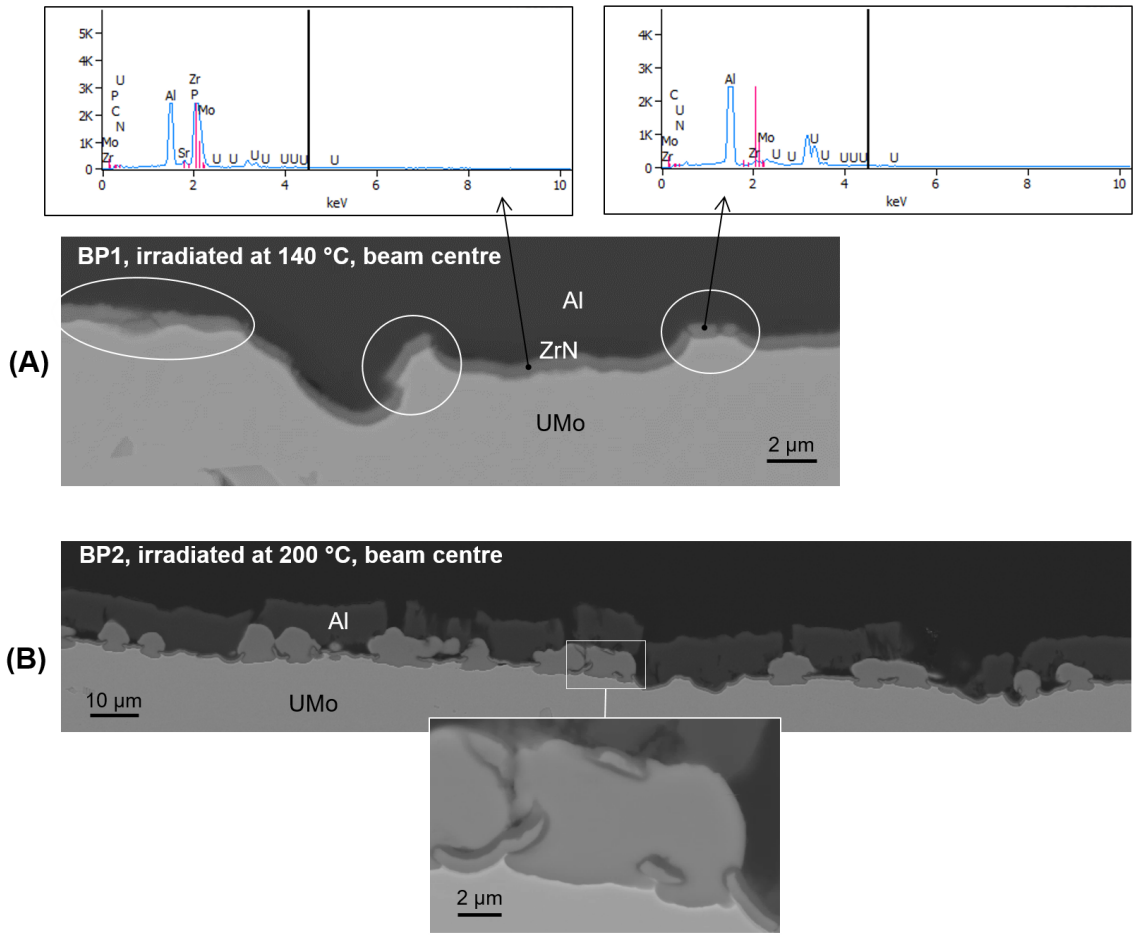

FIGURE 5.34: (A) SEM image of the beam centre region of BP1, where the U-Mo-Al IDLs were circled. EDX analysis distinguishes the ZrN coating and the IDL by the amount of Zr. The detected Al in the ZrN coating is perhaps due to the interaction between ZrN and Al or the measurement resolution or both. (B) The SEM image of the beam centre region of BP2 and an enlarged image of a volcano-like IDL. The double coating layer structure is clearly visible.

cracks consistently occur in ZrN coatings during dispersion fuel manufacturing. These cracks are hardly avoidable due to the brittleness of the ZrN coating. To study the irradiation behaviour of this kind of fuels, namely U-Mo fuels with cracks in the ZrN coatings, Al/ZrN/U-Mo tri-layer samples were prepared and irradiated with 80 MeV ^{127}I ions under different conditions, in which artificial cracks were produced in the ZrN coatings by using two methods, i.e. indentation by a Vickers hardness tester and pressing by a hydraulic press. The PIE results show that in the case of an intact and sufficiently thick ZrN coating layer, no interactions occur between the U-Mo and the Al. Nevertheless, similar to the three samples with intact ZrN coatings, the coating layer reacted tardily with the Al under irradiation, resulting in an Al-ZrN intermixing layer. By receiving a sufficiently high irradiation dose,

e.g. $8.2 \cdot 10^{17}$ ions/cm^2 (corresponds to a fission density of $8.6 \cdot 10^{20}$ f/cm^3), the ZrN coating can be completely consumed, establishing contact between the U-Mo and the Al in the Al-ZrN intermixing layer (Figure 5.32D). From a quantitative point of view, the 500 nm ZrN coating was completely consumed after being subjected to an ion fluence of $8.2 \cdot 10^{17}$ ions/cm^2 at an ion flux of $1.4 \cdot 10^{13}$ ions/ $\left(\text{cm}^2 \cdot \text{s}\right)$, which correspond to a fission density of $8.6 \cdot 10^{20}$ f/cm^3 and a fission rate of $1.5 \cdot 10^{16}$ f/ $\left(\text{cm}^3 \cdot \text{s}\right)$, respectively. The irradiation doses achieved in in-pile irradiations are usually much higher than those of ion irradiations. Nevertheless, it does not necessarily mean that a 500 nm thick ZrN coating will be totally consumed during in-pile irradiation when the fission density reaches $8.6 \cdot 10^{20}$ f/cm^3, because the irradiation dose rates of in-pile irradiations are usually much lower than that of ion irradiations.

Figure 5.35 compares the regions subjected to different irradiation conditions (indicated in the SEM images). The effect of ion fluence is visualized when comparing (A2) and (A3), as they were irradiated at similar ion fluxes but up to different ion fluences. By comparing (A4) with (A2), as well as (B3) with (B2), the temperature effect is clearly demonstrated. Further, the healing effect induced by irradiation is confirmed by comparing (A1) with (A2), as well as (B1) with (B2). In general, the following conclusions can be drawn:

- Some fine cracks (width $<$ 1 µm) in ZrN coating were healed during ion irradiation due to the irradiation enhanced diffusion bonding, which occurred between the Zr and the N atoms.
- ZrN coating layer interacted tardily with Al under irradiation, resulting in a double coating layer structure consisting of an Al-Zr-N layer and the remaining ZrN coating layer.
- With a sufficiently high irradiation dose, the ZrN coating can be completely consumed by reacting with Al. Consequently, the U-Mo touched the Al-ZrN intermixing layer and started to interact with the Al in it, resulting in the formation of U-Mo-Al IDL in the form of peaks.
- The development of IDL is much more intensive at 200 °C than at 140 °C. This effect can be well explained with the Arrhenius correlation of the IDL growth model as presented in Equation 3.4 of Chapter 3.
- Under a sufficiently high temperature, IDL breached the coating layer through the cracks, resulting in a volcano feature. The direction of the curvature of the coating layer at their edges and the distribution of the

coating fragments both indicate the direction of "eruption", which is likely from the U-Mo to the Al.

- The excessively growing IDL could cause detachment and tearing of the coating.
- On the whole, ZrN is considered a promising candidate for diffusion barriers in U-Mo/Al fuels as its presence (not damaged) can effectively suppress the IDL growth, which helps to delay the abnormal fuel swelling. Even with cracks in the coating, the IDL growth is still well restrained compared to that in the uncoated U-Mo/Al samples irradiated under similar conditions, such as sample S3-2 in 3.

Transferring this to in-pile irradiations, it should be kept in mind that the maximum ion irradiation dose achieved here is equivalent to the fission density of the early stage of in-pile irradiation, i.e. around 10% of maximum in-pile target burn-up, while the equivalent fission rate presented here reaches $\sim$ 20 times of the values seen during the first days of E-FUTURE [86] and SELENIUM [25] in-pile irradiation. In the SELENIUM test, three typical ways of IDL formation surrounding the fuel kernels were identified as shown in Figure 5.36 (A1 - A3), i.e. double coating layer, IDL volcano formation at a crack and IDL formation under the coating layer. These types of IDL formation were also found in the later performed SEMPER FIDELIS in-pile test, as shown in Figure 5.36 (B1 - B3). In this study, All three types of IDL formation were reproduced by heavy ion irradiation, as evidenced in Figure 5.36 (C1 - C3). It should be emphasized that during ion irradiation, the ions impinge on the Al surface from outside. During in-pile irradiation, the fission products originate from U-Mo and are emitted isotropically, resulting in an irradiation direction of from U-Mo to Al. Nevertheless, the ion irradiations of uncoated U-Mo/Al samples presented in Chapter 3 have proven that the irradiation direction has no noticeable effect on the IDL growth dynamics, if the maximum nuclear energy loss of the incoming ions occurs near the U-Mo/Al interface. Thus, the IDL growth dynamics at the cracks where the protection of ZrN coating is absent should also not be affected by the reversed irradiation direction. Indeed, the way of IDL "eruption" induced by ion irradiation at the coating cracks well resembles the one observed in those two in-pile tests, despite the opposite irradiation direction, as shown in Figure 5.36 (A2), (B2) and (C2). Further, the arrangement of the double coating layer structure, i.e. the Al-ZrN interaction layer and the remaining ZrN coating layer, is also consistent with the one observed in SELENIUM [25] and SEMPER FIDELIS in-pile tests [139][140], as shown in Figure 5.36 (A1), (B1) and (C1). It has

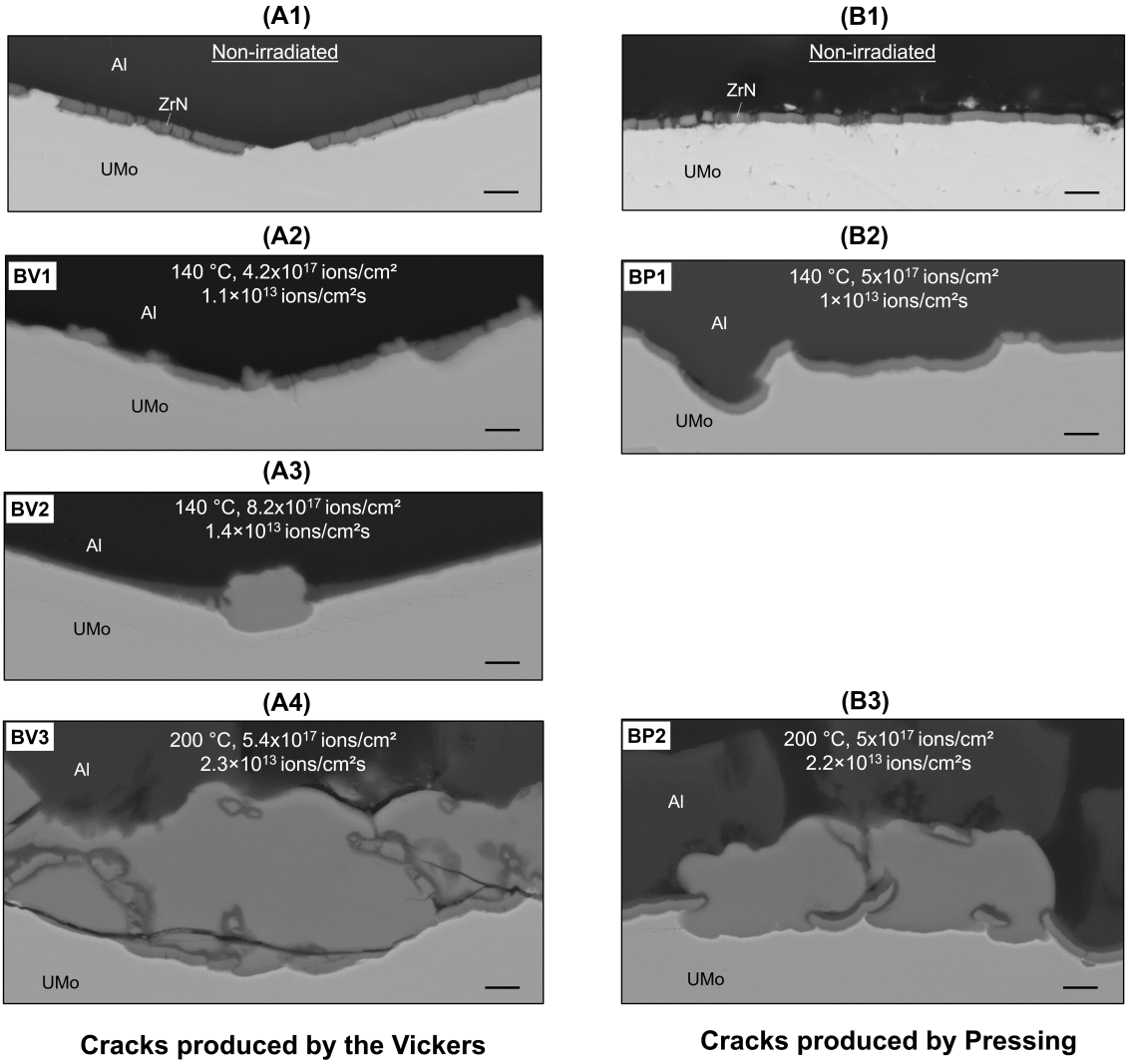

FIGURE 5.35: (A1) - (A4): regions with cracks made by the Vickers hardness tester. The irradiation conditions are indicated for each region. (B1) - (B3): regions with cracks made by using the hydraulic press. The irradiation conditions are indicated in the images. All the regions are displayed at the same magnification for comparison purposes. Scale bar: 2 µm.

been confirmed in [145] that the IDL formation under an intact coating layer in SELENIUM test is caused by a crack (or cracks) located in another plane. For the ion irradiated sample, no IDL formed completely under an intact coating layer in the plane of observation. However, as shown in Figure 5.36 (C3), if the observation was taken at the position of the dashed line and perpendicularly to the current observation plane, a fully covered IDL would be displayed like the one found in SELENIUM and SEMPER FIDELIS in-pile tests.

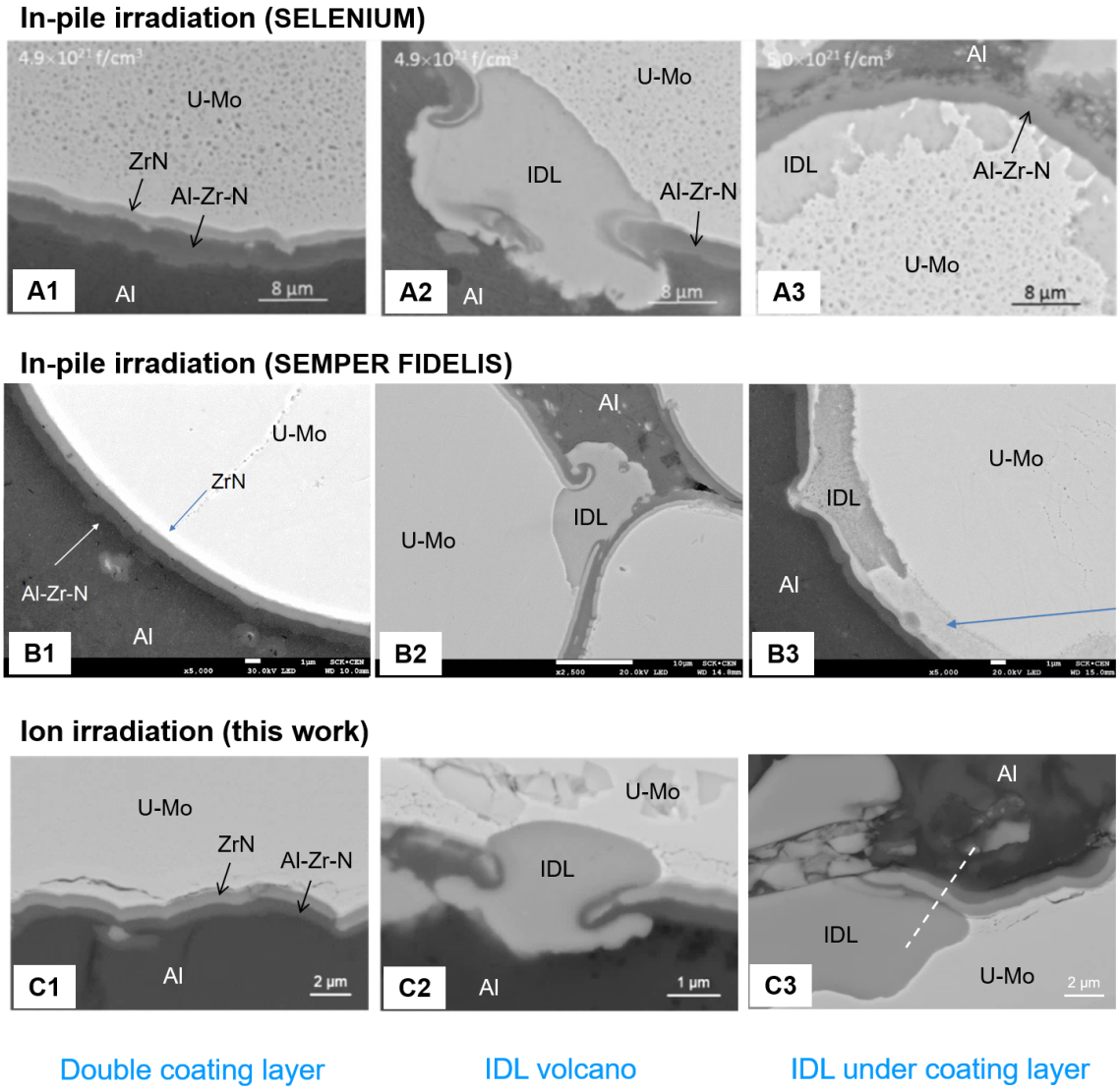

FIGURE 5.36: (A1), (A2) and (A3) present the three types of IDL found in the in-pile irradiated SELENIUM plate, i.e. double coating layer, IDL volcano formation at crack and IDL formation under the coating layer, respectively (images are taken from [24]). Similar results were obtained in SEMPER FIDELIS test, as shown in (B1), (B2) and (B3) (images are taken from [139] and [140]). The three types of IDL were successfully reproduced by ion irradiation in this study, shown in (C1), (C2) and (C3). In (C3), a part of the IDL lies under the coating layer. If the observation was taken at the position of the dashed line and perpendicularly to the current cross-section plane, a fully covered IDL would be displayed.

Chapter 6

U-Mo fuel restructuring induced by heavy ion irradiation

6.1 Restructuring in in-pile irradiated U-Mo

In-pile irradiated U-Mo reveals a restructuring i.e. grain refinement triggered at a certain fission density. This phenomenon is caused by accumulation of fission products as well as radiation induced defects. The resulted finer grains of sub-micron size accelerates the gas bubble growth kinetics and eventually speed up the fuel swelling [152][153]. In monolithic U-10Mo fuel, the restructuring usually starts at grain boundaries (GBs) at a fission density of $\sim 3.0 \cdot 10^{21}\,\mathrm{f/cm^3}$ and finished at $\sim 6.3 \cdot 10^{21}\,\mathrm{f/cm^3}$ [154][155]. In dispersion U-7Mo fuel, this effect is triggered at $\sim 2.1 \cdot 10^{21}\,\mathrm{f/cm^3}$, occurring at cell boundaries that are depleted in Mo. A fully restructured U-Mo microstructure is observed at a fission density of $\sim 4.9 \cdot 10^{21}\,\mathrm{f/cm^3}$ [25]. The earlier onset of the restructuring in dispersion fuels is found attributed to the lower Mo content at cell boundaries [25]. As explained in [156], GBs or cell boundaries can accumulate dislocations by inhibiting their motions, providing nuclei for polygonization. This phenomenon is often referred to as recrystallization in previous publications, which originally describes the phenomenon when cold worked metals are heated, new grains form and grow which consumes the cold worked portion [157]. Yet, from the perspective of metallurgical phenomenology, two underlying mechanisms for irradiation induced restructuring should be distinguished: recrystallization and polygonization, of which the newly formed sub-grains are separated by high-angle GBs and low-angle GBs, respectively. Jadernas et al. [158] pointed out that the grain subdivision in the irradiated U-Mo fuels was driven by polygonization rather than recrystallization.

6.2 Reproduction of U-Mo restructuring by heavy ion irradiation

To study this phenomenon, the fuel restructuring behaviour i.e. grain refinement should be reproduced. Taking advantage of the high irradiation dose rate, heavy ion irradiation is able to reach the threshold dose on short laboratory time scales and without activating the sample. The feasibility of inducing restructuring by ion irradiation has been demonstrated in amorphous MoNi and Fe-Cr-Ni-W alloys by Brimhall [159] in 1984.

In this study, ion irradiation was performed on an uncoated U-10Mo foil sample with ^{127}I ions at 80 MeV at 140 °C, which respectively represent the fission fragments (as explained in Chapter 2) and represents the estimated fuel peak temperature (as explained in Chapter 4). During irradiation, the sample was exposed to a Gaussian ion beam with an incident angle of 0°. The ion flux as well as the resulting ion fluence has a bivariate Gaussian distribution over the irradiated area of the sample.

SRIM/TRIM calculations were conducted to estimate the ion range and the energy loss along the incident ion trajectory. As shown in Figure 6.1, most ions rest at a path length of 5 µm, where the Bragg peak of nuclear energy loss also occurs. Consequently, the most irradiation damage is expected to be seen at this depth.

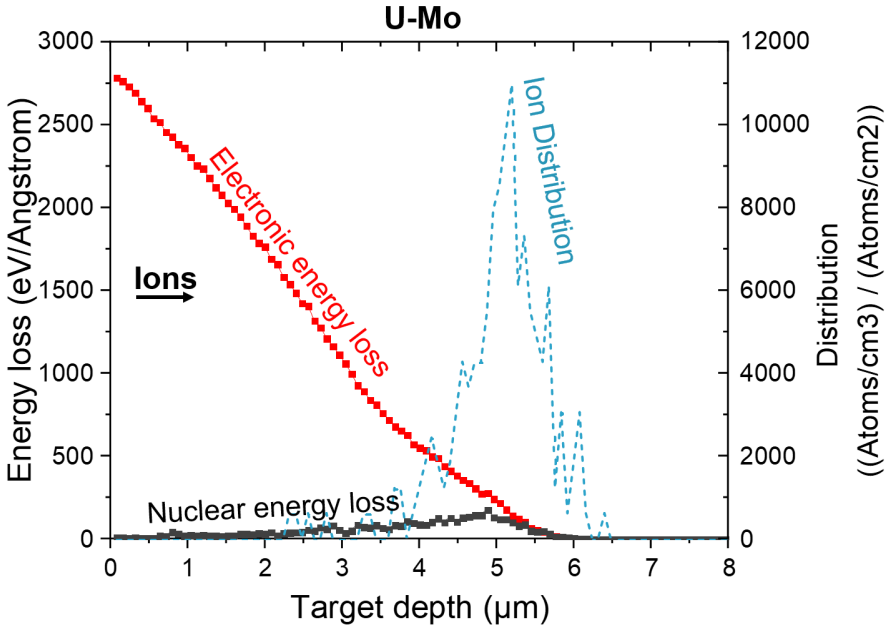

FIGURE 6.1: SRIM/TRIM calculated energy loss and ion range distribution of 80 MeV ^{127}I in an uncoated U-10Mo.

Prior to the ion irradiation, the oxides on the sample surfaces were removed by chemical de-oxidation using the method presented in [160]. During the ion irradiation, two electrical discharge sparks occurred, which divided the 44-hour-irradiation into three sub-irradiations with three individual but interfering ion beam spots, i.e. BS1, BS2 and BS3. Table 6.1 summarizes the irradiation conditions of each sub-irradiation, including the maximum ion fluence and flux occurring at each beam centre.

TABLE 6.1: Irradiation parameters

Sub-irradiation	Beam spot	Irradiation duration [h]	Total number of implanted ions	Ion fluence at beam centre [ions/cm^2]	Ion flux at beam centre [ions/cm^2]
1	BS1	9.0	$9.78 \cdot 10^{15}$	$6.7 \cdot 10^{15}$	$2.1 \cdot 10^{11}$
2	BS2	11.5	$2.11 \cdot 10^{16}$	$3.1 \cdot 10^{17}$	$7.4 \cdot 10^{12}$
3	BS3	23.5	$3.65 \cdot 10^{16}$	$2.0 \cdot 10^{18}$	$2.4 \cdot 10^{13}$

The beam profiles were captured by a CCD camera during each sub-irradiation (Figure 6.2A), from which the ion intensity distributions in arbitrary units are visualized by 3D surface plot in Figure 6.2A. Figure 6.2B shows an image of the sample right after irradiation. After removing the steel mask, the three beam spots are marked on the irradiated sample, as shown in Figure 6.2C.

For each sub-irradiation, the beam current was measured and the total ion number received during this sub-irradiation was calculated. Together with the obtained beam intensity distribution, the 3D ion flux profile and the ion fluence profile were reconstructed with the approach explained in Chapter 3. The final ion fluence distribution is given by the superposition of the fluence profiles of the three sub-irradiations. The three beam centres lie very close together. In order to characterise the microstructure and evaluate the irradiation effect, a cross-section along line 1 through the beam centres was selected, as indicated in Figure 6.3. To prepare the cross-section, the irradiated sample was first cut with a rotating blade microtome along the cutting line (also indicated in Figure 6.3) to get close to the beam centres. The sample was then vertically embedded in a resin and mechanically polished until reaching line 1, where the PIE was undertaken.

To enable quantitative analysis, e.g. the dependence of the microstructure on the irradiation dose, the spatial distribution of irradiation dose (ion fluence in case of ion irradiation) along the cross-section of line 1 should be determined. line 1 vertically cuts through the three Gaussians close to their maximum,

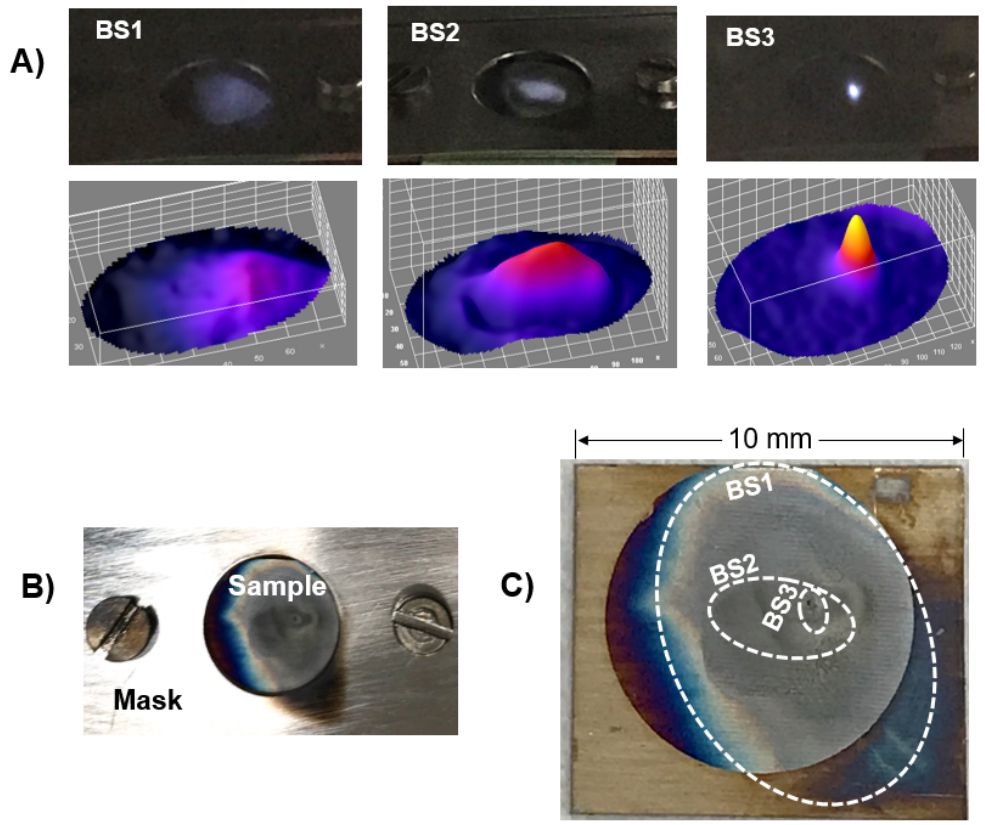

FIGURE 6.2: A) Images of the three ion beam spots with their intensity distributions in arbitrary units. B) Image of the sample right after irradiation. The steel mask for fixing the sample was not yet removed. C) Irradiated sample with the three beam spots (BS1, BS2 and BS3) marked on it.

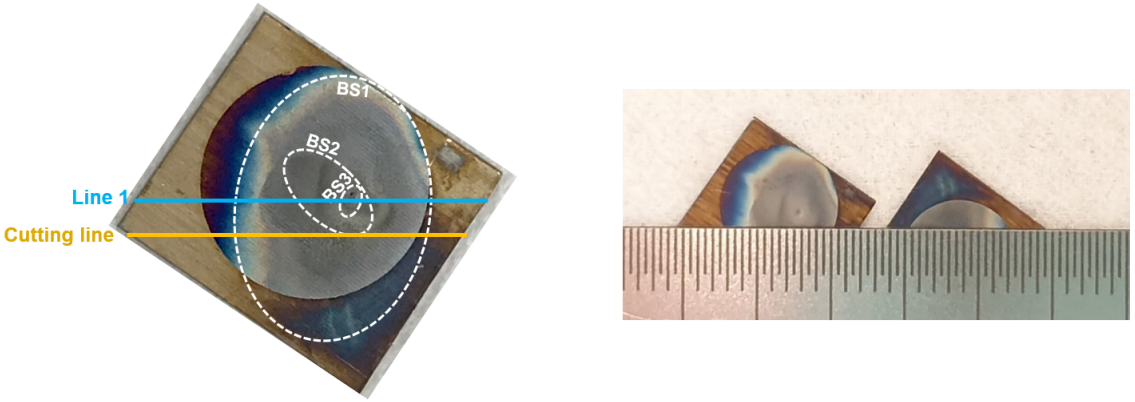

FIGURE 6.3: Cutting line and polishing line (line 1) shown on the irradiated sample.

leading to three superposed univariate Gaussians on the cross-section plane of line 1. To obtain a final fluence profile on this plane, the 1D ion fluence distribution of each sub-irradiation along line 1 was individually determined based on the reconstructed 3D ion fluence profile over the irradiated area. A final fluence distribution along line 1 is obtained by superposition of the three 1D fluence profiles. A conversion from ion fluence to fission density equivalent

was performed with the correlation 3.3 as explained in Chapter 3. Thus, a total ion dose distribution (ion fluence or fission density equivalent) along line 1 is established in Figure 6.4. The maximum irradiation dose of $\sim 2.1 \cdot 10^{18}$ ions/cm^2 as well as the corresponding fission density equivalent of $\sim 3.7 \cdot 10^{21}$ f/cm^3 occurs at the beam centre of BS3, where the coordinate is set to x = 0 mm. This location is referred to as beam centre in the following text.

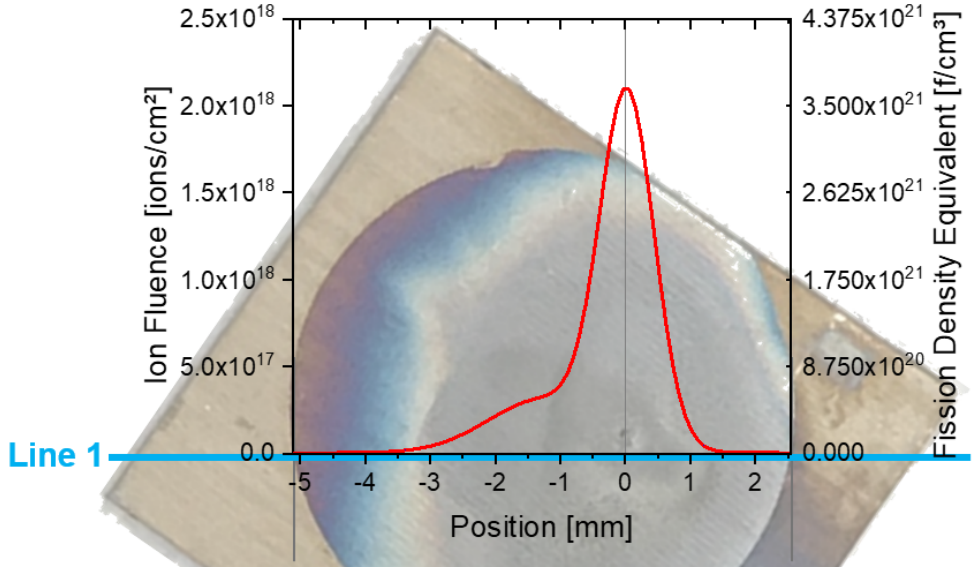

FIGURE 6.4: Reconstructed ion dose profile along line 1. The location of the maximum fluence or equivalent fission density occurs is set to x = 0 mm.

Further, the dpa distribution on the cross-section was calculated with the method explained in Section 2.4.3 to evaluate the irradiation damage. Figure 6.5 shows the dpa distribution in the cross-section plane in form of 3D plot. Line 1 and the irradiation direction are indicated. It shows that damage peak occurs at an ion penetration depth of ~5 µm.

It has been pointed out in [161] that irradiation temperature affects the grain structure of fuel materials. It is therefore necessary to know the temperature distribution along line 1 under irradiation. During irradiation, the presented temperature of the sample had three contributions: (i) heating of the copper stage by an electrical heating wire fixed on the side of the stage; (ii) automatically adjusting cooling on the backside of the stage; and (iii) ion beam power. The ion beam power stayed almost constant for each sub-irradiation. By adjusting the heating/cooling power, the sample temperature was maintained at 140 °C. The irradiation temperature was measured with a thermocouple clamped on the sample next to the beam spot. As a reference, the stage temperature was measured at the top of the stage. A small amount of thermally conductive

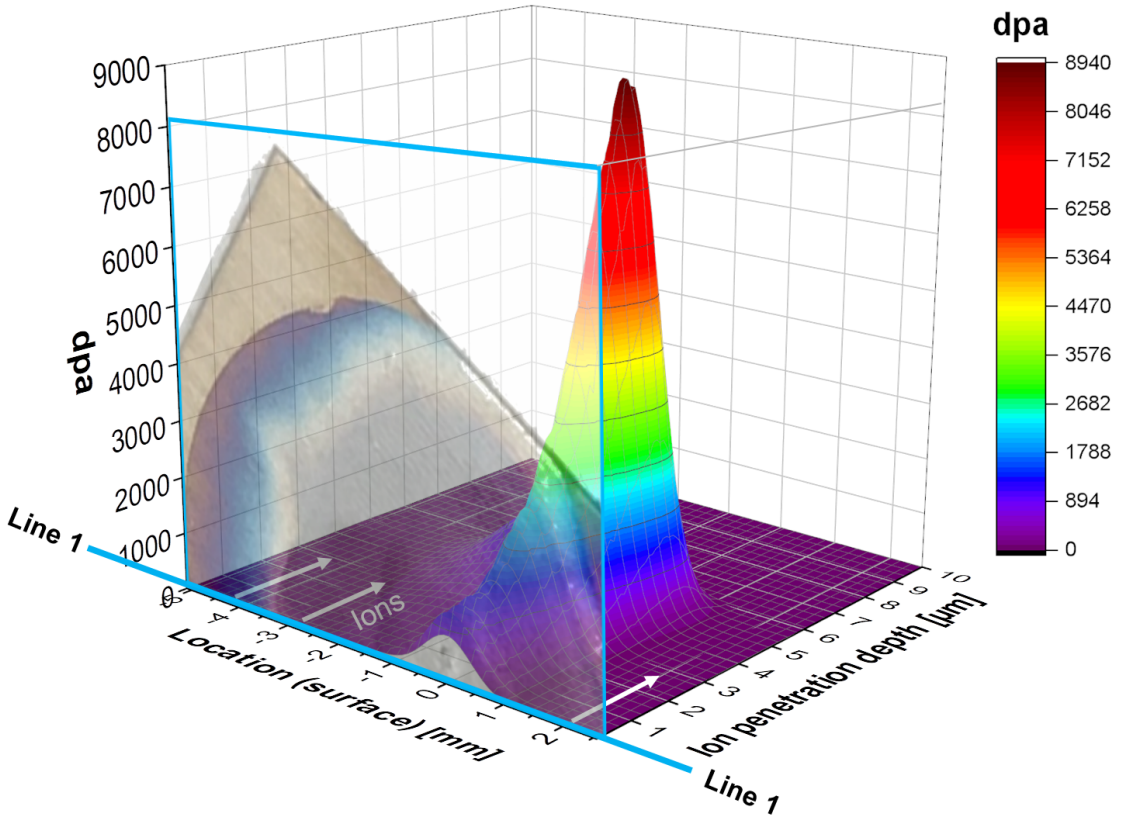

FIGURE 6.5: 3D plot of dpa distribution in the cross-section plane. Line 1 and the irradiation direction are indicated.

paste (TCP) with a thermal conductivity of 2.5 W/(m K) was applied between the sample and the stage to improve the thermal contact.

COMSOL Multi-physics finite element method (FEM) [162] was used to perform the simulation. During the simulation, it was assumed that the beam current was held constant at 400 nA, which is the average beam current measured during irradiation. The option "Thin Thermally Resistive Layer" was used to model the multiple layers structure, i.e. U(Mo) sample - thermally conductive paste - copper stage. The parameters for the FEM simulation are summarized in Table 6.2. Figure 6.6 shows the simulation of the steady-state temperature distribution. The estimated temperature at the beam centre was determined to be $\sim$ 160 °C, which is 20 °C higher than the temperature at the beam edge. The calculated stage temperature was $\sim$ 133 °C, which agrees with the measurement taken at the top of the stage (indicated in Figure 6.6). Those temperature differences are not expected to have noticeable impacts on fuel restructuring based on the experience gained from in-pile tests on U-Mo. For instance, the irradiation temperatures differed by the order of few tens of degrees for

SELENIUM and SELENIUM-1a in-pile irradiation tests, which did not affect the grain refinement kinetics as concluded in [77].

TABLE 6.2: Parameters for the FEM simulation

Parameter	Value
Power of the Gaussian beam	4.6 W
Average Gaussian width	∼1 mm
Density of U-10Mo	17.2 g/cm^3 [163]
Thermal conductivity of U-10Mo	14W/(mK) at 140 °C [164]
Specific heat capacity of U-10Mo	0.143 J/(mol K) at 140 °C [164]
Thermal conductivity of the TCP	0.143 J/(mol K)
Heating Power of the heating element	35 W

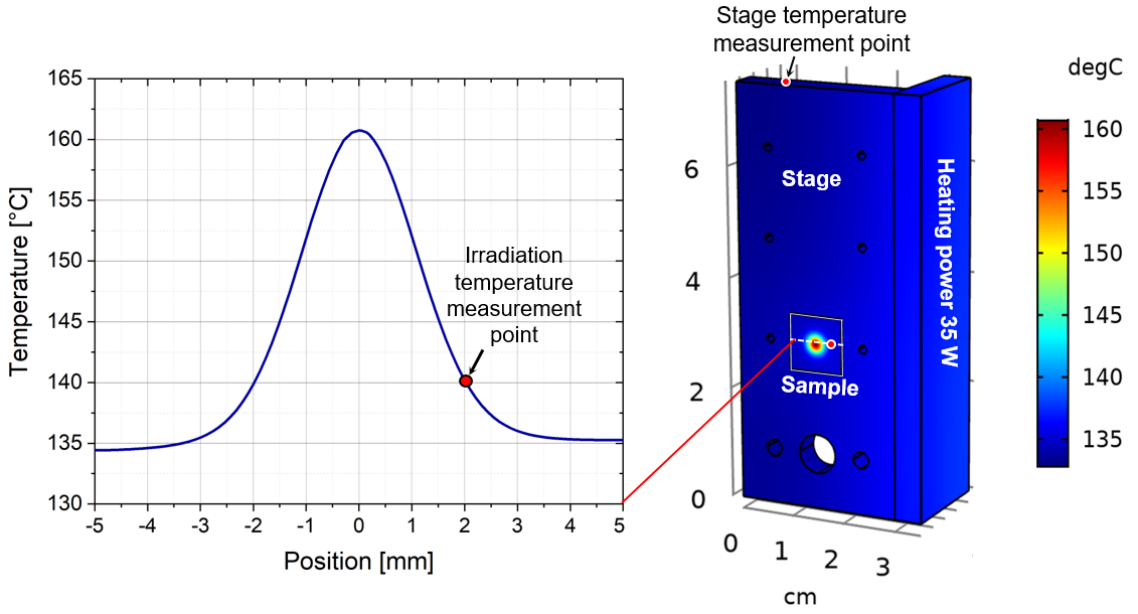

FIGURE 6.6: Simulation of steady-state temperature distribution using COMSOL Multi-physics finite element method. One-dimensional temperature distribution across the sample is shown on the left. The two temperature measurements points are indicated.

6.3 SEM analysis

To characterise the microstructure, SEM observations and EBSD analyses were performed on the prepared cross-section with a Thermo Scientific™ Scios™ DualBeam™ equipped with SE, BSE, EDS and EBSD detectors.

SEM micrographs were taken across the irradiated area in order to obtain a general overview of the cross-section. Figure 6.7 presented the BSE images

taken from regions subjected to different ion fluences. The location of analysis is represented by the coordinate of the axis along line 1 (beam centre is located at x = 0) and indicated on the top left. The local ion fluence is indicated on the top right. Images with a higher magnification were taken from those regions to show the microstructure with more details. Additionally, an image taken from a non-irradiated region is shown as well to reveal the microstructure without irradiation. Oxides were identified as irradiation-induced damage as they only appear in the irradiated regions and show a dependence on ion fluence, i.e. the higher ion fluence the region was subject to, the more and thicker oxides grew. The maximum intensity of oxidation was reached at the beam centre. Besides, the oxide layers grew irregularly, resulting in a wave-like distribution on the sample surface with a layer thickness up to ∼3 µm. Moreover, cracks formed in the beam centre region below the oxide layers.

6.4 EBSD analysis

6.4.1 Sample preparation

For some metals, mechanical polishing can produce good EBSD patterns. However, it fails to produce results out of U-Mo as shown in Figure 6.8 (left). Besides, the mechanically polished surface often exhibits defects in terms of scratches which can disturb the EBSD analysis. In this case, it is necessary to use another step to improve pattern quality. It has been found that ion polishing can remove residual lattice damage and contamination on the nanoscale. For instance, U-Mo oxidises rapidly when exposed to air, and the formed oxide layer can be easily removed by ion polishing. Thus, prior to the EBSD acquisition, ion polishing was performed by FIB in the same device using an ion beam of 5 nA in current and 30 kV in voltage under a 3°glancing angle. This combination of parameters has been proven to have the best result in terms of surface quality and milling time. This way, a clean and flat surface of the investigated cross-section is prepared for EBSD analysis. As was shown in Figure 6.8, the diffraction pattern quality is significantly improved after ion polishing. The determination of the crystal orientation and the characterisation of grain boundaries are presented in the following.

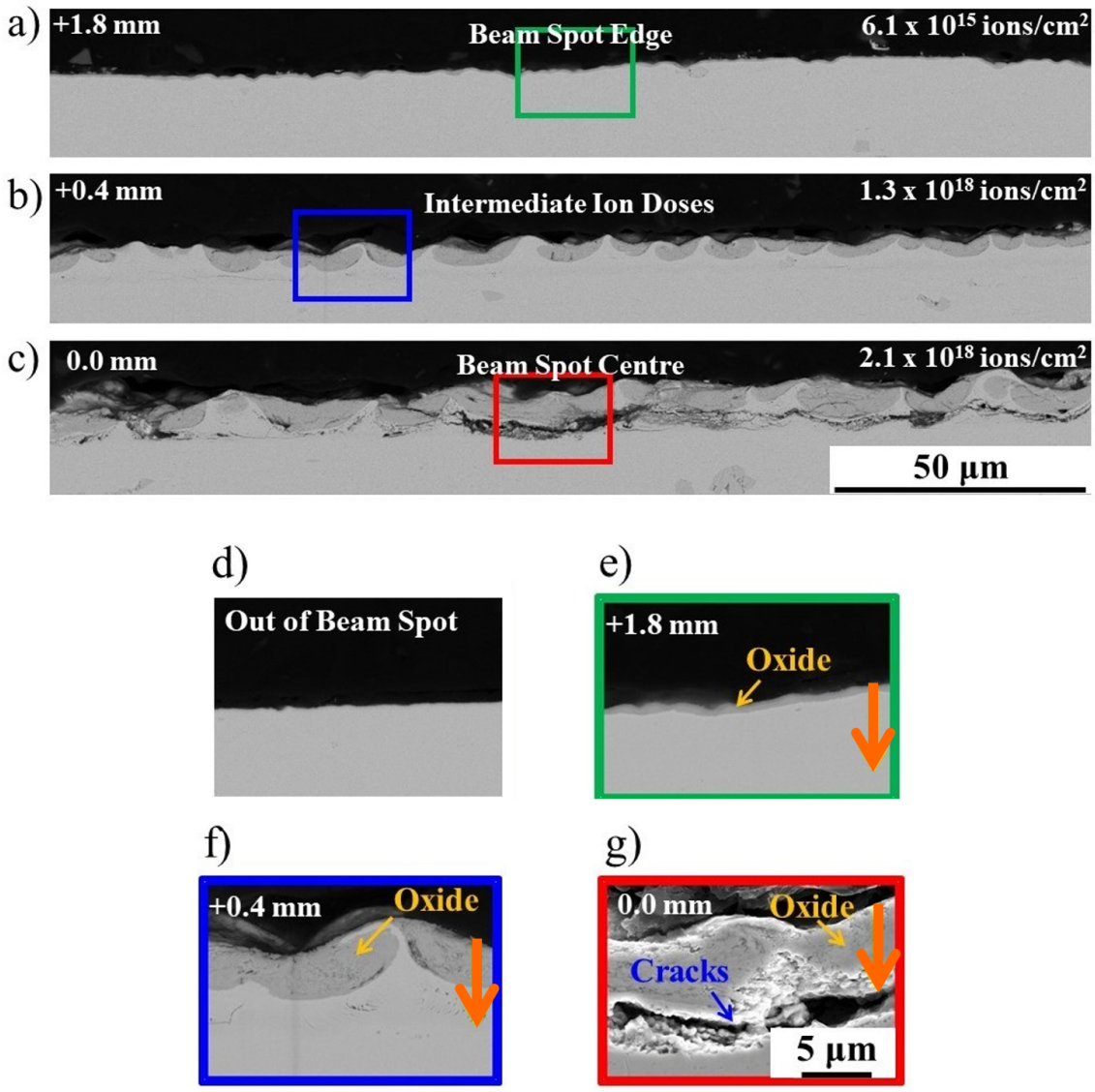

FIGURE 6.7: BSE images taken from the following regions: a) beam spot edge, b) region subjected to an intermediated ion fluence and c) beam centre. d) - g) Images of selected locations with a higher magnification. The ion penetration direction is indicated by the orange arrows. The iradiation induced oxides and cracks are also indicated.

6.4.2 Evidence of ion-induced oxidation

An EBSD phase map was taken to reveal the structure of a selected location subjected to an ion fluence of $5.5 \cdot 10^{17}$ ions/cm^2 or a fission density equivalent of $9.6 \cdot 10^{20}$ f/cm^3 (Figure 6.9). It was shown that the diffraction pattern of the phase below can be indexed with the crystallographic data of the body centred cubic (bcc) γ-U-Mo (marked in red), while the pattern obtained from the upper structure can be indexed with the crystallographic data of the face centred cubic (fcc) UO_2. Even though the vacuum in the irradiation chamber was kept at $\sim 10^{-6}$ mbar during irradiation, some oxygen contamination still formed. Together

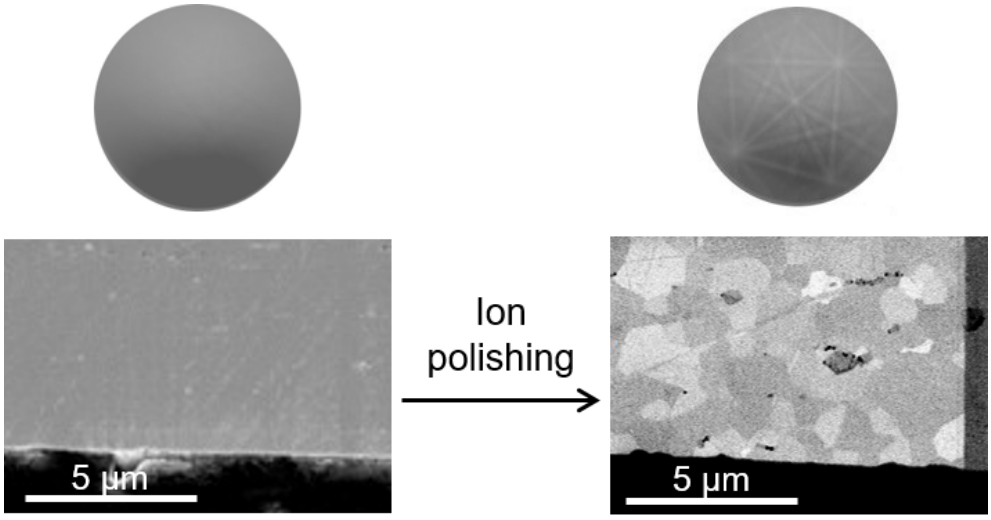

FIGURE 6.8: Left: cross-section without ion polishing. No Kikuchi lines are observed. Right: cross-section after being subjected to ion polishing. The Kikuchi pattern is visible and can be indexed.

with the findings of the SEM analysis (Figure 6.7), it can be concluded that the ion irradiation has induced the growth of the oxide layer perhaps by enhancing the diffusion of the residual oxygen from the sample surface into the U-Mo.

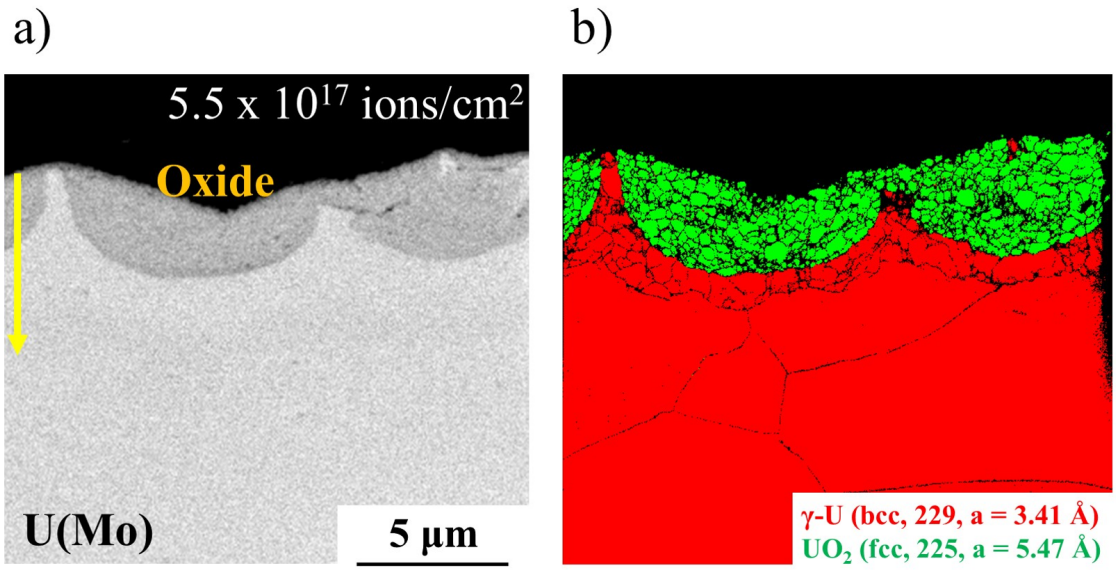

FIGURE 6.9: a) BSE image of a selected location subjected to an ion fluence of $5.5 \cdot 10^{17}$ ions/cm^2 or a fission density equivalent of $9.6 \cdot 10^{20}$ f/cm^3. b) Phase map was obtained, in which body centred cubic (bcc) γ-U-Mo and face centred cubic (fcc) UO_2 are shown in red and green, respectively.

6.4.3 Evolution of grain structure

The EBSD orientation measurement was first taken from a non-irradiated region to reveal the grain structure without being irradiated. Figure 6.10 shows the inverse pole figure (IPF) map superimposed with the GB map with respect to the [001] direction, which reveals the crystallographic orientations of the grains in this region. The equivalent grain size statistics and the GB misorientation statistics are given as well. Typically, GBs having a misorientation less than 15°are defined as low-angle GBs, whereas GBs with a misorientation of more than 15°are defined as high-angle GBs. From this analysis, one can conclude that the non-irradiation region of U-Mo reveals an average equivalent grain diameter of 7.2 µm, and high-angle GBs make up almost 90% of the GBs in the analysed region.

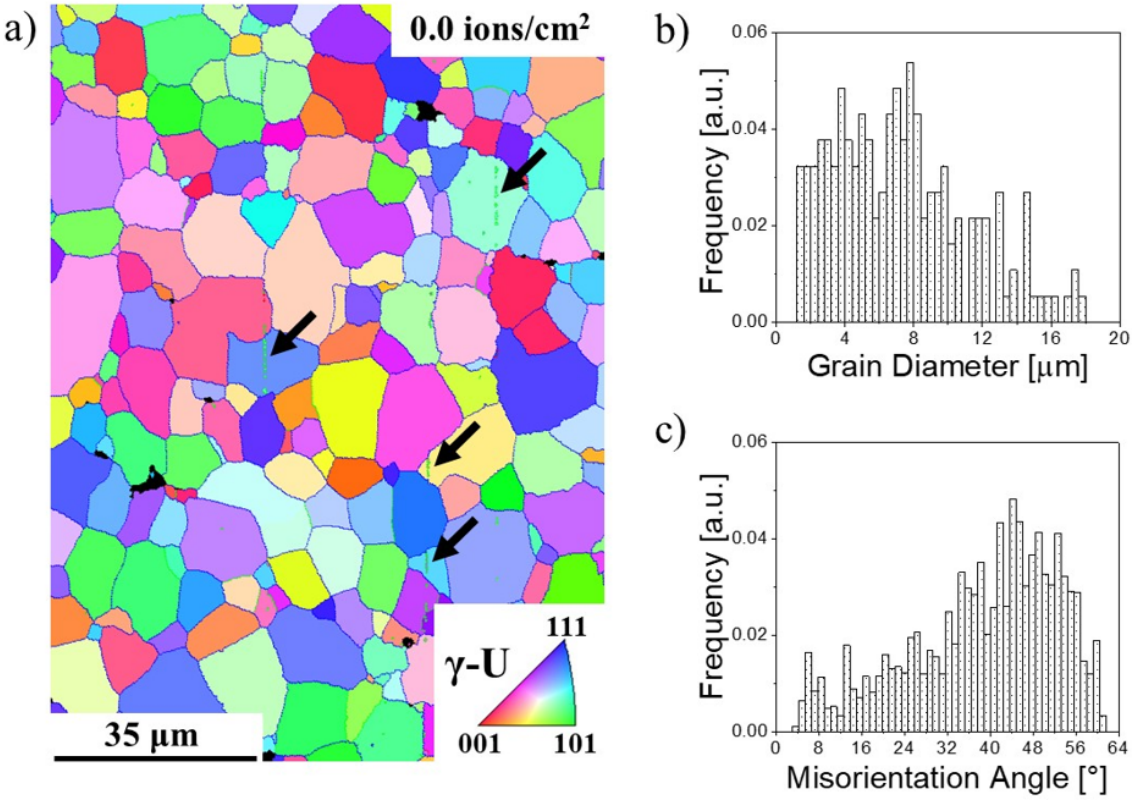

FIGURE 6.10: a) IPF map superimposed with GB map with respect to the [001] direction taken from a non-irradiation region. The key stereographic triangle below correlates colour with crystallographic orientations. A few scratches left from the mechanical polishing were confused for low-angle GBs, as indicated by the arrows. b) Distribution of equivalent grain size c) Distribution of GB misorientation angle

Moving to the ion-irradiated area, four locations were selected to study the effect of irradiation dose (ion fluence or fission density equivalent) on the grain

structure. The irradiation information of the four locations was summarized in Table 6.3. The coordinates correspond to the ones presented in Figure 6.4.

TABLE 6.3: Irradiation information of selected locations

Location	Coordinate	Ion fluence [ions/cm^2]	Fission density equivalent [f/cm^3]
Location 1	-2.13	$\sim 1.8 \cdot 10^{17}$	$\sim 3.2 \cdot 10^{20}$
Location 2	-1.39	$\sim 3.2 \cdot 10^{17}$	$\sim 5.6 \cdot 10^{20}$
Location 3	-0.76	$\sim 5.5 \cdot 10^{17}$	$\sim 9.6 \cdot 10^{20}$
Location 4	-0.07	$\sim 2.1 \cdot 10^{18}$	$\sim 3.1 \cdot 10^{21}$

The IPF map superimposed with the image quality (IQ) map[1] of location 1, 2, 3 and 4 are shown in Figure 6.11, 6.12, 6.13 and 6.14, respectively, giving the information on crystallographic orientations and sizes of the grains.

As presented in Figure 6.11, the grain structure of location 1 remains almost unchanged compared to the non-irradiated region (Figure 6.10). The yellow arrows indicate the ion penetration depth. Therefore no further analysis was taken at this location.

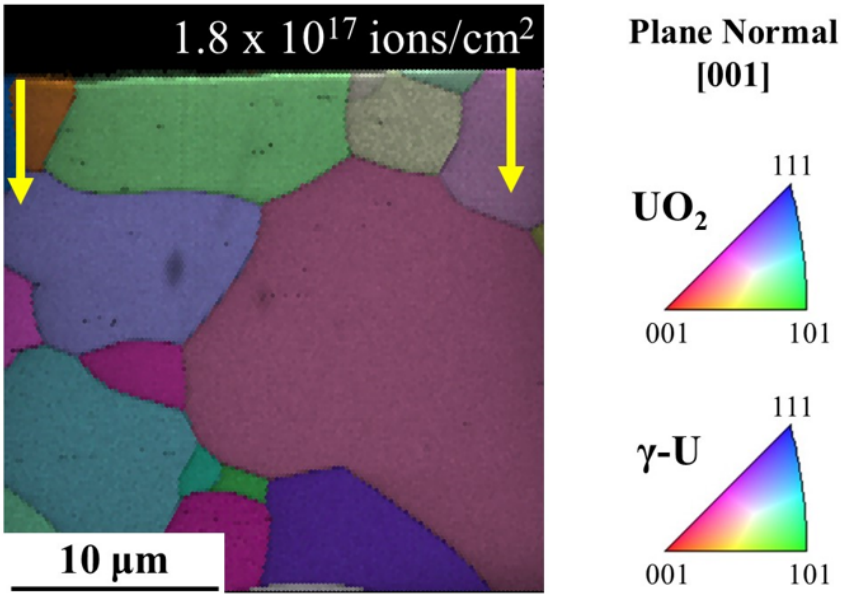

FIGURE 6.11: IPF map superimposed with IQ map with respect to the [001] direction of location 1. The ion penetration depth is indicated by the yellow arrows. The same key stereographic triangle is adopted for Figure 6.12 - 6.14.

[1]Image quality describes the contrast of the Kikuchi-Patterns, which arises from a variety of sources, including phase, strain, topography, and grain boundaries.[165]

At location 2, the ion fluence reached $5.5 \cdot 10^{17}$ ions/cm^2, and modifications of grains are observed as shown in Figure 6.12a. Additionally, a high-magnification map was taken to show the details of the grains (Figure 6.12b), where the oxide phase was removed to avoid possible distractions. The yellow arrows indicate the ion penetration depth. It was found that small grains with an equivalent diameter $< 1\,\mu$m formed close to the sample surface. They are separated mainly by low-angle GBs, which indicates that the underlying mechanism driving the grain refinement is polygonization. The affected depth in U-Mo is $\sim$500 nm. A possible intermediate phase of grain transformation is indicated by the white arrows, where incomplete GBs are identified. This phenomenon is also observed in in-pile irradiated U-Mo fuels as pointed out in [158].

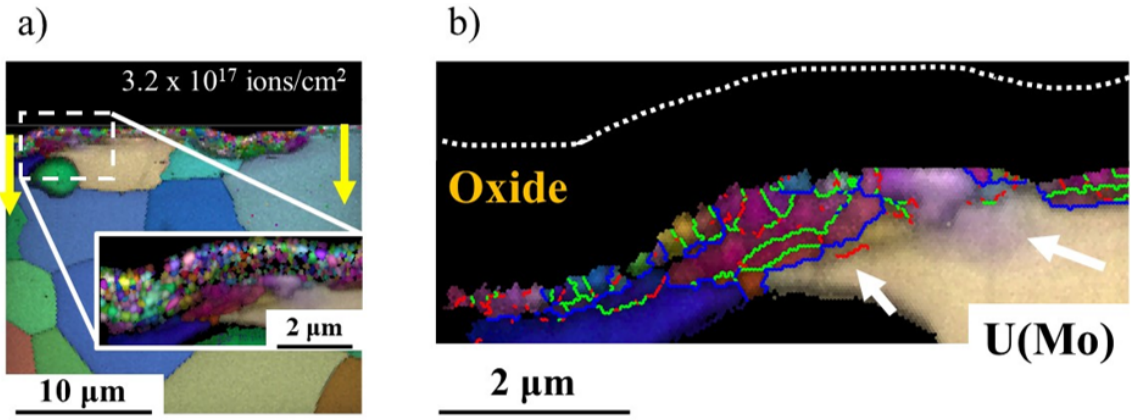

FIGURE 6.12: IPF map superimposed with IQ map with respect to the [001] direction of location 2. The ion penetration depth is indicated by the yellow arrows. b) IPF map superimposed with IQ map at a higher magnification. The oxide layer was removed to eliminate distractions. Possible intermediate phase of grain transformation is indicated by the white arrows.

Moving closer towards the beam centre, as shown in Figure 6.13, location 3 reveals more small grains having an equivalent diameter of $< 1\,\mu$m. The affected depth in U-Mo is extended to $\sim$1 µm. The yellow arrows indicate the ion penetration depth. Incomplete GBs are again observed under the already formed small grains.

Location 4 is closest to the beam centre and was therefore subjected to the highest ion fluence, which leads to the most significant restructuring as shown in Figure 6.14: Plenty of small grains formed, propagating up to $\sim$5 µm into U-Mo. The yellow arrows indicate the ion penetration depth. The completely formed small grains are however separated mainly by high-angle GBs. Similar to the observation of location 3, incomplete grains are found under those formed small grains (indicated by the white arrows), which are separated by low-angle GBs. Irradiation induced defects are presented in form of cracks or holes, which have

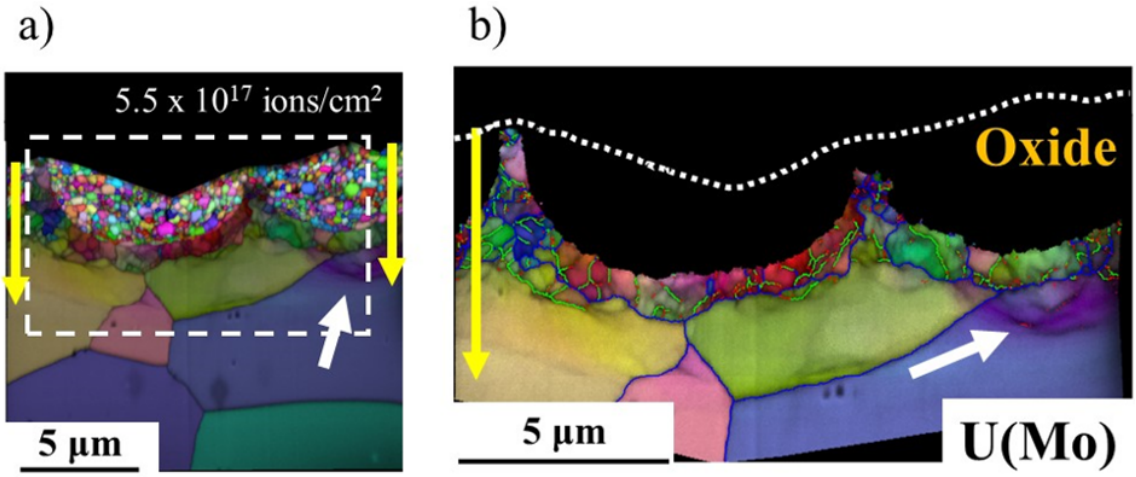

FIGURE 6.13: IPF map superimposed with IQ map with respect to the [001] direction of location 3. The ion penetration depth is indicated by the yellow arrows. b) IPF map superimposed with IQ map at a higher magnification. The oxide layer was removed to eliminate distractions. Incomplete GBs are indicated by the white arrows.

been revealed by SEM (Figure 6.7c). Indexing of such positions failed, resulting in "holes" in the map.

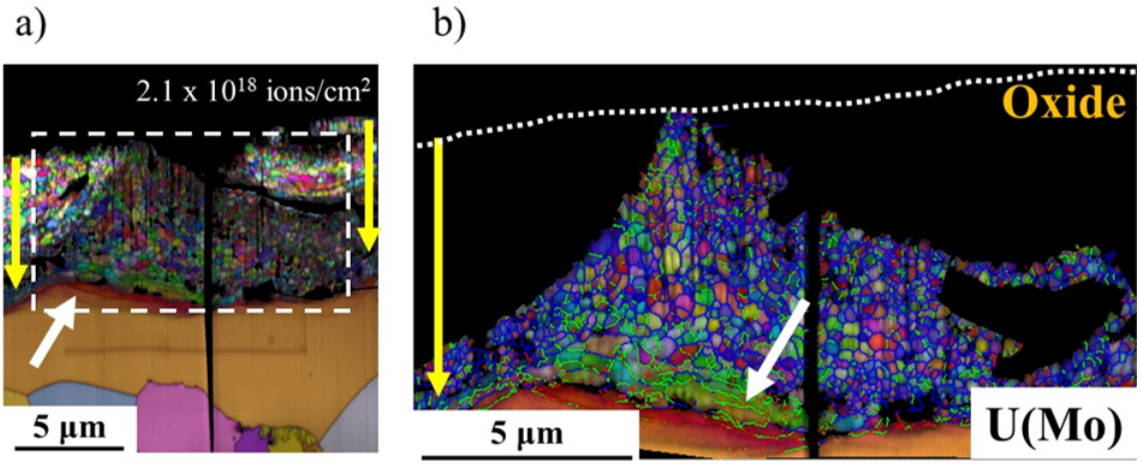

FIGURE 6.14: IPF map superimposed with IQ map with respect to the [001] direction of location 4. The ion penetration depth is indicated by the yellow arrows. b) IPF map superimposed with IQ map at a higher magnification. The oxide layer was removed to eliminate distractions. Incomplete GBs are low-angle and indicated by the white arrows.

6.5 Discussion

6.5.1 Driving force

In this study, it was shown that the newly formed small grains in the restructured U-Mo are separated by mainly low-angle GBs, indicating that the underlying

mechanism of the presented grain refinement is polygonization. Furthermore, as indicated by the IPF + IQ maps, the polygonization always started from the U-Mo surface, propagating into the material with increasing ion dose. There is no evidence that the polygonization has a preferential site in this sample.

Polygonization was also observed in other ion irradiation studies. For instance, Matzke et al. [166] reported polygonization in 300 keV Xe irradiated UO_2 samples, in which he suggested that a sufficiently high concentration of impurity (Xe or I) is necessary for triggering this effect, whereas damage accumulation alone is not sufficient for the phase change. By irradiating UO_2 with 84 MeV Xe at 350 °C up to a dpa of 1357, Miao [167] observed polygonization in the Xe deposition zone located 4 - 5 µm below the irradiated sample surface which is close to the dpa peak.

Returning to this study, as shown by the SRIM/TRIM calculation, the I-deposition peak lies ∼5 µm below the irradiated sample surface. The dpa peak, according to Figure 6.5, was also found ∼5 µm below the sample surface. Thus, both the peak concentration of impurity and the damage peak occur at the depth of ∼5 µm. This location, however, is fairly far away from the observed starting point of polygonization, namely the sample surface. Hence, It can be concluded that neither the impurity nor the damage deposition is the cause of the observed polygonization, at least not the main one. Since the polygonization is always accompanied by the growth of the oxide layer, it is reasonable to consider the correlation between them. As reported by Salvato et al. [168], local lattice stresses caused by accumulated fission gas over-pressurized bubbles at GBs are considered the driving force of polygonization in in-pile irradiated U-Mo. In this study, even though no fission gas participated in the ion irradiation experiment, it is suspected that the formation and growth of the UO_2 phase, due to its lower density, might have affected the U-Mo lattice parameter, resulting in lattice stresses in their surroundings. These stresses are believed to be responsible for this peculiar behaviour i.e. the polygonization starting from the U-Mo surface. Further, it was observed that the newly formed small grains are usually separated by low-angle GBs. In high-dose irradiated regions such as the beam centre region, as the polygonization front moved further into the U-Mo, the already formed low-angle GBs turned into high-angle GBs, which should be a result of consistently increasing lattice stresses.

On the other hand, as demonstrated in Chapter 2, Section 2.4.2, local heating can be generated by electronic energy loss, resulting in grain restructuring during irradiation. This mechanism well explained the directional recrystallization of IDL (Chapter 4, Section 4.4). In this study, according to the energy loss

distribution presented in Figure 6.1, the electronic energy loss of the incoming ions reaches its maximum at the sample surface, then decreases with the penetrating of the ions into the U-Mo, which seems consistent with the direction of the observed polygonization. Nevertheless, the local heat is unlikely the main cause of directional polygonization presented here, as the thermal conductivity of U-10Mo at 140 °C is 14W/(mK), which is much higher than that of the IDL (3 − 4W/(mK) measured in [130]), the produced local heating can therefore be rapidly dissipated.

6.5.2 Effect of irradiation dose

It was found that the fuel restructuring, i.e. grain refinement, took place in the region that was irradiated with ion fluences between $\sim 1.3 \cdot 10^{17}$ ions/cm^2 and $\sim 2.8 \cdot 10^{17}$ ions/cm^2, which correspond to FDs of $\sim 2.2 \cdot 10^{20}$ f/cm^3 and $\sim 4.9 \cdot 10^{20}$ f/cm^3, respectively. This range of FD approximately is one order of magnitude lower than the onset FD of polygonization observed in in-pile irradiated U-10Mo, namely $\sim 3 \cdot 10^{21}$ f/cm^3 [25]. The zones representing different grain structures and the corresponding irradiation dose (irradiation fluence or fission density) are visualised in Figure 6.15.

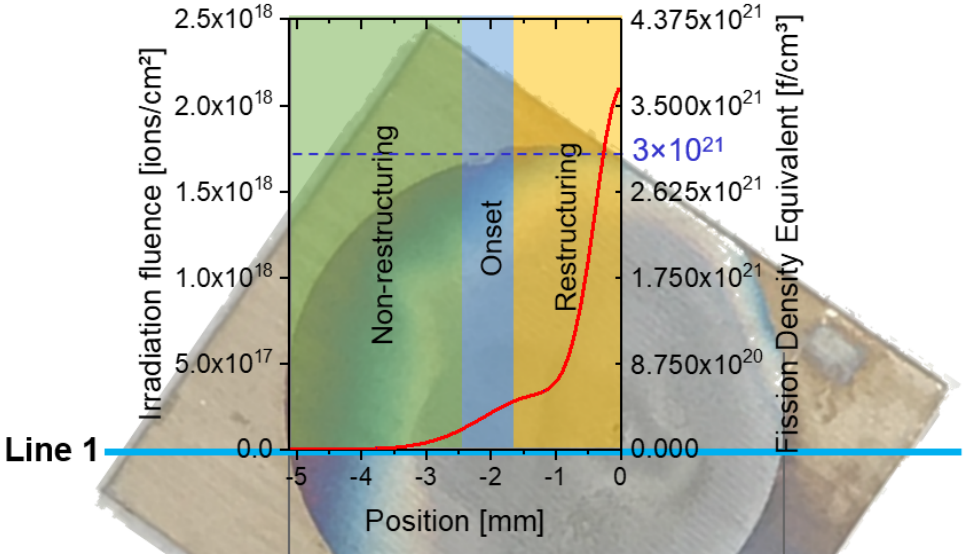

FIGURE 6.15: Visualisation of the non-restructuring zone, the transition zone and the restructuring zone in the irradiated sample. The onset fission density of restructuring observed in in-pile irradiated U-10Mo fuels, i.e. $\sim 3 \cdot 10^{21}$ f/cm^3 [25], is indicated by the blue dashed line.

Apart from the difference in driving force of the polygonization caused by the formation and growth of UO_2, another important difference between the

here presented ion irradiation and in-pile irradiation is the irradiation dose rate, i.e. ion flux for ion irradiation, and fission rate for in-pile irradiation. As shown in Table 6.1, the maximum ion flux in this experiment reached $\sim 2.4 \cdot 10^{13}\,\text{ions}/\left(\text{cm}^2 \cdot \text{s}\right)$, which corresponds to a fission rate equivalent of $\sim 4 \cdot 10^{16}\,\text{f}/\left(\text{cm}^3 \cdot \text{s}\right)$. This value is approximately 45 times higher than the peak fission rate seen in E-FUTURE [86] and SELENIUM [25] tests during the first days of irradiation, which was $\sim 8.9 \cdot 10^{14}\,\text{f}/\left(\text{cm}^3 \cdot \text{s}\right)$. Even though the in-pile test SELENIUM 1a [77] has shown that the fuel restructuring kinetic was not influenced by fission rate[2], its effect can still not be excluded in this study, because the difference in fission rate of the two in-pile irradiations was limited to $\sim 30\%$, which is far below than the difference discussed here, i.e. 45 times. From a microscopic point of view, as the irradiation dose rate is known to influence the production of vacancy-related point defects in solid. For instance, the ion flux influences the defect production in MeV proton-irradiated silicon [169]. It is believed that the significant difference in irradiation dose rate and the formation of oxides during irradiation facilitated the onset of polygonization.

[2]The restructuring in the SELENIUM 1a fuel was triggered at almost the same fission density as the one determined in the SELENIUM test, despite the different fission rates.

Chapter 7

Summary and outlook

Due to its undesirable properties, the excessive growth of IDL in U-Mo/Al fuels can lead to pillowing and may eventually cause breakaway swelling. To thoroughly understand this behaviour and find appropriate solutions to suppress it, a large number of irradiation tests should be implemented on such fuels. Swift heavy ion irradiation is considered the most adequate technique for simulating in-pile irradiation. Compared to the commonly used thermal anneals, irradiation with ^{127}I ions at 80 MeV can simulate to a large extent the radiation-enhanced processes because such ions well represent the fission products of ^{235}U. Therefore, this technique allows a realistic prediction of some in-pile behaviours. For instance, previous studies [85] [26] [28] [27] have demonstrated that the IDLs reproduced by 80 MeV ^{127}I ions are very similar to the ones formed in-pile. Swift heavy ion irradiation is not only time-saving and economic but also provides various possibilities for different purposes in fuel testing, thanks to its individually controllable parameters. Using this technique, this thesis systematically evaluated the irradiation behaviour of U-Mo/Al based fuels by quantitatively characterising the interfaces between U-Mo, diffusion barrier and Al. The main conclusions are drawn in the following sections.

7.1 Summary

7.1.1 Quantitative comparison between in-pile and ion irradiation

As the IDL growth is one of the deciding criteria for performance evaluation of U-Mo/Al based fuel, a model to predict the IDL development is necessary. An empirical in-pile model correlating fission rate, temperature and irradiation time was developed by Kim and Hofman [13] based on the data of several in-pile irradiation tests. This model can be statistically verified by a series of ion irradiations. A more recent study [29] proposed a proportional conversion of ion

flux in the corresponding fission rate equivalent, providing a direct connection between ion irradiation and in-pile irradiation. Taking advantage of this, the fission rate in the empirical in-pile model can be replaced by an equivalent ion flux. Eventually, an IDL growth model correlating IDL thickness, ion flux, temperature and irradiation time was established. By verifying this correlation with ion irradiation data, the empirical in-pile model can be accordingly verified. To this end, two approaches were adopted in this thesis.

- As the ion beam profile could not be accessed in the early time of this thesis, approach 1 employed the correlation $Y_{\mathrm{IDL}} \propto \dot{\Phi}^{\frac{1}{4}}$ to obtain the ion flux profile in order to determine local ion fluxes as well as ion fluences. This correlation assumes that the thickness of the generated IDL is proportional to ion flux to the 1/4 power, which is derived from the in-pile empirical model Euqation 3.1 when $p = 0.5$. In total five samples were irradiated and analysed with this approach. During PIE, the IDL thickness profile of each sample was determined, with which the ion flux profile of each irradiation was reconstructed by using the assumed correlation. The temperature, the irradiation time and the total number of ions can be obtained in the irradiation experiment. Thus, the predicted IDL thicknesses under the those conditions can be calculated with the IDL growth model. The obtained results show that the prediction agrees well with the measurement. Further, the fit constants including the proportionality factor A and the normalization parameter for temperature q of the in-pile model were verified. Yet, since the assumed correlation $Y_{\mathrm{IDL}} \propto \dot{\Phi}^{\frac{1}{4}}$ adopted $p = 0.5$, the value of the exponent p cannot be justified as it would lead to circular reasoning. This approach is therefore considered semi-quantitative.

- By utilizing a BPM, approach 2 allows the ion flux profile to be obtained from the measurements. In this manner, the predicted IDL thickness calculated with the IDL growth model is completely independent of any assumption. This approach enables a fully quantitative comparison between model prediction and experimental result and therefore is considered fully quantitative. For the verification of the in-pile empirical model, another five samples were irradiated and analysis with this approach. When comparing the measured IDL thicknesses with the predicted ones obtained by using the IDL growth model, a good agreement was reached. Furthermore, the fit parameters in the in-pile model including the value A, q and p were verified. At this point, the IDL growth dynamics

of the empirical model was successfully verified with ion irradiation data. Additionally, approach 1 was performed on one of these five samples. The result was compared with the one obtained with approach 2. The well-agreed results demonstrated that the relationship between ion flux and IDL thickness can be well described by the correlation $Y_{IDL} \propto \dot{\Phi}^{\frac{1}{4}}$, and the application of $p = 0.5$ in the IDL growth model in previous studies is reasonable.

At last, the temperature effect on the IDL growth dynamics was further investigated. By plotting the normalized IDL thickness to the fourth power against inverse temperature, a Q-curve behaviour was visualised and the diffusion process was divided into two regimes, i.e. a temperature-dependent regime and an athermal regime. The transition temperature of IDL growth dynamics was seen between $180 - 200\,°C$, below which the temperature plays a minor role in the mixing process of Al and U-Mo, above which the mixing is significantly accelerated by temperature and thus the IDL grows rapidly.

7.1.2 Temperature effect on the microstructure of IDL

Temperature has an important effect not only on the quantity of IDL, but also on its microstructure. Previous studies have shown that the IDL induced by heavy ion irradiation can be crystalline [31][32] or amorphous [33], depending on the irradiation conditions especially the temperature. In this thesis, the microstructural evolution and phase transformation were set into focus. For this purpose, five samples were irradiated with 80 MeV ^{127}I ions at selected temperatures, i.e. 140 °C, 180 °C, 200 °C, 220 °C and 275 °C. During the PIE, as revealed by the TEM analysis, a notable change in the IDL microstructure was witnessed at elevated temperatures. The selected area electron diffraction patterns showed that the IDLs are fully amorphous at an irradiation temperature up to 200 °C. At 220 °C, the IDL was subjected to a phase transformation, during which nanograins started to form at the Al/IDL interface. When 275 °C was reached, the nanocrystalline phase dominated the IDL by propagating towards the U-Mo. The EDX analysis unveiled the chemical composition of the IDLs. These findings lead to the following conclusions:

- The phase transition temperature (should not be confused with the transition temperature of IDL growth dynamics) determining the nature of IDL occurs at $\sim$ 220 °C at the giving ion conditions. The IDL remains amorphous below this temperature, while nanograins start to form in the IDL close to Al when the transition temperature is reached.

- The competition between the thermal annealing rate and the damage rate rules the nature of the generated IDL.
- The nanograins formed in the IDLs were identified as having a cubic Pm-3m structure like UAl_3, and a lattice parameter around 4.4 Å.
- The release of a large amount of energy by electronic energy loss mechanism at the Al/IDL interface is considered to be the underlying cause of the directional crystallization starting from the Al/IDL interface.
- The Al/(U + Mo) atomic ratio of IDL rises with increasing irradiation temperature in those samples as evidenced by both SEM/EDX and STEM/EDX, which is a result of combined effects of enhanced Al atomic flow and microstructural evolution of IDL.

7.1.3 Quantitative evaluation of transition metals as diffusion barriers

The application of a coating barrier between U-Mo and Al is an advantageous option to inhibit the interdiffusion of U-Mo and Al. Rather than being dispersed in the Al matrix like Si, the diffusion barrier is directly applied at the position where it is needed. Previous studies focusing on material down-selection have demonstrated that transition metals are potential candidates for diffusion barriers in the U-Mo/Al fuel system. Yet, no quantitative interpretation about coating effectiveness has been made.

This thesis presents a quantitative evaluation of transition metals Mo, Zr and W as diffusion barriers in U-Mo/Al fuels concerning coating thickness and irradiation dose by using heavy ion irradiation. For this purpose, four Al/Mo/U-Mo samples (Mo coating thickness: 50 nm, 150 nm, 500 nm, 2 µm), two Al/Zr/U-Mo samples (Zr coating thickness: 200 nm, 5 µm) and four Al/W/U-Mo samples (W coating thickness: 200 nm, 500 nm, 1 µm and 2 µm) were prepared by PVD sputtering. The surface conditions of the U-Mo substrates were improved by deoxidation and fine polishing to ensure high-quality coatings. Ion irradiation tests with 80 MeV ^{127}I ions were performed at 140 °C on those samples subsequently. During the PIE, representative locations, i.e. non-irradiated, low-fluence irradiated and high-fluence irradiated regions of the each irradiated sample, were selected and further analysed. The local ion fluences and the corresponding equivalent fission densities were determined with the method demonstrated in Chapter 3. Hence, a quantitative evaluation can be implemented. The main results are:

- In the Mo coated samples, Al interacted significantly with the Mo coatings. As a result, no pure Mo was left in the low-fluence irradiated region of 50 nm, 150 nm and 500 nm Mo coated samples, where the local irradiation dose was determined to be $\sim 1.4 \cdot 10^{17}$ ions/cm^2 in ion fluence or $\sim 1.5 \cdot 10^{20}$ f/cm^3 in fission density equivalent. Meanwhile, the formed Mo-Al intermixing layer shows transparency to the atomic transport between Al and U-Mo, prompting the growth of a U-Mo-Al IDL. Consequently, when the irradiation dose reached $4.2 - 4.5 \cdot 10^{17}$ ions/cm^2 (corresponds to fission density equivalent $\sim 4.4 - 5 \cdot 10^{20}$ f/cm^3), the sample structures were significantly altered by the intensively growing U-Mo-Al IDLs. In the 2 µm Mo coated sample, the Mo coating was not completely consumed due to a higher initial thickness. Yet, it is believed that at higher irradiation doses, the Mo will be eventually used up, triggering the growth of Al-U-Mo IDL. Hence, the Mo coating is not suggested as a diffusion barrier in the U-Mo/Al fuel system. The result agrees very well with the recently published PIE result of SEMPER FIDELIS test [139][140] in regard to fuel structure evolutions, which again demonstrates that swift heavy ion irradiation technique is a powerful tool for simulating in-pile irradiation.

- The two Al/Zr/U-Mo samples respectively coated with 200 nm and 5 µm Zr represent the two extremes of barrier thickness. The 200 nm Zr coating behaved in a similar manner to the 50 nm and 150 nm Mo coated samples. On the other hand, despite the slight growth of a thin Zr-Al intermixing layer, no excessive interaction occurred in the 5 µm Zr coated sample up to an irradiation dose of $\sim 3.3 \cdot 10^{17}$ ions/cm^2, which corresponds to a fission density equivalent of $\sim 3.4 \cdot 10^{20}$ f/cm^3. Nevertheless, as the Zr/Al interface was located rather far away from the damage peak (Bragg peak), further investigations are still needed in which the Zr/Al interface should be placed close to the damage peak.

- Among the three metallic coating barriers, the W coating shows a most promising irradiation behaviour: Once the coating thickness is beyond 1 µm, the irradiated sample could retain its structure. The intermixing phase was limited to a few hundred nanometers, in spite of the fact that the W coated samples were irradiated at even higher doses e.g. $\sim 7 \cdot 10^{17}$ ions/cm^2 (fission density equivalent $\sim 7.5 \cdot 10^{20}$ f/cm^3) compared to the Mo and Zr coated samples.

7.1.4 A systematic study of ZrN diffusion barrier

Recent studies show encouraging results of ZrN coating as a diffusion barrier in the U-Mo/Al fuel system. Yet, coating damage e.g. cracks in the brittle ZrN coatings caused by the mechanical processes during manufacturing is considered a concern as such cracks can provide entrance ports for the unfavoured U-Mo-Al diffusion. This thesis provided a systematic evaluation of this promising coating barrier in aspects of coating thickness and coating conditions.

The study of ZrN coating thickness were performed on three Al/ZrN/U-Mo tri-layer samples which have coating thicknesses of 100 nm, 200 nm and 500 nm, respectively. The ZrN coatings obtained from PVD sputtering are free of cracks. Irradiations with 80 MeV ^{127}I ions were undertaken on these samples under similar irradiation conditions. The maximum ion fluence at beam centre is estimated to be $\sim 5 \cdot 10^{17}$ ions/cm^2, which corresponds to a fission density equivalent of $\sim 5.3 \cdot 10^{20}$ f/cm^3. The PIE results showed that no notable interaction took place in all three samples based on the SEM observations. The ZrN coatings remained intact. The later performed FIB/SEM investigation revealed diffusional interactions occurring at the Al/ZrN and ZrN/U-Mo interfaces, resulting in a slow consumption of the ZrN coating. Further, void formation was observed in the Al layers, which might be related to the ballistic effect.

The impact of coating cracks in Al/ZrN/U-Mo fuels was extensively investigated. To reproduce similar cracks, a cut-out sample of an as-fabricated SELENIUM fuel plate was first characterised. The cracks in it were classified and successfully reproduced in ZrN coatings by two methods, i.e. indentation by a Vickers hardness tester and pressing by a hydraulic press. Five Al/ZrN/U-Mo samples with these artificial cracks were irradiated under various conditions. The irradiation behaviour with respect to irradiation conditions, namely the temperature, ion fluence and ion flux, were studied. The PIE revealed that the ZrN coating layer interacted with Al notably, resulting in the double coating layer. At a sufficiently high irradiation dose, the ZrN coating can be completely consumed by reacting with Al, albeit at a much slower rate compared to the Al-U-Mo interaction rate. Some fine cracks in the ZrN coatings with a width below 1 µm were healed by irradiation enhanced diffusion bonding in the ZrN coating due to the high damage rate (ion flux) of this technique. The growth rate of IDL showed a highly significant dependence on the temperature, which agrees with the Arrhenius correlation in the IDL growth model. Further, the volcano-like IDLs and the double coating layer observed in in-pile irradiated fuels were successfully reproduced in these ion-irradiated samples. Besides, it

was found that the eruption direction of the volcano-like IDLs, i.e. from U-Mo to Al, is independent of the irradiation direction. On the whole, in spite of the presence of cracks in the coating, ZrN is still considered a promising candidate for diffusion barriers in U-Mo/Al fuels as it can effectively delay the build-up of IDL and the subsequent fuel swelling.

7.1.5 U-Mo fuel restructuring under heavy ion irradiation

High burn-up structures are usually seen in in-pile irradiated fuels, due to the extremely high irradiation dose achieved in the reactor environment. In this thesis, a U-10Mo foil was irradiated with 80 MeV ^{127}I at 140 °C up to $\sim 2.1 \cdot 10^{18}$ ions/cm^2. Such an ion fluence is equivalent to a fission density equivalent of $\sim 3.7 \cdot 10^{21}$ f/cm^3. During the PIE, EBSD evidenced that polygonization was the underlying mechanism of the fuel restructuring i.e. grain refinement. It was observed that the polygonization started at the U-Mo surface and propagated into the U-Mo with increasing ion fluence, rather than starting from the position of irradiation damage peak, which can be attributed to the growth of UO_2 phases at U-Mo surface causing lattice stresses in their surroundings.

The Gaussian-distributed ion dose also allowed to study the dose-dependent behaviour of polygonization. It was revealed that this restructuring behaviour was triggered at ion fluences between $\sim 1.3 \cdot 10^{17}$ ions/cm^2 and $\sim 2.8 \cdot 10^{17}$ ions/cm^2, which correspond to FDs between $\sim 2.2 \cdot 10^{20}$ f/cm^3 and $\sim 4.9 \cdot 10^{20}$ f/cm^3. This range of FD approximately is one order of magnitude lower than the onset FD of polygonization observed in-pile, namely $\sim 3 \cdot 10^{21}$ f/cm^3 [25]. This difference might be caused by the significantly higher irradiation dose rate of the performed heavy ion irradiation and the formation of oxides during irradiation.

7.2 Outlook

In the last decades, the worldwide effort has been made for the development of metallic high-density uranium fuels and thereby enabling the conversion of research reactors to lower enriched fuels. With the help of swift heavy ion irradiation, the evaluation and qualification of these new fuels is given a versatile tool. Thus, comprehensive studies of irradiation behaviours and new ideas are always encouraged, including but not limited to:

- A series of ion irradiation tests under various conditions (ion flux, ion fluence, temperature, etc.) should be performed on the U-Mo/Al fuel

system with U-Mo layer on top, i.e. the ions impinge on the U-Mo surface which simulates the realistic irradiation direction occurring during in-pile irradiation, in order to support the proposed IDL growth dynamics and also to justify the directional crystallization of IDL.

- The irradiation behaviour of the Zr/Al and W/Al interfaces with respect to the ion fluence (corresponds to a fission density) with the damage peak of the ions placed right there should be investigated, in order to achieve a global understanding of the irradiation performance of Zr and W coated U-Mo/Al fuels.

- In this thesis, the IDL growth correlation from the in-pile empirical model for U-Mo/Al fuels without coating barriers has been successfully verified with ion irradiation data. Ye et al. [78] has extended the IDL growth correlation for U-Mo/Al fuels with improved designs, e.g. coated U-Mo kernels. It is advantageous to verify this correlation for the promising coating barrier candidate such as W with ion irradiation data. For this purpose, a series of W coated U-Mo/Al samples should be irradiated with swift heavy ions under different conditions (ion flux, ion fluence, temperature, coating quality etc.).

- A series of ion irradiations on Al/ZrN/U-Mo fuel system at different temperature are expected to be performed, where no cracks are introduced in the coating. The purpose is to study the temperature sensitivity of this ceramic coating barrier during irradiation.

- It is expected to irradiate uncoated U-Mo foils with swift heavy ions up to high doses (at least $\sim$ $2.1 \cdot 10^{18}$ ions/cm^2), however, with additional measures to avoid surface oxidation during irradiation, e.g. improving the vacuum in the irradiation chamber or/and pre-heating the sample at a reasonable temperature. The purpose is to investigate the mechanisms of irradiation-induced restructuring in U-Mo without the influence of oxidation. Alternatively, the U-Mo can be coated with a thin inert layer, preventing oxidation and not significantly reducing the ion penetration depth in U-Mo. The restructured foils can be further subjected to Xe or Kr irradiation to study the irradiation gas behaviour.

- More possibilities to avoid the formation of unfavoured interdiffusion phases between the fuel and the matrix/cladding should be explored. For instance, looking for new binary U-X or ternary U-X-Y alloys for further

fuel candidates and evaluating their irradiation performances with heavy ion irradiation is another possible research direction.

7.3 Conclusion

Ever since swift heavy ion irradiation was introduced to the research and test reactor fuels community, this technique is continuously evolving. For the purpose of simulating in-pile irradiations and predicting the irradiation behaviour of new fuels, significant efforts have been made from the first implementation of this technique (feasibility), over the utilization in a qualitative manner, to the application in a semi-quantitative way. Eventually, this thesis established a fully quantitative comparison between heavy-ion and in-pile irradiation, making heavy ion irradiation a more powerful tool in fuel development by achieving a more accurate prediction of in-pile behaviours of new fuels. Taking advantage of this tool, four coating barriers, i.e. Mo, Zr, W, and ZrN were quantitatively evaluated, where the irradiation behaviours of those fuels under different conditions were unveiled. Furthermore, two transition temperatures were determined, i.e. the one separating the athermal regime and the thermal regime of the IDL growth dynamics, and the other one being crystallization onset temperature which characterises the nature of IDL. In the end, the fuel restructuring i.e. the grain refinement occurring in U-Mo during in-pile irradiation at high burn-ups was reproduced by ion irradiation. The results obtained in this thesis benefit the fuel development, and with the presented potential future work, the conversion of research and test reactor fuels will be eventually facilitated.

Appendix A

Beam time and irradiated samples

During this thesis, in total 58 samples were irradiated in 10 beam time periods. The seriously ageing components largely degrade the performance of the MLL tandem accelerator. As a result, spark (electrical discharge) in the tandem occurred frequently during almost each beam time period in this thesis. Besides, the gas stripper located at the terminal of the tandem failed many times. These technical issues led to restarts of the tandem or the gas stripper. In each case, the ion beam had to be re-tuned, and the expected irradiation had to be repeated on a new sample. Table A1 summarizes the samples with irradiation conditions and the results. The irradiations suffered from severe technical issues are marked in red. They were not further discussed in this thesis. The rest of the samples have been presented in this thesis.

Beam time	Sample ID	Sample configuration	Study	I-energy MeV	Temperature °C	Duration h	Total fluence ions	Result
17-01	S2_1	U-Mo	GR	80	140	39.5	4.96E+16	Multiple footprints
17-03	S3_1	Al(13µm)/U-Mo	QC, T	80	160	4.0	4.31E+15	Al damaged
	S3_2	Al(13µm)/U-Mo	QC, T	80	140	12.5	9.50E+15	Stable
	S3_3	Al(13µm)/U-Mo	QC, T	80	110	6.0	5.90E+15	Al damaged
	S3_4	Al(13µm)/U-Mo	QC, T	80	180	3.5	3.55E+15	Stable
17-06	S4_1	Al(13µm)/U-Mo	QC, T	80	200	6.7	5.13E+15	Stable
	S4_2	Al(13µm)/U-Mo	QC, T	80	220	7.0	5.75E+15	Al damaged
	S4_3	Al(13µm)/U-Mo	QC, T	80	240	9.0	5.89E+15	Al damaged
	S4_4	Al(13µm)/U-Mo	QC, T	80	260	9.0	5.73E+15	Al damaged
	S4_5	Al(13µm)/U-Mo	QC, T	80	275	9.3	3.37E+15	Relatively stable
	S4_7	Al(13µm)/U-Mo	QC, T	80	220	11.0	4.29E+15	Stable
18-01	S5_1	Al(6µm)/U-Mo	E	60	140	8.0	1.20E+16	lens overloded
	S5_2	Al(6µm)/U-Mo	E	80	140	15.0	8.43E+15	Multiple sparks
	S5_4	Al(13µm)/U-Mo	QC, T	80	90	4.0	3.67E+15	Multiple sparks
	S5_3	Al(11µm)/ZrN(200nm)/U-Mo	ZrN	80	140	12.5	1.10E+16	Stable
18-03	S6_1	Al(11µm)/ZrN(500nm)/U-Mo	ZrN	80	140	8.0	7.50E+15	Stable
	S6_2	Al(11µm)/ZrN(200nm)/U-Mo	ZrN	80	140	29.5	2.17E+15	Low flux
	S6_3	Al(11µm)/ZrN(200nm)/U-Mo	ZrN	80	140	8.0	7.30E+15	Multiple sparks
	S6_4	Al(11µm)/ZrN(100nm)/U-Mo	ZrN	80	140	8.5	7.46E+15	Relatively stable
	S6_5	Al(6µm)/U-Mo	E	80	140	7.0	7.92E+15	Multiple sparks
18-09	S7_1	Al(11µm)/ZrN(200nm)/U-Mo	ZrN	80	140	17.0	2.60E+15	Foil stripper
	S7_1	Al(11µm)/ZrN(200nm)/U-Mo	ZrN	80	140	15.5	1.90E+15	Foil stripper
	S7_1	Al(11µm)/ZrN(200nm)/U-Mo	ZrN	80	140	19.0	2.30E+15	Foil stripper
	S7_1	Al(11µm)/ZrN(50nm)/U-Mo	ZrN	80	140	14.5	1.45E+15	Foil stripper

TABLE A1 (part 1): Total irradiated samples. Sample information and irradiation conditions are given. The abbreviations for the names of the study are explained after the table.

18-12 part1								
S8_4	Al(11µm)/ZrN(500nm)/U-Mo	ZrN-C	80	140	12.0	1.03E+16	Relatively stable
S8_1	Al(11µm)/ZrN(500nm)/U-Mo	ZrN-C	80	140	16.5	1.98E+16	Stable
S8_5	Al(11µm)/ZrN(500nm)/U-Mo	ZrN-C	80	200	6.0	1.02E+16	Stable
S8_7	Al(11µm)/ZrN(500nm)/U-Mo	ZrN-C	80	140	7.0	1.07E+16	Stable
S8_2	Al(11µm)/ZrN(500nm)/U-Mo	ZrN-C	80	140	9.5	1.06E+16	Beam unstable
S8_3	Al(11µm)/ZrN(500nm)/U-Mo	ZrN-C	80	140	14.0	9.98E+15	Gas stripper failed once
S8_6	Al(11µm)/ZrN(500nm)/U-Mo	ZrN-C	80	200	6.0	1.08E+16	Stable
S8_8	Al(11µm)/ZrN(500nm)/U-Mo	ZrN-C	80	140	7.5	1.07E+16	Multiple sparks
S8_9	Al(11µm)/ZrN(500nm)/U-Mo	ZrN-C	80	200	8.5	1.01E+16	Multiple sparks
18-12 part2							
S8_10	Al(13µm)/U-Mo	FQC, T	80	70	22	2.00E+16	stable
S8_11	Al(13µm)/U-Mo	FQC, T	80	140	18	2.02E+16	Beam unstable
S8_12	Al(6µm)/U-Mo	FQC, T	80	140	28	1.50E+16	Gas stripper failed once
S8_13	Al(12.4µm)/Mo(50nm)/U-Mo	Mo	80	140	27.5	2.04E+16	stable
S8_16	Al(12.1µm)/Mo(150nm)/U-Mo	Mo	80	140	21.5	2.00E+16	Gas stripper failed once
S8_14	Al(11.3µm)/Mo(500nm)/U-Mo	Mo	80	140	16.2	2.05E+16	Gas stripper failed twice
S8_15	Al(12µm)/Zr(200nm)/U-Mo	Zr	80	140	17.5	2.01E+16	Gas stripper failed twice
S8_17	Al(4.7µm)/Zr(5µm)/U-Mo	Zr	80	140	23	1.55E+16	Gas stripper failed twice
19-02							
S9_1	Al(7.5µm)/Mo(2µm)/U-Mo	Mo	80	140	21.5	9.72E+15	Ion source unstable
S9_2	Mo(5.4µm)/Al	Mo	80	140	15	6.20E+15	Sparkx1, long break
S9_3	Zr(8.1µm)/Al	Zr	80	140	15	7.60E+15	Sample failed
19-08							
S10_1	Al(9µm)/U-Mo	FQC	80	140	24.5	6.62E+15	Foil stripper
S10_2	Al(9µm)/U-Mo	FQC	80	?	(?)24	1.99E+16	Foil stripper
S10_3	Al(9µm)/U-Mo	FQC	80	?	19.0	1.55E+16	Ion source unstable
S10_4	Al(9µm)/U-Mo	FQC	80	140	26.5	6.63E+15	Ion source unstable
S10_5	Al(9µm)/U-Mo	FQC, T	80	110	20.0	8.10E+15	Relatively stable
S10_6	Al(9µm)/U-Mo	FQC, T	80	140	18.2	1.01E+16	Relatively stable

TABLE A1 (part 2): Total irradiated samples. Sample information and irradiation conditions are given. The abbreviations for the names of the study are explained after the table.

20-01								
S11_1	Al(12.8µm)/W(200nm)/U-Mo	W	80	140	27	1.51E+16	Relatively stable
S11_2	Al(11.5µm)/W(500nm)/U-Mo	W	80	140	31.2	1.50E+16	Stable
S11_3	Al(10µm)/W(1µm)/U-Mo	W	80	140	14.5	1.53E+16	Relatively stable
S11_4	Al(7.65µm)/W(2µm)/U-Mo	W	80	140	14	1.51E+16	Stable
S11_5	Al(13µm)/U-Mo	FQC	80	140	4.4	3.47E+15	Multiple sparks
S11_6	Al(13µm)/U-Mo	FQC	80	140	9	4.48E+15	Multiple sparks
S11_7	Al(13µm)/U-Mo	FQC	80	140	16	2.50E+16	Multiple sparks
S11_8	Al(13µm)/U-Mo	FQC	80	180	10	1.01E+16	Ion source unstable
S11_9	Al(13µm)/U-Mo	FQC	80	140	21	2.51E+16	Ion source unstable

- GR: Evolution of U-Mo grain structure.
- QC: Quantitative comparison between ion and in-pile irradiation.
- T: Temperature effect.
- E: Effect of ion energy.
- ZrN: Diffusion barrier effectiveness of dense ZrN coatings.
- ZrN-C: Diffusion barrier effectiveness of ZrN coatings with cracks.
- Mo: Diffusion barrier effectiveness of dense Mo coatings.
- Zr: Diffusion barrier effectiveness of dense Zr coatings.
- W: Diffusion barrier effectiveness of dense W coatings.
- FQC: Fully quantitative comparison between ion and in-pile irradiation.

TABLE A1 (part 3): Total irradiated samples. Sample information and irradiation conditions are given. The abbreviations for the names of the study are explained after the table.

Appendix B

Metallographic sample preparation

Metallographic preparation of cross-sections was conducted in this thesis to reveal the inner structure of the studied samples. The preparation procedure is introduced here. First of all, the samples were embedded in a transparent epoxy resin (EpoFix kit of Struers) to ensure that the sample and the beam footprint on it are visible. Then grinding and polishing were carried out to reach the region of interest, namely the beam spot centre in most cases. The utilized recipes are presented in the following.

Table B1 summarized the Fundamental grinding and polishing recipe for SS-based layered samples (SS is the major composition) embedded in a cylindrical epoxy with a diameter of 30 mm. The recipe varies slightly for the different second element, such as for Al/SS, Mo/SS, Zr/SS and W/SS samples. For samples containing ZrN coating, $\sim$ 2 N smaller force was applied for each step due to the brittleness of this material.

TABLE B1

Step	Grinding/ polishing disk	Suspension	Force	Speed	Time
2	MD-Piano 80	H_2O	25 N	300 r/min	Till plan
2	MD-Piano 220	H_2O	25 N	300 r/min	Till close to ROI
2	MD-Largo 9	Largo 9 µm	30 N	150 r/min	7 min
2	MD-Largo 3	Largo 3 µm	25 N	150 r/min	5 min
2	MD-Dur 1	Largo 1 µm	22 N	150 r/min	4 min
2	MD-Chem	UP-S/H_2O	5 - 15 N	150 r/min	90 s

The Fundamental grinding and polishing recipe for U-Mo-based layered samples (U-Mo is the major composition) embedded in a cylindrical epoxy with a diameter of 30 mm is presented in Table B2. The recipe varies slightly for additional elements, such as for Al/Zr/U-Mo, Al/Mo/U-Mo, Al/Mo/U-Mo and Al/W/U-Mo samples. Likewise, for samples containing a ZrN coating, $\sim$ 2 N smaller force was applied for each step.

TABLE B2

Step	Grinding/ polishing disk	Suspension	Force	Speed	Time
2	MD-Piano 80	H_2O	25 N	300 r/min	Till plan
2	MD-Piano 220	H_2O	25 N	300 r/min	Till close to ROI
2	MD-Largo 9	Largo 9 µm	30 N	150 r/min	7 min
2	MD-Largo 3	Largo 3 µm	22 N	150 r/min	5 min
2	MD-Dur 3	Largo 1 µm	18 - 20 N	150 r/min	4 min
2	MD-Chem	UP-U/H_2O	5 - 15 N	150 r/min	90 s

Bibliography

[1] W. Petry. “Neutrons for research, engineering and medicine in Germany”. In: *Atw Internationale Zeitschrift fuer Kernenergie* 64.10 (2019), pp. 455–462. ISSN: 1431-5254. URL: \url{http://inis.iaea.org/search/search.aspx?orig_q=RN:51004587}.

[2] L. Böning, A. Röhrmoser, W. Petry. “Conversion of the FRM-II”. In: *European Nuclear Society Transactions* (2004), pp. 91–95.

[3] International Atomic Energy Agency. *Data retrieved from the IAEA research reactor database (RRDB)*. 2020. URL: \url{https://nucleus.iaea.org/RRDB}.

[4] Forschungsneutronenquelle Heinz Maier-Leibnitz. *Homepage*. URL: \url{www.frm2.tum.de}.

[5] H. Breitkreutz. “Coupled Neutronics and Thermal Hydraulics of High Density Cores for FRM II”. PhD thesis. Technische Universität München, 2011.

[6] T. C. Wiencek. *Summary report on fuel development and miniplate fabrication for the RERTR program, 1978 to 1990*. 1995.

[7] Reduched Enrichment for Research and Test Reactors - Nuclear Science and Engineering Division at Argonne. URL: \url{https://www.rertr.anl.gov/index.html}.

[8] G. Beghi. “Gamma Phase Uranium–Molybdenum Fuel Alloys”. In: (1968). URL: \url{https://www.osti.gov/biblio/4798265,%20journal%20=}.

[9] G. Hofman. “Design of high density gamma-phase uranium alloys for LEU dispersion fuel applications”. In: (1998). URL: \url{https://www.osti.gov/biblio/11061,journal=}.

[10] R G Loasby. “The Gamma Phase in Uranium Alloys”. In: *Proceedings of the Physical Society* 72.3 (1958), pp. 425–428. DOI: \url{10.1088/0370-1328/72/3/312}.

[11] International Atomic Energy Agency. *Material Properties of Unirradiated Uranium–Molybdenum (U–Mo) Fuel for Research Reactors*. TECDOC Series. Vienna, 2020. ISBN: 978-92-0-115720-1. URL: \url{https://www.iaea.org/publications/14699/material-properties-of-unirradiated-uranium-molybdenum-u-mo-fuel-for-research-reactors}.

[12] Meyer, M. K., Gan, J., Jue, J. F., Keiser, D. D., Perez, E., Robinson, A., Wachs, D. M., Woolstenhulme, N., Hofman, G. L., Kim, Y. S. "Irradiation performance of U-Mo monolithic fuel". In: *Nuclear Engineering and Technology* 46.2 (2014), pp. 169–182. ISSN: 17385733. DOI: \url{10.5516/NET.07.2014.706}.

[13] Y. Kim, G. Hofman, H. Ryu, J. Park, A.B. Robinson, D.M. Wachs. "Modeling of interaction layer growth between U-Mo particles and an Al matrix". In: *Nuclear Engineering and Technology* 45.7 (2013), pp. 827–838. ISSN: 17385733. DOI: \url{10.5516/NET.07.2013.713}.

[14] M. Meyer, G. Hofman, S. Hayes, C. Clark, T. Wiencek, J. Snelgrove, R. Strain, and K.-H Kim. "Low-temperature irradiation behavior of uranium–molybdenum alloy dispersion fuel". In: *Journal of Nuclear Materials* 304.2-3 (2002), pp. 221–236. ISSN: 00223115. DOI: \url{10.1016/S0022-3115(02)00850-4}.

[15] F. Huet, V. Marelle, J. Noirot, P. Sacristan, P. Lemoine. "Full-sized plates irradiation with high UMo fuel loading - Final results of IRIS1 experiment". In: *Proceedings of Reduced Enrichment for Research and Test Reactors (RERTR)* (2003).

[16] F. Huet, J. Noirot, V. Marelle, S. Dubois, P. Boulcourt, P. Sacristan, S. Naury, P. "Post irradiation examinations on UMo full sized plates - IRIS 2 experiment". In: *Proceedings of Reduced Enrichment for Research and Test Reactors (RERTR)* (2005).

[17] A. Leenaers, S. van den Berghe, W. van Renterghem, F. Charollais, P. Lemoine, C. Jarousse, A. Röhrmoser, and W. Petry. "Irradiation behavior of ground U(Mo) fuel with and without Si added to the matrix". In: *Journal of Nuclear Materials* 412.1 (2011), pp. 41–52. ISSN: 00223115. DOI: \url{10.1016/j.jnucmat.2011.02.002}.

[18] A. Leenaers, S. van den Berghe, E. Koonen, C. Jarousse, F. Huet, M. Trotabas, M. Boyard, S. Guillot, L. Sannen, and M. Verwerft. "Post-irradiation examination of uranium-7wt molybdenum atomized dispersion fuel". In: *Journal of Nuclear Materials* 335.1 (2004), pp. 39–47. ISSN: 00223115. DOI: \url{10.1016/j.jnucmat.2004.07.004}.

[19] S. van den Berghe, W. van Renterghem, and A. Leenaers. "Transmission electron microscopy investigation of irradiated U–7wt%Mo dispersion fuel". In: *Journal of Nuclear Materials* 375.3 (2008), pp. 340–346. ISSN: 00223115. DOI: \url{10.1016/j.jnucmat.2007.12.006}.

[20] A. Röhrmoser, W. Petry, P. Boulcourt, A. Chabre, S. Dubois, P. Lemoine, C. Jarousse, J. Falgoux. "UMo full plate size irradiation experiment IRIS - TUM - a progress report". In: *Research Reactor Fuel Management (RRFM)* (2008).

[21] Van den Berghe. "Swelling of U(Mo)–Al(Si) dispersion fuel under irradiation – Non-destructive analyses of the LEONIDAS E-FUTURE plates". In: (2012).

[22] A. Leenaers, J. Van Eyken, S. Van den Berghe, E. Koonen. "LEONIDAS E-FUTURE : Results of the Destructive Analyses of the U(Mo)-Al(Si) Fuel Plates". In: *Proceedings of the European Research Reactor Conference (RRFM)* (2012).

[23] A. Leenaers, S. van den Berghe, S. Dubois, J. Noirot, M. Ripert, and P. Lemoine. "Microstructural analysis of irradiated atomized U (Mo) dispersion fuel in an Al matrix with Si addition". In: *Proceedings of the European Research Reactor Conference (RRFM)* (2008).

[24] A. Leenaers, S. Van den Berghe, E. Koonen, V. Kuzminov, and C. Detavernier. "Fuel swelling and interaction layer formation in the SELENIUM Si and ZrN coated U(Mo) dispersion fuel plates irradiated at high power in BR2". In: *Journal of Nuclear Materials* 458 (2015), pp. 380–393. ISSN: 00223115. DOI: \url{10.1016/j.jnucmat.2014.12.073}. URL: \url{http://www.sciencedirect.com/science/article/pii/S0022311514010150}.

[25] A. Leenaers, W. van Renterghem, and S. van den Berghe. "High burn-up structure of U(Mo) dispersion fuel". In: *Journal of Nuclear Materials* 476 (2016), pp. 218–230. ISSN: 00223115. DOI: \url{10.1016/j.jnucmat.2016.04.035}.

[26] R. Jungwirth. "Irradiation behavior of modified high-performance nuclear fuels". PhD thesis. Technische Universität München, 2011.

[27] T. Zweifel. "Fission Gas Behaviour and Interdiffusion Layer Growth in in-pile and out-of-pile Irradiated U-Mo/Al Nuclear Fuels". PhD thesis. Technische Universität München, 2014.

[28] Hsin-Yin Chiang. “Material Selection of UMo Fuel for Research Reactors: Swift Heavy Ion Irradiation Studies”. PhD thesis. Technische Universität München, 2014.

[29] H. Breitkreutz, J. Hingerl, A. Heldmann, Ch. Steyer, T. Zweifel, R. Jungwirth, J. Shi, W. Petry. “Quantitative comparability of heavy ion and in-pile irradiations on UMo fuel systems”. In: *Journal of Nuclear Materials* 507 (2018), pp. 276–287. ISSN: 00223115. DOI: \url{10.1016/j.jnucmat.2018.04.007}.

[30] K. T. Conlon and D. F. Sears. “Neutron powder diffraction of irradiated low-enriched uranium-molybdenum dispersion fuel”. In: *Proceedings of the European Research Reactor Conference (RRFM)* (2006), p. 104.

[31] H. Palancher, N. Wieschalla, P. Martin, R. Tucoulou, C. Sabathier, W. Petry, J.-F. Berar, C. Valot, and S. Dubois. “Uranium-molybdenum nuclear fuel plates behaviour under heavy ion irradiation: An X-ray diffraction analysis”. In: *Journal of Nuclear Materials* 385.2 (2009), pp. 449–455. ISSN: 00223115. DOI: \url{10.1016/j.jnucmat.2008.12.032}.

[32] B. Ye, S. Bhattacharya, K. Mo, D. Yun, W. Mohamed, M. Pellin, J. Fortner, Y. S. Kim, G. L. Hofman, A. M. Yacout, T. Wiencek, S. van den Berghe, and A. Leenaers. “Irradiation behavior study of U-Mo/Al dispersion fuel with high energy Xe”. In: *Journal of Nuclear Materials* 464 (2015), pp. 236–244. ISSN: 00223115. DOI: \url{10.1016/j.jnucmat.2015.04.051}.

[33] H.-Y. Chiang, T. Zweifel, H. Palancher, A. Bonnin, L. Beck, P. Weiser, M. Döblinger, C. Sabathier, R. Jungwirth, and W. Petry. “Evidence of amorphous interdiffusion layer in heavy ion irradiated U–8wt%Mo/Al interfaces”. In: *Journal of Nuclear Materials* 440.1-3 (2013), pp. 117–123. ISSN: 00223115. DOI: \url{10.1016/j.jnucmat.2013.04.053}.

[34] O. Hahn and F. Strassmann. “Über den Nachweis und das Verhalten der bei der Bestrahlung des Urans mittels Neutronen entstehenden Erdalkalimetalle”. In: *Naturwissenschaften* 27.1 (1939), pp. 11–15.

[35] L. WILETS. “Theories of nuclear fission”. In: *Nuclear Physics* 59.4 (1964), p. 691. ISSN: 0029-5582. DOI: \url{10.1016/0029-5582(64)90063-X}. URL: \url{http://www.sciencedirect.com/science/article/pii/002955826490063X}.

[36] H. J. Krappe and K. Pomorski. *Theory of nuclear fission: A textbook*. Vol. 838. Lecture notes in physics. Heidelberg: Springer, 2012. ISBN: 978-3-642-23515-3.

[37] M. Lounsbury. "The natural abundances of the uranium isotopes". In: *Canadian Journal of Chemistry* 34.3 (1956), pp. 259–264.

[38] J. Terrell. "Fission neutron spectra and nuclear temperatures". In: *Physical Review* 113.2 (1959), p. 527.

[39] Grummitt, W. E., Wilkinson, G. "Fission products of U235". In: *Nature* 158 (1946), p. 163. ISSN: 0028-0836. DOI: \url{10.1038/158163a0}.

[40] J. K. Shultis and R. E. Faw. *Fundamentals of nuclear science and engineering*. New York: Dekker, 2002. ISBN: 9780824708344. URL: \url{http://www.loc.gov/catdir/enhancements/fy0647/2002073395-d.html}.

[41] V. I. Kopeikin, L. A. Mikaelyan, and V. V. Sinev. "Reactor as a source of antineutrinos: Thermal fission energy". In: *Physics of Atomic Nuclei* 67.10 (2004), pp. 1892–1899. ISSN: 1562-692X. DOI: \url{10.1134/1.1811196}.

[42] J. A. Brinkman. "On the Nature of Radiation Damage in Metals". In: *Journal of Applied Physics* 25.8 (1954), pp. 961–970. ISSN: 0021-8979. DOI: \url{10.1063/1.1721810}.

[43] B. T. Kelly. *Irradiation damage to solids*. [1st ed.] The Commonwealth and international library. Metallurgy division. Oxford and New York: Pergamon Press, 1966. ISBN: 978-0080119113.

[44] K. E. Sickafus, E. A. Kotomin, and B. P. Uberuaga. *Radiation effects in solids*. Vol. 235. NATO science series 2, Mathematics, physics and chemistry. Dordrecht: Springer, 2007. ISBN: 978-1-4020-5295-8.

[45] Hj. Matzke. "Radiation damage in nuclear materials". In: *Nuclear Instruments and Methods in Physics Research Section B: Beam Interactions with Materials and Atoms* 65.1 (1992), pp. 30–39. ISSN: 0168583X. DOI: \url{10.1016/0168-583X(92)95010-O}. URL: \url{http://www.sciencedirect.com/science/article/pii/0168583X92950100}.

[46] R. J. Bosnak. "Radiation Damage: Its Mechanisms and Manifestations in Reactor Materials". In: *Journal of the American Society for Naval Engineers* 72.1 (1960), pp. 15–24. ISSN: 00997056. DOI: \url{10.1111/j.1559-3584.1960.tb02355.x}.

[47] Mark T. Robinson. "Basic physics of radiation damage production". In: *Journal of Nuclear Materials* 216 (1994), pp. 1–28. ISSN: 00223115. DOI: \url{10.1016/0022-3115(94)90003-5}. URL: \url{http://www.sciencedirect.com/science/article/pii/0022311594900035}.

[48] M. Nastasi and J. W. Mayer. *Ion Implantation and Synthesis of Materials: Displacements and Radiation Damage*. Berlin, Heidelberg: Springer Berlin Heidelberg, 2006. ISBN: 978-3-540-23674-0. DOI: \url{10.1007/978-3-540-45298-0}.

[49] J. Frenkel. "Über die Wärmebewegung in festen und flüssigen Körpern". In: *Zeitschrift fr Physik* 35.8-9 (1926), pp. 652–669. ISSN: 1434-6001. DOI: \url{10.1007/BF01379812}.

[50] K. Nordlund, S. J. Zinkle, A. E. Sand, F. Granberg, R. S. Averback, R. E. Stoller, T. Suzudo, L. Malerba, F. Banhart, W. J. Weber, F. Willaime, S. L. Dudarev, and D. Simeone. "Primary radiation damage: A review of current understanding and models". In: *Journal of Nuclear Materials* 512 (2018), pp. 450–479. ISSN: 00223115. DOI: \url{10.1016/j.jnucmat.2018.10.027}.

[51] M.J. Norgett, M.T. Robinson, and I.M. Torrens. "A proposed method of calculating displacement dose rates". In: *Nuclear Engineering and Design* 33.1 (1975), pp. 50–54. ISSN: 0029-5493. DOI: \url{10.1016/0029-5493(75)90035-7}. URL: \url{http://www.sciencedirect.com/science/article/pii/0029549375900357}.

[52] G. S. Was. *Fundamentals of radiation materials science: Metals and alloys*. Berlin: Springer, 2007. ISBN: 978-3-540-49471-3.

[53] "Chapter 4: Charged-Particle Stopping Powers and Related Quantities". In: *Journal of the International Commission on Radiation Units and Measurements* 14.1 (2016), pp. 21–30. ISSN: 1473-6691. DOI: \url{10.1093/jicru/ndw031}. URL: \url{https://academic.oup.com/jicru/article/14/1/21/2468580}.

[54] N. Tsoulfanidis. *Measurement and detection of radiation*. 2. ed. Washington: Taylor & Francis, 1995. ISBN: 1560323175.

[55] R. S. Averback and Diaz De La Rubia, T. "Displacement damage in irradiated metals and semiconductors". In: *Solid state physics (New York. 1955)* 51 (1997), pp. 281–402.

[56] J. Knipp and E. Teller. "On the Energy Loss of Heavy Ions". In: *Physical Review* 59.8 (1941), pp. 659–669. ISSN: 0031-899X. DOI: \url{10.1103/PhysRev.59.659}.

[57] William J. Weber, Dorothy M. Duffy, Lionel Thomé, and Yanwen Zhang. "The role of electronic energy loss in ion beam modification of materials". In: *Current Opinion in Solid State and Materials Science* 19.1 (2015), pp. 1–11. ISSN: 1359-0286. DOI: \url{10.1016/j.cossms.2014.09.003}. URL: \url{http://www.sciencedirect.com/science/article/pii/S135902861400059X}.

[58] Gary S. Was. "Ion beam modification of metals: Compositional and microstructural changes". In: *Progress in Surface Science* 32.3 (1989), pp. 211–332. ISSN: 0079-6816. DOI: \url{10.1016/0079-6816(89)90005-1}. URL: \url{http://www.sciencedirect.com/science/article/pii/0079681689900051}.

[59] Y.-T. Cheng, X.-A. Zhao, T. Banwell, T. W. Workman, M.-A. Nicolet, and W. L. Johnson. "Correlation between the cohesive energy and the onset of radiation–enhanced diffusion in ion mixing". In: *Journal of Applied Physics* 60.7 (1986), pp. 2615–2617. ISSN: 0021-8979. DOI: \url{10.1063/1.337131}.

[60] Y.-T. Cheng. "Thermodynamic and fractal geometric aspects of ion-solid interactions". In: *Materials Science Reports* 5.2 (1990), pp. 45–97. ISSN: 09202307. DOI: \url{10.1016/S0920-2307(05)80007-6}.

[61] B. M. Paine and J. S. Averback. "Ion beam mixing: Basic experiments". In: *Nuclear Instruments and Methods in Physics Research Section B: Beam Interactions with Materials and Atoms* 7-8 (1985), pp. 666–675. ISSN: 0168583X. DOI: \url{10.1016/0168-583X(85)90451-3}.

[62] P. Sigmund and A. Gras-Marti. "Theoretical aspects of atomic mixing by ion beams". In: *Nuclear Instruments and Methods* 182-183 (1981), pp. 25–41. ISSN: 0029554X. DOI: \url{10.1016/0029-554X(81)90668-6}.

[63] P. K. Haff and Z. E. Switkowski. "Ion–beam–induced atomic mixing". In: *Journal of Applied Physics* 48.8 (1977), pp. 3383–3386. ISSN: 0021-8979. DOI: \url{10.1063/1.324179}.

[64] A. Gras-Marti and P. Sigmund. "Distortion of depth profiles during ion bombardment II. Mixing mechanisms". In: *Nuclear Instruments and Methods* 180.1 (1981), pp. 211–219. ISSN: 0029554X. DOI: \url{10.1016/0029-554X(81)90032-X}.

[65] P. Sigmund and A. Gras-Marti. "Distortion of depth profiles during sputtering". In: *Nuclear Instruments and Methods* 168.1-3 (1980),

pp. 389–394. ISSN: 0029554X. DOI: \url{10.1016/0029-554X(80)91281-1}.

[66] D. Peak and J. S. Averback. "Influences of thermal spikes in ion beam mixing". In: *Nuclear Instruments and Methods in Physics Research Section B: Beam Interactions with Materials and Atoms* 7-8 (1985), pp. 561–565. ISSN: 0168583X. DOI: \url{10.1016/0168-583X(85)90433-1}.

[67] R. S. Averback, D. Peak, L. J. Thompson. "Ion-beam mixing in pure and in immiscible copper bilayer systems". In: *Applied Physics A* 39.1 (1986), pp. 59–64. ISSN: 1432-0630. DOI: \url{10.1007/BF01177164}.

[68] T. Diaz de la Rubia, R. S. Averback, R. Benedek, and W. E. King. "Role of thermal spikes in energetic displacement cascades". In: *Phys. Rev. Lett.* 59.17 (1987), pp. 1930–1933. DOI: \url{10.1103/PhysRevLett.59.1930}. URL: \url{https://link.aps.org/doi/10.1103/PhysRevLett.59.1930}.

[69] D. A. Thompson. "High density cascade effects". In: *Radiation Effects* 56.3-4 (1981), pp. 105–150. ISSN: 0033-7579. DOI: \url{10.1080/00337578108229885}.

[70] P. Sigmund. "Energy density and time constant of heavy–ion–induced elastic–collision spikes in solids". In: *Applied Physics Letters* 25.3 (1974), pp. 169–171. ISSN: 0003-6951. DOI: \url{10.1063/1.1655425}.

[71] S.-J. Kim, M-A. Nicolet, R. S. Averback, D. Peak. "Low-temperature ion-beam mixing in metals". In: *Physical review. B, Condensed matter* 37.1 (1988), pp. 38–49. ISSN: 0163-1829. DOI: \url{10.1103/PhysRevB.37.38}.

[72] G. J. Dienes and A. C. Damask. "Radiation Enhanced Diffusion in Solids". In: *Journal of Applied Physics* 29.12 (1958), pp. 1713–1721. ISSN: 0021-8979.

[73] R. Sizmann. "The effect of radiation upon diffusion in metals". In: *Journal of Nuclear Materials* 69-70 (1978), pp. 386–412. ISSN: 00223115. DOI: \url{10.1016/0022-3115(78)90256-8}.

[74] G. P. Srivastava and D. Weaire. "The theory of the cohesive energies of solids". In: *Advances in Physics* 36.4 (1987), pp. 463–517. ISSN: 0001-8732. DOI: \url{10.1080/00018738700101042}.

[75] F. Rossi, M. Nastasi, M. Cohen, C. Olsen, J. R. Tesmer, and C. Egert. "Ion beam mixing of U-based bilayers". In: *Journal of Materials Research* 6.6 (1991), pp. 1175–1187. ISSN: 0884-2914. DOI: \url{10.1557/JMR.1991.1175}.

[76] Xia, W., Fernandes, M., Hewett, C. A., Lau, S. S., Poker, D. B., & Biersack. "On the temperature dependence and the moving species during ion mixing". In: *Nuclear Instruments and Methods in Physics Research Section B: Beam Interactions with Materials and Atoms* 37-38 (1989), pp. 408–413. ISSN: 0168583X. DOI: \url{10.1016/0168-583X(89)90214-0}.

[77] A. Leenaers, Y. Parthoens, G. Cornelis, V. Kuzminov, E. Koonen, S. van den Berghe, B. Ye, G. L. Hofman, and J. Schulthess. "Effect of fission rate on the microstructure of coated UMo dispersion fuel". In: *Journal of Nuclear Materials* 494 (2017), pp. 10–19. ISSN: 00223115. DOI: \url{10.1016/j.jnucmat.2017.06.036}.

[78] B. Ye, G. L. Hofman, A. Leenaers, A. Bergeron, V. Kuzminov, S. van den Berghe, Y. S. Kim, and H. Wallin. "A modelling study of the inter-diffusion layer formation in U-Mo/Al dispersion fuel plates at high power". In: *Journal of Nuclear Materials* 499 (2018), pp. 191–203. ISSN: 00223115. DOI: \url{10.1016/j.jnucmat.2017.11.035}.

[79] A. R. Miedema. "A simple model for alloys: I. Rules for the alloying behaviour of transition metals". In: 33 (1973), pp. 149–160. URL: \url{https://www.pearl-hifi.com/06_Lit_Archive/02_PEARL_Arch/Vol_16/Sec_53/Philips_Tech_Review/PTechReview-33-1973-149.pdf}.

[80] J. Piraján. *Thermodynamics: Kinetics of Dynamic Systems*. IntechOpen, 2011. ISBN: 9789533076270. URL: \url{https://books.google.de/books?id=jjCaDwAAQBAJ}.

[81] R. F. Zhang and B. X. Liu. "Proposed model for calculating the standard formation enthalpy of binary transition-metal systems". In: *Applied Physics Letters* 81.7 (2002), pp. 1219–1221. ISSN: 0003-6951. DOI: \url{10.1063/1.1499510}.

[82] R. F. Zhang, S. H. Zhang, Z. J. He, J. Jing, and S. H. Sheng. "Miedema Calculator: A thermodynamic platform for predicting formation enthalpies of alloys within framework of Miedema's Theory". In: *Computer Physics Communications* 209 (2016), pp. 58–69. ISSN: 00104655. DOI: \url{10.1016/j.cpc.2016.08.013}.

[83] B. Beeler, Y. Zhang, M. Okuniewski, and C. Deo. "Calculation of the displacement energy of alpha and gamma uranium". In: *Journal of Nuclear Materials* 508 (2018), pp. 181–194. ISSN: 00223115. DOI: \url{10.1016/j.jnucmat.2018.05.039}.

[84] Maier-Leibnitz Laboratory. *Tandem accelerator: Homepage*. URL: \url{https://www.bl.physik.uni-muenchen.de/tandem/index.html}.

[85] N. Wieschalla, A. Bergmaier, P. Böni, K. Böning, G. Dollinger, R. Großmann, W. Petry, A. Röhrmoser, and J. Schneider. "Heavy ion irradiation of U–Mo/Al dispersion fuel". In: *Journal of Nuclear Materials* 357.1-3 (2006), pp. 191–197. ISSN: 00223115. DOI: \url{10.1016/j.jnucmat.2006.06.006}.

[86] S. van den Berghe, Y. Parthoens, F. Charollais, Y. S. Kim, A. Leenaers, E. Koonen, V. Kuzminov, P. Lemoine, C. Jarousse, H. Guyon, D. Wachs, D. Keiser Jr, A. Robinson, J. Stevens, and G. Hofman. "Swelling of U(Mo)-Al(Si) dispersion fuel under irradiation - Non-destructive analyses of the LEONIDAS E-FUTURE plates". In: *Journal of Nuclear Materials* 430.1-3 (2012), pp. 246–258. ISSN: 00223115. DOI: \url{10.1016/j.jnucmat.2012.06.045}.

[87] J. F. Ziegler and J. M. Manoyan. "The stopping of ions in compounds". In: *Nuclear Instruments and Methods in Physics Research Section B: Beam Interactions with Materials and Atoms* 35.3-4 (1988), pp. 215–228. ISSN: 0168583X. DOI: \url{10.1016/0168-583X(88)90273-X}.

[88] J. F. Ziegler, M. D. Ziegler, and J. P. Biersack. "SRIM – The stopping and range of ions in matter (2010)". In: *Nuclear Instruments and Methods in Physics Research Section B: Beam Interactions with Materials and Atoms* 268.11-12 (2010), pp. 1818–1823. ISSN: 0168583X. DOI: \url{10.1016/j.nimb.2010.02.091}.

[89] G H Kinchin and R S Pease. "The Displacement of Atoms in Solids by Radiation". In: *Reports on Progress in Physics* 18.1 (1955), pp. 1–51. DOI: \url{10.1088/0034-4885/18/1/301}.

[90] R.E. Stoller, M.B. Toloczko, G.S. Was, A.G. Certain, S. Dwaraknath, and F.A. Garner. "On the use of SRIM for computing radiation damage exposure". In: *Nuclear Instruments and Methods in Physics Research Section B: Beam Interactions with Materials and Atoms* 310 (2013), pp. 75–80. ISSN: 0168583X. DOI: \url{10.1016/j.nimb.2013.05.008}. URL: \url{http://www.sciencedirect.com/science/article/pii/S0168583X13005053}.

[91] W. J. Weber and Y. Zhang. "Predicting damage production in monoatomic and multi-elemental targets using stopping and range of ions in matter code: Challenges and recommendations". In: *Current Opinion in Solid State and Materials Science* 23.4 (2019), p. 100757. ISSN: 1359-0286. DOI: \url{10.1016/j.cossms.2019.06.001}.

[92] E10 Committee. *Practice for Neutron Radiation Damage Simulation by Charged-Particle Irradiation*. West Conshohocken, PA. DOI: \url{10.1520/E0521-96R03}.

[93] J. G. Webster. *Wiley Encyclopedia of Electrical and Electronics Engineering Plus Supplement 1*. [Place of publication not identified]: Wiley Interscience Imprint, 2001. ISBN: 047134608X.

[94] A. Leenaers, S. Van den Berghe and C. Detavernier. "Coated particle production in the SELENIUM project". In: *Proceedings of the European Research Reactor Conference (RRFM)* (2011).

[95] X. Iltis, H. Palancher, J. Allenou, F. Vanni, B. Stepnik, A. Leenaers, S. van den Berghe, D. D. Keiser, and I. Glagolenko. "Characterization of fresh EMPIrE and SEMPER FIDELIS U(Mo)/Al fuel plates made with PVD-coated U(Mo) particles". In: *EPJ Nuclear Sciences & Technologies* 4 (2018), p. 49. DOI: \url{10.1051/epjn/2018048}.

[96] A. Hecimovic, M. Böke, and J. Winter. "The characteristic shape of emission profiles of plasma spokes in HiPIMS: the role of secondary electrons". In: *Journal of Physics D: Applied Physics* 47.10 (2014), p. 102003. ISSN: 0022-3727. DOI: \url{10.1088/0022-3727/47/10/102003}.

[97] C. Schwarz. "Construction and Commissioning of a Pulsed-DC Sputtering System & Characterization of Sputtered ZrN Layers". In: *Technische Universität München, Master's thesis* (2017).

[98] C. Steyer. "Plasma- und festkörperphysikalische Optimierung eines Beschichtungsverfahrens für monolithische UMo-Kernbrennstoffe (Plasma and Solid-State Physics-Based Optimization of a Coating Process for Monolithic UMo Nuclear Fuels)". PhD thesis. Technische Universität München, 2019.

[99] A. Anders. "A structure zone diagram including plasma-based deposition and ion etching". In: *Thin Solid Films* 518.15 (2010), pp. 4087–4090. ISSN: 00406090. DOI: \url{10.1016/j.tsf.2009.10.145}.

[100] B. A. Movchan and A. V. Demchishin. "Structure and Properties of Thick Condensates of Nickel, Titanium, Tungsten, Aluminum Oxides, and Zirconium Dioxide in Vacuum". In: (1969). URL: \url{https://www.osti.gov/biblio/4181669,journal=Fiz.Metal.Metalloved.28:653-60(Oct1969).}.

[101] J. A. Thornton. "Influence of apparatus geometry and deposition conditions on the structure and topography of thick sputtered coatings". In: *Journal of Vacuum Science and Technology* 11.4 (1974), pp. 666–670. ISSN: 0022-5355. DOI: \url{10.1116/1.1312732}.

[102] J. I. Goldstein and H. Yakowitz. *Practical Scanning Electron Microscopy*. Boston, MA: Springer US, 1975. ISBN: 978-1-4613-4424-7. DOI: \url{10.1007/978-1-4613-4422-3}.

[103] E. Abbe. "Beiträge zur Theorie des Mikroskops und der mikroskopischen Wahrnehmung". In: *Archiv für mikroskopische Anatomie* 9.1 (1873), pp. 413–468.

[104] Z. Wang, W. Guo, L. Li, B. Luk'yanchuk, A. Khan, Z. Liu, Z. Chen, and M. Hong. "Optical virtual imaging at 50 nm lateral resolution with a white-light nanoscope". In: *Nature Communications* 2.1 (2011), p. 218. ISSN: 2041-1723. DOI: \url{10.1038/ncomms1211}.

[105] P. J. Goodhew, F. J. Humphreys, and R. Beanland. *Electron microscopy and analysis*. 3. ed. London: Taylor & Francis, 2001. ISBN: 0-748-40968-8. URL: \url{http://www.loc.gov/catdir/enhancements/fy0652/00037716-d.html}.

[106] L. A. Giannuzzi and F. A. Stevie. *Introduction to focused ion beams: Instrumentation, theory, techniques and practice*. New York: Springer, 2010. ISBN: 978-1441935748.

[107] S. J. Pennycook and P. D. Nellist. *Scanning Transmission Electron Microscopy*. New York, NY: Springer New York, 2011. ISBN: 978-1-4419-7199-9. DOI: \url{10.1007/978-1-4419-7200-2}.

[108] L. Reimer and H. Kohl. *Transmission electron microscopy: Physics of image formation*. 5. ed. Vol. 36. Springer series in optical sciences. New York, NY: Springer, 2008. ISBN: 978-0-387-40093-8.

[109] D. C. Bell and N. Erdman. *Low Voltage Electron Microscopy*. Chichester, UK: John Wiley & Sons, Ltd, 2012. ISBN: 9781118498514. DOI: \url{10.1002/9781118498514}.

[110] R. Erni, M. D. Rossell, C. Kisielowski, and U. Dahmen. "Atomic-Resolution Imaging with a Sub-50-pm Electron Probe". In: *Phys. Rev. Lett.* 102.9 (2009), p. 096101. DOI: \url{10.1103/PhysRevLett.102.096101}. URL: \url{https://link.aps.org/doi/10.1103/PhysRevLett.102.096101}.

[111] S. Utsunomiya and R. C. Ewing. "Application of high-angle annular dark field scanning transmission electron microscopy, scanning transmission electron microscopy-energy dispersive X-ray spectrometry, and energy-filtered transmission electron microscopy to the characterization of nanoparticles in the environment". In: *Environmental science & technology* 37.4 (2003), pp. 786–791. ISSN: 0013-936X. DOI: \url{10.1021/es026053t}.

[112] R. M. Langford and C. Clinton. "In situ lift-out using a FIB-SEM system". In: *Micron (Oxford, England : 1993)* 35.7 (2004), pp. 607–611. ISSN: 0968-4328. DOI: \url{10.1016/j.micron.2004.03.002}.

[113] R. M. Langford and M. Rogers. "In situ lift-out: steps to improve yield and a comparison with other FIB TEM sample preparation techniques". In: *Micron (Oxford, England : 1993)* (2008), pp. 1325–1330. ISSN: 0968-4328. DOI: \url{10.1016/j.micron.2008.02.006}.

[114] A. J. Schwartz. *Electron backscatter diffraction in materials science*. 2. ed. New York, NY: Springer, 2009. ISBN: 978-0-387-88135-5.

[115] A. J. Wilkinson and P. B. Hirsch. "Electron diffraction based techniques in scanning electron microscopy of bulk materials". In: *Micron (Oxford, England : 1993)* 28.4 (1997), pp. 279–308. ISSN: 0968-4328. DOI: \url{10.1016/S0968-4328(97)00032-2}.

[116] J. Hingerl. "Evolution of the inter diffusion layer of UMo/Al nuclear fuels during heavy ion irradiation: Bachelor's thesis". In: *Technische Universität München* (2016).

[117] Y. S. Kim and G. L. Hofman. "Interdiffusion in U3Si-Al, U3Si2-Al, and USi-Al dispersion fuels during irradiation". In: *Journal of Nuclear Materials* 410.1-3 (2011), pp. 1–9. ISSN: 00223115. DOI: \url{10.1016/j.jnucmat.2010.12.031}.

[118] Y. S. Kim, G. L. Hofman, H. J. Ryu, and S. L. Hayes. "Irradiation-enhanced interdiffusion in the diffusion zone of U-Mo dispersion fuel in Al". In: *Journal of Phase Equilibria and Diffusion* 27.6 (2006), pp. 614–621. ISSN: 1547-7037. DOI: \url{10.1007/BF02736563}.

[119] I. Wolfram Research. *Mathematica*. Version 12.1. Champaign, Illinois: Wolfram Research, Inc. URL: \url{https://www.wolfram.com/mathematica}.

[120] Renuka Krishnakumar. "Scintillation Screen Materials for Beam Profile Measurements of High Energy Ion Beams". PhD thesis. Darmstadt: Technischen Universität Darmstadt, 2016.

[121] D. Varentsov, A. D. Fertman, V. I. Turtikov, A. Ulrich, J. Wieser, V. E. Fortov, A. A. Golubev, D. H. H. Hoffmann, A. Hug, M. Kulish, V. Mintsev, P. A. Ni, D. Nikolaev, B. Y. Sharkov, N. Shilkin, V. Y. Ternovoi, and S. Udrea. "Transverse Optical Diagnostics for Intense Focused Heavy Ion Beams". In: *Contributions to Plasma Physics* 48.8 (2008), pp. 586–594. ISSN: 08631042. DOI: \url{10.1002/ctpp.200810092}.

[122] B. Ye, Y. Miao, J. Shi, D. Salvato, K. Mo, L. Jamison, A. Bergeron, G. L. Hofman, A. Leenaers, A. Oaks, A. M. Yacout, S. van den Berghe, W. Petry, and Y. S. Kim. "Temperature Effects on Interdiffusion of Al and U-Mo under Irradiation". In: *Journal of Nuclear Materials* 544 (2021), p. 152684. ISSN: 00223115. DOI: \url{10.1016/j.jnucmat.2020.152684}.

[123] C. Reiter and K. Shehu. *Fuel temperature of FRM II*.

[124] Languille, A, Plancq, D, Huet, F, Guigon, B, Lemoine, P, Sacristan, P, Hofman, G, Snelgrove, J, Rest, J, Hayes, S, Meyer, M, Vacelet, H, Leborgne, E and G. Dassel. *Experimental irradiation of UMo fuel: Pie results and modeling of fuel behaviour*. 2002.

[125] H. J. Ryu, Y. S. Kim, and G. Hofman. "Amorphization of the interaction products in U–Mo/Al dispersion fuel during irradiation". In: *Journal of Nuclear Materials* 385.3 (2009), pp. 623–628. ISSN: 00223115. DOI: \url{10.1016/j.jnucmat.2009.01.306}.

[126] M. I. Mirandou, S. N. Balart, M. Ortiz, and M. S. Granovsky. "Characterization of the reaction layer in U-7wt%Mo/Al diffusion couples". In: *Journal of Nuclear Materials* 323.1 (2003), pp. 29–35. ISSN: 00223115. DOI: \url{10.1016/j.jnucmat.2003.07.006}.

[127] O. A. Golosov, v. B. Semerikov, A. E. Teplykh, M. S. Lyutikova, E. F. Kartashev, and v. A. Lukichev. "Structure studies of dispersed U-Mo fuel after irradiation and isochronous annealing within the temperature range of 150-580 deg C by the neutron diffraction method". In: *Proceedings of the European Research Reactor Conference (RRFM)* (2007).

[128] Y. Miao, B. Ye, J. Shi, K. Mo, L. Jamison, S. Bhattacharya, A. Oaks, W. Petry, and A. M. Yacout. "Microstructure investigations of temperature effect on Al-UMo diffusion couples irradiated by swift Xe ions". In: *Journal of Nuclear Materials* 547 (2021), p. 152757. ISSN: 00223115. DOI: \url{10.1016/j.jnucmat.2020.152757}.

[129] P. Villars, L. D. Calvert, and W. B. Pearson. *Pearson's handbook of crystallographic data for intermetallic phases*. Metals Park, Ohio: ASM Internat, 1985. ISBN: 978-0871704160.

[130] Y. Miao, L. A. Nimmagadda, M. C. Rajagopal, K. Mo, J. Shi, B. Ye, L. Jamison, Y. S. Kim, W. Petry, S. Sinha, and A. M. Yacout. "Thermal conductivity measurement of the interaction layer between UMo and Al produced by high-energy heavy ion irradiation". In: *Journal of Nuclear Materials* 539 (2020), p. 152262. ISSN: 00223115. DOI: \url{10.1016/j.jnucmat.2020.152262}.

[131] C. Trautmann, W. Brüchle, R. Spohr, J. Vetter, and N. Angert. "Pore geometry of etched ion tracks in polyimide". In: *Nuclear Instruments and Methods in Physics Research Section B: Beam Interactions with Materials and Atoms* 111.1-2 (1996), pp. 70–74. ISSN: 0168583X. DOI: \url{10.1016/0168-583X(95)01264-8}.

[132] M. Toulemonde, S. Bouffard, and F. Studer. "Swift heavy ions in insulating and conducting oxides: tracks and physical properties". In: *Nuclear Instruments and Methods in Physics Research Section B: Beam Interactions with Materials and Atoms* 91.1-4 (1994), pp. 108–123. ISSN: 0168583X. DOI: \url{10.1016/0168-583X(94)96200-6}.

[133] F. Huet, J. Noirot, V. Marelle, S. Dubois, P. Boulcourt, P. Sacristan, S. Naury, and P. Lemoine. *Post irradiation examinations on UMo full-sized plates-IRIS2 experiment*. 2005.

[134] G. V. Samsonov. *Refractory Transition Metal Compounds: High Temperature Cermets*. Burlington: Elsevier Science, 1964. ISBN: 9781483228037.

[135] H.-Y. Chiang, S.-H. Park, M. Mayer, K. Schmid, M. Balden, U. Boesenberg, R. Jungwirth, G. Falkenberg, T. Zweifel, and W. Petry. "Swift heavy ion irradiation induced interactions in the UMo/X/Al trilayer system (X=Ti, Zr, Nb, and Mo): RBS and micro-XRD studies". In: *Journal of Alloys and Compounds* 626 (2015), pp. 381–390. ISSN: 09258388. DOI: \url{10.1016/j.jallcom.2014.12.041}.

[136] F. R. d. Boer. *Cohesion in metals: Transition metal alloys*. 2., corr. print. Vol. 1. Cohesion and structure. Amsterdam: North Holland, 1988. ISBN: 0-444-87098-9.

[137] H. Bakker. *Enthalpies in Alloys: Miedema's semi-empirical model*. Vol. 1. Materials science foundations. Ueticon-Zuerich: Trans Tech Publ, 1998. ISBN: 9780878497836.

[138] Sabine Matuschik. "Production and Heavy-Ion Irradiation of Tungsten Coatings as Diffusion Barrier in the U-Mo/Al Fuel System". In: *Technische Universität München, Bachelor's thesis* (2020).

[139] A. Leenaers, J. Van Eyken, J. Wight, S. Van den Berghe, B. Stepnik, B. Baumeister, H. Palancher, Y. Calzavara. "SEMPER FIDELIS - PIE progress (presentation)". In: *Proceedings of the European Research Reactor Conference (RRFM)* (2019).

[140] A. Leenaers, J. Van Eyken, J. Wight, S. Van den Berghe. "First PIE results (presentation)". In: *Proceedings of Reduced Enrichment for Research and Test Reactors (RERTR)* (2019).

[141] A. Leenaers. "Surface-engineered low-enriched Uranium-Molybdenum fuel for research reactors". PhD thesis. University of Ghent, 2014.

[142] A. L. Izhutov, V. V. Alexandrov, N. A.E., V. A. Starkov, V. E. Fedoseev, V. V. Pimenov, A. V. Sheldyakov, V. Y. Shishin, V. V. Yakovlev, I. V. Dobrikova, A. V. Vatulin, V. B. Suprun and K. G.V. "The main results of investigation of modified dispersion LEU U-Mo Fuel tested in the MIR reactor". In: *Proceedings of Reduced Enrichment for Research and Test Reactors (RERTR)* (2010).

[143] R. Jungwirth, T. Zweifel, H.-Y. Chiang, W. Petry, S. van den Berghe, and A. Leenaers. "Heavy ion irradiation of UMo/Al samples PVD coated with Si and ZrN layers". In: *Journal of Nuclear Materials* 434.1-3 (2013), pp. 296–302. ISSN: 00223115. DOI: \url{10.1016/j.jnucmat.2012.11.032}.

[144] A. Leenaers, S. van den Berghe, E. Koonen, V. Kuzminov, and C. Detavernier. "Fuel swelling and interaction layer formation in the SELENIUM Si and ZrN coated U(Mo) dispersion fuel plates irradiated at high power in BR2". In: *Journal of Nuclear Materials* 458 (2015), pp. 380–393. ISSN: 00223115. DOI: \url{10.1016/j.jnucmat.2014.12.073}.

[145] B. D. Miller, D. D. Keiser, M. Abir, A. Aitkaliyeva, A. Leenaers, B. J. Hernandez, W. van Renterghem, and A. Winston. "3D reconstructions of irradiated U Mo fuel to understand breaching effects in ZrN diffusion barriers". In: *Journal of Nuclear Materials* 510 (2018), pp. 431–436. ISSN: 00223115. DOI: \url{10.1016/j.jnucmat.2018.08.016}.

[146] F. Housaer, F. Vanni, M. Touzin, F. Béclin, J. Allenou, A. Leenaers, A. M. Yacout, H. Palancher, B. Stepnik, and O. Tougait. "Morphological characterization of the fresh ZrN coated UMo powders used in EMPIrE irradiation experiment: A practical approach". In: *Journal of Nuclear*

Materials 533 (2020), p. 152087. ISSN: 00223115. DOI: \url{10.1016/j.jnucmat.2020.152087}.

[147] A. Singh, P. Kuppusami, S. Khan, C. Sudha, R. Thirumurugesan, R. Ramaseshan, R. Divakar, E. Mohandas, and S. Dash. "Influence of nitrogen flow rate on microstructural and nanomechanical properties of Zr–N thin films prepared by pulsed DC magnetron sputtering". In: *Applied Surface Science* 280 (2013), pp. 117–123. ISSN: 01694332. DOI: \url{10.1016/j.apsusc.2013.04.107}.

[148] J. Adachi, K. Kurosaki, M. Uno, and S. Yamanaka. "Thermal and electrical properties of zirconium nitride". In: *Journal of Alloys and Compounds* 399.1-2 (2005), pp. 242–244. ISSN: 09258388. DOI: \url{10.1016/j.jallcom.2005.03.005}.

[149] K. M. Ralls, T. H. Courtney, and J. Wulff. *Introduction to materials science and engineering*. New York: Wiley, 1976. ISBN: 0471706655.

[150] D. D. Keiser, E. Perez, T. Wiencek, A. Leenaers, and S. van den Berghe. "Microstructural characterization of a thin film ZrN diffusion barrier in an As-fabricated U–7Mo/Al matrix dispersion fuel plate". In: *Journal of Nuclear Materials* 458 (2015), pp. 406–418. ISSN: 00223115. DOI: \url{10.1016/j.jnucmat.2014.12.036}.

[151] Johannes Gallitscher. "Bildung von UMo-Al-Interdiffusionsschichten durch Risse im ZrN Coating". In: *Technische Universität München, Master's thesis* (2019).

[152] J. Rest. "The effect of irradiation-induced gas-atom re-solution on grain-boundary bubble growth". In: *Journal of Nuclear Materials* 321.2-3 (2003), pp. 305–312. ISSN: 00223115. DOI: \url{10.1016/s0022-3115(03)00303-9}.

[153] J. Rest. "A model for the effect of the progression of irradiation-induced recrystallization from initiation to completion on swelling of UO2 and U–10Mo nuclear fuels". In: *Journal of Nuclear Materials* 346.2-3 (2005), pp. 226–232. ISSN: 00223115. DOI: \url{10.1016/j.jnucmat.2005.06.012}.

[154] Y. S. Kim, G. Hofman, and J. S. Cheon. "Recrystallization and fission-gas-bubble swelling of U–Mo fuel". In: *Journal of Nuclear Materials* 436.1-3 (2013), pp. 14–22. ISSN: 00223115. DOI: \url{10.1016/j.jnucmat.2013.01.291}.

[155] J. Gan, B. Miller, D. Keiser, J. Jue, J. W. Madden, A. Robinson, H. Ozaltun, G. A. Moore, and M. K. Meyer. "Irradiated microstructure of U-10Mo monolithic fuel plate at very high fission density". In: *Journal of Nuclear Materials* 492 (2017), pp. 195–203. ISSN: 00223115.

[156] K. Nogita, K. Une, M. Hirai, K. Ito, and Y. Shirai. "Effect of grain size on recrystallization in high burnup fuel pellets". In: *Journal of Nuclear Materials* 248 (1997), pp. 196–203. ISSN: 00223115. DOI: \url{10.1016/S0022-3115(97)00156-6}.

[157] C. M. Sellars. "Recrystallization of metals during hot deformation". In: *Philosophical Transactions of the Royal Society of London. Series A, Mathematical and Physical Sciences* 288.1350 (1978), pp. 147–158. ISSN: 0080-4614. DOI: \url{10.1098/rsta.1978.0010}.

[158] D. Jadernas, J. Gan, D. Keiser, J. Madden, M. Bachhav, J.-F. Jue, and A. Robinson. "Microstructural characterization of as-fabricated and irradiated U-Mo fuel using SEM/EBSD". In: *Journal of Nuclear Materials* 509 (2018), pp. 1–8. ISSN: 00223115. DOI: \url{10.1016/j.jnucmat.2018.06.007}.

[159] J. L. Brimhall. "Effect of irradiation particle mass on crystallization of amorphous alloys". In: *Journal of Materials Science* 19.6 (1984), pp. 1818–1826. ISSN: 1573-4803. DOI: \url{10.1007/BF00550252}.

[160] C. Schwarz, T. Dirks, B. Baumeister, C. Steyer, W. Petry. "All-in-one chemical cleaning and deoxidation process for monolithic uranium-molybdenum foils". In: *Proceedings of the European Research Reactor Conference (RRFM)* (2016).

[161] V. V. Rondinella and T. Wiss. "The high burn-up structure in nuclear fuel". In: *Materials Today* 13.12 (2010), pp. 24–32. ISSN: 13697021. DOI: \url{10.1016/S1369-7021(10)70221-2}.

[162] COMSOL Inc. *COMSOL*. 2020. URL: \url{http://www.comsol.com/products/multiphysics/}.

[163] J. Rest, Y. S. Kim, G. L. Hofman, M. K. Meyer, and S. L. Hayes. "U-Mo fuels handbook". In: *Nuclear Engineering Division, Argonne National Laboratory, Argonne/IL* (2009).

[164] Burkes, G. S. Mickum, D. M. Wachs, et al. *Thermo-physical Properties of U-10Mo Alloy*. 2010.

[165] S. I. Wright and M. M. Nowell. "EBSD image quality mapping". In: *Microscopy and microanalysis : the official journal of Microscopy Society of America, Microbeam Analysis Society, Microscopical Society of Canada* 12.1 (2006), pp. 72–84. ISSN: 1431-9276. DOI: \url{10 . 1017 / S1431927606060090}.

[166] H. Matzke and M. Kinoshita. "Polygonization and high burnup structure in nuclear fuels". In: *Journal of Nuclear Materials* 247 (1997), pp. 108–115. ISSN: 00223115. DOI: \url{10.1016/S0022-3115(97)00081-0}.

[167] Y. Miao, T. Yao, J. Lian, S. Zhu, S. Bhattacharya, A. Oaks, A. M. Yacout, and K. Mo. "Nano-crystallization induced by high-energy heavy ion irradiation in UO2". In: *Scripta Materialia* 155 (2018), pp. 169–174. ISSN: 13596462. DOI: \url{10.1016/j.scriptamat.2018.04.006}.

[168] D. Salvato, A. Leenaers, W. Van Renterghem, S. Van den Berghe, C. Detavernier, and J.H. Evans. "The initial formation stages of a nanobubble lattice in neutron irradiated U(Mo)". In: *Journal of Nuclear Materials* 529 (2020), p. 151947. ISSN: 00223115. DOI: \url{10.1016/j.jnucmat.2019.151947}. URL: \url{http://www.sciencedirect.com/science/article/pii/S0022311519313388}.

[169] A. Hallén, D. Fenyö, B. U. R. Sundqvist, R. E. Johnson, and B. G. Svensson. "The influence of ion flux on defect production in MeV proton–irradiated silicon". In: *Journal of Applied Physics* 70.6 (1991), pp. 3025–3030. ISSN: 0021-8979. DOI: \url{10.1063/1.349333}.

Publications

- Shi, J., Onofri, C., Palancher, H., Iltis, X., Drouan, D., Breitkreutz, H., Petry, W. (2020). Microstructure evolution and phase transformation of heavy-ion irradiated U–Mo/Al fuels. Journal of Nuclear Materials, 541(152399), 152399.

- Shi, J., Salvato, D., Breitkreutz, H., Van Renterghem, W., Baumeister, B., Schwarz, C., Leenaers, A., Van den Berghe, S., Detavernier, C., Petry, W. (2021). U(Mo) grain refinement induced by irradiation with high energy iodine. Journal of Nuclear Materials, 548(152850), 152850.

- Ye, B., Miao, Y., Shi, J., Salvato, D., Mo, K., Jamison, L., Bergeron, A., Hofman, G. L., Leenaers, A., Oaks, A., Yacout, A. M., Van den Berghe, S., Petry, W., Kim, Y. S. (2021). Temperature effects on interdiffusion of Al and U-Mo under irradiation. Journal of Nuclear Materials, 544(152684), 152684.

- Miao, Y., Ye, B., Shi, J., Mo, K., Jamison, L., Bhattacharya, S., Oaks, A., Petry, W., Yacout, A. M. (2021). Microstructure investigations of temperature effect on Al-UMo diffusion couples irradiated by swift Xe ions. Journal of Nuclear Materials, 547(152757), 152757.

- Breitkreutz, H., Heldmann, A., Hingerl, J., Jungwirth, R., Shi, J., Petry, W. (2018). Quantitative comparability of heavy ion and in-pile irradiations on UMo fuel systems. Journal of Nuclear Materials, 507, 276–287.

- Miao, Y., Nimmagadda, L. A., Rajagopal, M. C., Mo, K., Shi, J., Ye, B., Jamison, L., Kim, Y. S., Petry, W., Sinha, S., Yacout, A. M. (2020). Thermal conductivity measurement of the interaction layer between UMo and Al produced by high-energy heavy ion irradiation. Journal of Nuclear Materials, 539(152262), 152262.

- Shi, J., Breitkreutz, H., Petry, W. (2018). Quantitatively simulating fission-enhanced diffusion in U-Mo/Al bilayer systems by swift heavy ion irradiation. In Proceedings of the European Research Reactor Conference (RRFM), Munich, Germany.

Acknowledgements

A PhD is an arduous journey, but fortunately, I was never alone in this adventure. Without the support of many people, I would not be able to arrive at the final destination. Each of you has played an important role during this journey and contributed to this work. I owe you all my sincere thanks.

First and foremost, I would like to express my deep gratitude to my supervisor **Prof. Dr. Winfried Petry** for your guidance and unrelenting support. Your dynamics and immense knowledge have inspired me all the time. You are my best role model for a scientist.

I cannot express enough thanks to **Dr. Harald Breitkreutz** for being a generous and inspirational mentor throughout my PhD, and for all the insightful discussions you provided me. Your solid advice continually steering me in the right direction – just like the steerers do to the ion beam at the accelerator!

My former and present colleagues from the HEU-MEU group of the FRM II:

Christian Schwarz, **Kaltrina Shehu**, **Dr. Tobias Chemnitz**, **Julia Mausz**, **Bruno Baumeister**, **Dr. Christian Reiter**, **Silvia Valentin** and **Dr. Christian Steyer**. Thank you for making the office an enjoyable place.

Nicholas Rehms, **Thomas Kerschl** and **Serhat Polat**. Working with uranium is impossible without your excellent collaboration.

And of course our enthusiastic students, your dedicated involvement contributed to this work.

It should be emphasized that the beamtimes would not have been accomplished without your generous support by taking shifts even during nights or on holidays!

The beamtimes were not possible without the continued support of the professional team of the MLL accelerator in Garching: **Dr. Ludwig Beck**, **Peter Hartung**, **Michael Pelzer** and **Christine Singer**. I especially thank **Michael Wiesheu** for solving many tricky technical issues of the accelerator and rescuing our beamtime many times!

I thank **Dr. Abdellatif M. Yacout**, **Dr. Bei Ye** and **Dr. Yinbin Miao** from

Argonne National Laboratory, not just for hosting me during my stay, but also for your consistent help and advise. I look forward to our continued collaboration.

I would like to thank **Dr. Ann Leenaers**, **Dr. Salvato Daniele** and **Dr. Vouter Van Renterghem** from SCK CEN for the fruitful collaborations. It has truly been a pleasant experience working with you.

With many thanks to **Dr. Hervé Palancher** and **Dr. Claire Onofri** form CEA Cadarache. I appreciate all the support I received during the TEM experiments and the inspiring discussions.

I also thank **Manfred Pfaller** and **Manfred Reither** from the central workshop of the TUM physics department for their professional advice. Every part of my requests was neatly done!

I cannot forget to thank my dear friends in Germany, China, and the United States for always being there for me especially when things were a bit discouraging. I cannot list all the names but you know who you are!

I am deeply indebted to my parents. Even with the distance of 8120 km, your unceasing encouragement was always the "fuel" throughout my years of study. I believe the situation will get better soon and we will finally see each other again after two years.

List of Figures

List of Tables